



## **Terms and Conditions of Use of Digitised Theses from Trinity College Library Dublin**

### **Copyright statement**

All material supplied by Trinity College Library is protected by copyright (under the Copyright and Related Rights Act, 2000 as amended) and other relevant Intellectual Property Rights. By accessing and using a Digitised Thesis from Trinity College Library you acknowledge that all Intellectual Property Rights in any Works supplied are the sole and exclusive property of the copyright and/or other IPR holder. Specific copyright holders may not be explicitly identified. Use of materials from other sources within a thesis should not be construed as a claim over them.

A non-exclusive, non-transferable licence is hereby granted to those using or reproducing, in whole or in part, the material for valid purposes, providing the copyright owners are acknowledged using the normal conventions. Where specific permission to use material is required, this is identified and such permission must be sought from the copyright holder or agency cited.

### **Liability statement**

By using a Digitised Thesis, I accept that Trinity College Dublin bears no legal responsibility for the accuracy, legality or comprehensiveness of materials contained within the thesis, and that Trinity College Dublin accepts no liability for indirect, consequential, or incidental, damages or losses arising from use of the thesis for whatever reason. Information located in a thesis may be subject to specific use constraints, details of which may not be explicitly described. It is the responsibility of potential and actual users to be aware of such constraints and to abide by them. By making use of material from a digitised thesis, you accept these copyright and disclaimer provisions. Where it is brought to the attention of Trinity College Library that there may be a breach of copyright or other restraint, it is the policy to withdraw or take down access to a thesis while the issue is being resolved.

### **Access Agreement**

By using a Digitised Thesis from Trinity College Library you are bound by the following Terms & Conditions. Please read them carefully.

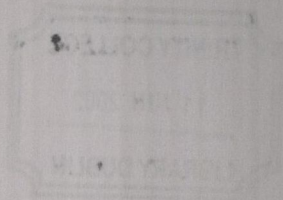
I have read and I understand the following statement: All material supplied via a Digitised Thesis from Trinity College Library is protected by copyright and other intellectual property rights, and duplication or sale of all or part of any of a thesis is not permitted, except that material may be duplicated by you for your research use or for educational purposes in electronic or print form providing the copyright owners are acknowledged using the normal conventions. You must obtain permission for any other use. Electronic or print copies may not be offered, whether for sale or otherwise to anyone. This copy has been supplied on the understanding that it is copyright material and that no quotation from the thesis may be published without proper acknowledgement.



**The University of Dublin  
Trinity College**



**Dispersion of the Third Order Optical  
Nonlinearity & All-Optical Switching  
Figures of Merit in Molecularly  
Engineered Polymers**



*Thesis submitted for the degree of  
Doctor in Philosophy*

***Kieran Ryder***

***Department of Pure and Applied Physics,  
University of Dublin,  
Trinity College,  
Dublin 2.***

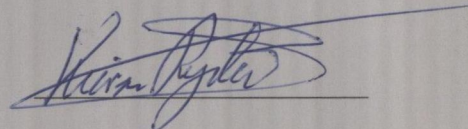
November 2001

## Declaration

This thesis is submitted to the University of Dublin for the degree of Doctor in Philosophy. The work described herein is entirely my own, with the exception of the assistance mentioned in the acknowledgements.

This thesis has not been submitted as an exercise for a degree to this or any other university.

I agree that the University of Dublin may lend or copy this thesis upon request.

A handwritten signature in blue ink, reading "Kieran Ryder", written over a horizontal line.

Kieran Ryder

*For Mum, Dad, Mary, Tom & Christine*

## **Acknowledgements**

I would like to thank my supervisor Professor Werner Blau for giving me the opportunity to do this Ph.D. as a part of his group at the University of Dublin, and for his understanding and support at all times. This is especially true for the last two years. The subtle encouragement at key times seems to have done the trick. Thank you Werner. Thank you to all members of group Bu, past and present, for good company, for many discussions on physics and other issues, and for many good times.

Thank you especially to Andy Davey for his assistance on all aspects of chemistry and physics. His talks and advice were invaluable. His talents I think would put many a physicist to shame, despite having his Ph.D. in Chemistry. In a way, he was my role model while I was there. I think however, that I failed miserably at achieving anything close to the level of professionalism, which Andy seemed to have at his disposal. Thanks to Anna Drury for synthesising the polymers all the enforced tidying up sessions. She had a tough time trying to keep everything and everyone in check over the years, all the while being in seemingly good form – a rare trait indeed. Some of her “stories” which privileged few were treated to on the yearly trips were very interesting and “colourful”. . Many thanks Anna.

To David Gray I owe thanks for the many informative talks and demonstrations on the YAG laser. He showed me just the right places to “tap” the mode locker to get it into a good mood. He was also invaluable in helping me put together the C++ program to control all of the experiments. His temperament was exceptional, especially whenever I “borrowed” some equipment on occasion. I don’t think the lad ever learned to scream or lose his temper. Mind you I definitely don’t want to be around whenever he snaps! To Seamus Curran who was there at the very beginning. After Werner introduced us, Seamus, with a great sigh (he was winning a game of Risk) and just the faint hint of a smile (it was pay day after all) introduced me to Kennys. He told me that many’s a day would be spent in there pondering “stuff”. You’re not wrong there! He also introduced me to the concept of the “quick and dirty” (try it before you ‘dis it) experiment. If it weren’t for some initial “quick and dirty” experiments, this thesis may certainly not have taken direction it currently has. To Adrian Boyle for the early explanations about the inherent problems on just using a “wavelength-o-meter” and the difficulties in finding one at short notice. His hints and tips helped me to “see the light”. Robert Howard and his anecdotes. These were invaluable over the years. It reminds me that I must call into that lad and catch up on any

crack and scandal that I've missed over the last three years or so. To Stenafie, I haven't forgot about that bottle of red. I'll surprise you one of these days, weeks, months or years.

Thanks also to the technical staff within the physics department, James Egan, Joe McCauley, Dave Grouse for their excellent craftsmanship and to Tom Burke for his unsurpassable organisational ability.

A great deal of gratitude is also owed to many people not associated with college. I would especially like to thank my parents and family for their constant encouragement, interest and support over the many years of my education, however disguised, as it may have seemed sometimes.

To the Systems section within International Banking, I owe thanks too. Pat Linehan & Peter Dowd have gone out of their way to encouraging me to finish this thesis. Well Pat I think that I will be collecting that week of promised study leave. To the rest of the Systems people, thank you for making me feel welcome from the beginning.

I owe the submission of this thesis to Dr. Aileen Lynch who has come to be a very important person in my life. Without her constant cajolements over the last year or so, this thesis would have long since been in the bin. Thank you for all your help. I love you lots.

Sincere apologies to anyone I've missed. This is mainly due to the fact that these acknowledgements are been written in a state of delirium due to deadline being in a few hours time and the long uptime since early this a.m. Thanks for all your help and otherwise over the years.

## Abstract

Solid state and solution measurements of the effective third order nonlinear absorption and refraction, have been carried out on poly(2,5-dioctyloxy-paraphenylene-vinylene-co-2,5-pyridinyl) (Pyridinyl PAV), poly(2,5-dioctyloxy-paraphenylene-vinylene-co-2,5-thienyl) (Thienyl-PAV), poly(2,5-dioctyloxy-paraphenylene-ethynylene-co-2,5-pyridinyl) (Pyridinyl-PAE) and poly(2,5-dioctyloxy-paraphenylene-ethynylene-co-2,5-thienyl) (Thienyl-PAE) using the Z-Scan experimental technique. The experiments were carried out on two different laser systems. Twenty three wavelengths ranging from 465nm through to 685nm were obtained using a nitrogen pumped Dye laser with pulse lengths of ~500 picoseconds, while the remaining two wavelengths are the 1064nm main line and the frequency doubled 532nm line from a Nd:YAG laser which had pulse lengths of ~40 picoseconds.

The effective third order nonlinear refraction coefficients ( $\eta_2$ ) obtained for solid state films ranged from  $-2.00 \times 10^{-16} \text{ m}^2/\text{W}$  for Pyridinyl-PAV at 1064nm, up to  $-2.43 \times 10^{-13} \text{ m}^2/\text{W}$  for Pyridinyl-PAV at 465nm, while the effective third order nonlinear absorption ( $\beta$ ) coefficients obtained for the solid state films ranged from  $+3.27 \times 10^{-7} \text{ m/W}$  for Pyridinyl-PAV to  $-1.4 \times 10^{-6} \text{ m/W}$  for Thienyl-PAE.

Semi-empirical computer modelling was also performed for each of the four polymers. The calculated ground state electronic absorption trends, for all four polymers, agree with the experimentally measured solution absorption trends. This agreement does not extend to the solid state absorption trends, although the trends within each polymer family (for solution and solid state) are in agreement. Any trends obtained from semi empirical computer modelling of absorption must therefore be treated with caution when investigating solid state polymers properties.

The all optical switching figures of merit for each polymer was calculated at each of the measured wavelengths. All four polymers are suitable for all optical switching at various wavelengths. The PAV polymers have more favourable figures of merit for all optical switching over a greater wavelength range compared to the PAE polymers, even though the Thienyl-PAE polymer has  $\eta_2$  coefficients which are consistently larger than the Pyridinyl-PAV.

The varying trends observed in nonlinear absorption measurements between solution and solid state indicate that solid state measurements must be performed when materials are being evaluated for solid state applications.

It is not possible to unambiguously state whether or not the four polymers satisfy all the criteria for all optical switching. However, it is possible to unambiguously state that each of the four polymers can not be ruled out as possible candidates for all optical switching at various wavelengths over the range 465nm to 685nm, based on the results presented in this thesis.

# Table of Contents

Title Page	i
Declaration	ii
Acknowledgements	iv
Abstract	vi
Table of Contents	vii
<b>1. General Introduction</b>	<b>1</b>
1.1 Introduction to Nonlinear optics	1
1.2 Objective of thesis	3
1.3 Thesis Structure	3
<b>2. Nonlinear Optics</b>	<b>6</b>
2.1 Linear Optical Phenomena	6
2.1.1 Refraction and Absorption	8
2.1.2 Photophysical Processes in Aromatic Structures	10
2.1.3 Scattering Effects	13
2.2 Nonlinear Optical Phenomena	15
2.2.1 Nonlinear Refractive Index	17
2.2.2 Nonlinear Absorption	19
2.2.3 Frequency Mixing	25
2.3 Origin of Nonlinear Optical Response	26
2.3.1 Nonresonant Contributions	27
2.3.2 Resonant Contributions	28
2.4 Nonlinear Optical Materials and Applications	28
2.4.1 Inorganic Dielectrics for Nonlinear Optics	28
2.4.2 Organic Materials for Nonlinear Optics	31
2.4.3 All Optical Switching	33
<b>3. Z-Scan</b>	<b>40</b>
3.1 Z-Scan Technique	40
3.1.1 Overview	40
3.1.2 Theory	43
3.1.2.1 Gaussian Beam, $\Delta n \neq 0$ , $\Delta\alpha = 0$ and "Thin Sample"	45
3.1.2.2 Gaussian Beam, $\Delta n \neq 0$ , $\Delta\alpha \neq 0$ and "Thin Sample"	50
3.2 Z-Scan in Non-Ideal Conditions	52
3.2.1 Non-Gaussian Beam, $\Delta n \neq 0$ , $\Delta\alpha \neq 0$ and "Thin Sample"	53
3.2.2 Non-Gaussian Beam, $\Delta n \neq 0$ , $\Delta\alpha \neq 0$ and "Thick Sample"	55
3.2.3 Background Subtraction	56
3.3 Z-Scan Technique Variations	57
3.3.1 Eclipsing Z-Scan	57
3.3.2 Excite-Probe Z-Scan	57
3.4 Interpretation of Z-Scan Results	58
<b>4. Polymer Samples</b>	<b>60</b>
4.1 Materials Studied	60
4.1.1 Poly(aryleneethynylene)s	61
4.1.2 Poly(arylenevinylene)s	61
4.2 Linear Optical Properties	63
4.2.1 Poly(aryleneethynylene)s	64
4.2.2 Poly(arylenevinylene)s	66
4.3 Computer Modelling	69
4.3.1 Geometry Optimisation	70
4.3.2 Linear Absorption and Polarisability	73
4.4 Discussion	81
4.4.1 Linear Absorption Trends	81
4.4.2 Optical Switching Figure of Merit	84



<b>5.</b>	<b>Experimental Details</b>	<b>91</b>
5.1	Introduction.....	91
5.2	Sample Preparation.....	92
	5.2.1 Solution Samples	92
	5.2.2 Solid State Samples	95
5.3	Z-Scan Apparatus.....	99
	5.3.1 Experimental Overview	99
	5.3.2 Data Capture	102
5.4	Z-Scan Measurements.....	103
	5.4.1 Nd:YAG Laser Measurements	104
	5.4.2 Dye Laser Measurements	110
<b>6.</b>	<b>Results &amp; Discussion</b>	<b>113</b>
6.1	Pyridinyl PAV Results.....	113
	6.1.1 Solution and Solid State Measurements	113
	6.1.2 Nonlinear Optical Switching Figure of Merit	120
6.2	Thienyl PAV Results.....	123
	6.2.1 Solution and Solid State Measurements	123
	6.2.2 Nonlinear Optical Switching Figure of Merit	130
6.3	Pyridinyl PAE Results.....	133
	6.3.1 Solution and Solid State Measurements	133
	6.3.2 Nonlinear Optical Switching Figure of Merit	140
6.4	Thienyl PAE Results.....	143
	6.4.1 Solution and Solid State Measurements	143
	6.4.2 Nonlinear Optical Switching Figure of Merit	150
6.5	Discussion of Results.....	153
	6.5.1 Dispersion of Third Order Nonlinearity	153
	6.5.2 Nonlinear Optical Switching Figure of Merit	162
	6.5.3 Resonant versus Non-Resonant Nonlinearity	164
	6.5.4 Possible Thermal Contributions	165
	6.5.5 Related Publications	166
<b>7.</b>	<b>Conclusions</b>	<b>170</b>
7.1	Nonlinear Refraction and Absorption.....	170
7.2	Nonlinear Optical Switching Figures of Merit.....	171
7.3	Proposed Future Work.....	171
	<b>Appendices</b>	<b>174</b>
	Appendix 1: List of Z-Scan Program.....	174

# 1 General Introduction

Physics - the science dealing with the properties and interactions of matter and energy<sup>1</sup>.

## 1.1 Introduction to Nonlinear Optics

Optical physics is the study of the physical phenomena that occur when light interacts with matter. This light-matter interaction may be classified into two groups - linear optical phenomena and nonlinear optical phenomena. Linear optical phenomena occur when the electric field strength of the light is weak relative to the electric field strength of the atoms or molecules of which the material is composed. Absorption, refraction and scattering are regarded as linear optical phenomena, which are dependent on wavelength but independent of the intensity of the light. Nonlinear optical phenomena occur when the electric field strength of the light is comparable to the electric field strength of the atoms or molecules of which the material is composed. At this field strength, the optical properties begin to depend on the intensity and other characteristics of the light. The light waves may then interact with one another as well as with the medium, giving rise to such nonlinear phenomena as optical limiting, self phase modulation and harmonic generation.

Up until 1960, the usual sources of light available for optical investigations tended to be weak, broadband and incoherent. It was the discovery of laser sources in 1960<sup>2,3</sup> and the experimental demonstration of the nonlinear optical phenomenon of second harmonic generation shortly afterwards<sup>4</sup>, which heralded in the new era of nonlinear optics with which we are familiar with today. Since then the realisation has been growing that by gaining insight into the fundamental physical processes responsible for nonlinear optical effects, it may be possible to tailor the development of new materials to enhance their nonlinear optical properties.

The nonlinear optical properties of conjugated organic polymeric materials have been studied extensively over the past two decades<sup>5</sup>. The primary motivation for this effort has been the production of materials for all optical switching in the telecommunications industry and sensor protection applications, which concern both nonlinear refraction and nonlinear absorption. Suitable materials for these applications should have large, yet fast nonlinearities. Optical transmission of data in the telecommunications industry is already the method of choice owing to its wide bandwidth and freedom from electromagnetic interference. Fibre-optic cables have such low absorption that they can transmit signals

over many kilometres, but eventually the signals need to be switched. Presently, this is achieved by converting the optical signal to an electronic one. The signal is next switched electronically, and then re-converted into a strong optical signal again. At present, the electronic components are the limiting factor where the fastest switches operate at frequencies of  $\approx 10\text{GHz}$ <sup>6</sup>. As the need for faster communications arises and the core elements speed up, there needs to be technology that will suffice to speed up the bottlenecks. One way to do this is to replace as many of the “slow” electronic components with faster components in a cost-effective manner. It would obviously be more efficient if the light beam could be switched directly by a laser in a suitable medium. By completely eliminating the electronic components and using all-optical switching techniques several orders of magnitude, more information may be transmitted over fibre optic cable.

All-optical processing in telecommunications is primarily concerned with optical communications over long distances and takes place in the near-infra red wavelengths primarily due to the near zero loss in silica fibres at 1500nm. There is however another genre of optical communications called “fibre to the home” and this is concerned with high bandwidth communications over short distances. Wavelengths that are typically considered are 650nm (close to the red attenuation minimum of PMMA) and more recently 570nm and 520nm (even lower attenuation, and upcoming very powerful light sources)<sup>7</sup>. All the technologies are already available. The only thing missing are suitable materials and if there are no natural materials available to do the job one can always try to engineer some.

Previous measurements carried out on organic materials for optical telecommunications in the 1500nm-wavelength region are mainly off resonant. These materials will most likely have different values of nonlinearity at 650nm where they may be resonantly enhanced. Resonance enhancement of nonlinearity may degrade the material’s figure of merit (through excessive absorptive losses) for ultra-fast optical switching which is a measure of the device’s overall viability. For ultra-fast all-optical switching, it is essential to minimise the resonant contribution to the optical nonlinearities. If a material is being considered for all-optical switching for “fibre to the home” applications, it is necessary to investigate the materials nonlinear properties at the wavelength in question. One way to proceed is to simulate the proposed new material before undertaking the time consuming route of synthesising the material. Although computer simulations are getting faster and more accurate (complex) with respect to structure/property relationship predictions, it is currently the case that the calculated results typically disagree with the experimentally

measured ones. The real world is currently much too complex on which to build firm theories, which can predict the correct structure/property trends for materials that have not yet been characterised. Direct measurement, remains the best way to determine new material nonlinearities.

## 1.2 Objective of Thesis

The database for nonlinear optical properties of materials, particularly organic, is in many cases inadequate for determining trends to guide synthesis efforts. Thus, there is a need to expand the database. Consequently, the work presented in this thesis is based on dispersion measurements of the third order optical nonlinearity on a range of molecularly engineered polymers in the visible region of the electromagnetic spectrum. The polymers under investigation were synthesised with these measurements in mind. The objective of the measurements was to investigate the suitability of the polymers for all-optical switching applications at close to 650nm. A secondary objective was to gain some insight (through solution and solid state measurements) into the relationships between the different polymer moieties and their relative contribution to the overall nonlinearity within their respective polymers over the wavelength range of 465nm to 1064nm. This understanding may eventually lead to the fabrication of low-cost, all-optical switches, which could be used for future low cost fibre to the home applications.

## 1.3 Thesis Structure

This chapter introduced the concept of Nonlinear Optics, as well as all optical switching within the telecommunications industry. The motivation behind the subject undertaken was also discussed.

Chapter 2 deals mainly with the theory relating to nonlinear optics. This is developed within the context of classical electromagnetic theory. It begins with a brief review of linear optical behaviour. This is then followed by a more rigorous look at the different nonlinear optical phenomena that are pertinent to this thesis.

Chapter 3 presents an in depth rigorous description of the Z-Scan experiment in its many guises, which is the experiment of choice for this thesis.

Chapter 4 concentrates on the polymer samples used for this work. This starts by outlining the reasoning leading up to the choice of the specific polymers used in this thesis. This is

followed by an analysis of the four polymers, during which their chemical structure and linear optical properties are presented. Computer modelling results for each of the polymers are also presented and the trends obtained are compared with experimentally measured properties. Finally any expected trends for nonlinear refraction and nonlinear absorption based on the linear properties and the molecular modelling are discussed.

Chapter 5 begins with a brief outline of the two laser systems that were used to perform the measurements in this thesis. This is followed by a review of the methods used to characterise these systems. This includes establishing baselines, accuracy, and reproducibility between successive measurements. The experimental procedures and the method of analysis are presented which are subsequently utilised in chapter 6 for actual sample measurements.

Chapter 6 is the results chapter where the nonlinear measurements for each of the four polymers are presented. The dispersion of the third order nonlinear refraction coefficient  $\eta_2$  and the third order nonlinear absorption coefficient  $\beta$  over the wavelength range is plotted and evaluated. The polymer's suitability for nonlinear optical switching is then investigated via calculation of the refractive and absorptive figure of merits for each polymer at each wavelength. A general discussion of the results obtained follows, in which the observed trends are correlated with the ground state electronic absorption spectra and computer modelling from chapter 4.

Chapter 7 presents the general conclusions based on the results in chapter six. Further experimental measurements that may be needed are discussed as well as some proposed improvements to the current Z-Scan experimental set-up.

## References

- 1 The Concise Oxford Dictionary, Oxford Press, *Ninth Edition*
- 2 R. J. Collins, D. F. Nelson, A. L. Schawlow, W. Bond, C. G. B. Garrett and W. Kaiser, *Phys. Rev. Lett.* 7, 118, 1961.
- 3 T. H. Maiman, *Nature*, 187, 493, 1960.
- 4 P. A. Franken, A. E. Hill, C. W. Peters, and G. Weinreich, 'Generation of Optical Harmonics', *Phys. Rev. Lett.* 7, 118, (1961).
- 5 A. Garito, R. F. Shi, M. Wu, *Physics Today*, May, 1994.
- 6 A. Driessen, H. J. Hoekstra, F. C. Blom, F. Horst, G. J. Krijnen, "Evaluation of Polymer Based Third Order Nonlinear Integrated Optics Devices", *Optical Materials*, 9, 329, 1998.
- 7 Ziemann et al., "Comparison of source properties for polymer optical fiber links", Proc. 7<sup>th</sup> Int'l POF Conference POF'98, Berlin (Germany), 123, 1998.

## 2 Nonlinear Optics

This chapter will present a general review of the nonlinear optics relevant to this thesis, covering theoretical aspects as well as some of the applications for nonlinear optics. Inorganic materials and second order optical nonlinear effects are outside the scope of this thesis. The emphasis will be placed upon organic materials and third order nonlinear optical effects.

### 2.1 Linear Optical Phenomena

Fundamental interactions between electromagnetic fields and matter are described classically by Maxwell's Equations. For the majority of situations considered in nonlinear optics, and for all the materials within this thesis, it can be assumed that there is no macroscopic magnetisation in the material (i.e. no microscopic magnetic dipoles). The material is also electrically neutral and nonconducting, so that no free charge or current density exists. Under these conditions Maxwell's equations may be expressed as<sup>1</sup>

$$\nabla \cdot \mathbf{D} = 0 \quad (2.1)$$

$$\nabla \cdot \mathbf{B} = 0 \quad (2.2)$$

$$\nabla \times \mathbf{E} = -\frac{\partial \mathbf{B}}{\partial t} \quad (2.3)$$

$$\nabla \times \mathbf{H} = \frac{\partial \mathbf{D}}{\partial t} \quad (2.4)$$

where  $\mathbf{E}$  and  $\mathbf{H}$  represent the electric and magnetic field strengths and  $\mathbf{B}$  and  $\mathbf{D}$  represent the magnetic and electric displacement vectors.  $\mathbf{B}$  and  $\mathbf{D}$  are defined as

$$\mathbf{B} = \mu_0 \mathbf{H} \quad (2.5)$$

$$\mathbf{D} = \epsilon_0 \mathbf{E} + \mathbf{P} \quad (2.6)$$

where  $\mu_0$  is the magnetic permeability of free space and  $\epsilon_0$  is the permittivity of free space.  $\mathbf{P}$  is the polarisation or electric dipole moment per unit volume and is the only term in Maxwell's Equations relating directly to the medium. By performing some differential operations and re-arranging the above equations it is possible to derive the following equation

$$\nabla^2 \mathbf{E} - \frac{1}{c^2} \frac{\partial^2 \mathbf{E}}{\partial t^2} = \mu_0 \frac{\partial^2 \mathbf{P}}{\partial t^2} \quad (2.7)$$

Equation 2.7 is the inhomogeneous wave equation and is the fundamental equation for classical electromagnetic field propagation and light-matter interactions. It can be seen that the polarisation term on the right hand side acts as a source term. The polarisation induced in a medium under the influence of an electromagnetic field is a property of the medium in which the electric field propagates. It is thus directly related to how a material will respond to excitation by a light field and has enormous significance for nonlinear optics. For free space the polarisation may be neglected and equation 2.7 becomes the homogenous wave equation.

$$\nabla^2 \mathbf{E} = \frac{1}{c^2} \frac{\partial^2 \mathbf{E}}{\partial t^2} \quad (2.8)$$

This can be shown to support only transverse wave solutions which propagate with a phase velocity,  $c$ , of  $3 \times 10^8$  m/s. One such solution is the plane wave of the following equation

$$\mathbf{E}_{(r,t)} = \hat{\mathbf{e}} E_0 \cos(\omega t - \mathbf{k} \cdot \mathbf{r}) \quad (2.9)$$

where  $\hat{\mathbf{e}}$  represents the polarisation of the wave,  $\omega$  the radian frequency and  $\mathbf{k}$  is the wave vector of propagation which obeys a dispersion relation given by

$$\mathbf{k} = \frac{\omega}{c} \quad (2.10)$$

The manner in which a material responds to an applied optical field may thus be quantified by summing the induced dipole response of the material's individual atoms or molecules to the applied optical field. This gives a value for the induced macroscopic polarisation. In conventional or linear optics, this macroscopic polarisation may be determined by considering the fundamental microscopic unit as a classical electron bound to a fixed nucleus by a spring<sup>2</sup>. The response of this electron to an applied field is then that of a forced harmonic oscillator and the macroscopic polarisation, is in units of C/m<sup>2</sup>,

$$\tilde{\mathbf{P}}^{(1)}_{(r,\omega)} = \epsilon_0 \chi^{(1)}_{(-\omega;\omega)} \tilde{\mathbf{E}}_{(r,\omega)} \quad (2.11)$$

where  $\epsilon_0$  is the vacuum permittivity,  $\omega$  the angular frequency,  $\chi^{(1)}_{(-\omega;\omega)}$  is the linear susceptibility which is related to the polarizability of the atoms or molecules constituting the material, and is  $\tilde{\mathbf{E}}_{(r,\omega)}$  the applied optical field in V/m.  $\chi^{(1)}_{(-\omega;\omega)}$  is a second rank tensor and describes linear optical properties such as refractive index, birefringence, absorption and emission. The resonance properties of  $\chi^{(1)}_{(-\omega;\omega)}$  as a function of  $\omega$  are then approximated to the resonance properties of the forced harmonic oscillator, as a function of the frequency of the driving force.



### 2.1.1 Refraction and Absorption

Under the above example electron displacement is a linear function of the applied optical field only under the condition that the electric field strength of the applied optical field is much smaller than the internal electric field that binds the electron to the nucleus. All linear optical phenomena are dependent on wavelength but independent of the intensity of the light.

The dielectric constant of a material be written as

$$\epsilon_{(\omega)} = \tilde{n}_{(\omega)}^2 = \epsilon_0 (1 + \chi_{\text{eff}(\omega)}) \quad (2.12)$$

where  $\tilde{n}$  is the complex refractive index of the material and  $\chi_{\text{eff}(\omega)}$  is the effective susceptibility. In the linear case  $\chi_{\text{eff}} = \chi^{(1)}$  and equation 2.12 can be written as

$$\epsilon_{(\omega)} = \tilde{n}_{(\omega)}^2 = \epsilon_0 (1 + \chi^{(1)}_{(\omega)}) = (\eta_{1(\omega)} + ik_{(\omega)})^2 \quad (2.13)$$

where  $\eta_1$  is the linear refractive index, and  $k$  in this case is the absorptive index which is related to the attenuation coefficient  $\alpha$  by

$$k_{(\omega)} = \frac{\alpha_{(\omega)}}{4\pi} \quad (2.14)$$

The absorption coefficient  $\alpha$  has units of  $\text{m}^{-1}$  while  $\eta_1$  has no units. If the refractive index and absorption coefficients of a material are written as

$$n_{(\omega)} = \eta_{1(\omega)} \quad (2.15)$$

$$\alpha_{(\omega)} = \alpha_{1(\omega)} \quad (2.16)$$

then the refractive index may be related to the real part of the linear susceptibility and the absorption coefficient to the imaginary part by

$$\eta_{1(\omega)} = \sqrt{1 + \text{Re}\chi^{(1)}_{(\omega)}} \quad (2.17)$$

$$\alpha_{1(\omega)} = \frac{\omega}{\eta_{1(\omega)}c} \text{Im}\chi^{(1)}_{(\omega)} \quad (2.18)$$

The refractive index,  $\eta_{1(\omega)}$ , of a medium is a measure of the ratio of speed of light in a vacuum,  $c$ , to its speed in the medium,  $v$ , where<sup>3</sup>

$$\eta_{1(\omega)} = \frac{c}{v_{(\omega)}} \quad (2.19)$$

The refractive index depends on the strength of the interaction of the electromagnetic field with the medium, and hence in a microscopic way, on the polarisability of the molecules or atoms from which it is made. From a macroscopic view the refractive index depends on the optical susceptibility of the material. As can be seen from equation 2.12 the effective susceptibility  $\chi_{\text{eff}}(\omega)$  and hence the complex refractive index  $\tilde{n}^2(\omega)$  and the dielectric constant  $\epsilon(\omega)$  are functions of  $\omega$  the angular frequency and hence the wavelength  $\lambda$ . This dispersion arises from the fact that the electric polarisability, and hence the refractive index, of an atom or molecule varies with the frequency with which the distorting electric field is oscillating (see figure 2.1).

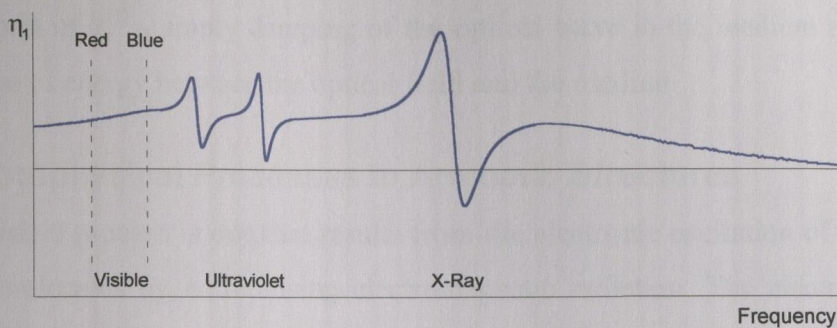


**Figure 2.1:** A schematic dispersion curve showing how the refractive index of a medium varies with the frequency of the incident radiation. The sharp oscillations occur when the incident electric field frequency matches an absorption frequency of the medium. Note how the refractive index increases with frequency in the visible region. At very high frequencies the refractive index approaches unity because (in classical terms) even electrons are too massive to follow the rapidly changing direction of the electric field of the radiation.

Within the forced harmonic oscillator model, the origin of the dispersion can be viewed as the response of an electron with a natural frequency  $\nu_0$  to an oscillating driving force (the applied electric field). When the frequency of the driving force is considerably less than  $\nu_0$ , the motion of the electron oscillator is only slightly perturbed and the electric polarization will be nearly in phase with the applied electric field. The dielectric constant and the corresponding index of refraction will both be greater than unity. When the frequency of the driving force is considerably greater than  $\nu_0$ , the oscillator undergoes displacements that are approximately 180 degrees out of phase with the driving force. The resulting electric polarisation will therefore be similarly out of phase with the applied electric field. The dielectric constant and therefore the index of refraction will both be mathematically less than unity. At frequencies very much higher than  $\nu_0$ , the electron oscillator barely responds at all because the driving force changes direction very rapidly and its effect averages to zero, thus leaving the dielectric constant equal to unity. The response is greatest when the frequency of the driving force nearly matches the natural frequency of

the electron oscillator. At optical frequencies, the increase in refractive index with increasing frequency is attributed to the higher energy/frequency photon's ability to excite the electrons in a given medium to a greater extent, compared with the lower energy/frequency photons. The spatial dispersion of the colours of white light using an prism is a direct consequence of the above phenomenon.

The linear absorption coefficient  $\alpha_1$ , just like the linear refractive index, is independent of the intensity of the optical field and thus a linear material will show no change in absorption with intensity. Within the forced harmonic oscillator model absorption can be taken into account by introducing a dampening term. Therefore processes involving the imaginary part of  $\chi^{(1)}(\omega)$  imply damping of the optical wave in the medium resulting from the exchange of energy between the optical field and the medium.

### 2.1.2 Photophysical Processes in Aromatic Structures

A photophysical process is one that results from the electronic excitation of a molecule or system of molecules by non-ionising electromagnetic radiation. The electronic states of diatomic molecules may be described in terms of a Morse potential curve of the form

$$E(r) = E_b (\exp - 2a(r - r_0) - 2\exp - a(r - r_0)) \quad (2.20)$$

Where  $E_b$  is the binding energy,  $r$  the internuclear separation and  $a$  an arbitrary constant. A sample curve with three levels is shown in figure 2.2 below. Such curves represent good approximations to the anharmonic oscillator model of diatomic molecules.

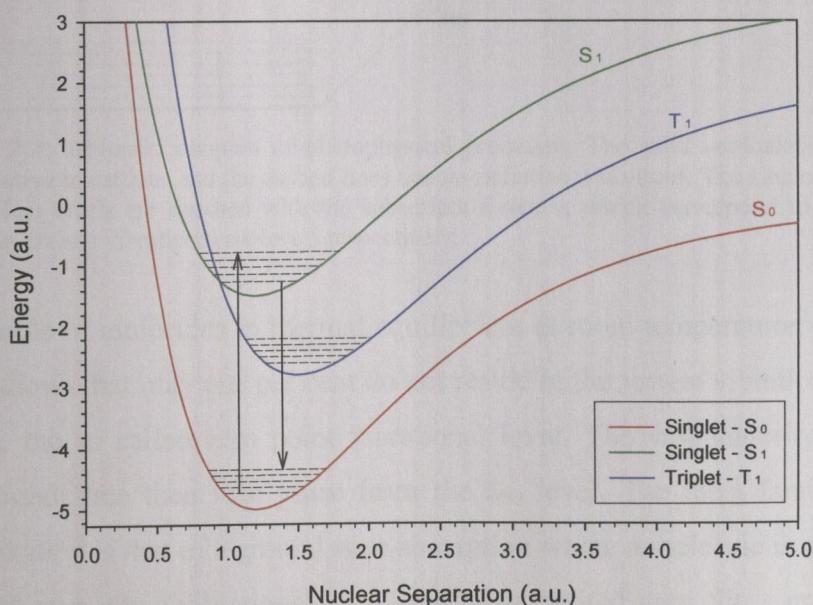


**Figure 2.2:** Configurational co-ordinate diagram showing the potential energy curves of singlet and triplet states.

The energy in figure 2.2 refers to the total energy, which includes both vibrational and electronic components. A similar set of levels can be used for the qualitative discussion of more complex polyatomic molecules, such as aromatic organic compounds, though the nuclear separation parameter is replaced by a nuclear configuration co-ordinate. In the above scheme the molecular electronic levels are divided into singlet ( $S_{nv}$ ) and triplet levels ( $T_{nv}$ ), the lowest or ground state being singlet and the next highest state generally being triplet in accordance with Hund's Rule which states that terms with greatest multiplicity lie lowest. The electronic levels are vibrationally broadened into bands, typically 50nm (0.2eV) FWHM. The vibrational levels are separated by  $\sim 0.05\text{eV}$  (1000K), and are themselves broadened by rotational sublevels (not shown in figure 2.2) of  $\sim 10^{-3}\text{eV}$  (100K) separation. The various transitions that can take place between the electronic and vibrational levels can be presented schematically in a Jablonski diagram such as figure 2.3, where the solid vertical lines denote non-radiative transitions and the dashed lines radiative transitions.

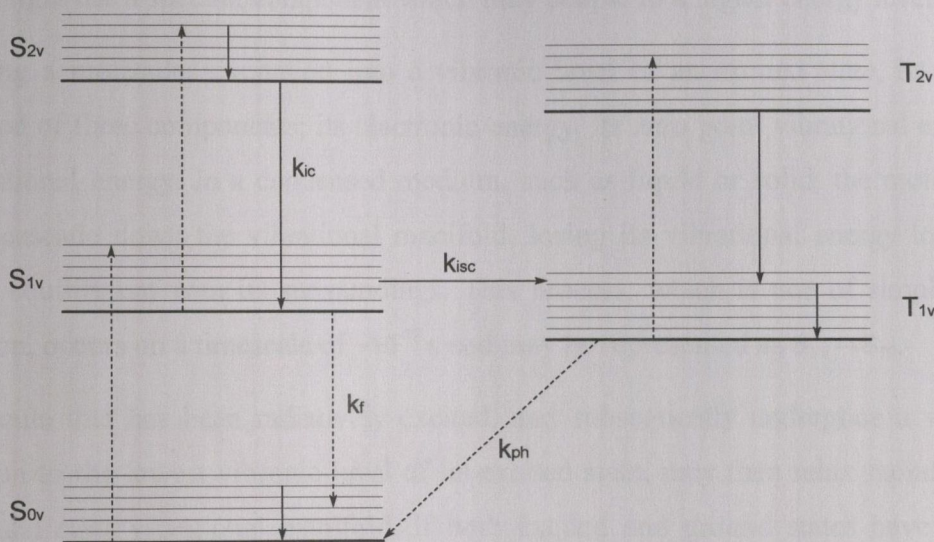


**Figure 2.3:** Jablonski diagram of photophysical processes. The solid vertical lines denote non-radiative transitions and the dashed lines denote radiative transitions. The singlet ( $S_{nv}$ ) and triplet ( $T_{nv}$ ) levels are denoted with the subscripts  $n$  and  $v$ , which correspond to electronic energy levels and vibrational sublevels respectively.

For an ensemble of molecules in thermal equilibrium at room temperature, the Boltzmann distribution shows that only one per cent do not reside in the lowest vibrational level of the ground state, the so called zero point vibrational level. The vast majority of transitions from the ground state then take place from the  $S_{00}$  level. The most familiar form of a radiative excitation is that of a ground state absorption where a molecule is excited from its lowest ground state into a vibrational level in the first excited state. Since excitation occurs from only one level in the ground state to any or all of the vibrational levels in the excited

state (depending on excitation wavelength), an absorption spectrum hence yields information on the vibrational energy distribution in the excited state. Absorption processes occur on a timescale of  $\sim 10^{-15}$  s, which is much too rapid a time to allow nuclear motion, and hence there is no change in the nuclear co-ordinate for an electronic transition. This corresponds to the case of maximum overlap between the ground state vibrational wavefunction and that of the excited state. This is a statement of the Frank-Condon Principle. On a Morse potential energy curve such a transition is represented as a vertical line. The envelope of the vibronic bands within an absorption band is referred to as the Frank-Condon envelope and its maximum corresponds to the Frank-Condon maximum. This approximates to the position of the most intense vibronic absorption band. Absorption is also possible out of an excited state, and this form of radiative absorption is known as excited state absorption. The incidence of such excitations is rare, except under conditions of high radiant fluxes which appreciably deplete the ground state population and where the incident light has a spectral component which may couple to a higher energy level.

Following a molecule's excitation into a vibronic level of an excited state, its energy is composed of three components; its electronic energy, its zero point vibrational energy and its vibrational energy. In a condensed medium, such as liquid or solid, the molecule will rapidly cascade down the vibrational manifold, losing its vibrational energy to establish thermal equilibrium with its surroundings. This process, which is one of simple thermal relaxation, occurs on a timescale of  $\sim 10^{-13}$  s and may be represented as  $S_{1v} \rightarrow S_{10}$ .

A molecule that has been radiatively excited, and subsequently undergone a vibrational relaxation to the lowest vibronic level of its excited state, may then relax radiatively into the ground state vibrational manifold. If both excited and ground states have the same multiplicity, this process is known as fluorescence. It is a spin-allowed process and occurs over a timescale of 1-100 ns. Since emission proceeds from the lowest vibrational level in the first excited state to the vibrational levels in the ground state, a fluorescence spectrum yields information concerning the vibrational energy level distribution in the ground state. The vibrational relaxation (thermalisation) which ensues after initial excitation causes the molecule to lose energy. This loss of energy is manifested as a red shift in the emission spectrum compared to that of the absorption and is termed the Stokes Shift. Both spectra, due to the complementary nature of the transitions, should share an approximate mirror symmetry, though in condensed media such as solvents, the two states may be solvated differently and the symmetry may not be so obvious. Such a mirror symmetry is also taken to denote a similar nuclear configuration in the ground and excited states. In situations

where the molecule is excited into a higher state such as  $S_{2v}$  and has subsequently undergone vibrational relaxation to the  $S_{20}$ , it may transfer to a high vibronic level of  $S_{1v}$  through an isoenergetic transition known as internal conversion. When in an excited state a molecule may also undergo an isoenergetic transition into a triplet state, a process which is spin forbidden and is termed intersystem crossing. It may occur from the zero point vibrational level of  $S_1$  or a thermally populated vibrational level. The transition may be into an excited vibrational level of  $T_1$  or more probably into a higher excited triplet state such as  $T_2$ , which is closer in energy to  $S_1$ , e.g.  $S_{1v} \rightarrow T_{2v}$ . In the lowest vibronic level of the triplet state a molecule may radiatively relax to the ground state through a process known as phosphorescence. This transition, since it involves a change of multiplicity unlike fluorescence, is forbidden and regularly occurs on a millisecond timescale. The emission is weak due to there being ample time for more rapid competing processes to quench the phosphorescence.

### 2.1.3 Scattering Effects

When an optical wave interacts with a medium, the atoms or molecules constituting the medium can react to the oscillating electric field in two different ways, depending on the incident frequency<sup>4</sup>. If the photon energy matches that of one of the excited states, resonant scattering occurs. The atom or molecule will “absorb” the photon, making a quantum jump to that energy level. In most cases the excitation energy will rapidly be transferred, via collisions, to random atomic motion (thermal energy) before a photon can be emitted. This is referred to as dissipative absorption. If however, the photons energy is lower than the resonance frequencies, non-resonant scattering occurs. The electric field of the light can be supposed to drive the atoms or molecule’s electron or electron cloud, into oscillation at the frequency of the incident electric field. Once the electron cloud starts to vibrate with respect to the positive nucleus, the system constitutes an oscillating dipole. This oscillating dipole or oscillating polarisation acts as the source term on the right hand side in equation 2.7. The system will immediately begin to radiate at that same frequency, and the resulting scattered light consists of a photon that moves off in some direction carrying the same amount of energy as did the incident photon. This is referred to as elastic scattering and in fact the processes of transmission, reflection and refraction are manifestations of scattering occurring on a sub-microscopic level. The intensity radiated from an single oscillating dipole is given by

$$I_{(\theta)} = \frac{p_0^2 \omega^4}{32\pi^2 c^3 \epsilon_0} \frac{\sin^2 \theta}{r^2} \quad (2.21)$$

where  $p_0 = qd$ . The initial maximum separation between the centres of the two charges  $q$ , is  $d$  and  $r$  is the distance from the oscillating dipole to the point of observation. Note that  $l(\theta)$  is a function of  $\theta$ , the angle between the symmetry axis of the dipole and the Poynting vector. The dependency of  $l(\theta)$  on  $\omega^4$  implies that the higher the frequency, the stronger the radiation. This feature is important for scattering processes which are reviewed next.

### i) Coherent Forward Scattering

Transmission of light through a medium is an ongoing repetitive process of scattering and rescattering. Each scattering event can be thought of as an oscillating dipole emitting a secondary wavelet. These wavelets travel outwards from the oscillating dipoles at speed  $c$ . The electron or dipole oscillators will be able to vibrate almost completely in-phase with the incident electric field only at relatively low frequencies. As the frequency of the electric field increases, the oscillators will fall behind, lagging in phase by a proportionately larger amount. The secondary wavelets will thus have a phase shift compared to the incident electric field. In a homogeneous medium the secondary wavelets interfere with each other in a way which results in total constructive interference in the forward direction only. Thus a completely homogeneous material can scatter light only in the forward direction. This is known as coherent forward scattering, and is the origin of the index of refraction. Other types of scattering reduce the intensity of the optical field by scattering light both elastically and inelastically in a direction other than the forward direction. So the overall dampening in the oscillator model has two contributions; one in the form of dissipative absorption as discussed above, the other contribution coming from the various forms of dissipative lateral scattering. Dissipative light scattering occurs as a consequence of fluctuations in the optical properties of the medium.

### ii) Rayleigh Scattering

A collection of atoms or molecules at a sufficiently low concentration so that they are too far apart to interact appreciably with one another will scatter light in such a way that the waves in all but the forward direction will be incoherent. The resultant lateral scattering will therefore be the sum of the intensities of the scattering from individual particles. This type of elastic scattering involves particles smaller than a wavelength (i.e. particles less than  $\lambda/15$ ). Atoms and ordinary molecules fit the bill since they are a few tenths of a nanometer in diameter compared to light with wavelength 500nm. The scattered intensity depends on  $1/\lambda^4$  due to the  $\omega^4$  dependency in equation 2.21 above. One of the features of Rayleigh scattering is its symmetry in the forward and backward direction. Transparent amorphous solids, such as glass and polymers will scatter light laterally, but very weakly.

Scattering from inhomogeneities in density is of interest whenever light travels great distances in a medium, such as a glass fibre of a communications link. A dense uniform substance will not appreciably scatter laterally. As a rule the denser the substance through which light advances, the less the lateral scattering.

### iii) Mie Scattering

As the size of the scattering centres increase from a fraction of a wavelength, the amount of scattering of the longer wavelengths increases proportionately. Mie scattering depends only weakly on wavelength and becomes independent of it (white light in, white light out) when the particle size exceeds  $\lambda$ . With increasing particle size there is an increase in forward scattering.

### iv) Raman and Brillouin Scattering

The scattering processes reviewed so far are all examples of elastic scattering, where the frequency of the scattered radiation is equal to that of the incident oscillating electric field. If the oscillating electric field which induces the oscillating dipole exchanges energy with the atom or molecule, then the scattered radiation may have a higher or lower frequency than the incident electric field. Since the relevant energy levels of atoms or molecules are quantised, this means that for a incident electric field with frequency  $\omega$ , the scattered radiation may have discrete frequencies above or below  $\omega$ . Such scattering is inelastic and was first observed by Raman in 1928. If instead, the oscillating electric field which induces the oscillating dipole exchanges energy with the lattice vibrations of a solid medium, which may be thought of as plane acoustic wave propagating through the medium another form of inelastic scattering called Brillouin is observed.

## 2.2 Nonlinear Optical Phenomena

Typically, the internal binding field is  $\sim 3 \times 10^8$  V/m.<sup>5</sup> Should the electric field strength of the applied optical field approach this value, the electron displacement will no longer be a linear function of the applied optical field within the forced harmonic oscillator model and the oscillator response becomes anharmonic. High power pulsed lasers provide the electric field strengths necessary to create this response and nonlinear optics is the study of the resulting light-matter interactions. The anharmonic oscillator model then results in the inclusion of additional higher order perturbation terms (H.O.T) in the expression for the induced polarisation<sup>5,6,7</sup>

$$\tilde{\mathbf{P}}_{(\mathbf{r},\omega)} = \tilde{\mathbf{P}}_{(\mathbf{r},\omega)}^{(1)} + \tilde{\mathbf{P}}_{(\mathbf{r},\omega_3)}^{(2)} + \tilde{\mathbf{P}}_{(\mathbf{r},\omega_4)}^{(3)} + \text{H.O.T.} \quad (2.22)$$



The quadratic polarisation  $\tilde{\mathbf{P}}^{(2)}(\omega_3)$  in equation 2.22 above represents the polarisation of the frequency component at  $\omega_3$  and can be written as

$$\tilde{\mathbf{P}}^{(2)}(\mathbf{r}, \omega_3) = \epsilon_0 \mathbf{K}^{(2)} \chi^{(2)}(-\omega_3; \omega_1, \omega_2) \tilde{\mathbf{E}}(\mathbf{r}, \omega_1) \tilde{\mathbf{E}}(\mathbf{r}, \omega_2) \quad (2.23)$$

where  $\tilde{\mathbf{E}}(\mathbf{r}, \omega_n)$  is the electric field at angular frequency  $\omega_n$ .  $\mathbf{K}^{(2)}$  is a constant defined by

$$\mathbf{K}^{(n)}(-\omega_\sigma; \omega_1, \dots, \omega_n) = 2^{l+m-n} p \quad (2.24)$$

where  $p$  is the number of distinct permutations of  $\omega_1, \dots, \omega_n$ ,  $n$  is the order of the nonlinearity, in this case  $n = 2$ ,  $m$  is the number of frequencies in the set  $\omega_1, \dots, \omega_n$  that are DC fields (zero frequency) and  $l = 1$  if  $\omega_\sigma \neq 0$  otherwise  $l = 0$ , and  $\chi^{(2)}(-\omega_3; \omega_1, \omega_2)$  is the second order susceptibility and is a third rank tensor.

Studies in the field of nonlinear optics have demonstrated that each term in the expansion may be identified with observable physical phenomena. In the case of one applied optical field the quadratic polarisation results in optical rectification  $\chi^{(2)}(0; \omega, -\omega)$  and second harmonic generation  $\chi^{(2)}(-2\omega; \omega, \omega)$ . If a D.C. electric field is added the result is the linear electro-optic effect  $\chi^{(2)}(-\omega; 0, \omega)$ . In the case of two applied optical fields sum and difference frequency mixing, parametric amplification and oscillation can occur  $\chi^{(2)}(-\omega_3; \omega_1, \pm \omega_2)$ <sup>8</sup>. Parametric amplification and oscillation is a similar process to second harmonic generation but permits the generation of a wide band of continually variable frequencies through the interaction of two beams in a suitable nonlinear material. In equation 2.23 above,  $\chi^{(2)}$  is a third rank tensors. In general,  $\chi^{(n)}$  are  $(n+1)$  rank tensors<sup>9</sup>. In crystals or molecules that possess inversion symmetry, the symmetry requirement that the polarisation induced by a positive or negative field be equal, implies that even order susceptibilities may only be observed in non-centrosymmetric materials. In isotropic materials therefore,  $\chi^{(2)}$  and all other even order terms are zero and only the odd terms contribute to the induced polarisation. In such materials the third order susceptibility is the first nonlinear term and is always non-zero. Conjugated polymers are intrinsically centrosymmetric and all odd rank tensors are vanishing.

The cubic polarisation  $\tilde{\mathbf{P}}^{(3)}(\mathbf{r}, \omega_4)$  in equation 2.22 above represents the polarisation of the frequency component at  $\omega_4$  and can be written as

$$\tilde{\mathbf{P}}^{(3)}(\mathbf{r}, \omega_4) = \epsilon_0 \mathbf{K}^{(3)} \chi^{(3)}(-\omega_4; \omega_1, \omega_2, \omega_3) \tilde{\mathbf{E}}(\mathbf{r}, \omega_1) \tilde{\mathbf{E}}(\mathbf{r}, \omega_2) \tilde{\mathbf{E}}(\mathbf{r}, \omega_3) \quad (2.25)$$

and is always non-zero. The cubic polarisation is a fourth rank tensor with 81 tensor components. Depending on the crystal symmetry the number of non-zero and independent components varies. For an isotropic material there are 21 non-zero tensor components of which only three are independent. They are<sup>8</sup>

$$\begin{aligned} yyzz &= zzyy = zzxx = xxzz = xxyy = yyxx \\ yzzy &= zyyz = zxxz = xzzx = xyyx = yxyx \\ yzyz &= zyzy = zxzx = xzxx = xyxy = yxyx \end{aligned} \quad (2.26)$$

and

$$xxxx = yyyy = zzzz = xxyy + xyxy + xyyx$$

In the case of an isotropic material, and where there is a single input beam or where all four (three input and one resultant) beams have the same polarisation (i.e. third harmonic generation, self phase modulation, degenerate four wave mixing) there is only one independent tensor component  $xxxx$ .

The cubic polarisation is responsible for the processes of intensity dependent refractive index  $\chi^{(3)}_{(-\omega; \omega, \omega, -\omega)}$ , two-photon absorption  $\chi^{(3)}_{(-\omega_1; -\omega_2, \omega_2, \omega_1)}$ <sup>8</sup>, D.C. Kerr effect  $\chi^{(3)}_{(-\omega; 0, 0, \omega)}$ , D.C. induced second harmonic generation  $\chi^{(3)}_{(2\omega; 0, \omega, \omega)}$ , third harmonic generation  $\chi^{(3)}_{(-3\omega; \omega, \omega, \omega)}$ , four wave mixing  $\chi^{(3)}_{(-\omega_4; \omega_1, \omega_2, \omega_3)}$ , sum and difference frequency mixing  $\chi^{(3)}_{(-\omega_3; \pm \omega_1, \omega_2, \omega_2)}$ , coherent anti-Stokes Raman scattering  $\chi^{(3)}_{(-\omega_{as}; \omega_p, \omega_p, -\omega_s)}$  and the optical Kerr effect  $\chi^{(3)}_{(-\omega_s; \omega_p, -\omega_p, \omega_s)}$ .

## 2.2.1 Nonlinear Refractive Index

The propagation of a high intensity optical field through a cubic nonlinear material modifies the material's refractive index and absorption coefficient. The change in the refractive index is dependent on the intensity of the optical field and the magnitude of the real part of the cubic susceptibility. This modification of the refractive index has the effect of introducing an additional contribution to the total susceptibility which is dependent on the intensity of the incident field. The effective susceptibility  $\chi_{\text{eff}(\omega)}$  is changed to

$$\chi^{(1)} + \frac{3}{4} \chi^{(3)}_{(\omega)} |\tilde{\mathbf{E}}_{(r, \omega)}|^2 \quad (2.27)$$

The dielectric constant of such a material can then be written as

$$\epsilon_{(\omega)} = \tilde{n}^2_{(\omega)} = \epsilon_0 (1 + \chi_{(\omega)}) = \epsilon_0 \left( 1 + \chi^{(1)}_{(\omega)} + \frac{3}{4} \chi^{(3)}_{(\omega)} |\tilde{\mathbf{E}}_{(r, \omega)}|^2 \right) \quad (2.28)$$

where  $\tilde{n}(\omega)$  is the complex refractive index of the material. The factor of  $\frac{3}{4}$  is the K value for the degenerate nonlinearity (equation 2.24) and the frequency arguments for the susceptibilities have been dropped for clarity. With these high intensity optical fields, the refractive index of a material can be written as

$$\eta(\omega, I) = \eta_1(\omega) + \eta_2(\omega) I \quad (2.29)$$

where  $\eta_1$  is the linear refractive index,  $I$  is the cycle averaged optical intensity in  $W/m^2$  and is defined as

$$I = \frac{1}{2} \epsilon_0 \eta_1(\omega) c |\tilde{E}(r, \omega)|^2 \quad (2.30)$$

$\eta_2$  is the nonlinear refractive coefficient in  $m^2/W$ , which relates to  $\chi^{(3)}$  by<sup>11</sup>

$$\eta_2(\omega) = \frac{3}{4\epsilon_0 c \eta_1^2} \text{Re } \chi^{(3)}_{xxxx(-\omega; \omega, -\omega, \omega)} \quad (2.31)$$

where Re denotes the real part of the complex  $\chi^{(3)}$  in  $m^2/V^2$ . The subscripts of  $\chi^{(3)}$  represent the polarisation of the light, and here linear polarised light is assumed, and the arguments represent the frequency of the optical light.  $c$  is the speed of light in m/s and  $\eta_1$  is the linear refractive index. Nonlinear refraction is responsible for important phenomena such as self-focusing and self-defocusing, where the light intensity is sufficiently high to cause a well collimated beam to focus or defocus (through self-phase modulation, which is discussed next) as it traverses a suitable nonlinear medium. Detuning of resonant optical cavities is sometimes an unwanted consequence of the self-focusing/defocusing phenomenon. To see how the nonlinear refractive index may be implemented in an all-optical switch (section 2.4.3) it is instructive to first consider the phase of the propagating field. The phase shift experienced by an optical field propagating in any dielectric medium is defined as<sup>10</sup>

$$\phi = \frac{2\pi}{\lambda} \eta_1 L \quad (2.32)$$

where  $L$  is the propagation distance in m,  $\lambda$  is the wavelength of light in m. In the presence of a nonlinear refractive index further contributions to the phase shift occur. Substitution of the intensity dependent refractive index (equation 2.29) into equation 2.32 results in a total phase shift given by<sup>10</sup>

$$\phi_{\text{Total}} = \phi_L + \phi_{\text{NL}} \quad (2.33)$$

where

$$\phi_{\text{NL}} = \frac{2\pi}{\lambda} \eta_2(\omega) I L \quad (2.34)$$

This self induced nonlinear phase shift is called self phase modulation (SPM) and is the mechanism behind many nonlinear phenomena such as the optical Kerr effect, self focusing of laser light, spectral broadening of short pulses and temporal solitons in optical fibre. The induced phase shift experienced by an optical field at one frequency due to a colinearly propagating optical field at a second frequency is called cross phase modulation (XPM). In this case the total phase shift experienced by the second field is given by<sup>10</sup>

$$\phi_{NL} = \frac{2\pi}{\lambda} \eta_2 (2I_1 + I_2) L \quad (2.35)$$

Due to the tensorial nature of the third order susceptibility, cross phase modulation is twice as efficient as self phase modulation at generating phase shifts for the same optical intensity. For all-optical modulation experiments the important parameter is the amount of nonlinear phase shift that can be accumulated over the sample interaction length.

### 2.2.2 Nonlinear Absorption

The propagation of a high intensity optical field through a cubic nonlinear material can also modify the materials absorption coefficient. In this case, the change in the absorption coefficient is dependent on the intensity of the optical field and the magnitude of the imaginary part of the cubic susceptibility. Under these circumstances, the absorption coefficient of a material can be written in a form similar to that of the refractive index (equation 2.29), namely

$$\alpha_{(\omega, I)} = \alpha_1(\omega) + \beta_{(\omega)} I \quad (2.36)$$

where  $\alpha_1(\omega)$  is the linear absorption coefficient,  $I$  is the optical intensity in  $W/m^2$ , and  $\beta_{(\omega)}$  is the nonlinear absorption coefficient which relates to the imaginary part of  $\chi^{(3)}$  by<sup>11</sup>

$$\beta_{(\omega)} = \frac{3\omega}{4\epsilon_0 c^2 \eta_1^2} \text{Im} \chi^{(3)}_{xxxx(-\omega; \omega, \omega, -\omega)} \quad (2.37)$$

Processes involving the imaginary part of  $\chi^{(3)}$  imply damping of the optical wave in the medium resulting from the exchange of energy between the optical field and the nonlinear medium. However, as we shall see in section 2.4.3, a large imaginary  $\chi^{(3)}$  is detrimental to all optical switching. Under conditions of low light intensity materials typically respond with a Beer's Law like dependence characterised by the following differential equation

$$\frac{dI}{dz} = -\alpha_1 I \quad (2.38)$$

whose solution is the following

$$T = \exp(-\alpha_1 z) = \exp(-\sigma N z) \quad (2.39)$$

where  $\alpha_1$  is the linear absorption coefficient,  $z$  the path length and  $T$  the transmission is independent of intensity. In the second part of the equation  $\sigma$  refers to the absorption cross section and  $N$  is the number density of absorbing centres. An examination of a generalised diagram such as figure 2.2 assists in explaining why: At low light levels the ground state is never significantly depopulated and, correspondingly, the excited state never succeeds in accruing a significant level of population. Under these conditions the linear absorption coefficient remains essentially constant. As the light intensity increases to levels where the photon flux is comparable to the population density, this situation may change. The transmission may increase or decrease depending on the respective absorption cross-sections of the ground and excited states<sup>12</sup>.

### i) Saturable Absorption

This refers to the case where the transmission increases with intensity and indicates that the ground state absorption has bleached. Saturable absorbers are materials whose ground state absorption cross-section exceeds that of the excited state. These materials show a decrease in absorption with increasing intensity, and so the process is effectively a resonant nonlinear process by which a material becomes more transmitting under the influence of high intensity light. The development of passively modelocked lasers of high intensity required materials which behave as saturable absorbers. Hercher<sup>13</sup> conducted a general analysis of saturable absorbers using a three level scheme. Under steady state approximation, where the populations remain constant, he derived a general expression for the absorption coefficient in terms of a parameter called the saturation intensity,  $I_s$

$$\alpha_{(\omega)} = \frac{\alpha_1(\omega)}{1 + \frac{I}{I_s}} \quad \text{and} \quad I_s = \frac{\hbar\omega}{\sigma\tau} \quad (2.40A+B)$$

and  $\sigma$  and  $\tau$  refer to the absorption cross-section and lifetime of the bleaching transition,  $I_s$  is the intensity at which the absorption coefficient drops to half its normal steady state value. He also investigated the effect of excited state absorption on the transmission of a saturable absorber and noted that it precluded the possibility of the absorption bleaching totally to give a transmission of 100%.

### ii) Multi-Photon Absorption

This is another mechanism which exists and causes light to be absorbed in a nonlinear manner. This involves a simultaneous absorption of multiple ( $n$ ) photons of frequency  $\omega$  by a single electron and its subsequent promotion from the ground state into an otherwise

unavailable excited state at energy  $n\omega$ . An example of this kind of process is two-photon absorption which was one of the first nonlinear optical effects to be discovered<sup>14,15</sup>. This process occurs when the material has an electronically accessible level at twice the frequency  $\omega$  of the input beam. Such a process is forbidden under dipole selection rules and the excited state is therefore of the same parity as the ground state. Two photon absorption is thus a useful tool in identifying states which would not otherwise be seen in a linear absorption spectrum<sup>16</sup>. The role of two-photon absorption is an important factor in the performance of third-order nonlinear materials as it can reduce the materials all-optical switching absorptive figure of merit through depletion of the incident light<sup>17</sup>. In the case of two photon absorption, the absorption coefficient increases linearly with increasing intensity, resulting in the expression for the intensity dependent absorption coefficient of equation 2.36 above. Insertion of the expression for the intensity dependent absorption coefficient into equation 2.38 results in an extension of the Lambert-Beer Law:

$$\frac{dl}{dz} = -(\alpha_1 + \beta I)l \quad (2.41)$$

Separation of the variables and subsequent integration of both sides over the pathlength yields an expression for the transmission of

$$\frac{1}{T} = \frac{1}{T_0} (1 + \beta L_{\text{eff}} I) \quad (2.42)$$

where  $T_0$  is the initial transmission and  $L_{\text{eff}}$  the effective length  $(1 - \exp(-\alpha l))/\alpha$ . The transmission varies inversely with increasing light intensity. Where there is negligible low intensity attenuation, the expression for the transmission reduces to

$$T = \frac{1}{1 + \beta I L} \quad (2.43)$$

Since it depends on the simultaneous absorption of two photons, the process is extremely rapid and requires high intensities to proceed with any efficiency. These intensities are typically a few hundred MW/cm<sup>2</sup> and require picosecond pulsewidths or nanosecond pulses of considerable energy density.

### iii) Reverse Saturable Absorption

This is the opposite case of saturable absorption, where the transmission decreases with increasing intensity. This occurs when the excited state absorption state cross section is greater than that of the ground state. These type of materials show an increase in

absorption with increasing intensity. One potential application for this type of effect is sensor protection where the amount of light that can be passed through the protecting medium is limited. This limiting effect only gets stronger, the more intense the light becomes, and can be used to protect sensitive optics from becoming exposed to light of sufficient intensity which would otherwise cause permanent damage. To discuss the importance of the various parameters which influence reverse saturable absorption the example of Li *et al.*<sup>18,19</sup> will be used. An arbitrary five level system such as figure 2.4 is used to help simulate the changes which accompany excitation of the system by a laser pulse. The vibrational levels of the electronic states are ignored and for the sake of simplicity, the laser pulse width is assumed to be longer than any of the lifetimes associated with the levels. To further simplify matters it is assumed that relaxation out of states  $S_2$  and  $T_2$  is very rapid so that the population of these two levels may be neglected.

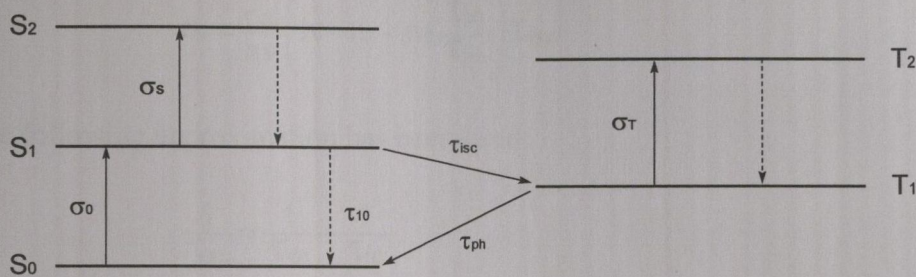


**Figure 2.4:** Generalised five level system. The solid vertical lines denote non-radiative transitions and the dashed lines denote radiative transitions.

After initial excitation, the first excited singlet state is populated. From here the electrons may be subsequently excited into state  $S_2$  within the pulsewidth of the laser. Once in  $S_2$  the electrons rapidly relax to  $S_1$  again. From  $S_1$  the population may undergo an intersystem crossing to the first excited triplet  $T_1$ , with a lifetime  $\tau_{isc}$  and thereafter be excited into state  $T_2$ . Once in state  $T_2$  the electrons rapidly relax again into state  $T_1$ , where the population is cyclically exchanged between these two triplet states, due to the lifetime of state  $T_1$  ( $\tau_{ph}$ ) being much longer than the intersystem crossing time ( $\tau_{isc}$ ). Furthermore, stimulated emission from state  $S_1$  is excluded by assuming a small fluorescence quantum yield. The system now reduces to the following set of three differential rate equations,

$$\frac{\partial n_1}{\partial t} = -\frac{\sigma_0 I}{h\nu} n_1 + \frac{n_2}{\tau_{10}} + \frac{n_3}{\tau_{ph}} \quad (2.44)$$

$$\frac{\partial n_2}{\partial t} = -\frac{\sigma_0 I}{h\nu} n_2 - \frac{n_2}{\tau_{isc}} - \frac{n_3}{\tau_{10}} \quad (2.45)$$

$$\frac{\partial n_3}{\partial t} = \frac{n_2}{\tau_{isc}} - \frac{n_3}{\tau_{ph}} \quad (2.46)$$

where  $n_1$ ,  $n_2$ , and  $n_3$  refer to the populations of  $S_0$ ,  $S_1$  and  $T_1$ . Attenuation of the laser beam is now governed by a propagation equation where the absorption coefficient now includes the excited state absorption from  $S_1$  and  $T_1$ :

$$\frac{\partial I}{\partial z} = -\alpha I = -(\sigma_0 n_1 + \sigma_S n_2 + \sigma_T n_3) I \quad (2.47)$$

Under the steady state approximation, which is valid when the pulsewidth is much longer than any relaxation times, all the time derivatives may be set equal to zero. The total population,  $N$ , is introduced, and  $n_1$  is expressed in terms of it, i.e.

$$n_1 = N - n_2 - n_3 \quad (2.48)$$

Substituting  $n_1$  into equation 2.45 and using equation 2.46 to obtain an expression for  $n_3$ , the following expression for  $n_2$  is obtained:

$$n_2 = \frac{\sigma_0 I}{h\nu} \left( N - n_2 - n_2 \frac{\tau_{ph}}{\tau_{isc}} \right) \tau_{isc} \quad (2.49)$$

where the following approximation has been used:

$$\frac{1}{\tau_{isc}} \approx \frac{1}{\tau_{isc}} + \frac{1}{\tau_{10}} \quad (2.50)$$

Rearranging equation 2.49, noting that  $\tau_{isc} \ll \tau_{ph}$  and using the substitution

$$I_s = \frac{h\nu}{\sigma_0 \tau_{ph}} \quad (2.51)$$

an expression for  $n_2$  in terms of the total population  $N$  is found to be:

$$n_2 = \frac{\tau_{isc}}{\tau_{ph}} \times \frac{I}{I_s} \times \frac{N}{1 + \frac{I}{I_s}} \quad (2.52)$$

Substituting equation 2.51 into equation 2.46,  $n_3$  is found in terms of  $N$  to be:

$$n_3 = \frac{I}{I_s} \times \frac{N}{1 + \frac{I}{I_s}} \quad (2.53)$$

Combining equations 2.53 and 2.52,  $n_1$  is found in terms of  $N$  to be:

$$n_1 = \frac{N}{1 + \frac{I}{I_s}} \quad (2.54)$$

Substituting the above expressions for the populations of each level into equation 2.47, the expression for the absorption coefficient is:



$$\alpha = \frac{\sigma_0 N}{1 + \frac{I}{I_s}} \left[ 1 + \left( \frac{\sigma_s}{\sigma_0} \times \frac{\tau_{isc}}{\tau_{ph}} \times \frac{I}{I_s} \right) + \left( \frac{\sigma_T}{\sigma_0} \times \frac{I}{I_s} \right) \right] \quad (2.55)$$

Making use of the abbreviations  $I' = I/I_s$ ,  $\alpha_0 = \sigma_0 N$ ,  $K = \sigma_T/\sigma_0$ , assuming that the absorption cross-sections for the singlet and triplet excited states are similar ( $\sigma_T \sim \sigma_s$ ) and knowing that  $\tau_{isc} \ll \tau_{ph}$  the expression for the absorption coefficient under steady state conditions becomes:

$$\alpha = \alpha_0 \left[ \frac{1 + KI'}{1 + I'} \right] \quad (2.56)$$

The changes in the normalised absorption coefficient with intensity are displayed for different values of  $K$  in figure 2.5 below.

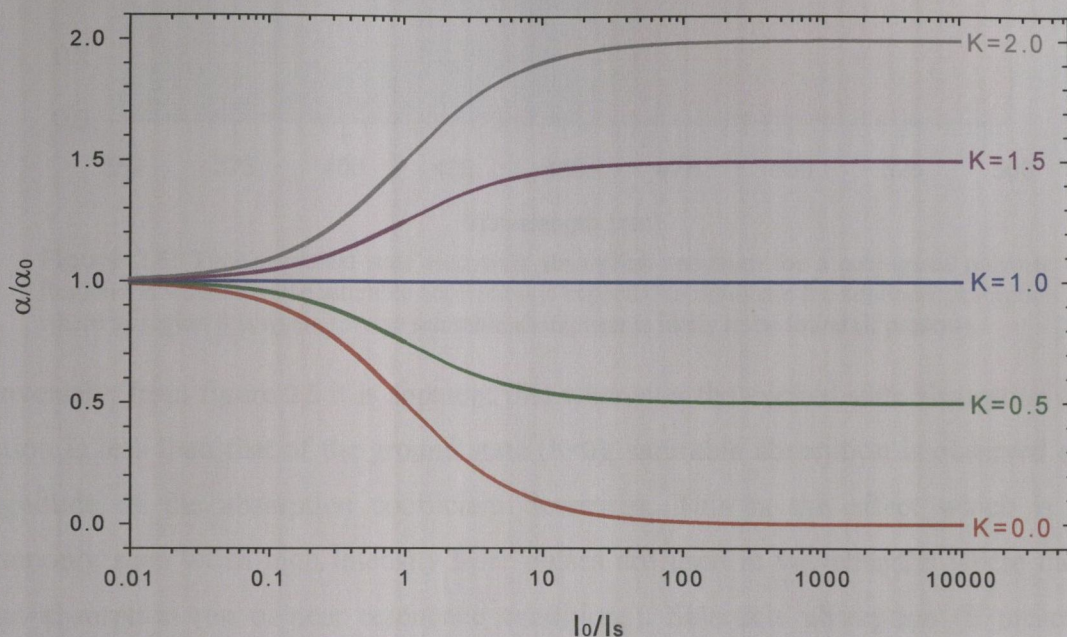


**Figure 2.5:** Plot of  $a/a_0$  versus  $I_0/I_s$  for different values of  $K$ , where  $K = s_T/s_0$ . The plot helps to illustrate how the ratio of ground state absorption cross-section to excited state absorption cross-section can effect the nonlinear absorption.

From figure 2.5 it is apparent that whenever the excited state absorption cross-section is greater than that of the ground state ( $K > 0$ ), reverse saturable absorption is observed as the magnitude of the absorption coefficient increases. The energy difference between the  $S_1$  and  $S_2$  electronic states (ground state electronic absorption) in conjugated polymers is typically smaller than the energy difference between the  $S_0$  and  $S_1$  electronic states excited state electronic absorption). The laser pulse has a narrow spectral linewidth, therefore in order for reverse saturable absorption to occur an electron in the excited state must be able to absorb a photon of the same energy as it absorbed in being promoted to the excited state

(from the ground state). Typically, only the lower energy wavelengths of the ground state absorption overlap in energy with the highest energy excited state electronic absorption wavelengths. Figure 2.6 below shows a typical ground state electronic absorption spectrum for a conjugated polymer. Reverse saturable absorption (if present) is therefore expected to occur for wavelengths in region II of figure 2.6.

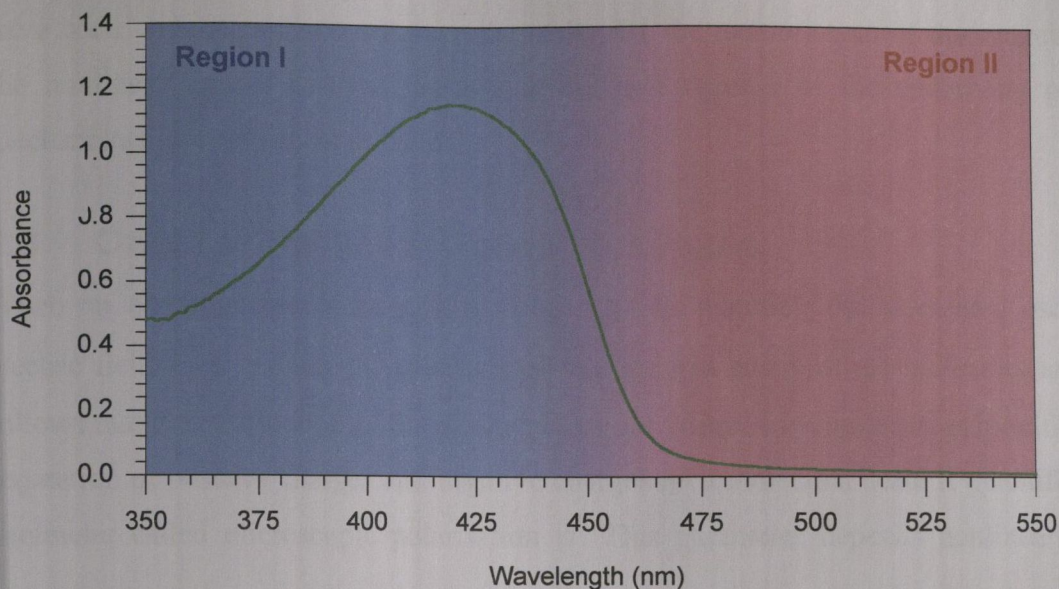


**Figure 2.6:** Typical ground state electronic absorption spectrum for a conjugated polymer. Region I is where reverse saturable absorption is expected to dominate the nonlinear absorption whereas region II is where reverse saturable absorption is likely to be found (if present).

Conversely, from figure 2.5 it is apparent that whenever the excited state absorption cross-section is less than that of the ground state ( $K < 0$ ), saturable absorption is observed as the magnitude of the absorption coefficient decreases. This is the effect which is most commonly seen when high intensity laser pulses are used at wavelengths where there is large absorption (on or near resonance conditions). Saturable absorption (if present) is therefore expected to occur for wavelengths in region I of figure 2.6. In certain circumstances, between the regions I and II, no change of absorption may be observed at high intensities, even though substantial dynamic changes in level populations is occurring ( $K=1$ ). This can occur when for a given intensity saturable absorption balances out reverse saturable absorption, resulting in no net nonlinear absorption. This crossover can have important consequences (nonlinear absorption can be eliminated) for all optical switching as will be discussed in chapters four and six.

### 2.2.3 Frequency Mixing

In frequency mixing, laser radiation at one frequency is converted into coherent radiation at a new frequency by, for example, second or third harmonic generation, sum-frequency

and difference-frequency generation<sup>20</sup>. Because the converted frequency may be at a frequency that is not directly available from a laser source, these frequency conversion techniques provide an important means of extending the spectral range covered by coherent sources<sup>21</sup>.

The cubic processes mentioned here in this section about nonlinear optical phenomena have been widely implemented experimentally for the measurement of the magnitude of the nonlinear optical susceptibilities and the investigation of the underlying physical mechanisms that contribute to them.

### 2.3 Origin of Nonlinear Optical Response

When an electromagnetic wave falls upon a given material, the associated oscillating electric field  $\tilde{\mathbf{E}}_{(r,\omega)}$  excites the electrons of the external layers of the molecules atoms. It follows that the distribution of the electrical charges within each molecule is modified. The separation of positive charges and negative charges on a molecular scale is quantified by a parameter called microscopic polarisation  $\tilde{\mathbf{p}}$ . This parameter depends nonlinearly upon  $\tilde{\mathbf{E}}_{(r,\omega)}$  and can be expanded as a power series<sup>11</sup> giving

$$\tilde{\mathbf{p}} = \mathbf{p}_0 + \alpha \tilde{\mathbf{E}}_{(r,\omega)} + \beta \tilde{\mathbf{E}}_{(r,\omega)} \tilde{\mathbf{E}}_{(r,\omega)} + \gamma \tilde{\mathbf{E}}_{(r,\omega)} \tilde{\mathbf{E}}_{(r,\omega)} \tilde{\mathbf{E}}_{(r,\omega)} + \dots \quad (2.57)$$

where  $\mathbf{p}_0$  is a constant and corresponds to the intrinsic polarisation, and  $\alpha$ ,  $\beta$  and  $\gamma$  are referred to as the polarizability, first hyperpolarizability and second hyperpolarizability, respectively (note that  $\beta$  in the above equation is not the same  $\beta$  as defined earlier in equation 2.37). Similarly, the macroscopic polarisation induced in the bulk media can be expressed in a power series in the external field such that

$$\tilde{\mathbf{P}} = \mathbf{p}_0 + \chi^{(1)} \tilde{\mathbf{E}}_{(r,\omega)} + \chi^{(2)} \tilde{\mathbf{E}}_{(r,\omega)} \tilde{\mathbf{E}}_{(r,\omega)} + \chi^{(3)} \tilde{\mathbf{E}}_{(r,\omega)} \tilde{\mathbf{E}}_{(r,\omega)} \tilde{\mathbf{E}}_{(r,\omega)} + \dots \quad (2.58)$$

where  $\chi^{(1)}$ ,  $\chi^{(2)}$  and  $\chi^{(3)}$  are the first, second and third-order nonlinear optical susceptibilities and have similar meanings to their microscopic counterparts  $\alpha$ ,  $\beta$  and  $\gamma$ . The bulk nonlinear susceptibility  $\chi^{(3)}$  is linked to the molecular hyperpolarizability  $\gamma$  according to

$$\chi^{(3)} = f^4 N \gamma \quad (2.59)$$

where  $N$  is the number of molecules per unit volume,  $f$  is the Lorentz correction factor for the local field given by

$$f = (\eta_1^2 + 2) / 3 \quad (2.60)$$

where  $\eta_1$  is the index of refraction of the material. The molecular hyperpolarizability  $\gamma$  is averaged over all molecular directions  $i,j,k,l$ <sup>22</sup>. The first two terms of the series in equation 2.58 describe all phenomena regarded as linear optical properties of materials, dependent on wavelength but independent of the light intensity as discussed in section 2.1. In this linear case the third and higher terms are completely negligible compared with the second term at “ordinary” optical field strengths (i.e. sunlight for which  $\mathbf{E}$  is of the order of hundreds of volts per meter, and radiation from most non-laser light sources). The third and higher order terms in equations 2.57 and 2.58 above become non-negligible at high intensities and describe nonlinear effects. For many materials of importance in the field of nonlinear optics, the third and higher-order terms begin to be of importance for values of  $\mathbf{E}$  of the order  $10^6 \text{Vm}^{-1}$ . Such values required for the observation, and therefore study, of such phenomena became available to scientists with the demonstration of the first operating laser in 1960 by Maiman<sup>15</sup>. Since then, the field of nonlinear optics has gone through a dramatic growth.

In terms of the classical electric dipole oscillator model, the higher order terms in equations 2.57 or 2.58 may be considered the result of anharmonic motion of the bound electrons of the atom or molecule under the influence of an applied electric field. The higher order terms represent perturbations to the harmonic case and as such, decrease in magnitude with increasing order. There are several contributions to the nonlinear polarization. These different contributions are discussed in the next section. Each contribution has its own typical magnitude and response time. In some cases the measured nonlinearity has several processes contributing to the nonlinear polarization and this must be taken into account when choosing a material for a specific requirement.

### 2.3.1 Nonresonant Contributions

Electronic hyperpolarizabilities arise from virtual transitions and give a coherent nonlinear response with a well-defined phase relationship with optical excitations<sup>11</sup>. In other words, they originate from the anharmonic terms in the electron potential categories. Typical values for the third order electronic hyperpolarizabilities is of the order  $10^{-22} \text{m}^2/\text{V}^2$ , and response times are of the order  $10^{-15}$  seconds. These are the fastest response times possible for all the different contributions and are sought after for ultrafast nonlinear optical switching. In the nonresonant limit  $\chi^{(3)}$  is not proportional to the optical pulse width and therefore  $\eta_2$  is not proportional to the optical pulse width.

### 2.3.2 Resonant Contributions

Incoherent nonlinearities occur in the presence of energy absorption through one- or multiple-photon processes. Then, the dissipative phenomena, which are particularly important in polymers because of strong electron-phonon coupling, lead to a loss of coherence within a few picoseconds between the absorbed energy and the exciting fields. These processes are accompanied by such nonlinear optical phenomena as refractive index variations of the medium. This is due to secondary phenomena associated with energy absorption, such as conformational changes, thermal dilatations and compressions due to electrostriction. Each of these processes can be, at least formally, described by a nonlinear susceptibility of third or higher order. Typical values for the third order absorption hyperpolarizabilities is of the order  $10^{-16} \text{ m}^2/\text{V}^2$ , and response times are of the order  $10^{-8}$  seconds. As can be seen the values of the nonlinearity are high compared to those for third order electronic hyperpolarizabilities, but this comes at the cost of response time. In contrast to the above case,  $\chi^{(3)}$  is proportional to the pulse width in the resonant limit. Therefore  $\eta_2$  is also proportional to the pulse width. This is due to causality and is described by the Kramers-Kronig relationship<sup>30</sup>.

## 2.4 Nonlinear Optical Materials and Applications

Much of the early work on nonlinear optical processes involved the study of atomic resonances in gases and alkali metal vapours<sup>23</sup>. Due to the narrow line widths of the optical transitions, this provided an ideal environment for testing the then developing theories of nonlinear optics. Although this work continues, the emphasis has more recently been placed on the search for new artificial solid state environmentally stable and processable dielectric materials with large and rapid nonlinear optical coefficients; in particular those that will allow nonlinear-optical devices to operate efficiently at relatively low power levels. Such applications for new materials include compact optical-frequency doublers and parametric-amplifiers from the aspect of  $\chi^{(2)}$ . However, materials with large third-order nonlinearities are perhaps of greater interest currently, since their nonlinear refractive index can be exploited for a wider range of phenomena such as all-optical switching, optical bistability, phase conjugation and other types of signal processing<sup>9</sup>.

### 2.4.1 Inorganic Dielectrics for Nonlinear Optics

Silica glass (as used in optical fibre) has an absorption in the ultra-violet wavelength range. The nonlinear refractive index measured in the near infra-red is due to excitation to virtual

energy levels. Therefore, the nonlinearity is purely non-resonant and ultrafast. Optical fibre communications and nonlinear fibre optics were revolutionised by the fabrication of low loss glass optical fibre in 1979 when fibre with losses as low as 0.2 dB/km were obtained in the 1550nm window of silica optical fibre<sup>24</sup>. The invention of Erbium Doped Fibre Amplifiers (EDFAs)<sup>25</sup> allows average powers of 100mW at 1550nm to be generated in an optical fibre. For a 40GHz pulse train of 5ps pulses this corresponds to a peak power value of 0.5W. The typical effective area of an optical fibre is  $50\mu\text{m}^2$  and the nonlinear refractive index coefficient  $\eta_2$  is typically  $2 \times 10^{-20} \text{m}^2/\text{W}^2$ . Based on these figures the effective length of fibre required to obtain a phase shift of  $\pi$  is found to be 2.6 kilometers from equation 2.34. This does not bode well for small scale device integration.

The observation of optical bistability in GaAs provided the realisation that nonlinear effects in semiconductors were possibly large enough to be useful in optical device applications on an integrated optical scale<sup>27</sup>. Measurement of the coefficients of nonlinear refraction in GaAs multiple quantum wells at room temperature<sup>28</sup> provided verification of this and at 1550nm similar measurements in InGaAsP multiple quantum wells yielded  $\eta_2$  values over 10 orders of magnitude larger than those of glass<sup>29</sup> (table 2.1). In each case the resonant enhancement of the nonlinear refractive index close to the absorption edge was exploited. This exploitation was not without cost. The excitation of carriers from the ground state valence band to exciton or conduction band states results in a population redistribution which is responsible for the modification of the material refractive index which may be quantified through the Kramers-Kronig relationships<sup>30</sup>. However, because the carriers take a time interval between 1 and 30ns to recombine, there is a limit on the amount of information that may be processed without distortion due to this relatively long lived excitation. Virtual excitation and the associated ultrafast recovery is a fundamental requirement for ultrafast all-optical switching in optical time division multiplexed systems. Essentially, for a 1 nanosecond carrier recombination time in a semi-conductor, the fastest switching rate possible is 1 Gbit/s. Although devices based on these nonlinear effects have been utilised in low bit rate signal processing devices for local area networks<sup>31</sup> an alternative must be found for high bit rate all optical switching.

Table 2.1 below summarises the findings of experiments on the materials discussed in this section in the context of how they meet the requirements outlined in the next section for high bit rate all optical signal processing. In each case the recovery time,  $\tau$ , quoted in column 5, refers to decay time of the induced refractive index change.

Material	$\eta_2$ (m <sup>2</sup> /W)	Mechanism	Experiment	$\tau$	Ref
GaAs	$2 \times 10^{-9}$	Resonant	Absorption Saturation	21ns	28
GaAs	$2 \times 10^{-8}$	Resonant	DFWM	21ns	32
InGaAsP	$5.3 \times 10^{-10}$	Resonant	DFWM	20ns	29
AlGaAs	$3.6 \times 10^{-18}$	Electronic-2PA Resonant	SPM	fs	34
Silica fibre	$3 \times 10^{-20}$	Non-resonant	SPM	fs	11
As <sub>2</sub> S <sub>3</sub> Doped optical fibre	$2 \times 10^{-18}$	Non-resonant	SPM	fs	33

**Table 2.1:** Parameters measured for candidate materials for all-optical switching. DFWM is degenerate four wave mixing, SPM is self phase modulation and 2PA is two photon absorption.

An investigation of the nonlinear refractive index in AlGaAs bulk and multiple quantum well waveguides at 1550nm showed that an ultrafast nonlinear refractive effect existed far from resonance<sup>34</sup>. Values of  $\eta_2$  between two and three orders of magnitude larger than glass were found in the 1550 to 1600nm region of the spectrum. The magnitude of this effect was found to depend strongly on the proximity of the operating wavelength to the two-photon resonance and switching was demonstrated in directional couplers with negligible two-photon absorption<sup>35</sup>. Self phase modulation experiments showed that nonlinear phase shifts of up to  $4.5\pi$  could be achieved with high power pulses from a colour centre laser<sup>34</sup>. The device structures were fabricated using molecular beam epitaxy and measurements were performed with high peak power pulses from mode-locked colour centre lasers. This material (AlGaAs) is perhaps the ideal material for the demonstration of integrated optic nonlinear optical processes at 1550nm, but the dependence of the nonlinear refractive index on nonlinear absorption (Kramers-Kronig), allows little scope for improvement in the magnitude of the nonlinear refractive index coefficient<sup>34</sup>.

Although the material can be somewhat bandgap tuned through changes in the Al/Ga proportions, and the use of quantum wells allow further adjustment of the bandgap and optical linear properties, the (relatively) limited change in band gap energy (and hence absorption maximum) which may be achieved does not permit this material to be optimised for applications at other arbitrarily defined (visible) wavelengths. Organic materials on the other hand can be engineered with these different wavelengths in mind.

## 2.4.2 Organic Materials for Nonlinear Optics

Organic materials emerged in the mid 1970s as a possible alternative to semiconductors and glasses for integrated optical nonlinear optical switching<sup>36</sup>. The bright prospects of organic materials, particularly conjugated polymers is due to the fact that they display a large NLO figure of merit, high optical damage thresholds, ultra fast optical responses, architectural flexibility, and ease of fabrication<sup>37,38</sup>. As stated earlier  $\chi^{(n)}$  are  $(n+1)$  rank tensors, and any odd rank tensor like  $\chi^{(2)}$  is equal to zero in a medium with inversion symmetry, referred to as a centrosymmetric medium, while even rank tensors like  $\chi^{(3)}$  does not have any symmetry restrictions. Conjugated polymers are intrinsically centrosymmetric and all odd rank tensors are vanishing. Therefore, any nonlinear process in such materials will first be described by the third order nonlinear optical susceptibility  $\chi^{(3)}$ .

The conventional perception of a polymer is what is commonly known as 'plastics'. At a molecular levels these materials are long linear organic molecules with simple units repeated hundreds or thousands of times along a chain. A molecule is said to be conjugated if it contains alternating single and multiple carbon-carbon bonds. In contrast, a molecule with no multiple bonds is said to be saturated. Conjugated structures exhibit two types of bonding;  $\sigma$  and  $\pi$  bonds. A representative structure is the symmetric polyene shown in figure 2.7<sup>39</sup>.

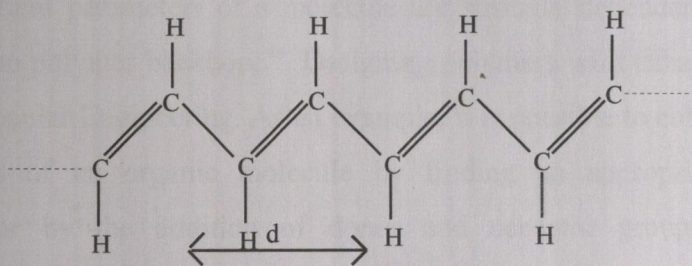


**Figure 2.7:** Linear polyene structure with N double bonds.

In carbon-carbon bonding, a maximum of four bonds can be formed. The carbon orbitals of the polyene are  $sp^2$  hybridised. These hybrid orbitals and the hydrogen 1s orbital provide cylindrically symmetrical molecular orbitals, called  $\sigma$  bonds, for the hydrogen 1s and three of the carbon 2s,2p electrons. The remaining electrons (one electron per carbon atom) are free to move or are delocalised in what is called the  $\pi$  orbital. The  $\pi$  and  $\sigma$  electrons have very different optical properties. Unlike  $\sigma$  electrons,  $\pi$  electrons are delocalised over an effective conjugation length. This high delocalization of the  $\pi$  electrons is the source of the large nonlinear optical parameters of the conjugated polymers. Because these are not



tightly bound to the individual positive nuclear sites, their paths, and orbitals extend over long distances, often spanning an entire molecule<sup>40,41</sup>. The large nonlinear response can be understood by considering that the origin of the cubic susceptibility, and therefore the nonlinear refractive index, is in the anharmonic response of these electrons to the incident optical field. In long chain conjugated polymers there are a large number of delocalised  $\pi$  electrons that can contribute to this anharmonic response. By attaching appropriate side groups to the conjugated polymer chains they can be effectively isolated from each other in the solid state. In this way it is, at least theoretically, possible to create ideal one dimensional confinement and maximise the nonlinear response. The first recognition of the contribution of  $\pi$  electrons to nonlinear processes was a theoretical proposal, based on the free electron model, that  $\chi^{(3)}$  was dependent on conjugation length<sup>42</sup>. The model showed that  $\chi^{(3)}$ , and therefore  $\eta_2$ , could be increased by increasing the degree of delocalization of the  $\pi$  electrons.

Experimental results showed that the second hyperpolarizability,  $\gamma$ , or  $\chi^{(3)}$  per molecule (see equation 2.59), increased as the fifth power of the number of double bonds until this dependence saturated when the number of double bonds was greater than ten and no further increase in  $\gamma$  could be found. For saturated molecules no such dependence was found and  $\gamma$  increased linearly with the number of carbon atoms<sup>43</sup>.

The nonlinear optical parameters of a molecule are strongly dependent on the geometry and structure of the polymer backbone<sup>43</sup>. Designing polymers with enhanced nonlinearities is the aim of Molecular Engineering. As an example, it is possible to enhance the nonlinear optical properties of an organic molecule by finding an appropriate length of the molecule<sup>41</sup>, and/or by the addition of donor and acceptor groups to the polymer backbone<sup>42</sup>, whose effects are to enhance the charge separation under light excitation.

Theoretical calculations within the Hückel or Hartree-Fock formalism have been used primarily to get a better evaluation of  $\gamma$  in conjugated polymers<sup>44</sup>. They allowed explanation of the observed strong increase of  $\gamma$  with increasing conjugation length  $L$  ( $\gamma \propto L^5$ ). Self-consistent finite field methods, which take electron-electron correlations into account, have been used by André *et al.*<sup>45</sup>, though with limited accuracy. More promising are the complete (or incomplete) neglect of differential overlap methods<sup>46</sup>. They allow determination of the dipolar transition moments between fundamental and excited states as well as the energy of excited levels. Coupled with time-dependent perturbation calculations of  $\gamma$ , they give the magnitude of  $\gamma$  as a function of frequency and the position of one-, two-,

and three-photon resonances. However, this field is still under heavy investigation and direct measurement still remains the best way to determine  $\gamma$ . For more in-depth information, an excellent and comprehensive review of nonlinear properties of organic polymers has been published by P. N. Prasad *et al.*<sup>47</sup>.

### 2.4.3 All-Optical Switching

All-optical switching can be achieved by cross phase modulation, and in these optical modulation experiments the important parameter is the amount of nonlinear phase shift that can be accumulated over the sample interaction length as discussed in section 2.2.1. Other than the magnitude of the nonlinear refraction coefficient, there are several factors that must be considered in order to minimise the power required to induce the necessary phase shift. These factors will now be considered.

#### i) Phase shift requirement for all-optical switching

The magnitude of the nonlinear phase shift required to observe all-optical switching depends on the specific device geometry<sup>48</sup>.

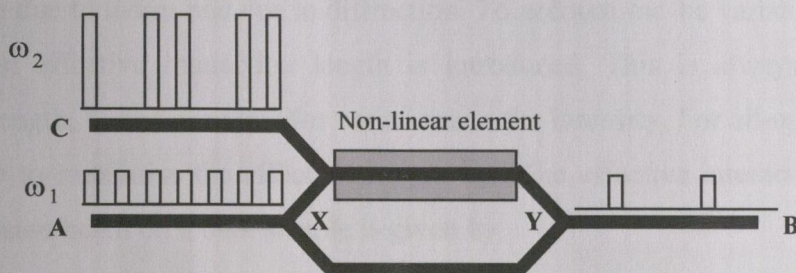


**Figure 2.8:** The integrated Optical Mach-Zehnder interferometer

The particular structure shown in figure 2.8 above, is a schematic of an integrated optical waveguide Mach Zehnder interferometer<sup>49</sup> which will serve as an example of an all optical switching device. If one, low intensity pulse train at frequency  $\omega_1$  is launched into the device at point A it propagates in the channel waveguide to point X where it is equally divided into two parallel channel waveguides by an optical power divider or Y-coupler. The two low intensity pulse trains then travel to point Y where they recombine constructively to emerge unmodified (but with a 50% power loss) at point B. The introduction of a second, modulated, pulse train of frequency  $\omega_2$  at point C induces a nonlinear phase shift on the low intensity pulse train through cross phase modulation in the nonlinear section of the structure. If the intensity of the pulse train at  $\omega_2$  is sufficient to

induce a nonlinear phase shift of  $\pi$  on the pulse train at  $\omega_1$  then when the pulse train travelling in the nonlinear section recombines with the pulse train travelling in the linear section, destructive interference occurs between the pulses resulting in the absence of a pulse at B. Constructive interference occurs if the pulses at  $\omega_1$  travelling in the nonlinear section, have not experienced the phase shift (where pulses at  $\omega_2$  are absent) resulting in the presence of a pulse at B. The output at point B at frequency  $\omega_1$  is therefore a data inverted copy of the modulated signal at frequency  $\omega_2$ . This switching function is an all-optical exclusive or (XOR) logic gate<sup>50</sup>. In summary, all-optical switching through induced nonlinear phase shifts requires phase shifts of order of  $\pi$  in magnitude. This, however, is not necessarily the minimum phase shift that can be detected in an interferometric measurement and it is possible to apply interferometric techniques to the measurement of the nonlinear refractive index coefficient.

## ii) Interaction length

In equation 2.34 it was assumed that the optical intensity  $I$  remains constant during propagation over the entire length  $L$  of the nonlinear sample. In reality  $I$  varies over the sample length due to losses and due to diffraction. To account for the variation in  $I$  over the distance  $L$ , an effective interaction length is introduced. This is always less than the geometrical length,  $L$ , and accounts for variations in the intensity. For all-optical switching it is desirable to maximise the effective length,  $L_{\text{eff}}$ . The effective interaction length of a focused Gaussian beam on a bulk sample is given by

$$L_{\text{eff}}(\text{bulk}) = \frac{\pi\omega_0^2}{\lambda} \quad (2.61)$$

where  $\omega_0$  is the beam radius and  $\lambda$  the wavelength (both measured in meters). Increased focusing leads to increased intensity at focus but to greater divergence which ultimately results in a shorter interaction length. To overcome this problem and to reduce the power requirements for the observation of nonlinear effects, dielectric optical confinement or optical waveguiding of the incident radiation is necessary. Such structures allow the diffractionless propagation of the incident radiation with the only limit on propagation distance being the losses due to absorption and scattering. This loss is quantified through the absorption coefficient ( $\alpha$ ), which may be incorporated into the length to define the effective length<sup>51</sup>

$$L_{\text{eff}}(\text{waveguide}) = \int_0^L \exp(-\alpha L) = \frac{1 - \exp(-\alpha L)}{\alpha} \quad (2.62)$$

The increase in efficiency of the nonlinear interaction may then be calculated by evaluating the ratio

$$\eta = \frac{L_{\text{eff}}(\text{bulk})}{L_{\text{eff}}(\text{waveguide})} = \frac{\lambda}{\pi\omega_0^2} \frac{1 - \exp(-\alpha L)}{\alpha} \approx \frac{\lambda}{\pi\omega_0^2 \alpha} \quad (2.63)$$

For silica glass, as used in commercially available optical fibre in the low loss 1550nm window,  $\alpha=5 \times 10^{-7} \text{cm}^{-1}$ ,  $\omega_0=8 \times 10^4 \text{cm}^{-1}$  and the improvement in efficiency is  $6.2 \times 10^8$ . This represents a reduction in power of  $10^9$  to see the same nonlinear phase shift in an optical fibre as in a bulk sample with a focused gaussian beam. From this calculation it is clear that the first criterion in the choice of material for optical switching functions, should be that the material is processable into a low loss optical waveguide geometry.

### iii) Induced loss

According to equation 2.34 any shortfall in the magnitude of  $\eta_2$  required to generate a suitable phase shift may be compensated for by an increase in intensity. This may not be true if the material possesses a large nonlinear absorption coefficient, equation 2.63. Intensity dependent absorption results in depletion of the actual propagating intensity and reduces the achievable phase shift. A requirement for devices based on nonlinear phase shifts is that the figure of merit defined by<sup>48</sup>

$$T = \frac{\lambda\beta}{2\eta_2} \quad (2.64)$$

should be less than unity. This parameter quantifies the amount of nonlinear phase shift that can be achieved in one absorption length of the material in the limit that two-photon absorption is the dominant loss mechanism. There is another figure of merit which is related to the nonlinear index of refraction and is defined by<sup>48</sup>

$$W = \frac{\eta_2 l_0}{\alpha\lambda} \quad (2.65)$$

Conversely, this value should be above unity for favourable materials. It is the combination of equations 2.64 and 2.65, that govern a materials prospect as a suitable material for all-optical switching.

Thus it can be seen that the spectral position, frequency dispersion and magnitude of the resonances in  $\eta_2(\omega)$  and  $\beta(\omega)$  in candidate materials for all-optical devices are of fundamental importance.

## iv) Response time:

High bit rate data transmission utilises short optical pulses from mode-locked lasers each of which when modulated represent one bit of a binary data stream<sup>52</sup>. Optical Time Division Multiplexing (OTDM) aims to exploit the bandwidth available in optical fibre lines by transmitting high bit rates in short time intervals at a single wavelength. To do this the encoded data is passively interleaved to form a high bit rate data stream at the transmitter<sup>18</sup>. At the receiver end of the optical fibre link it is then necessary to actively demultiplex the data<sup>18</sup>. Direct modulation of light at the transmitter has been demonstrated up to 40Gbit/s using electro-optic<sup>53</sup> and electro-absorption modulators<sup>54</sup>. At the receiver end electronic clock recovery at 40GHz has been demonstrated<sup>55</sup>, both in a laboratory. These speeds are close to the fundamental bandwidth of electronic components<sup>56</sup>.

All-optical switching provides a means to overcome the limitations imposed by electronics. The ultrafast or instantaneous phase shifts available in optical fibre through all optical interactions have been demonstrated in demultiplexing at the receiver end of OTDM systems<sup>57</sup>, optical clock recovery<sup>58</sup>, and optical modulation of laser sources<sup>59</sup>. Because the effect is instantaneous it is then possible to increase the bit rate as required without significant alteration to the transmitter or receiver ends of the fibre link.

If the full bandwidth of optical fibre or any other all optical switching material is to be utilised it is necessary that candidate materials for all optical switching must satisfy the requirement that the nonlinear effect in the material act instantaneously.

Previous measurements of nonlinear refraction have used a variety of techniques including nonlinear interferometry<sup>60,61</sup>, degenerate four-wave mixing<sup>62</sup>, nearly degenerate three-wave mixing<sup>63</sup>, ellipse rotation<sup>64</sup> and beam distortion measurements<sup>65</sup>. Nonlinear interferometry and wave mixing are potentially sensitive techniques but require relatively complex experimental apparatus. Beam distortion measurements, on the other hand, are relatively insensitive and require detailed wave propagation analysis. The Z-scan technique (chapter 3) utilised in this thesis is based on the principles of spatial beam distortion, but offers relative practical/experimental simplicity as well as very high sensitivity (better than  $\lambda/300$  wavefront distortion).

## References

- 1 D.M. Spirit and M. J. O'Mahony, High Capacity Optical Transmission Explained (John Wiley, New York, 1995).
- 2 R. W. Ditchburn, Light, (New York, Dover, 1991).
- 3 P.W Atkins, Quanta – A Handbook of Concepts, Second Edition, Page 306
- 4 Eugene Hecht, Optics – Third Edition, 1998, Page 67.
- 5 P.N. Butcher and D.N. Cotter, The Elements of Nonlinear Optics, (Cambridge University Press, Cambridge, 1990).
- 6 Y.R. Shen, The Principles of Nonlinear Optics, (John Wiley, New York, 1980).
- 7 A. C. Newell and J. V. Moloney, Nonlinear optics, from the series on advanced topics in the interdisciplinary mathematical sciences, (Addison-Wesley, 1992).
- 8 R.W. Boyd, Nonlinear Optics, (Academic Press, San Diego, 1992).
- 9 F. Kajzar, J. Messier, J. M. Nunzi and P. Raimond, in 'Polymers for lightwave and integrated optics', ed. by L. A. Hornak, 595, (1992).
- 10 C. flytzanis, in Quantum electronics, ed. by H. Rabin and C. L. Tang, Academic Press, New York, (1975).
- 11 Y. R. Shen, The Principles of Nonlinear Optics, John Wiley & Sons, Chapter 1, (1984).
- 12 C.R. Guiliano, L.D. Hess, IEEE J. Quantum Elec. QE-3, 338, 1967.
- 13 M. Hercher, Applied Optics, 6, 947, 1967.
- 14 R. J. Collins, D. F. Nelson, A. L. Schawlow, W. Bond, C. G. B. Garrett and W. Kaiser, Phys. Rev. Lett., 7, 118, (1961).
- 15 T. H. Maiman, Nature, 187, 493, (1960).
- 16 P. F. Liao and J. E. Bjorkholm, 'Direct Observation of Atomic Energy Level Shifts in Two-Photon Absorption', Phys. Rev. Lett. 34, 1, (1975).
- 17 W. Kaiser and G. C. B. Garrett, Phys. Rev. Lett. 8, 404, (1961).
- 18 Li, C., Zhang, L., Yang, M., Wang, H. and Wang, Y., Phys. Rev. A, 49, 1149, 1994.
- 19 Li, C., Zhang, L., Wang, R., Song, Y. and Wang, Y., J. Opt. Soc. Am. B, 11, 1356, 1994.
- 20 C. C. Wang and G. W. Racette, 'Measurement of Parametric Gain Accompanying Optical Difference Frequency Generation', Appl. Phys. Lett. 6, 169, (1965).
- 21 P.W. Smith, IEEE Circuits and Devices Magazine, 9-14, May, (1987).
- 22 C. Flytzanis, in Quantum Electronics, ed. by H. Rabin and C. L. Tang, Academic Press, New-York, I-A, 1975, 9.
- 23 R. B. Miles, S. E. Harris, IEEE J. Quant. Electron., QE-9, 470, (1973).
- 24 T. Miya, Y. Terunuma, T. Hosaka and T. Miyashita, Electron. Lett., 15, 106, (1979).
- 25 R. J. Mears, L. Reekie, I. M. Jauncey and D. N. Payne, 'Low-noise erbium doped fibre amplifier operating at 1.54 $\mu\text{m}$ ', Electron. Lett., 23, 1026, (1987).
- 26 Q.Z. Wang, Q.D. Liu, D. Liu, P.P. Ho, and R.R. Alfano, 'High-resolution spectra of self-phase modulation in optical fibers', J. Opt. Soc. Am. B, 11, 1084 (1994).
- 27 H. M. Gibbs, S. L. McCall, S. L. Venkatesan, T. N. C. Gossard, A. C. Passner and W. Wiegmann, 'Optical bistability in semiconductors', Appl. Phys. Lett, 35, 451, (1979).
- 28 D. A. B. Miller, D. S. Chemla, D. J. Eilenberger, P. W. Smith, A. C. Gossard and W. T. Tsang, 'Large room temperature optical nonlinearity in GaAs/Ga<sub>1-x</sub>Al<sub>x</sub>As multiple quantum well structures', Appl. Phys. Lett., 41, 8, (1982).
- 29 M. N. Islam, E. P. Ippen, E. G. Burkhardt and T. J. Bridges, 'Picosecond nonlinear absorption and four wave mixing in GaInAsP', Appl. Phys. Lett., 47,10, (1985).

- 30 Y. H. Lee, A. Chavezpiron, S. W. Koch, H. M. Gibbs, S. H. Park, J. Morhange, A. Jeffery, N. Perghambarian, L. Banyai, A. C. Gossard and W. Wiegmann, 'Room temperature optical nonlinearities in GaAs', *Phys. Rev. Lett.*, 57,2446, (1986).
- 31 D. W. Smith, *Optical network technology*, BT (British Telecom) telecommunications series, (London, Chapman & Hall, 1995).
- 32 A. C. Gossard and W. Wiegmann, 'Degenerate four wave mixing in room temperature GaAs/GaAlAs multiple quantum well structures', *Appl. Phys. Lett.*, 42, 925, (1983).
- 33 M. Asobe, T. O'Hara, I. Yokohama and T. Kaino, 'Low-power all-optical switching using chalcogenide glass fibres', Paper FB1-1 at Nonlinear guided waves and their applications, Cambridge, England, August 1993.
- 34 S. T. Ho, C. E. Socolich, M. N. Islam, W. S. Hobson, A. F. J. Levi and R. E. Slusher, 'Large nonlinear phase shifts in low loss Al<sub>x</sub>Ga<sub>1-x</sub>As waveguides near half-gap', *Appl. Phys. Lett.*, 59, 20, (1991).
- 35 C. C. Yang, A. Villeneuve, G. I. Stegeman and J. S. Aitchison, 'Effects of three photon absorption on nonlinear directional coupling', *Opt. Lett.*, 17, 710, (1992).
- 36 C. Sauteret, J.-P. Hermann, R. Frey, F. Pradere, J. Ducuing, R.H. Baughman and R.R. Chance, 'Optical nonlinearities in one-dimensional conjugated polymer crystals', *Phys. Rev. Lett.*, 36, 956 (1976).
- 37 T. Kaino and S. Tomaru, *Adv. Mater.* 5, 172, (1993).
- 38 H. S. Nalwa, *Adv. Mater.* 5, 341, (1993).
- 39 B. S. Hudson, B. E. Kohler and K. Schulten, 'Linear polyene electronic structure and potential surfaces', in *Excited states: Volume 6*, edited by C. Lim, (Academic press, 1982).
- 40 M. Blanchard-Desce, *La Recherche*, 25, 581, (1994).
- 41 A. Garito, R. F. Shi and M. Wu, *Physics Today*, May, 5, (1994).
- 42 K. C. Rustagi and J. Ducuing, 'Third-order polarizability of conjugated organic molecules', *Opt. Commun.*, 10, 258, (1974).
- 43 J. Ducuing, in *Proceedings of the international school of physics 'Enrico Fermi', Course LXIV*, edited by N. Bloembergen, (North Holland, Amsterdam, 1977).
- 44 K. C. Rustagi and J. Ducoing, *Opt. Commun.*, 10, 1974, 158.
- 45 J. M. André, C. Barbier, V. Bodart and J. Delhalle, *Nonlinear optical properties of organic molecules and crystals*, ed. by D. S. Chemla and J. Zyss, Academic Press, Orlando, FL, II, 1987, 137.
- 46 B. J. Orr and J. F. Ward, *Mol. Phys.*, 20, 1971, 513.
- 47 P. N. Prasad and D. J. Williams, *Introduction to nonlinear effects in molecules and polymers*, John Wiley & Sons, 1991.
- 48 G.I. Stegeman and E.M. Wright, 'All-optical waveguide switching ', *J. Optical and Quantum Electronics*, 22, 95 (1990).
- 49 J.G. Fujimoto, 'Femtosecond techniques for the characterisation of nonlinear and linear properties of waveguide devices and studies of all-optical switching', from *Waveguide Optoelectronics*, edited by J.H. Marsh and R.M. De La Rue (Kluwer, Dordrecht, 1992).
- 50 M. Bate, 'Logic gates', (Longbridge Deverill : Soft-Teach Educational, 1988).
- 51 G.P. Agrawal, *Nonlinear Fibre Optics*, (Academic Press, San Diego, 1989).
- 52 D.M. Spirit and M.J. O'Mahony, *High Capacity Optical Transmission Explained*, (Wiley, Chichester, 1995).
- 53 K. Noguchi, H. Miyazawa and O. Mitomi, '75GHz broadband Ti:LiNbO<sub>3</sub> optical modulator with ridge structure', *Electron. Lett.*, 30, 949 (1994).

- 54 F. Devaux, P. Border, A. Ougazzaden, M. Carre and F. Huet, 'Experimental optimisation of MQW electro-absorption modulators with up to 40GHz bandwidth', *Electron. Lett.*, 30, 1347 (1994).
- 55 A.D. Ellis, T. Widdowson, X. Shan, G.E. Wickens, and D.M. Spirit, 'Transmission of a true single polarisation 40Gbit/s soliton data signal over 205km using a stabilised erbium fibre ring laser and 40GHz electronic timing recovery', *Electron. Lett.*, 29, 990 (1993).
- 56 P.W. Smith, 'On the physical limits of digital optical switching and logic elements', *Bell System Technical J.*, 61, 1975 (1982).
- 57 D.M. Patrick, A.D. Ellis and D.M. Spirit, 'Bit-rate flexible all-optical demultiplexing using a nonlinear optical loop mirror', *Electron. Lett.*, 29, 702 (1993).
- 58 A.D. Ellis, K. Smith and D.M. Patrick, 'All-optical clock recovery at bit rates up to 40Gbit/s', *Electron. Lett.*, 29, 1323 (1993).
- 59 A.D. Ellis, W.A. Pender, T. Widdowson and D.J. Richardson, 'All-optical modulation of a 40GHz beat frequency conversion soliton source', *Electron. Lett.*, 31, 1362 (1995).
- 60 M. J. Weber, D. Milam, and W. L. Smith, "Nonlinear refractive index of glasses and crystals," *Opt. Eng.*, vol 17, pp. 463-469, 1978.
- 61 M. J. Moran, C. Y. She, and R. L. Carman, "Interferometric measurements of nonlinear refractive-index coefficient relative to CS<sub>2</sub> in laser-system-related materials," *IEEE J. Quantum Electron.*, vol QE-11, pp. 259-263, 1975.
- 62 S. R. Friberg and P. W. Smith, "Nonlinear optical glasses for ultra-fast optical switches," *IEEE J. Quantum Electron.*, vol. QE-23, pp. 2089-2094, 1987.
- 63 R. Adair, L. L. Chase, and S. A. Payne, "Nonlinear refractive index measurements of glasses using three-wave frequency mixing," *J. Opt. Soc. Amer. B*, vol. 4, pp. 875-881, 1987.
- 64 A. Owyong, "Ellipse rotations studies in laser host materials," *IEEE J. Quantum Electron.*, vol. QE-9, pp. 1064-1069, 1973.
- 65 W. E. Williams, M. J. Soileau, and E. W. van Stryland, "Optical switching and n<sub>2</sub> measurements in CS<sub>2</sub>," *Opt. Commun.*, vol. 50, pp. 256-260, 1984.



### 3 Z-Scan

The Z-Scan technique will be presented in this chapter. After a brief introduction an overview of the standard Z-scan technique is presented. The relevant equations and relationships used in data analysis are derived for the case of an ideal Gaussian beam. Nonlinear refraction and nonlinear absorption with respect to the Z-scan technique and the methodologies that are employed to extract the pertinent information from experimental results will be discussed. Modifications to equations derived for the ideal case, that become necessary when dealing with non-ideal beam profiles, are subsequently reviewed. Next, variations of the standard Z-scan technique are discussed including any advantages or disadvantages over the standard Z-scan technique. The chapter concludes by looking at the precautions to be observed, and relevant information to be taken into account, during the interpretation of Z-scan results.

#### 3.1 Z-Scan Technique

The Z-scan technique is one of the numerous tools available to the experimental physicist to access the third-order nonlinear coefficients of a material. It measures both nonlinear absorption and nonlinear refraction in solids, liquids and liquid solutions. The technique was first documented in 1989 by Sheik-Bahae *et al.*<sup>1</sup> and has gained immediate acceptance by the nonlinear optics community as a standard technique for separately determining the nonlinear changes in both refractive index and absorption. In experiments the index change ( $\Delta n$ ) and absorption change ( $\Delta\alpha$ ) can be accurately determined directly from the data without necessarily resorting to computer fitting. The basis of the Z-scan technique is to scan the relevant sample through the focus of a laser beam. It follows that in one scan, the sample is subject to a large range of intensities and the induced nonlinear effects are recorded.

##### 3.1.1 Overview

Let us consider a Gaussian beam in a tight focus geometry as depicted in Figure 3.1. This is the standard “closed aperture” Z-scan apparatus for determining nonlinear refraction. The transmittance of a nonlinear medium is recorded through the finite aperture in the far field, as a function of the sample position  $z$ , measured with respect to the linear optics focal position. Let us assume that the material sample has a negative nonlinear refractive index, has no absorptive nonlinearities and has a thickness smaller than the diffraction length of

the focused beam (i.e. a “thin” sample). The conditions above ensure that the sample can be regarded as a thin lens of variable focal length.

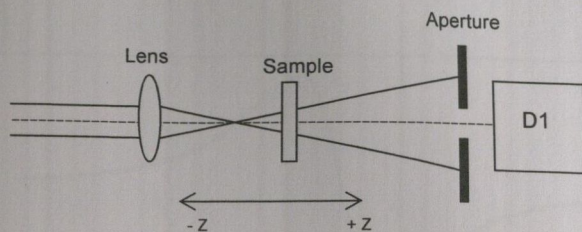


**Figure 3.1:** Typical Z-scan set-up. The signal measured by the photo diode D1 is recorded as a function of sample position  $z$ .

If the scan is initiated from a distance far away from the focus (negative  $z$ ), the beam irradiance is low and negligible nonlinear refraction occurs. The transmittance remains relatively constant. As the sample is brought closer to the focus, the beam irradiance increases, leading to self-lensing (self focusing) in the sample. A negative self-lensing prior to focus will tend to collimate the beam (Figure 3.2a), causing the beam to narrow at the aperture, which results in an increase in the measured transmittance. As the scan in  $Z$  continues and the sample passes the focal plane to the right (positive  $z$ ), the same self defocusing increases the beam divergence, leading to beam broadening at the aperture, and thus a decrease in transmittance (Figure 3.2b). This suggests that there is a null as the sample crosses the focal plane. This is analogous to placing a thin lens at or near the focus, resulting in a minimal change of the far-field pattern of the beam. The Z-scan is completed as the sample is moved away from focus (positive  $z$ ) such that the transmittance becomes linear since again, the irradiance is low.

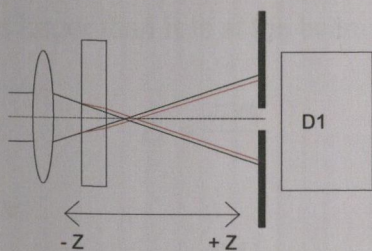


**Figure 3.2a:** Negative self-lensing prior to focus.

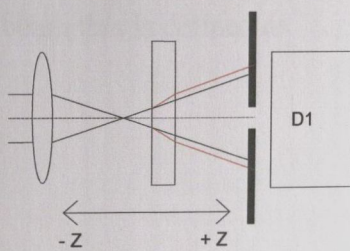


**Figure 3.2b:** Negative self-lensing after focus

A pre-focal transmittance maximum (peak) followed by a post-focal transmittance minimum (valley) is therefore the Z-scan signature of a negative refractive nonlinearity as depicted in Figure 3.3. Following the same analogy, positive nonlinear refraction gives rise to a pre-focal transmittance minimum (valley) followed by a post focal transmittance

maximum (peak). The sign of the nonlinear index is immediately obvious from the measurements obtained.

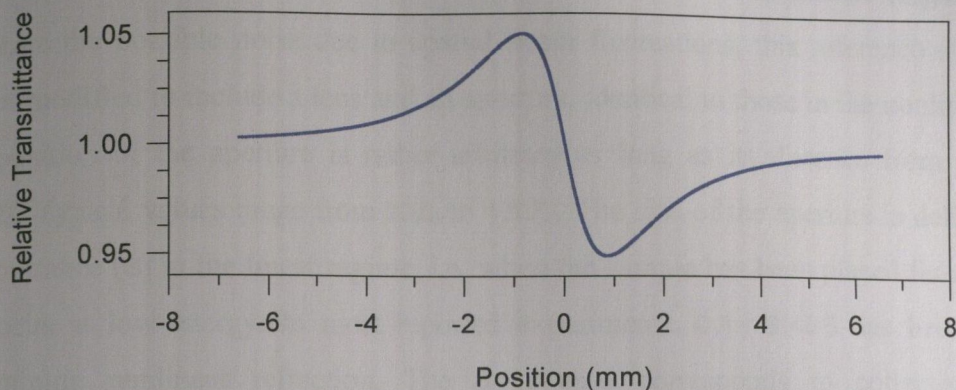


**Figure 3.3:** Normalised Z-scan signature for a negative refraction nonlinearity resulting from pre-focal beam narrowing (Figure 3.2a) followed by post-focal beam broadening (Figure 3.2b).

In the picture above (Fig 3.3) describing the Z-scan, one must bear in mind that a purely refractive nonlinearity is considered and assumes that no absorptive nonlinearities are present (i.e. multiphoton or saturation of absorption). Qualitatively, multiphoton absorption or inverse saturation suppresses the peak and enhances the valley. Alternatively, saturation will produce the opposite effect<sup>2</sup>. The sensitivity to nonlinear refraction is entirely due to the aperture, and removal of the aperture completely removes the effect. Nonlinear absorption coefficients can be extracted from such “open aperture” Z-scans.

The required scan range in an experiment depends on the beam parameters and the sample thickness  $L$ . A critical parameter is the diffraction length or Rayleigh range,  $Z_0$ , of the focused beam. This is defined as the distance from the beam waist to where the beam is  $\sqrt{2}$  times larger than it is at the beam waist. For a Gaussian beam this is defined as

$$Z_0 = \frac{\pi w_0^2}{\lambda} \quad (3.1a)$$

where

$$w_0 = \frac{2\lambda f}{\pi r} \quad (3.1b)$$

is the focal spot size (half width at the  $1/e^2$  maximum in the irradiance),  $f$  is the focal distance of the lens and  $r$  is the beam radius at the focusing lens. For “thin” samples (i.e.  $L \leq \eta_1 Z_0$  where  $\eta_1$  is the linear index), although all the information is theoretically contained within a scan range of  $\pm Z_0$ , it is preferable to scan the sample by at least  $\pm 5Z_0$ . This requirement simplifies data interpretation when the sample’s surface roughness or optical

beam imperfections introduce background “noise” into the measurement system. In many practical cases where considerable laser power fluctuations may occur during the scan, a reference detector can be used to monitor and normalise the transmittance (Figure 3.4). To eliminate the possible noise due to spatial beam fluctuations, this reference arm can be further modified to include a lens and an aperture, identical to those in the nonlinear arm<sup>3</sup>. The position of the aperture is rather arbitrary as long as its distance from the focus,  $d \gg Z_0$ . Typical values range from  $20Z_0$  to  $100Z_0$ . The size of the aperture is defined by its transmittance ( $S$ ) in the linear regime, i.e. when the sample has been placed far away from the focus at low energy. In most reported experiments,  $0.1 < S < 0.5$  has been used for determining nonlinear refraction. The  $S = 1$  case corresponds to collecting all the transmitted light and therefore is insensitive to any nonlinear beam distortion due to nonlinear refraction. Such a scheme, referred to as an “open aperture” Z-scan, is suitable for measuring nonlinear absorption ( $\Delta\alpha$ ) in the sample.

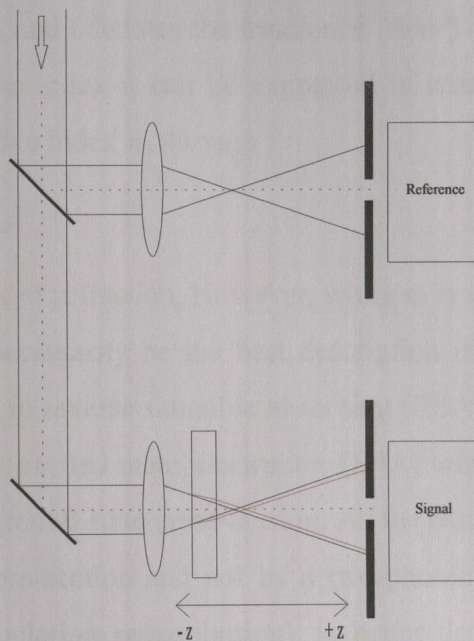


**Figure 3.4:** The Z-scan apparatus used to reduce noise by monitoring the ratio of detector outputs of signal to reference. “Open aperture” Z-scans are obtained by removing the apertures shown in front of the signal and reference detectors and carefully collecting all of the transmitted light.

### 3.1.2 Theory

This section reviews the theoretical basis of Z-scan experimentation. A lot of work has been performed with respect to investigating the propagation of intense laser beams inside a nonlinear material and the ensuing self-refractive<sup>4,5</sup>. The following method for analysing the Z-scan data is based on modifications of existing theories<sup>6</sup>. A number of cases are

discussed. The first example is the ideal case of a Gaussian beam and a “thin” sample, and equations are given which allow the coefficients of nonlinear refraction to be extracted from experimental data. Nonlinear absorption effects are ignored in this first case. The next example extends the treatment to include the effects of nonlinear absorption as well as nonlinear refraction. After these ideal beam cases are analysed, the modifications necessary to extract useful data where the beam is not Gaussian and/or the sample is not “thin” are investigated. In general, nonlinearities of any order can be considered. However, once a specific type of nonlinearity is assumed (e.g. an ultra fast  $\chi^{(3)}$  response), a Z-scan can be rigorously modelled for any beam shape and sample thickness by solving the appropriate Maxwell’s equations. Within the assumption of cubic nonlinearities we define the intensity dependent refractive index change as:

$$\Delta\eta = \eta_2 I \quad (3.2)$$

where  $\eta_2$  ( $\text{m}^2/\text{W}$ ) is the third order nonlinear index of refraction coefficient which can be either positive or negative, and  $I$  denotes the irradiance ( $\text{W}/\text{m}^2$ ) of the laser beam within the sample. Thus the refractive index  $\eta$  can be expressed in terms of the coefficient of the intensity dependent refractive index  $\eta_2$  through :

$$\eta^{(0)} = \eta_1 + \eta_2 I \quad (3.3)$$

where  $\eta_1$  is the linear index of refraction. However, while  $\eta_2$  is used here for *any* third order nonlinearity, it may not necessarily be the best description of cumulative nonlinearities. These occur, for example, in reverse saturable absorbing (RSA) dyes<sup>7</sup>. In such dyes, linear absorption is followed by excited state absorption (ESA) where the excited state cross-section is larger than the ground state cross-section. As the resulting changes in absorption is best described by a cross-section and not by a two-photon absorption coefficient, the index change (due to population redistribution), is better described by refractive cross-sections than by an  $\eta_2$ . Such an “ $\eta_2$ ” (or  $\beta$ ) would change with the laser pulse-width<sup>8,9</sup>. Also within the assumption of cubic nonlinearities the intensity dependent absorption change is defined as:

$$\Delta\alpha = \beta I \quad (3.4)$$

where  $\beta$  ( $\text{m}/\text{W}$ ) denotes the third order nonlinear absorption coefficient, which for ultrafast nonlinear absorption is equal to the multi-photon absorption coefficient (section 2.2.2).

Thus the absorption coefficient  $\alpha$  can be expressed in terms of the intensity dependent absorption coefficient  $\beta$  through:

$$\alpha_{(I)} = \alpha_1 + \beta I \quad (3.5)$$

where  $\alpha_1$  is the linear absorption coefficient.

### 3.1.2.1 Gaussian Beam, $\Delta n \neq 0$ , $\Delta\alpha = 0$ and "Thin Sample"

In this initial ideal case the beam profile is Gaussian, both temporally and spatially. A number of assumptions are made; namely that there is no nonlinear absorption present in the sample and only cubic nonlinear refraction. In addition, the sample is "thin" as defined below.

We start the analysis by assuming a TEM<sub>00</sub> Gaussian beam, of beam waist radius  $w_0$  travelling in the +z direction and entering the nonlinear sample (as in Figure 3.1 above), and so we can write the field  $\mathbf{E}$  as:

$$\mathbf{E}_{(z,r,t)} = \mathbf{E}_{0(t)} \frac{w_0}{w(z)} \exp \left[ -r^2/w^2(z) - ikr^2/2R(z) - i\phi_{(z,t)} \right] \quad (3.6)$$

where  $w(z) = w_0 (1+z^2/z_0^2)$  is the beam radius and  $w_0$  is the beam waist at the focus.  $R(z) = z (1 + z_0^2/z^2)$  is the radius of curvature of the wavefront at  $z$ ,  $z_0 = kw_0^2/2$  is the diffraction length of the beam,  $k = 2\pi/\lambda$ , and  $\lambda$  is the laser wavelength, all in free space.  $\mathbf{E}_{0(t)}$  denotes the radiation electric field at the focus and contains the temporal envelope of the laser pulse. The intensity  $I$  (W/m<sup>2</sup>) of the beam is equal to :

$$I_{(z,r,t)} = \frac{1}{2} \epsilon_0 c \eta_1 \left| \mathbf{E}_{(z,r,t)} \right|^2 \quad (3.7)$$

i.e.

$$I_{(z,r,t)} = I_{0(z)} \exp \left[ -2 \left\{ r/w(z) \right\}^2 \right] \exp \left[ -(t/\tau)^2 \right] \quad (3.8)$$

where  $\tau$  is the temporal half width at  $\exp[-1]$  of the maximum intensity. The peak intensity distribution along the z-axis is determined to be :

$$I_{0(z)} = \frac{2E}{\pi^{3/2} \tau W(z)^2} \quad (3.9)$$

where  $E$  is the energy in a laser pulse (Joules). Once the amplitude and the phase of the beam exiting the sample is known, the field distribution at the far field aperture can be calculated using diffraction theory (Huygen's principle) in the case of radially symmetric systems. Making a number of valid assumptions and approximations leads to relatively simple analytical expressions, making data analysis easier yet accurate. A major simplification results if we assume that the nonlinear sample is "thin", so that neither

diffraction nor nonlinear refraction, cause any change of beam profile within the nonlinear sample. In this case the self-refraction process is referred to as “external self-action” and simply states that the effective focal length of the induced lens in the sample, should be much larger than the sample thickness<sup>10</sup>. That implies that for linear diffraction the sample thickness  $L \ll n_0 Z_0$  and for nonlinear refraction the sample thickness  $L \ll Z_0/\Delta\phi_0$ , where  $\Delta\phi_0$  is the maximum nonlinearly induced phase change. In most experiments using the Z-scan technique, we find that this second criterion is automatically met since  $\Delta\phi_0$  is small. For the sample to be safely regarded as “thin”, the first criterion for linear diffraction is more restrictive than it need be, and the condition  $L < n_0 Z_0$  is sufficient<sup>6</sup>. As we are only concerned with calculating the radial field variations  $\Delta\phi(r)$  of the beam profile, the slowly varying envelope approximation (SVEA) applies, and all other phase changes that are uniform in  $r$  are ignored, where  $r$  is the radial distance from the centre of the beam. The external self-action limit simplifies the problem considerably, and the amplitude  $|I|$  and nonlinearly induced phase  $\Delta\phi_0$  of the electric field  $E$  are now governed by the following pair of equations:

$$d\Delta\phi/dz' = \Delta\eta_{(l)} (2\pi/\lambda) \quad (3.10)$$

and

$$dI/dz' = -\alpha_{(l)} I \quad (3.11)$$

where  $z'$  is the propagation depth in the sample and  $\alpha_{(l)}$  in general includes linear and nonlinear absorption terms. Note that  $z'$  should not be confused with sample position  $z$ . The phase shift of the beam at the exit surface,  $I_e$  and  $\Delta\phi$ , of a sample exhibiting a third order nonlinear refractive index are obtained by simultaneously solving equations 3.10 and 3.11 to give:

$$\Delta\Phi_{0(l)} = \Delta\eta_{1(l)} (2\pi/\lambda) L_{\text{eff}} \quad (3.12)$$

where  $\Delta\Phi_{0(l)}$  is the (maximum) on-axis nonlinearly induced phase shift at the focus,  $L_{\text{eff}} = (1 - e^{-\alpha_1 l}) / \alpha_1$ , with  $l$  the sample length and  $\alpha_1$  the linear absorption coefficient. Here,  $\Delta\eta_1 = \eta_2 I_{0(l)}$  with  $I_{0(l)}$  being the on axis irradiance at focus (i.e.  $z = 0$ ). Note that equation 3.8 describes the case where there is no nonlinear absorption and hence equation 3.5 reduces to  $\alpha_{(l)} = \alpha_1$ . Note also that Fresnel reflection losses are ignored and therefore  $I_{0(l)}$  is the irradiance within the sample. To convert  $\Delta\Phi_{0(l)}$  into  $\Delta\phi(z,r,t)$  we must first convert it to  $\Delta\phi_{0(z,t)}$  thus:

$$\Delta\phi_{0(z,t)} = \Delta\Phi_{0(l)} / (1+z^2/z_0^2) \quad (3.13)$$

The attenuation term  $(1+z^2/z_0^2)$  is specific to a Gaussian beam and takes into account the fact that as the beam propagates along the z-axis the beam spreading will reduce the on-axis ( $r = 0$ ) irradiance, which in turn reduces the nonlinear phase shift amplitude. The last noteworthy step is that the radial component of the nonlinear phase shift  $\Delta\phi(r)$  simply follows the radial variation of the incident irradiance, at a given position of the sample z (i.e. a Gaussian profile). We therefore lead into the following expression for the nonlinearly induced phase shift at the exit surface of the sample:

$$\Delta\phi_{(z,r,t)} = \Delta\phi_{0(z,t)} \exp \left[ -2r^2 / w^2(z) \right] \quad (3.14)$$

The complex electric field exiting the sample  $E_e$  can now be written in a form which contains the nonlinear phase distortion:

$$E_{e(z,r,t)} = E_{(z,r,t)} e^{-\alpha L/2} e^{i\Delta\phi_{(z,r,t)}} \quad (3.15)$$

In the equation above  $E_{(z,r,t)}$  is the incident electric field; the first exponent represents the beam attenuation owing to the sample absorption; while the second exponent is the term with the nonlinear phase distortion whose distribution follows a Gaussian profile. Note, again that the equation above (3.15) is valid for cubic refractive nonlinearity only (i.e. there is no third order nonlinear absorption present).

By virtue of Huygen's principle, one can obtain the far-field pattern of the beam at the aperture plane through a zeroth-order Hankel transformation of  $E_e$  <sup>11</sup>. In this case a more convenient treatment applicable to Gaussian beams is followed, which is referred to as the "Gaussian Decomposition" method given by Weaire *et al* <sup>12</sup>. The complex electric field at the exit plane of the sample is decomposed into a summation of Gaussian beams with varying beam parameters through a Taylor series expansion of the nonlinear phase term  $e^{i\Delta\phi_{(z,r,t)}}$  in equation 3.15. That is:

$$e^{i\Delta\phi_{(z,r,t)}} = \sum_{m=0}^{\infty} \frac{[i\Delta\phi(z,t)]^m}{m!} e^{-2mr^2 / w^2(z)} \quad (3.16)$$

Each Gaussian beam can be propagated to the aperture plane where they will be re-summed to reconstruct the beam. When including the initial beam curvature for the focused beam, we derive the resultant electric field pattern at the aperture as:

$$E_a(r,t) = E_{(z,r=0,t)} e^{-\alpha L/2} \sum_{m=0}^{\infty} \frac{[i\Delta\phi(z,t)]^m}{m!} \frac{w_{m0}}{w_m} \exp \left( -\frac{r^2}{w_m^2} - \frac{ikr^2}{2R_m} + i\theta_m \right) \quad (3.17)$$



Defining  $d$  as the propagation distance in free space from the sample to the aperture plane and  $g = 1+d / R(z)$ , the remaining parameters in equation 3.17 are expressed as:

$$w_{m0}^2 = \frac{w^2(z)}{2m+1} \quad (3.18)$$

$$d_m = \frac{kw_{m0}^2}{2} \quad (3.19)$$

$$w_m^2 = w_{m0}^2 \left[ g^2 + \frac{d^2}{d_m^2} \right] \quad (3.20)$$

$$R_m = d \left[ 1 - \frac{g}{g^2 + d^2/d_m^2} \right]^{-1} \quad (3.21)$$

$$\theta_m = \tan^{-1} \left[ \frac{d/d_m}{g} \right] \quad (3.22)$$

The expression given by equation 3.17 is a general case of that derived by Weaire et al <sup>12</sup> where they considered a collimated beam ( $R = \infty$ ) for which  $g = 1$ . This Gaussian Decomposition method is useful for the small phase distortions detected with the Z-scan method since only a few terms of the sum in equation 3.16 are needed. The method can in principle be extended to account for higher order nonlinearities<sup>6</sup>. The transmitted power through the aperture is obtained by spatially integrating  $E_{a(r,t)}$  up to the aperture radius  $r_a$ , giving:

$$P_{T(\Delta\Phi_0(t))} = c\epsilon_0\eta_1 \int_0^{r_a} |E_{a(r,t)}|^2 r dr \quad (3.23)$$

where  $\epsilon_0$  is the permittivity of vacuum. Including the pulse temporal variation, the normalised closed aperture Z-Scan transmittance  $T_{cl(z)}$  can be calculated as:

$$T_{cl(z)} = \frac{\int_{-\infty}^{\infty} P_{T(\Delta\Phi_0(t))} dt}{S \int_{-\infty}^{\infty} P_{I(t)} dt} \quad (3.24)$$

where  $P_{i(t)} = \pi w_0 |I_0(t)|/2$  is the instantaneous input power (within the sample) and  $S=1-\exp(-2r_a^2/w_a^2)$  is the aperture linear transmittance, with  $w_a$  denoting the beam radius at the aperture in the linear regime. For a cubic nonlinearity and a small phase change ( $|\Delta\Phi_0| \ll 1$ ) the on-axis electric field at the aperture plane can be obtained by letting  $r=0$  in equation

3.17. Furthermore, only two terms of the sum in equation 3.17 need be retained. Far-field conditions ( $d \gg z_0$ ) lead to a geometry-independent normalised transmittance with:

$$T_{cl(z, \Delta\Phi_0)} \approx 1 - \frac{4\Delta\Phi x}{(x^2 + 9)(x^2 + 1)} \quad (3.25)$$

where  $x = z/z_0$ . The above equation can be fitted to a set of data in order to obtain a value for  $\Delta\Phi$ . The extrema (peak and valley) of the Z-Scan transmittance can be calculated by solving the equation  $dT_{cl(z, \Delta\Phi_0)}/dz = 0$ . Solutions to this equation yield:

$$x_{p,v} = \pm \sqrt{\frac{\sqrt{52} - 5}{3}} \approx \pm 0.858 \quad (3.26)$$

Therefore the peak-valley separation can be written as:

$$\Delta Z_{p-v} \approx 1.7 z_0 \quad (3.27)$$

The above equation can be used to determine a value for  $w_0$  via equation 3.1a (assuming a Gaussian beam profile). Inserting the  $x_{p,v}$  values from equation 3.26 into equation 3.25 yields a peak-valley transmittance change of:

$$\Delta T_{p-v} \approx \frac{8|x_{p-v}|}{(x_{p,v}^2 + 9)(x_{p,v}^2 + 1)} \Delta\Phi_0 = 0.406 \Delta\Phi_0 \quad (3.28)$$

Numerical calculations show that the above relation is accurate to within 0.5 percent for  $|\Delta\Phi_0| \leq \pi$ . Equation 3.28 is only valid for the on axis change in transmission (i.e. for a vanishingly small aperture size  $S$ ). Numerical calculations show that the following relationship can be used (within a 2% accuracy) when using a finite aperture:

$$\Delta T_{p-v} \approx 0.406(1-S)^{0.25} |\Delta\Phi_0| \quad (3.29)$$

where as above  $S = 1 - \exp(-2r_a^2/w_a^2)$  is the aperture linear transmittance, with  $w_a$  denoting the beam radius at the aperture in the linear regime. Equation 3.29 is valid for  $|\Delta\Phi_0| \leq \pi$ . Therefore equation 3.29 can be used to readily estimate the nonlinear refractive index ( $\eta_2$ ) with good accuracy without necessarily resorting to a computer fitting of equation 3.25 after a Z-Scan is performed. Once  $\Delta\Phi_0$  is known  $\eta_2$  may be calculated from equation 3.12. For pulsed radiation, transient effects are included by using the time-averaged refractive index change  $\langle \Delta\eta_{1(t)} \rangle$  which is related to  $\langle \Delta\Phi_{0(t)} \rangle$  through equation 3.12. With a nonlinearity having ultrafast response and decay times relative to the pulse-width of the laser, one obtains a temporally Gaussian pulse:

$$\langle \Delta\eta_{1(t)} \rangle = \frac{\Delta\eta_1}{\sqrt{2}} = \frac{\eta_2 I_{0(t=0)}}{\sqrt{2}} \quad (3.30)$$

where  $\Delta\eta_1$  now represents the peak-on-axis index change at the focus. With a cumulative nonlinearity having a decay time much longer than the pulse width (e.g. thermal), the time-averaged refractive index change can be written as:

$$\langle \Delta\eta_1 \rangle = \frac{1}{2} AF \quad (3.31)$$

where  $A$  is a constant which depends on the nature of the nonlinearity.  $F$  is the pulse fluence at focus within the sample. The factor of  $\frac{1}{2}$  is independent of the temporal pulse shape. For a given  $\Delta\Phi_0$ , the magnitude and shape of  $T_{cl(z)}$  does not depend on the wavelength or geometry as long as the far-field condition for the aperture plane ( $d \gg z_0$ ) is satisfied. However, the aperture size ( $S$ ) is an important parameter since a large aperture reduces the variations in  $T_{cl(z)}$ . For very large apertures or no aperture ( $S=1$ ), the peak-valley effect vanishes and  $T_{cl(z)} = 1$  for all  $z$  and  $\Delta\Phi_0$ . An open Z-Scan is when the Z-Scan is performed without an aperture.

### 3.1.2.2 Gaussian Beam, $\Delta n \neq 0$ , $\Delta\alpha \neq 0$ and “Thin Sample”

In the second ideal case, the beam profile is again Gaussian, both temporally and spatially. However, both nonlinear absorption and nonlinear refraction are present in the sample. Again, cubic nonlinearity is assumed as well as a “thin” sample.

The open Z-scan corresponds to the measurement of the total transmittance through the sample i.e. with no aperture in front of the signal detector ( $S=1$ ). It only sees the nonlinear imaginary component of the material i.e. nonlinear absorption. Such Z-scan traces are expected to be symmetrical with respect to the focus ( $z=0$ ) where they have a minimum transmittance (e.g. multi-photon absorption) or maximum transmittance (e.g. saturation of absorption) as illustrated in Figure 3.5.

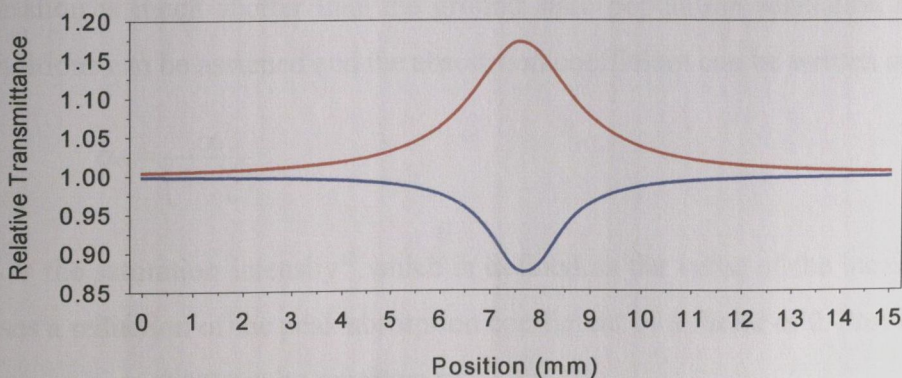


**Figure 3.5:** The blue curve shows a typical normalised open aperture Z-scan signature for an imaginary nonlinearity due to multi-photon absorption resulting in a minimum transmittance at the focus ( $z=0$ ). The red curve shows a typical normalised signature due to saturation of absorption resulting in a maximum transmittance at the focus ( $z=0$ ).

The Z-scan transmittance variations can be calculated by following the same process used for the nonlinear refraction. Two-photon absorption, which is described by equation 3.5, has  $\beta$  positive, the energy transmittance as a function of position  $z$ ,  $T_{op(z)}$  is calculated and equal to<sup>6</sup>:

$$T_{op(z)} = T_0 \sum_{m=0}^{\infty} \frac{[-q_0(z,0)]^m}{(m+1)^2} \quad (3.32)$$

where  $T_0$  is the linear transmittance at low intensity and is equal to  $\exp[-\alpha_0 L]$ , and:

$$q_0(z,0) = \frac{\beta I_0(z=0) L_{eff}}{\left(1 + \frac{z^2}{z_0^2}\right)} \quad (3.33)$$

where  $L_{eff} = (1 - e^{-\alpha_1 l}) / \alpha_1$ , with  $l$  the sample length and  $\alpha_1$  the linear absorption coefficient. However, equation 3.32 is only true for small nonlinear losses, i.e. where:

$$|q_0(z=0,0)| < 1 \quad (3.34)$$

Equation 3.32 can be fitted to a set of open aperture Z-scan data in order to obtain a value for  $\beta$ . The equation mimics the on-axis intensity distribution with  $z$  for a focused Gaussian beam as seen in Figure 3.5 above.

When the Z-scan is performed at a wavelength where the sample shows a strong absorption, saturation is likely to occur due to the high on-axis intensities experienced by the sample as it gets near and passes through the focus. As photons from the incident light pump electrons into the upper energy level in a two-level system, the ground state becomes depleted. The increased population of the upper state also leads to the spontaneous and stimulated emission of photons. The net result is that the system cannot absorb as large a fraction of the incident light as it can under low-intensity conditions. When the optical pulse duration is much shorter than the ground state population relaxation time, steady-state conditions can be assumed and the absorption coefficient can be written as:

$$\alpha_{(0)} = \frac{\alpha_1}{\left(1 + I/I_s\right)} \quad (3.35)$$

where  $I_s$  is the saturation intensity<sup>13</sup> which is defined as the value of the incident intensity that causes a reduction of the peak absorption coefficient by a factor of 2. Providing that  $I/I_s \ll 1$ , then equation (3.35) can be rewritten as:

$$\alpha_{(0)} \approx \alpha_1 \left(1 - \frac{I}{I_s}\right) \quad (3.36)$$

which has a similar form to equation 3.5. It is then possible to derive the transmittance as a function of  $z$ , following the same development as in the previous case. It is also given by equation 3.32 with:

$$Q_{0(z,0)} = \frac{(\alpha_1/l_s)I_{0(t=0)}L_{\text{eff}}}{\left(1 + \frac{z^2}{z_0^2}\right)} \quad (3.37)$$

Nonlinear absorption in a material arising from either direct multi-photon absorption, saturation of the single photon or dynamic free-carrier absorption, has strong effects on the measurements of nonlinear refraction using the Z-scan technique. When both nonlinear absorption and nonlinear refraction occur, the absorptive and refractive contributions to the far-field beam profile, and hence to the Z-scan transmittance in the case of the closed aperture Z-scan, are coupled. The closed Z-scan signature of Figure 3.3 loses its symmetry under these conditions. In the case of two-photon absorption, the valley is enhanced whereas in the case of saturable absorption, the peak is enhanced. This renders the closed aperture Z-scan curves more difficult to analyse. However, it has been shown that dividing the closed aperture Z-scan by the open aperture Z-scan will give a new Z-scan result, which agrees to within  $\pm 10\%$  of that obtained with a purely refractive index Z-scan<sup>6</sup>. This method is valid provided that equation 3.34 is true and that

$$\frac{\beta}{2k\eta_2} \leq 1 \quad (3.38)$$

In the literature, the ratio  $(T_{\text{cl}(z)} / T_{\text{op}(z)}) / T_0$ , rather than  $T_{\text{cl}(z)} / T_{\text{op}(z)}$  is usually plotted versus  $z$ , and is referred as the normalised transmittance.

## 3.2 Z-Scan in Non-Ideal Conditions

While Gaussian beams are extremely convenient (a Gaussian beam remains Gaussian throughout a linear optical system in the absence of aberrations), the output of many lasers do not possess a Gaussian profile either temporally or spatially. This is due to imperfections within the laser and relates to typical experimental conditions within the laboratory. The following sub-sections will outline cases where the beam profile is not Gaussian, either temporally or spatially. As we will see later, even slight deviations from a perfect Gaussian beam can (theoretically) greatly influence the magnitude of the Z-scan experimental results. Conditions where the “thin” sample approximation are violated will also be discussed.

### 3.2.1 Non-Gaussian Beam, $\Delta n \neq 0$ , $\Delta \alpha \neq 0$ and “Thin Sample”

Zhao and Palffy-Muhoray derived the results of performing a Z-scan using a focused “top-hat” beam, where the profile at the initial focusing lens is approximately a step function in the radial coordinate  $r$ <sup>14</sup>. They investigated the case of nonlinear refraction only (i.e. no nonlinear absorption present). In, practice, the “top-hat” beam profile can be produced by taking a small portion of the expanded beams from lasers with arbitrary profiles, and using a circular aperture to make the required profile at the focusing lens. The lens focuses this beam to an Airy pattern in the absence of aberrations. If the aperture A1 in front of the focusing lens L1 has a diameter of  $d$  and the focal length of the lens is  $f$ , then the Airy radius of the focused spot of the top-hat beam is  $1.22\lambda F$ , where  $F=f/d$  (see Figure 3.6) is the F number of the system<sup>14</sup>.

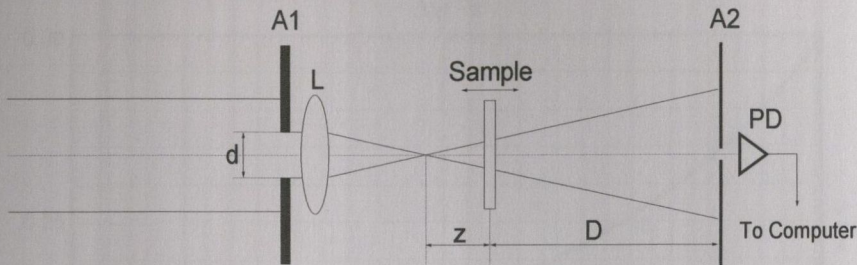


**Figure 3.6:** Schematic of top-hat Z-scan set-up. A1 is the expanded beam circular aperture clipper. A2 is the closed aperture. L is the focusing lens with focal length  $f$ . The signal measured by the photo diode PD is recorded as a function of sample position  $z$ .

The waist of the focused top-hat beam is defined to be

$$w_0 = \lambda f \quad (3.39)$$

and the diffraction length or Rayleigh range is again given by equation 3.1a. The nonlinear coefficients were numerically derived by decomposing the top-hat function in terms of Lommel functions. The empirical expression relating  $\Delta T_{cl p-v}$  to  $\Delta \Phi_0$  and aperture transmittance  $S$  is given by<sup>14</sup>:

$$\Delta \Phi_0 = 2.7 \tanh^{-1} \left( \frac{\Delta T_{cl p-v}}{2.8(1-S)^{1.14}} \right) \quad (3.40)$$

where  $\Delta \Phi_0$  is the peak nonlinear phase shift at the centre of the Airy disk at the focal plane. For  $S \approx 0$  and small  $\Delta \Phi_0$ , equation 3.40 gives:

$$\Delta T_{cl p-v} \approx 1.036 \Delta \Phi_0 \quad (3.41)$$

indicating approximately a 2.5 times larger sensitivity (compare to equation 3.29) than for a Gaussian beam Z-scan. This enhanced sensitivity is due to the steeper beam curvature gradients encountered by the nonlinear sample at  $z$  positions, near the focal plane. It also indicates that the peak-valley transmittance difference, which is the measure of the refractive nonlinearity, can vary by a factor of 2.5 due to variations in beam profile. Once  $\Delta\Phi_0$  is known  $\eta_2$  can be calculated from equation 3.12.

In a later paper<sup>15</sup> the same authors further simplified Z-scan analysis using top-hat beams. A graphical method was developed which allows straightforward determination of the nonlinear refraction and absorption coefficients from experimental data with the help of a chart. Part of this chart is shown (Figure 3.7) and illustrates the case for nonlinear absorption ( $\beta > 0$ ).

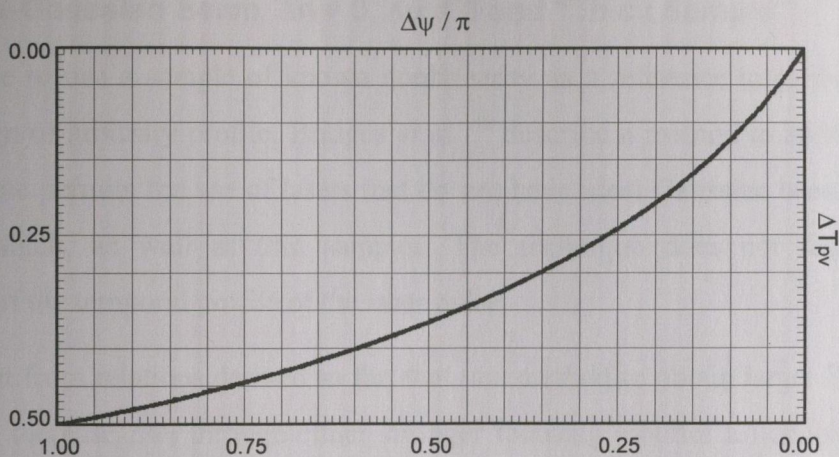


**Figure 3.7:** Chart for top-hat beam Z-scan which shows the relation between the imaginary phase shift  $\Psi/\pi$  and the open aperture transmittance peak-valley difference  $\Delta T_{op\ p-v}$  for the case of nonlinear absorption ( $\beta > 0$ ).

The paper also contains curves corresponding to saturable absorption ( $\beta < 0$ ) as well as closed aperture Z-scan corresponding to a range of  $S$  values. The curve corresponding to saturable absorption shows the relation between the imaginary phase shift  $\Delta\Psi/\pi$  and the open aperture transmittance peak valley difference  $\Delta T_{op\ p-v}$ . The curve corresponding to the closed aperture Z-scan shows the relation between the imaginary phase shift  $\Delta\Psi/\pi$  and the real nonlinear phase shift  $\Delta\Phi_0/\pi$  for different values of closed aperture transmittance peak-valley difference  $\Delta T_{cl\ p-v}$ . When a value for the real nonlinear phase shift  $\Delta\Phi_0$  is obtained from the relevant chart,  $\eta_2$  can be calculated from equation 3.12. Similarly, when a value for the imaginary phase shift  $\Delta\Psi$  is needed, the following equation may be used to calculate  $\beta$ :

$$\Delta\Psi = \beta I_0 L_{eff} \quad (3.42)$$

For the Gaussian beam Z-scan, the closed aperture Z-scan has to be divided by the open aperture Z-scan to give a trace which represents a purely refractive index Z-scan. This is only valid if equations 3.34 and 3.38 are both true. The charts mentioned above cover a wide range of circumstances including the case where:

$$\frac{\beta}{2k\eta_2} > 1 \quad (3.43)$$

Advantages of the top-hat Z-scan scheme include the relative ease of producing top-hat beams and the increased sensitivity of the Z-scan method. However, much of the pulse energy may be thrown away in forming a top-hat beam, so care must be taken to ensure sufficient pulse energy remains so that measurable nonlinear effects can be observed.

### 3.2.2 Non-Gaussian Beam, $\Delta n \neq 0$ , $\Delta \alpha \neq 0$ and "Thick Sample"

It is possible to use a sample of known nonlinearity as a reference to calibrate a system using a beam of arbitrary profile. Bridges *et al.*<sup>16</sup> describe a method to address this case. The technique permits the use of lasers that do not have ideal Gaussian beams and can be used with thick, as well as thin samples. The technique does not require detailed knowledge of the temporal profile of the laser pulse.

It is apparent from relations derived so far, that one method to obtain larger Z-scan signals ( $\Delta T_{p-v}$ ) is to increase  $\Delta \Phi_0$  through either stronger focusing (shorter  $z_0$ ) or thicker samples (larger  $L$ ). In both cases the validity of all the equations becomes questionable once the "thin sample" criterion (i.e.  $L \leq \eta_1 z_0$ ), is violated. The relative method also allows violation of the thin sample approximation as long as the reference sample has the same thickness as the sample being measured, and, the intensity is adjusted so that the  $\Delta T_{p-v}$ 's in both measurements are nearly equal. Z-scans using reference sample calibrations are useful, provided that the order of magnitude of each nonlinearity is the same (e.g. both are  $\chi^{(3)}$  type) and conditions and parameters of both experiments are maintained as close as possible. The measurement procedure is as follows<sup>16</sup>:

- 1 Obtain reference and test samples of equal thickness  $L$  for which  $|L/\eta_{1t} - L/\eta_{1r}| \ll z_0$  where  $z_0$  is the Rayleigh range in free space,  $\eta_{1t}$  and  $\eta_{1r}$  are the linear indices of refraction of the test sample and the reference sample, respectively.
- 2 Make a Z-scan measurement of one of the samples. The exact size and shape of the aperture do not matter.



- 3 Insert the second sample and adjust the input power  $P$  until the normalised peak-to-valley transmittance matches that of the first sample.
- 4 Calculate the nonlinear index of refraction using the formula:

$$\eta_{2t} = \eta_{2r} \frac{P_r}{P_t} \quad (3.44)$$

where  $\eta_{2t}$  and  $\eta_{2r}$  are the third order optical nonlinear indices of refraction of the test sample and the reference sample, respectively.  $P_r$  corresponds to the reference sample input power while  $P_t$  corresponds to the test sample input power.

For a thin sample, it is not necessary to match the lengths as indicated in step 1, since the beam does not evolve appreciably (in either size or shape) in traversing the sample. Moreover, when the nonlinear phase shift is much less than unity, step 3 may also be simplified which results in a new equation:

$$\eta_{2t} = \eta_{2r} \frac{\Delta T_{p-v,t} L_r P_r}{\Delta T_{p-v,r} L_t P_t} \quad (3.45)$$

where  $\Delta T_{p-v,t}$  and  $\Delta T_{p-v,r}$  correspond to normalised peak-to-valley transmittance for test and reference samples, respectively. Likewise  $L_t$  and  $L_r$  correspond to test and reference sample length respectively.

This technique makes it possible to measure nonlinearities using lasers that previously would have been unsuitable for Z-scan measurements because of either inadequate beam quality or inadequate power. Another advantage of the technique is that it does not require detailed knowledge of the temporal characteristics of the laser pulse. However, this method leads to relative values only and cannot be used when there is linear or nonlinear absorption present.

### 3.2.3 Background Subtraction

Where possible, it is often beneficial to perform experiments at high and low intensity levels (low enough that the nonlinear response is negligible) and then subtract the two sets of data<sup>6</sup>. This greatly reduces background signals due, for example, to sample inhomogeneities or sample wedge. A necessary condition for this background subtraction process to be effective is that the sample position be reproducible for both high and low intensity scans (i.e. laterally, vertically and along  $z$ ). It is also important that the datasets be normalised before subtraction such that  $T(|z| \gg z_0)$  are made equal for high and low

intensity Z-scans. Experience has shown that even when the signal is indistinguishable in a background that this subtraction can often uncover a usable signal<sup>1</sup>.

### 3.3 Z-Scan Technique Variations

To show the versatility of Z-Scan as a measurement technique, a number of variations have been developed since it's first inception. Two of the main variations are outlined briefly below.

#### 3.3.1 Eclipsing Z-Scan

As the Z-scan method relies on propagation of a phase distortion to produce a transmittance change, the minimum detectable signal is determined by how small a transmittance change can be measured. The high sensitivity comes about from the interference (diffraction) of different portions of the spatial profile in the far field. Recently, it was realised that this sensitivity could be greatly increased by looking at the outer edges of the beam in the far field rather than the central portion, as in the standard Z-scan<sup>17</sup>. This is accomplished by replacing the apertures in Figure 3.1, with disks that block the central part of the beam. The light that leaks around the edges appears as an eclipse, thus the name "EZ-scan".

However, the enhancement of sensitivity in the EZ-scan, is at the expense of signal photons, as well as a reduction in the accuracy and absolute calibration capability. This added uncertainty originates from the deviations of the laser beams from a Gaussian distribution, and the fact that we need to know  $S$  very accurately. This technique is only recommended when the additional sensitivity is required and when a known reference sample is available to calibrate the system.

#### 3.3.2 Excite-Probe Z-Scan

Excite-probe techniques in nonlinear optics have been commonly employed in the past to deduce information that is not accessible with a single beam geometry. The most significant application of such techniques concerns the ultra-fast dynamics of the nonlinear optical phenomena. There has been a number of investigations that have used Z-scan in an excite-probe scheme<sup>18</sup>. Due to collinear propagation of the excitation and probe beams, they can be separated only if they differ in wavelength or polarisation. The former scheme, known as a 2-color Z-scan, has been used to measure the non-degenerate  $\eta_2$  and  $\beta$  in semiconductors. The time-resolved studies can be performed in two ways. In one scheme,

Z-scans are performed at various fixed delays between excitation and probe pulses. In the second scheme, the sample position is fixed (e.g. at the peak or the valley position), while the transmittance of the probe is measured as the delay between the two pulses is varied. The analysis of the a 2-color Z-scan is naturally more involved than that of a single beam Z-scan. The measured signal, in addition to being dependent on the parameters discussed for the single beam geometry, also depend on parameters such as the excite-probe beam waist ratio, pulse-width ratio and the focal separation due to chromatic aberration of the lens.

### 3.4 Interpretation of Z-Scan Results

One of the disadvantages of the Z-scan technique is that it is sensitive to all nonlinear optical mechanisms that give rise to a change of the refractive index and/or absorption coefficient. As is the case with most nonlinear optical measurement techniques, the measured quantities are the time average nonlinearity induced  $\langle \Delta\eta \rangle$  and/or  $\langle \Delta\alpha \rangle$ , where  $\langle \rangle$  denotes the time-average over the time corresponding to the temporal resolution of the detection system. Because the different nonlinear mechanisms respond at different timescales, time-averaged experiments often measure several competing nonlinear mechanisms (e.g. multi-photon absorption competing with saturable absorption, or ultrafast electronic nonlinear refraction competing with slower thermally induced nonlinear refraction), so that the nonlinear optical results can depend strongly on the temporal profile of the laser pulse.

Although many observed nonlinear optical effects give index changes proportional to the intensity ( $\Delta\eta \propto I$ ), higher order effects can be encountered where  $\Delta\eta \propto I^p$ , with  $p > 1$ . For example, a fifth order nonlinear refraction ( a  $\chi^{(5)}$  type nonlinearity where  $p=2$ ) becomes the dominant mechanism in semiconductors, when  $\Delta\eta$  is induced by two-photon generated free-carriers<sup>19</sup>. Where  $\chi^{(3)}$  and  $\chi^{(5)}$  processes are simultaneously involved, the data analysis becomes more complicated. A procedure is documented in the literature for separating the two processes using a number of Z-scans at different intensities<sup>19</sup>. To unambiguously determine the underlying physical processes responsible for the nonlinear property of a particular sample, a variety of additional experiments are sometimes needed such as a series of Z-scans at varying pulse-widths, frequencies and focal geometries.

---

## References

- 1 M. Sheik-Bahae, A. A. Said, and E.W. Van Stryland, "High Sensitivity, Single Beam  $n_2$  Measurements", *Opt. Lett.* **14**, 955 (1989).
- 2 L. Yang, R. Dorsinville, Q. Z. Wang, P. X. Ye, R. R. Alfano, R. Zamboli and C. Taliani, *Opt. Lett.* **17**, 323 (1992).
- 3 H. Ma, A. S. Gomez, and C. B. de Araujo, "Measurement of nondegenerate optical nonlinearity using a two-color single beam method", *Appl. Phys. Lett.* **59**, 2666 (1991).
- 4 S. A. Akhmanov, A. D. Sukhorokov, and R. V. Khokhlov, "Self focusing and diffraction of light in a nonlinear medium", *Sov. Phys. Uspekhi (English transl.)*, **10**, 609 (1968).
- 5 W. L. Smith, J. H. Bechtel, and N. Bloembergen, "Dielectric-breakdown threshold and nonlinear-refractive index measurements with picosecond laser pulses", *Phys. Rev. B*, **12**, 706 (1975).
- 6 M. Sheik-Bahae, A. A. Said, T. H. Wei, D. J. Hagan, and E.W. Van Stryland, "Sensitive Measurement of Optical Nonlinearities Using a Single Beam", *JQE*, **QE26**, 760 (1990).
- 7 C. R. Giuliano, and L. D. Hess, "Nonlinear Absorption of Light: Optical Saturation of Electronic Transitions in Organic Molecules with High Intensity Laser Radiation", *IEEE J. Quant. Electron*, **QE-3**, 338 (1967).
- 8 T. H. Wei, D. J. Hagan, M. J. Sence, E. W. Van Stryland, J. W. Perry, and D. R. Coulter, "Direct Measurements of Nonlinear Absorption and Refraction in Solutions of Phthalocyanines", *Applied Physics B*, **54**, 46 (1992).
- 9 E.W. Van Stryland, M. Sheik-Bahae, A. A. Said, and D. J. Hagan, "Characterization of Nonlinear Optical Absorption and Refraction", *Prog. Crystal Growth and Charact.*, **27**, 279 (1993).
- 10 A. E. Kaplan, "External Self-Focusing of Light by a Nonlinear Layer", *Radiophys. Quant Electron.*, **12**, 692 (1969).
- 11 J. D. Gaskill, "Linear systems, Fourier Transforms, and Optics", New York: Wiley (1978).
- 12 D. Weaire, B. S. Wherrett, D. A. B. Miller and S. D. Smith, "Effect of low-power nonlinear refraction on laser beam propagation in InSb", *Opt. Lett.*, **4**, 331 (1974).
- 13 P.N. Butcher and D. Cotter, "The Elements of Nonlinear Optics", Cambridge Univ. Press, 150 (1990).
- 14 W.Zhao, P. Palffy-Muhoray, "Z-scan technique using top-hat beams" *Appl. Phys. Lett.* **63**, 1613 (1993).
- 15 W.Zhao, P. Palffy-Muhoray, "Z-scan measurement of  $\chi^{(3)}$  using top-hat beams" *Appl. Phys. Lett.* **65**, 673 (1994).
- 16 R. E. Bridges, G. L. Fischer and R. W. Boyd, *Opt. Lett.* **20**, 1821 (1995).
- 17 T. Xia, D.J. Hagan, M. Sheik-Bahae, E. W. Van Stryland, "Eclipsing Z-scan measurement of  $\lambda/10^4$  wave front distortion", *Optics Letters*, **19**, 317 (1994).
- 18 H. Ma, B. Cid de Araujo, "Two-color Z-scan technique with enhanced sensitivity", *App. Phys. Lett.* **66**, 1581 (1995).
- 19 A. A. Said, M. Sheik-Bahae, D. J. Hagan, T. H. Wei, J. Wang, J. Young, and E. W. Van Stryland, "Determination of Bound and Free-Carrier Nonlinearities in ZnSe, GaAs, CdTe, and ZnTe", *JOSA B*, **9**, 405 (1992).

## 4 Polymer Samples

This chapter begins by introducing the reasons behind the selection of the polymers which were studied. This is followed by a look at each of the four polymers, during which their chemical structure and linear optical properties are presented. Computer modelling results for each of the polymers are also presented and the trends obtained are compared with experimentally measured properties. Any expected trends for nonlinear refraction and nonlinear absorption based on the linear properties and the molecular modelling are discussed.

Considerable research has been undertaken to find polymers which would be suitable for all optical switching at the telecommunications wavelength of 1550nm. This wavelength is best suited (low absorption and low dispersion) for high speed optical communications over long distances in optical fibres<sup>1</sup>. Research has also been undertaken to find polymers which would be suitable for all optical switching applications at wavelengths between 500-800nm, the so called "fibre to the home" wavelength region<sup>2</sup>. Polymer optical fibres (POF) are seen as a promising solution to provide the necessary increase in bandwidth which will be needed in the future home network<sup>3</sup>. Wavelengths typically considered are 650nm (close to the red attenuation minimum of PMMA) and more recently 570nm and 520nm (even lower attenuation, and upcoming very powerful light sources)<sup>4</sup>.

With this in mind, polymers were synthesised and experiments were carried out to evaluate the suitability of each polymer as an all optical switching material, specifically at the shorter fibre to the home wavelengths. Computer modelling of the polymers was also carried out in order to compare the theoretically predicted trends with experimentally measured ones.

### 4.1 Materials Studied

Four polymers were synthesised in all. Two of the polymers are members of the poly(aryleneethynylene) (PAE) family. The other two polymers are poly(arylenevinylene) (PAV) counterparts of the first two. In the sections to follow it will be seen that the all four polymers have a well defined structural relationship to each other. It was hoped that the relationships between the polymers would have some sort of correlation to the experimentally measured values for linear optical absorption, as well as the nonlinear refraction and absorption. This may help the design and optimisation of new polymers with

properties tailored for all optical switching applications at visible or near infra red “fibre to the home” wavelengths. All of the polymers in this thesis were synthesised by Dr. Andy Davey and Ms. Anna Drury in the Physics Department, Trinity College.

#### 4.1.1 Poly(aryleneethynylene)s

In the hunt towards organic materials with large and good processability, the family of poly(aryleneethynylene)s (PAE) are relatively new and have not yet been subject to extensive study. They are characterised by aromatic moieties connected by carbon-carbon triple bonds. The chemical structure and names of the two materials which belong to the PAE family of polymers are shown in figure 4.1 and 4.2 below. For information on their chemical synthesis, the reader should refer to reference 2.

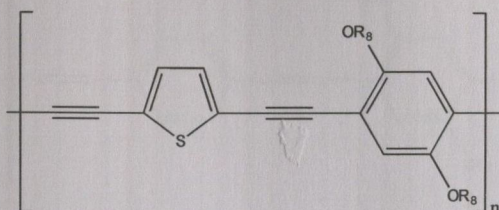


**Fig 4.1:** Chemical Structure of poly(2,5-dioctyloxy-paraphenylene-ethynylene-co-2,5-thienyl) (Thienyl-PAE). The  $R_8$  refer to the Octyl side-groups.

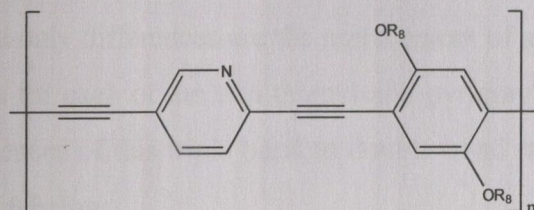


**Fig 4.2:** Chemical Structure of poly(2,5-dioctyloxy-paraphenylene-ethynylene-co-2,5-pyridinyl) (Pyridinyl-PAE). The  $R_8$  refer to the Octyl side-groups.

Early studies have shown that the obtained polymers have high molecular weights ( $M_w \sim 10^5$  which correspond to long polymer chains of several tens of repeat units) and a rigidly linear structure (rod like in solution)<sup>5</sup>. The rigid backbone structure is imparted by carbon-carbon triple bond linkages. A rigid backbone with a large number of delocalized electrons makes this family of polymers promising materials in the field of nonlinear optics. Both polymers have been found to be soluble in toluene and chloroform.

#### 4.1.2 Poly(arylenevinylene)s

The two remaining polymers belong to the poly(arylenevinylene) (PAV) family of polymers. They are characterised by aromatic moieties connected by carbon-carbon double

bonds. Their chemical structure and names are shown below in figure 4.3 and 4.4 below. These two polymers were chosen as they were the double bond analogues of the above PAE polymers. This ensures that all four polymers have a well defined structural relationship between them.

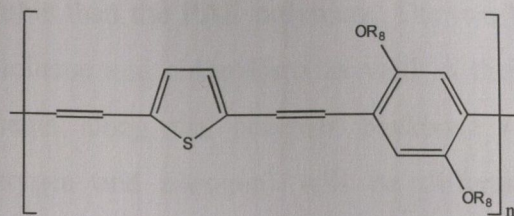


**Fig 4.3:** Chemical Structure of poly(2,5-dioctyloxy-paraphenylene-vinylene-co-2,5-thienyl) (Thienyl-PAV). The  $R_8$  refer to the Octyl side-groups.

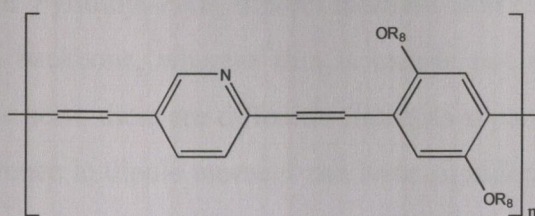


**Fig 4.4:** Chemical Structure of poly(2,5-dioctyloxy-paraphenylene-vinylene-co-2,5-pyridinyl) (Pyridinyl-PAV). The  $R_8$  refer to the Octyl side-groups.

As can be seen from figures 4.1 through 4.4 the PAE and PAV polymers have very similar chemical structures. The only differences are the replacement of all the (PAE) triple bonds by (PAV) double bonds for each of the two thienyl and pyridinyl family members. There are some other consequences of this triple bond to double bond substitution, which can be seen in figures 4.5 and 4.6 below.

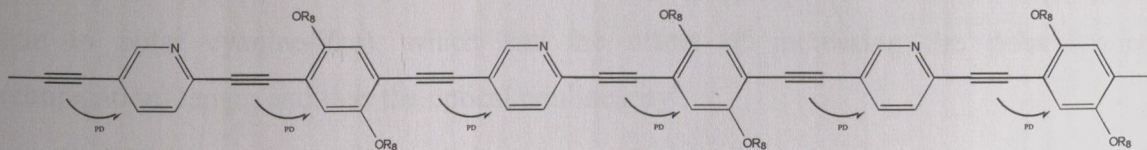


**Fig 4.5:** Chemical Structure of a Pyridinyl-PAE polymer showing several repeat units. Note the linearity of the backbone. Also indicated are some of the permanent dipole (PD) moments along the polymer backbone due to the different electronegativities of oxygen and nitrogen.

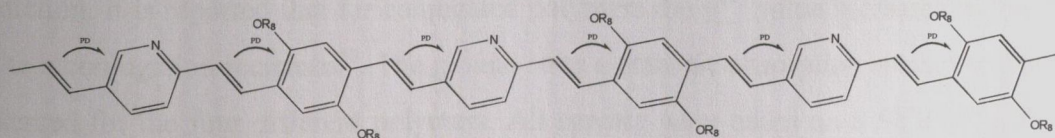


**Fig 4.6:** Chemical Structure of a Pyridinyl-PAV polymer showing several repeat units. Note the kinks along the backbone in this case compared to the above PAE. Also indicated are some of the permanent dipole (PD) moments along the polymer backbone due to the different electronegativities of oxygen and nitrogen.

The PAV polymers do not have a rigid, linear backbone structure in contrast to the PAE polymers. This is imparted by the carbon-carbon double bond linkages which do not support a linear structure. This alternation in direction can be viewed as an increase in disorder and usually serves to increase the solubility. The PAV polymers are therefore expected to be more soluble than the PAE polymers. The two PAV polymers have been found to be soluble in toluene and chloroform as well as their PAE counterparts. The permanent dipole moments along the polymer backbone (caused by the different electronegativities of oxygen and nitrogen) will be different for any two polymer analogues. One reason for this is the difference in charge distribution between the double and triple bonds. Another reason for the difference in dipole moment is the different backbone geometry, the Pyridinyl-PAE dipole moment acts along an essentially one dimensional conjugated backbone, whereas this is clearly not so for its Pyridinyl-PAV analogue. As can also be seen, there are different distances separating the different charge distributions. This difference in dipole moment can have significant effects with respect to the third order optical nonlinearities. Different permanent dipole moments lead to different intramolecular charge transfer (CT) interactions in the  $\pi$ -conjugation system. This CT interaction has been linked with third order nonlinear absorption and refraction enhancement within other PAE polymers<sup>6</sup>.

Theoretical and experimental studies of different polymers show that the different bond-length alternation present for each different type of polymer can make significant contributions to the overall nonlinearity of a given polymer<sup>7,8</sup>. A permanent dipole moment can help reduce the bond length alternation (changing the structure from neutral polyene-like to polar cyanine-like), which has the effect of increasing the delocalisation (conjugation) length and thus the optical nonlinearity<sup>9</sup>.

## 4.2 Linear Optical Properties

The linear optical absorption spectrum can be an important characteristic in  $\chi^{(3)}$  trend prediction. It is reported that for conjugated polymers the  $\chi^{(3)}$  value increases as the extent of the  $\pi$  conjugation increases<sup>10</sup>. The ground state electronic absorption spectra will now be presented for the four different polymers. All spectra were taken on a Shimadzu UV-1601 spectrometer. Computer modelling which predicts theoretical linear optical absorption trends for the polymers is presented in section 4.3. The theoretical and experimental results are then compared and discussed in section 4.4



### 4.2.1 Poly(aryleneethynylene)s

This section contains the ground state linear absorption spectra for both the Pyridinyl-PAE (figure 4.7) and Thienyl-PAE (figure 4.8) polymers. The solid state curves are for a 75nm thick solid state film of Pyridinyl-PAE polymer and 52nm thick solid state film of Thienyl-PAE polymer respectively. In each case a blank borosilicate substrate identical to the ones which the polymers used as substrates, was used as a reference. The spectra are taken from the same films which were used for all subsequent solid state nonlinear measurements. Each graph also contains data curves for two different solution concentrations. The low concentration curve is for a 0.250 g/l solution in a quartz cuvette which had a 1mm optical path length. The measurement used a toluene filled cell as a reference. The other remaining high concentration curve is for a 0.875 g/l solution in a quartz cuvette which had a 10mm optical path length. The high concentration linear absorption spectra were taken so that more accurate absorption coefficients (which are needed for subsequent nonlinear optical measurements) could be obtained.

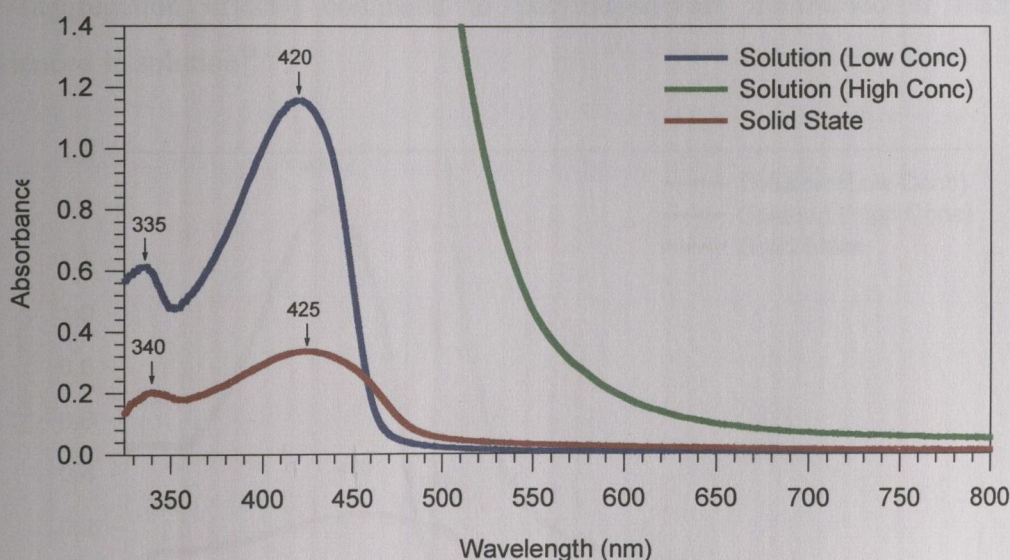


**Figure 4.7:** Spectra of Pyridinyl-PAE Polymer showing the polymer Solid State spectrum as well as solution measurements. The solvent is Toluene and the solution concentration is 0.250 g/l in the case of the “low concentration” spectrum and 0.875g/l in the case of the “high concentration” spectrum.

Both of the above absorption spectra for Pyridinyl-PAE in figure 4.7 are characterised by two absorption bands. The solution spectrum bands are centred at 335nm and 420nm, while the solid state absorption bands are both red shifted by 5nm to 340nm and 425nm respectively. The dominant maximum linear absorption peaks ( $\lambda_{max}$ ) at 420nm and 425nm (solution and solid state respectively) can be attributed to a highest occupied molecular orbital to lowest unoccupied molecular orbital (HOMO-LUMO)  $\pi$ - $\pi^*$  excitation. It is also

referred to as the  $S_0$ - $S_1$  (ground state singlet to first excited state singlet) electronic transition, or the ground state ( $^1A_g$ ) to the first one-photon excited state ( $^1B_u$ ) electronic transition depending on the terminology used. The absorption bands at 335nm in solution and 340nm in solid state both belong to a higher electronic transition<sup>11,12</sup>. Both absorption spectra have similar profiles. The smooth longer wavelength  $S_1$ -absorption bands ( $\lambda_{\max}$  at 420nm and 425nm for the solution and solid state respectively) are compatible with a semiconductor-like band structure<sup>13,14</sup> or a strong inhomogeneous broadening of a chromophore-like  $S_0$ - $S_1$  transition<sup>14,15,16</sup>. The inhomogeneous broadening (different polymer and molecule conformations are involved) results in a broad distribution of effective conjugation lengths, which may mask any vibronic structure in either spectra<sup>12,14</sup>.

The solid state absorption  $\lambda_{\max}$  (425nm) is shifted to longer wavelengths (red shifted) and spectrally broadened compared to the solution  $\lambda_{\max}$  (420nm). These changes in absorption spectra suggest that the electronic states are different in solid state and solution. This is attributed to the different polymer-polymer intermolecular (inter-chain) interactions in solid state (aggregation effects) compared to polymer-solvent intermolecular interactions experienced in solution<sup>12,17</sup>.

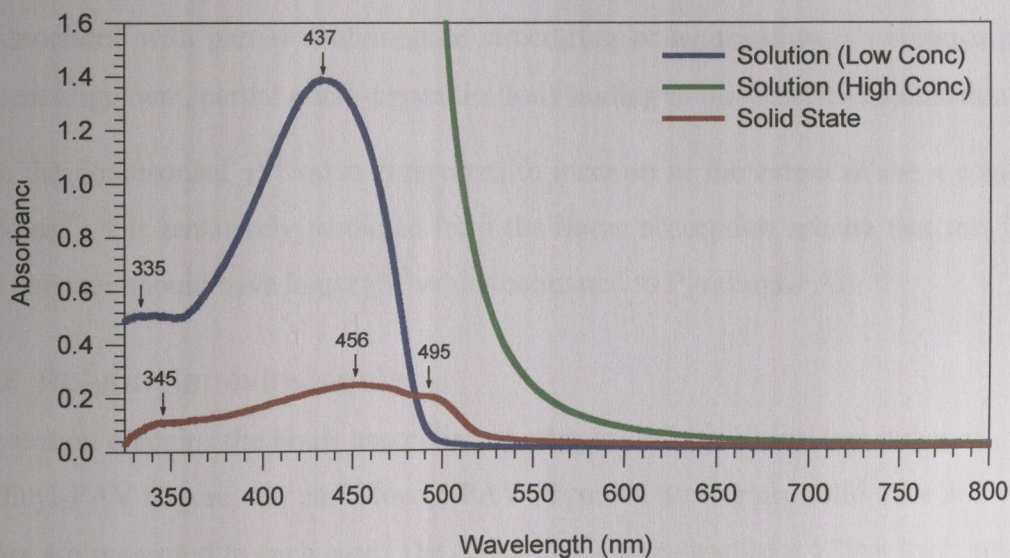


**Figure 4.8:** Spectra of Thienyl-PAE Polymer showing the polymer Solid State spectrum as well as solution measurements. The solvent is Toluene and the solution concentration is 0.250 g/l in the case of the “low concentration” spectrum and 0.875g/l in the case of the “high concentration” spectrum.

Both of the above absorption spectra for Thienyl-PAE in figure 4.8 are again characterised by two absorption bands. The solution absorption spectrum bands are centred at 335nm (again) and 437nm. The solid state shorter wavelength absorption band is red shifted by

10nm in this case to 345nm, while the dominant longer wavelength absorption band is red shifted by 19nm to 456nm. The shorter wavelength solution and solid state absorption bands for Thienyl-PAE are less pronounced than the Pyridinyl PAE ones in figure 4.7.

The Thienyl-PAE solution and solid state absorption maxima (437nm and 465nm) are respectively red-shifted compared to their Pyridinyl-PAE counterparts (420nm and 425nm). This indicates that replacement of the  $\pi$ -electron deficient pyridine unit by the  $\pi$ -electron excessive thiophene unit causes the red shift. It is suggested that the charge transfer interaction between the arylenes and the ethynylenes is strengthened by the introduction of the thiophene rings, further stabilising the  $\pi$ -conjugation which leads to the red shift.

The  $\lambda_{\max}$  for the solid state is again red shifted and spectrally broadened from the solution spectrum. This is consistent with the Pyridinyl-PAE, but the solution to solid state red shift is greater for Thienyl-PAE (19nm) in comparison to Pyridinyl-PAE (5nm). This indicates that Thienyl-PAE undergoes a larger  $\pi$ -stabilising intermolecular interaction in the solid state compared to Pyridinyl-PAE.

A new long wavelength absorption shoulder is clearly resolved at 495nm for the solid state Thienyl-PAE. Similar features have been observed with other polymers in solid state and are associated with partial conformation structuring or aggregation (short-range polymer segment alignment, partial micro-crystallisation) leading to increased  $\pi$ -stabilisation<sup>18,19,20</sup>.

Since the nonresonant  $\chi^{(3)}$  value is reported to increase as the extent of the  $\pi$  conjugation increases<sup>10</sup>, it is tentatively predicted from the linear absorption spectra that the Thienyl-PAE polymer should have larger  $\chi^{(3)}$  values compared to Pyridinyl-PAE.

### 4.2.2 Poly(arylenevinylene)s

This section contains the linear absorption spectra for the remaining two polymers, namely Pyridinyl-PAV (figure 4.9) and Thienyl-PAV (figure 4.10). Again, solid state and solution spectra are presented in each case. The Solid state curves are for a 170nm thick solid state film of Pyridinyl-PAV polymer and a 230nm thick solid state film of Thienyl-PAV polymer respectively. Each plot also contains data curves for two different solution concentrations. The low concentration curve is for a 0.250 g/l solution in a quartz cuvette which had a 1mm optical path length. The other remaining high concentration curve is for a 0.875 g/l solution in a quartz cuvette which had a 10mm optical path length.

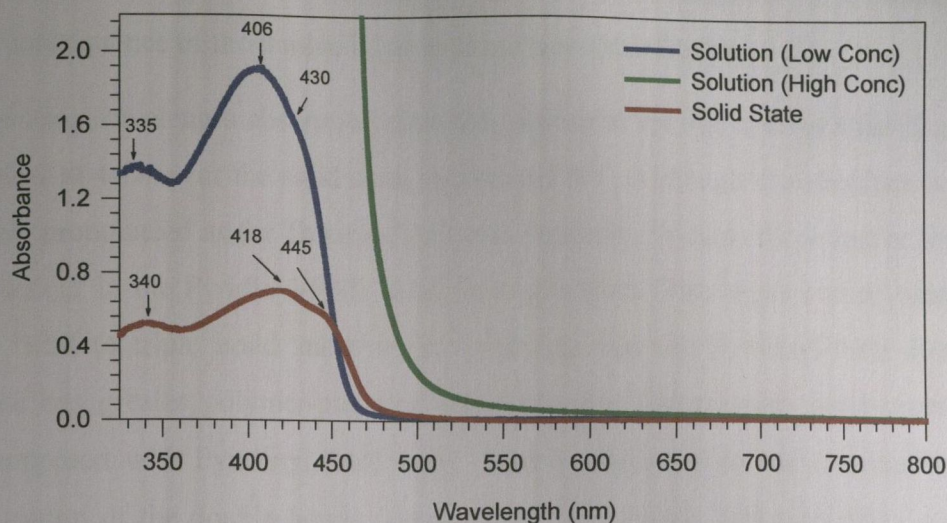


**Figure 4.9:** Spectra of Pyridinyl-PAV Polymer showing the polymer Solid State spectrum as well as solution measurements. The solvent is Toluene and the solution concentration is 0.250 g/l in the case of the low concentration spectrum and 0.875g/l in the case of the high concentration spectrum.

Both of the absorption spectra for Pyridinyl-PAV in figure 4.9 are again characterised by two absorption bands. The shorter wavelength solution absorption spectrum band is centred about 335nm similar to both Pyridinyl-PAE and Thienyl-PAE polymers. The longer wavelength absorption band is composed of two closely spaced (24nm) peaks. The higher energy one is centred about 406nm while the lower energy (longer wavelength) peak is centred about 430nm. The solid state shorter wavelength absorption band is red shifted by 5nm in this case to 340nm, while the dominant longer wavelength absorption band is red shifted by 12nm to 418nm.

The Pyridinyl-PAV solution and solid state absorption maxima (406nm and 418nm) are respectively blue-shifted compared to their Pyridinyl-PAE counterparts (420nm and 425nm). This indicates that replacement of the localised  $\pi$ -electron triple bond by the more polarisable and delocalised  $\pi$ -electron double bond causes the shift to shorter wavelengths. It is suggested that the  $\pi$ -electron deficient pyridine unit partially localises the  $\pi$ -electron from the more polarisable double bond, thus de-stabilising the  $\pi$ -conjugation with respect to the triple bond polymer. This  $\pi$ -conjugation reduction leads to the observed blue shift in the absorption spectrum.

The  $\lambda_{\max}$  for the solid state is again red shifted and spectrally broadened from the solution spectrum. The solution to solid state red shift is greater for Pyridinyl-PAV (12nm) in comparison to Pyridinyl-PAE (5nm). This indicates that Pyridinyl-PAV undergoes a larger

$\pi$ -stabilising intermolecular interaction in the solid state compared to Pyridinyl-PAE, a further consequence of the double bond to triple bond substitution.

Another long wavelength absorption shoulder similar to the one observed for Thienyl-PAE is resolved at 445nm for the solid state Pyridinyl-PAV. Although this shoulder is not quite as clearly pronounced as for Thienyl-PAE, it is however, in marked contrast to the absence of a shoulder in the Pyridinyl-PAE solid state spectrum. This again can be related to the double bond to triple bond substitution, implying that the Pyridinyl-PAE double bond analogue has greater polymer-polymer intermolecular (inter-chain) interactions in solid state compared with Pyridinyl-PAE itself. This is attributed to the increased  $\pi$ -electron delocalisation of the double bonds compared to triple bonds which in effect enables one Pyridinyl-PAV polymer chain to better “see” another Pyridinyl-PAV polymer chain, which leads to increased  $\pi$ -stabilisation through short range ordering as mentioned previously.

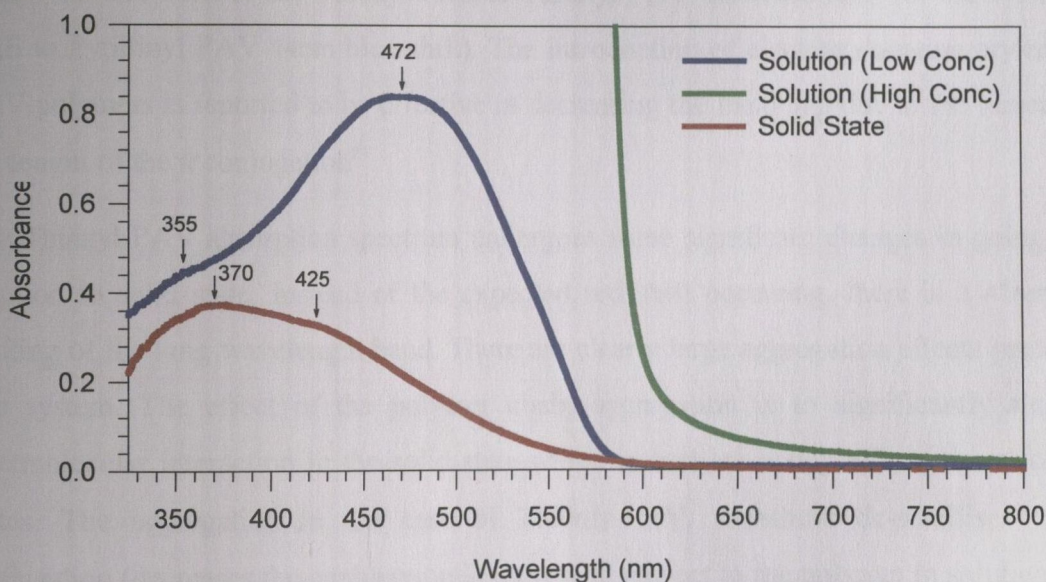


**Figure 4.10:** Spectra of Thienyl-PAV Polymer showing the polymer Solid State spectrum as well as solution measurements. The solvent is Toluene and the solution concentration is 0.250 g/l in the case of the low concentration spectrum and 0.875g/l in the case of the high concentration spectrum.

Both of the absorption spectra for Thienyl-PAV in figure 4.10 are again characterised by two absorption bands. The two spectra are in contrast to the spectra of the other three polymers where two peaks can be clearly identified for each spectrum (excluding the long wavelength shoulder in the solid state spectra, where present). The shorter wavelength solution absorption spectrum band is barely resolved, but is centred about 355nm, while the second longer wavelength dominant absorption band is centred about 472nm. The solid state shorter (and now dominant) wavelength absorption band is red shifted by 15nm in this

case to 370nm, while the longer wavelength absorption band (barely noticeable) is blue shifted by 47nm to 425nm.

The Thienyl-PAV solution long wavelength absorption maximum at 472nm is significantly red-shifted compared to the 406nm Pyridinyl-PAV absorption maximum. This indicates that replacement of the  $\pi$ -electron deficient pyridine unit by the  $\pi$ -electron excessive thiophene unit causes the red shift which is consistent with the trends observed with the PAE polymers. It is suggested in this case that the charge transfer interaction between the arylenes and the vinylenes is strengthened (even more so than for the PAE counterparts) by the introduction of the thiophene rings, further stabilising the  $\pi$ -conjugation which leads to the red shift. The combination of the more delocalised  $\pi$ -electrons associated with the double bonds, together with the  $\pi$ -electron excessive thiophene unit, red shifts the long wavelength absorption maximum by 66nm compared with the Pyridinyl-PAE to Thienyl-PAE 17nm red shift or the Thienyl-PAE to Thienyl-PAV 35nm red shift (or the Pyridinyl-PAE to Pyridinyl PAV 14nm blue shift). The introduction of electron donating arylenes to PAV polymers is reported to be effective in decreasing the band gap due to the increase in the length of the  $\pi$  conjugation<sup>21</sup>.

The Thienyl-PAV absorption spectrum undergoes some significant changes in going from solution to solid state. Instead of the expected red shift occurring, there is a 47nm blue shifting of the long wavelength band. There are clearly large aggregation effects present in this system. The effect of the polymer chain aggregation is to significantly alter the intermolecular interaction in the solid state which in turn adversely effects the electronic states. The aggregation in the case of Thienyl-PAV, somehow de-stabilises the  $\pi$ -conjugation (decreases the conjugation length) with respect to the polymer in solution. One possible explanation is that any steric hindrance in the solid state (caused by the side groups/chains, which do not take part in the  $\pi$  bands; or possibly the way the polymer tries to orientate or pack itself) could induce considerable inter-ring twisting, giving rise to a substantial reduction of the polymer conjugation length. The reduction in conjugation length will show as a blue shift in the absorption spectrum.

### 4.3 Computer Modelling

With the major advances that have been made in computer power of desktop workstations it is now possible to perform quantum mechanical calculations on segments of polymer (not infinite polymer chains) long enough to approximate the actual polymer. There are two

main types of theoretical calculations performed in computational chemistry; *Ab initio* and semiempirical<sup>22</sup>. *Ab initio* roughly translated from Latin means 'from scratch'. The term is applied to calculations of molecular structure that use no input other than the Schrödinger equation, the values of the fundamental constants (specifically,  $e$ ,  $m_e$ , and  $\hbar$ ), and the atomic number of the atoms present, and is also referred to as the self-consistent field (SCF) method<sup>23</sup>. The procedure begins with a set of approximate orbitals for all the electrons in the system under investigation. One electron is then selected and the potential in which it moves is calculated by freezing the distribution of all the other electrons and treating their averaged distribution as a centrosymmetric source of potential. The Schrödinger equation for the electron is solved for this potential, which gives a new orbital for it. The procedure is then repeated for all the other electron in the system, using the electrons in the frozen orbitals as the source of the potential. At the end of one complete cycle, there is a new set of orbitals which differs from the original set. The cycle is then repeated, but the improved wavefunctions generated by the first cycle are used as the starting point. Another complete cycle generates yet another new set of further improved functions. The sequence is continued until passing a set of orbitals through the cycles leaves them unchanged. The orbitals are then self-consistent. However, these type of calculations are complicated and extremely computationally intensive. When the labour of a self-consistent field molecular orbital calculation appears too great (or actually is), approximations are introduced and integrals are estimated from empirical data. Such methods give rise to numerous semiempirical techniques of molecular orbital calculation. The programs that are available typically require very little knowledge of quantum mechanics and are widely used as a resource in industry. Traditionally semiempirical methods have been the only way to study molecules of more than about 30 atoms. The semi-empirical quantum mechanical calculations which are typically performed are still approximations and consequently the results are not always entirely accurate. However, there are cases where semi-empirical calculations can be quite accurate, especially for predicting relative trends between similar molecular systems<sup>22</sup>.

### 4.3.1 Geometry Optimisation

All four polymers were modelled using the commercially available Hyperchem© Professional version 6. Semi-empirical calculations were used to predict the optimised ground state geometry for each of the polymers. From these optimised structures the ground state electronic absorption spectra (unbroadened and *in vacuo*) along with the

linear polarisability were calculated. For each polymer various oligomers (monomers to heptamers for PAE and monomers to pentamers for PAV) with and without side-groups were modelled. The results enable comparison of the electronic absorption trends between the oligomers with side-groups attached and the oligomers without side-groups attached. Calculations involving side groups are significantly more computationally intensive than without the side groups as there is a significant reduction of atoms.

The starting geometry is first approximated by the MM+ molecular mechanics method within the Hyperchem package. The MM+ is the most general method, developed principally for organic molecules and calculates the potential energy of molecular systems as a function of the coordinates of their atomic nuclei. This method treats the nuclei as Newtonian particles under the influence of a potential energy function or force field and uses empirical data to determine individual force constants. Once the starting geometry has been approximated, the program calculates the energy minimised geometry by use of the parametric model 3 (PM3) semi-empirical parameterisation. For further details about MM+, PM3 and the ZINDO/S (discussed in 4.3.2) semiempirical methods used, the reader is referred to the two Hyperchem manuals<sup>24</sup> which cover the topics and their respective suitability in greater detail. Figures 4.11 through 4.17 below show the PM3 semiempirical method calculated energy minimised geometries for each of the four polymers.

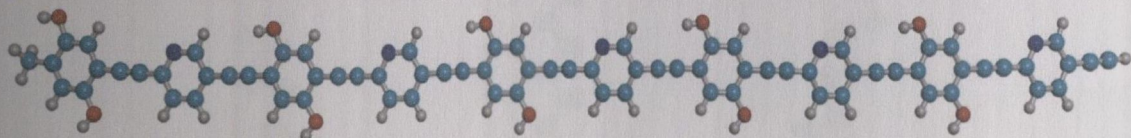


**Figure 4.11:** PM3 semiempirical method calculated energy minimised geometry (2-dimensional x-y plane representation of the 3-dimensional structure) of the Pyridinyl-PAE linear backbone pentamer without side groups attached.

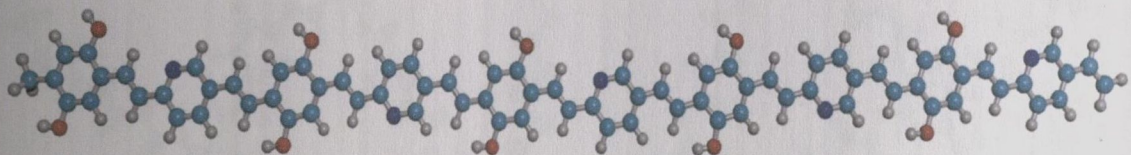


**Figure 4.12:** PM3 semiempirical method calculated energy minimised geometry (2-dimensional x-y plane representation of the 3-dimensional structure) of the Pyridinyl-PAV linear backbone pentamer without side groups attached.

All the calculations show that the Polymers like to adopt a planar structure. This type of structure maximises the  $\pi$ - $\pi$  electron overlap, which increases the conjugation length and also serves to increase the nonresonant  $\chi^{(3)}$ .



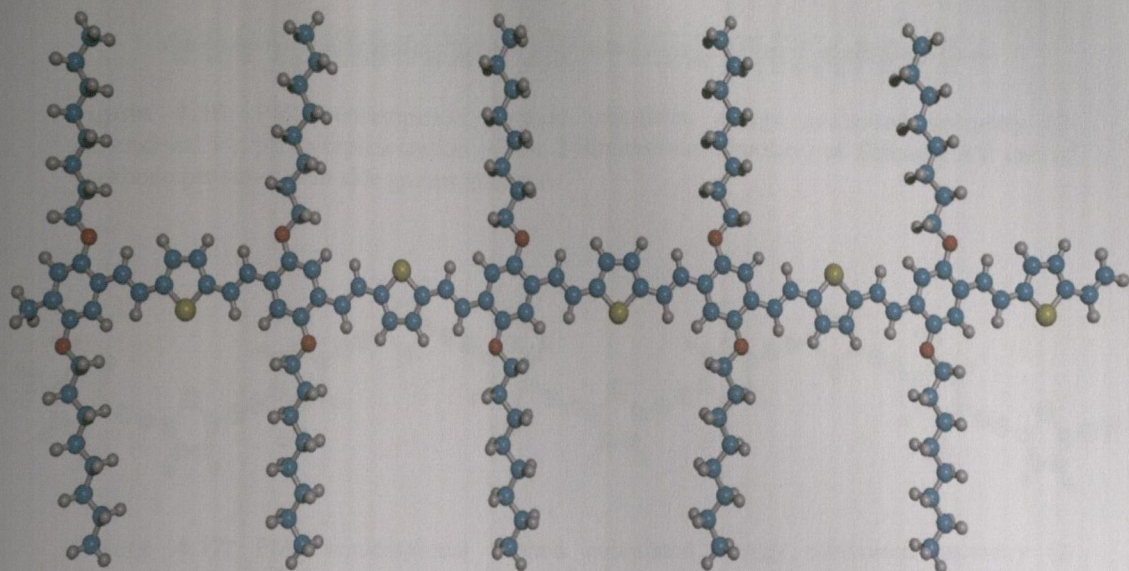


**Figure 4.13:** PM3 semiempirical method calculated energy minimised geometry (2-dimensional x-y plane representation of the 3-dimensional structure) of the Thienyl-PAV linear backbone pentamer with side groups attached.

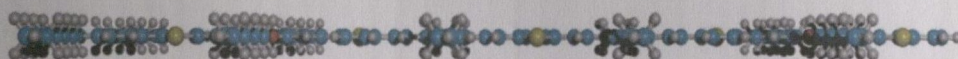


**Figure 4.14:** PM3 semiempirical method calculated energy minimised geometry (2-dimensional x-z plane representation of the 3-dimensional structure) of the Thienyl-PAV linear backbone pentamer with side groups attached.

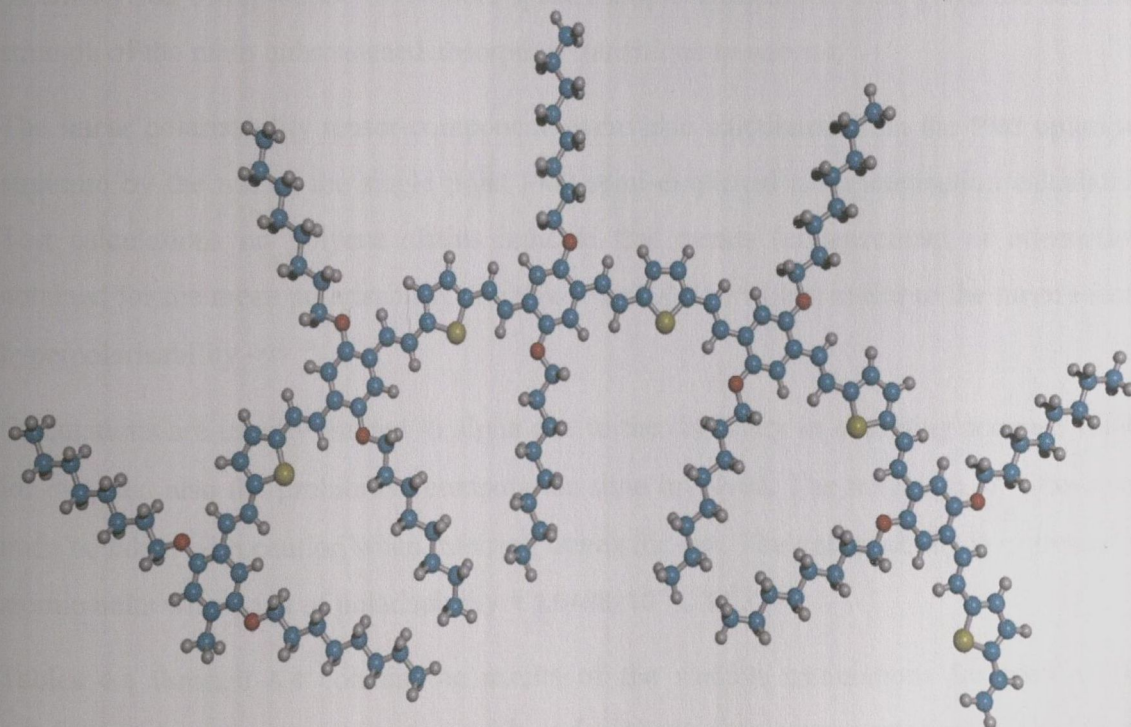


**Figure 4.15:** PM3 semiempirical method calculated energy minimised geometry (2-dimensional x-y plane representation of the 3-dimensional structure) of the Thienyl-PAV curved backbone pentamer with side groups attached.

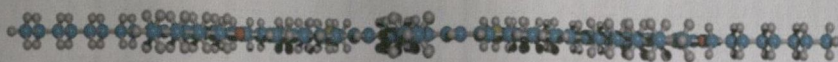


**Figure 4.16:** PM3 semiempirical method calculated energy minimised geometry (2-dimensional x-z plane representation of the 3-dimensional structure) of Thienyl-PAV curved backbone pentamer with side groups attached.

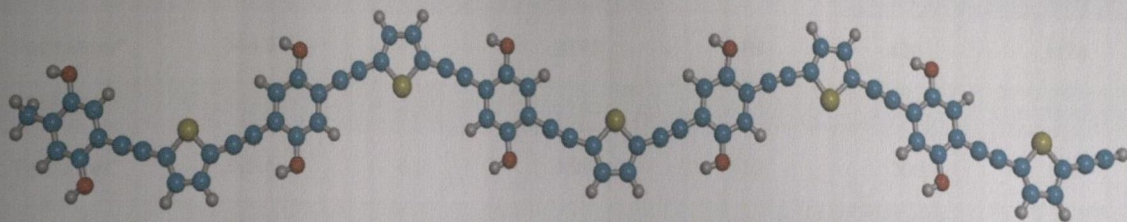


**Figure 4.17:** PM3 semiempirical method calculated energy minimised geometry (2-dimensional x-y plane representation of the 3-dimensional structure) of the Thienyl-PAE linear backbone pentamer without side groups attached.

### 4.3.2 Linear Absorption and Polarizability

The unbroadened absorption spectrum was calculated from the PM3 optimised structure using the use of the **Zener Intermediate Neglect of Differential Overlap for Spectroscopy (ZINDO/S)** semiempirical parameterisation. The ZINDO/S method is a method specifically parameterised to reproduce UV/visible spectroscopic transitions. This gives the oscillator strength of the main unbroadened absorption transitions *in vacuo*.

The linear polarisability tensor components were also calculated from the PM3 optimised structure by the use of the single point PM3 semi-empirical parameterisation calculation. Test calculations on polyene chains indicate that trends (enhancement or attenuation) obtained for the mean polarisability  $\langle P \rangle$  ( $\{P_{xx}+P_{yy}+P_{zz}\}/3$ ) will be similar to the mean second hyperpolarisability  $\langle \gamma \rangle$ <sup>25</sup>.

Calculations are usually limited to alpha due to the difficulty in obtaining accurate values for  $\langle \gamma \rangle$ , and also the prohibitive computation time involved. The trends on  $\langle P \rangle$ , however, must be taken with caution when inferring trends for  $\langle \gamma \rangle$ . The polarisability is expressed in atomic units where  $1\text{au of polarisability} = 1.6488 \times 10^{-41} \text{C}^2 \text{M}^2 \text{J}^{-1}$ .

Tables 4.1 through 4.4 contain the results of the various calculations for each of the polymers (monomers to pentamer) with and without side groups attached. Calculations involving side groups are significantly more computationally intensive than without the side groups as there is a significant reduction of atoms.

### Pyridinyl PAE – Molecular Modelling Results

	Abs. $\lambda_{\max}$	O.S.	$P_{xx}$ (AU)	$P_{yy}$ (AU)	$P_{zz}$ (AU)	$\langle P \rangle$ (AU)
Heptamer*	344.9	11.0	2930	1474	627	1677
Hexamer*	344.6	9.4	2530	1003	743	1426
Pentamer	348.3	7.8	2932	1441	1005	1792
Pentamer*	344.9	7.9	2272	826	426	1174
Tetramer	349.2	6.5	2250	1196	801	1415
Tetramer*	345.5	6.5	1858	610	300	923
Trimer	345.4	4.9	1631	887	604	1041
Trimer*	340.6	5.0	1336	454	227	672
Dimer	335.4	3.2	1054	686	266	669
Dimer*	332.2	3.2	820	298	154	424
Monomer	309.1	1.1	418	321	182	307
Monomer*	306.4	1.1	330	141	84	185

**Table 4.1:** Ground state absorption and linear polarisability components for various Pyridinyl-PAE oligomers calculated using Hyperchem 6.0 ©. The asterisks correspond to oligomers without side-groups. Abs.  $\lambda_{\max}$  = ground state HOMO-LUMO absorption maximum in nm; O.S. = oscillator strength (dimensionless);  $P_{xx}$ ,  $P_{yy}$ ,  $P_{zz}$ ,  $\langle P \rangle$  and their units are defined in section 4.3.1.

### Pyridinyl-PAV – Molecular Modelling Results

	Abs. $\lambda_{\max}$	O.S.	$P_{xx}$ (AU)	$P_{yy}$ (AU)	$P_{zz}$ (AU)	$\langle P \rangle$ (AU)
Pentamer	396.4	7.1	2612	1652	1066	1777
Pentamer*	388.2	7.3	2043	940	480	1155
Tetramer	394.9	5.8	2045	1314	851	1403
Tetramer*	387.2	5.9	1589	752	378	907
Trimer	386.4	4.4	1486	967	642	1032
Trimer*	380.6	4.5	1146	554	282	660
Dimer	370.7	3.0	932	617	439	663
Dimer*	367.3	3.0	702	363	183	416
Monomer	324.3	1.3	385	332	201	306
Monomer*	320.6	1.3	257	227	64	183

**Table 4.2:** Ground state absorption and linear polarisability components for various Pyridinyl-PAV oligomers calculated using Hyperchem 6.0 ©. The asterisks correspond to oligomers without side-groups. Abs.  $\lambda_{\max}$  = ground state HOMO-LUMO absorption maximum in nm; O.S. = oscillator strength (dimensionless);  $P_{xx}$ ,  $P_{yy}$ ,  $P_{zz}$ ,  $\langle P \rangle$  and their units are defined in section 4.3.1.

### Thienyl-PAE – Molecular Modelling Results

	Abs. $\lambda_{\max}$	O.S.	$P_{xx}$ (AU)	$P_{yy}$ (AU)	$P_{zz}$ (AU)	$\langle P \rangle$ (AU)
Heptamer*	396.6	9.5	3717	1213	168	1700
Hexamer*	397.0	8.2	3154	1034	149	1445
Pentamer	400.5	7.1	3210	1609	652	1824
Pentamer*	396.7	7.0	2545	855	125	1175
Tetramer	396.9	5.8	2535	1273	522	1444
Tetramer*	392.9	5.8	2077	658	102	946
Trimer	390.3	4.4	1808	973	394	1058
Trimer*	387.2	4.4	1494	498	78	690
Dimer	374.8	3.0	1131	641	267	679
Dimer*	372.2	3.0	934	318	55	436
Monomer	333.1	1.3	473	320	137	310
Monomer*	333.1	1.3	375	159	31	188

**Table 4.3:** Ground state absorption and linear polarisability components for various Thienyl-PAE oligomers calculated using Hyperchem 6.0 ©. The asterisks correspond to oligomers without side-groups. Abs.  $\lambda_{\max}$  = ground state HOMO-LUMO absorption maximum in nm; O.S. = oscillator strength (dimensionless);  $P_{xx}$ ,  $P_{yy}$ ,  $P_{zz}$ ,  $\langle P \rangle$  and units are defined in section 4.3.1.

### Thienyl-PAV – Molecular Modelling Results

	Abs. $\lambda_{\max}$	O.S.	$P_{xx}$ (AU)	$P_{yy}$ (AU)	$P_{zz}$ (AU)	$\langle P \rangle$ (AU)
Pentamer	456.1	7.0	2986	1447	742	1824
Pentamer*	450.3	7.1	2043	941	480	1155
Tetramer	451.8	5.7	2302	1351	681	1445
Tetramer*	446.9	5.8	1589	752	378	907
Trimer	443.7	4.4	1655	1015	507	1059
Trimer*	438.4	4.4	1146	554	281	661
Dimer	419.1	3.0	1017	679	334	677
Dimer*	415.9	3.0	702	363	183	416
Monomer	354.6	1.5	424	336	165	308
Monomer*	352.3	1.5	341	171	45	186

**Table 4.4:** Ground state absorption and linear polarisability components for various Thienyl-PAV oligomers calculated using Hyperchem 6.0 ©. The asterisks correspond to oligomers without side-groups. Abs.  $\lambda_{\max}$  = ground state HOMO-LUMO absorption maximum in nm; O.S. = oscillator strength (dimensionless);  $P_{xx}$ ,  $P_{yy}$ ,  $P_{zz}$ ,  $\langle P \rangle$  and units are defined in section 4.3.1.

Figures 4.18 through 4.21 below show how the unbroadened absorption HOMO-LUMO spectrum maximum (Abs.  $\lambda_{\max}$ ) evolves on going from the monomer to the pentamer for both of the PAV polymers and to the heptamer for both of the PAE polymers.

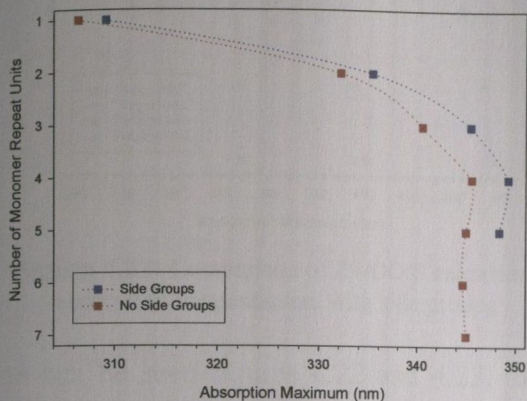


**Figure 4.18:** Evolution of ZINDO/S calculated absorption maxima for Pyridinyl PAE oligomers

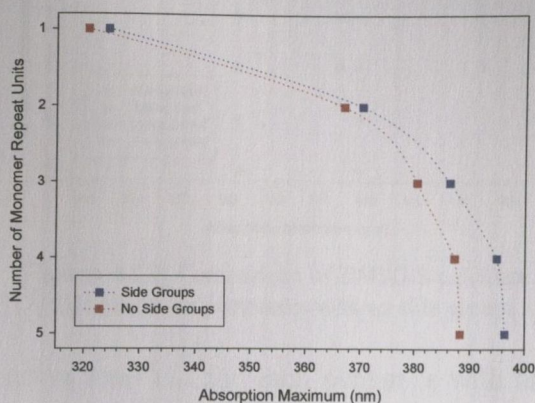


**Figure 4.19:** Evolution of ZINDO/S calculated absorption maxima for Pyridinyl PAV oligomers

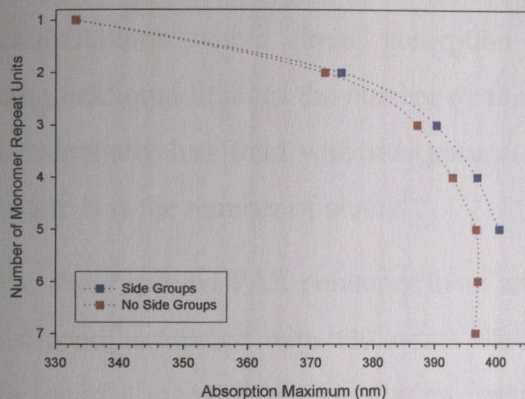


**Figure 4.20:** Evolution of ZINDO/S calculated absorption maxima for Thienyl PAE oligomers

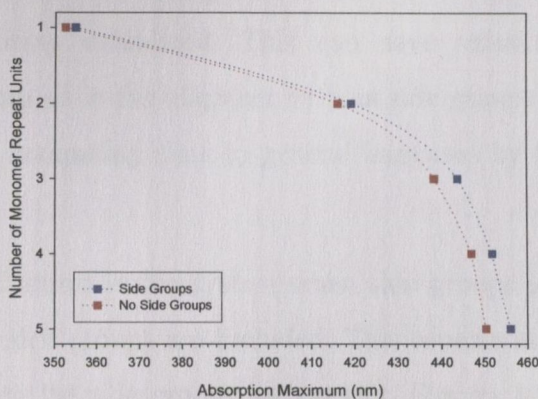


**Figure 4.21:** Evolution of ZINDO/S calculated absorption maxima for Thienyl PAV oligomers

From the four figures above it can be seen that unbroadened HOMO-LUMO absorption maximum for the oligomers with side groups attached, is consistently shifted to longer wavelengths compared to the oligomers with no side groups attached. This would appear to be the only significant effect of the inclusion of the side groups in the computer modelling of the absorption spectra. This observation is consistent with measurements on other conjugated polymers<sup>26,22</sup>. The figures above also show that the Abs.  $\lambda_{\max}$  increases in wavelength as the number of monomer repeat units increase. The largest increase is the change from monomer to dimer. The Abs.  $\lambda_{\max}$  no longer increases by the time the pentamer is measured. This would indicate that the pentamer in each case is representative of the long chain polymer. This is again consistent with other reported measurements<sup>22</sup>. Figures 4.22 and 4.23 below compare the unbroadened HOMO-LUMO absorption spectrum maximum (Abs.  $\lambda_{\max}$ ) for each of the four pentamers .

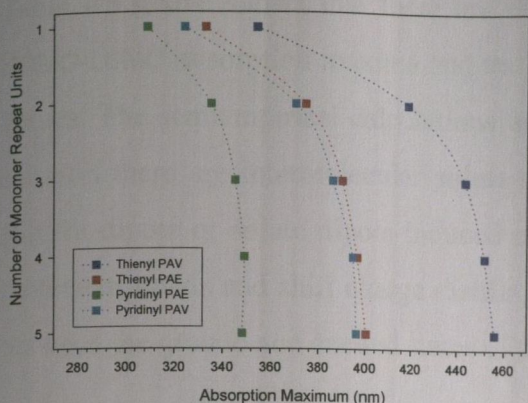


**Figure 4.22:** Comparison of ZINDO/S calculated absorption for pentamers with side groups

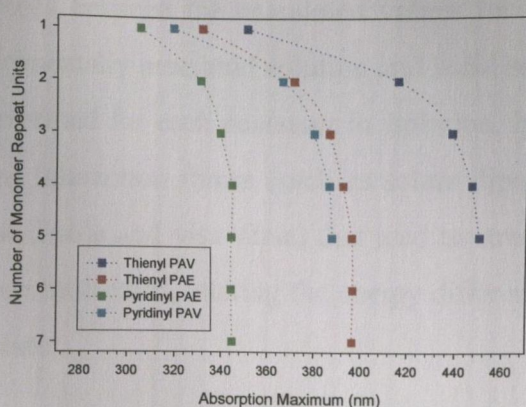


**Figure 4.23:** Comparison of ZINDO/S calculated absorption for pentamers with no side groups

As can be seen figures 4.22 and 4.23, the trend in Abs.  $\lambda_{\max}$  for each pentamer with and without side groups is identical, apart from the shift to longer wavelengths when the side groups are attached. This would indicate that the side groups need not be included in computations where linear absorption is being calculated. This can save valuable computational time, as the number of atoms present in the oligomer without side groups is substantially less than with side groups. The computing time in general increases by  $N^2$  where  $N$  is the number of atoms<sup>24</sup>.

For the Pyridinyl-PAE pentamer there are 370 atoms in the system when side groups are included, compared with 130 atoms when no side groups are included. This represents a factor of 8 increase in computation times when the side groups are present. Figures 4.22 and 4.23 again indicate that the pentamer in each case is representative of the long chain polymer. The only exception to this may be the Thienyl-PAV where the Abs.  $\lambda_{\max}$  may not have fully stabilised yet. This is consistent with Thienyl-PAV in solution having the lowest HOMO-LUMO energy separation, which in section 4.2 is attributed to the  $\pi$ -electron excessive thiophene unit in combination with the delocalised  $\pi$ -electrons from the double bonds having the largest conjugation length. It is expected that the HOMO-LUMO Abs.  $\lambda_{\max}$  will have stabilised by the hexamer or pentamer.

	Pyridinyl PAE $\lambda_{\max}$	Pyridinyl PAV $\lambda_{\max}$	Thienyl PAE $\lambda_{\max}$	Thienyl PAV $\lambda_{\max}$
Calculated	348	396	401	456
Experimental Sol.	420	430	437	472
Experimental S. S.	425	418	456	425

**Table 4.5:** Comparison between experimental and calculated absorption  $\lambda_{\max}$  for pentamers. Sol. refers to solution measurements and S.S. refers to solid state measurements.

Table 4.5 above shows that there are differences between the calculated values for the HOMO-LUMO absorption maxima and the experimentally measured solution and solid state values. The semiempirical calculations are performed for each pentamer in isolation. In a solution there are intermolecular solute-solvent interaction forces (such as solute dipole-solvent dipole or solute dipole-induced solvent dipole and visa versa) that tend to stretch molecular bonds and shift charge distribution on molecules, altering the energy difference between the ground and excited states of the solute.

In solid state films, the solute-solvent interaction is replaced by the solute-solute interaction (polymer chain-polymer chain interaction) which have different solute-solute dipole coupling. There is also inhomogeneous broadening present in the solutions and solid state samples, as discussed in section 4.2, as well as homogeneous broadening of the spectral lines due to thermal motion. These intermolecular interactions and temperature effects are not taken into account in the model and may explain the observed differences.

Table 4.5 also shows that the calculated absorption trends agree with the experimentally measured solution HOMO-LUMO absorption trends, whereas they do not agree with the experimentally measured solid state HOMO-LUMO absorption trends. This can be seen clearly from the table. However, the trends within each polymer family (for solution and solid state) as predicted. This indicates that the semiempirical calculations do not or cannot take into account the aggregation effects (short-range polymer segment alignment, partial micro-crystallisation) which play a significant role in the four polymers solid state absorption spectra. This is consistent with other computer modelling measurements on PAE oligomers<sup>27</sup>.

The above results also indicate that semiempirical calculations may, in closely related polymers families, be used to investigate the solution HOMO-LUMO absorption trends. Any trends obtained from semi-empirical computer modelling of absorption must therefore be treated with caution when comparing polymers from different structural families in their solid state.

Graphs 4.24 through 4.27 below, show how the linear polarisability tensor components evolve on going from the monomer oligomer to the pentamer oligomer for each of the four polymers.

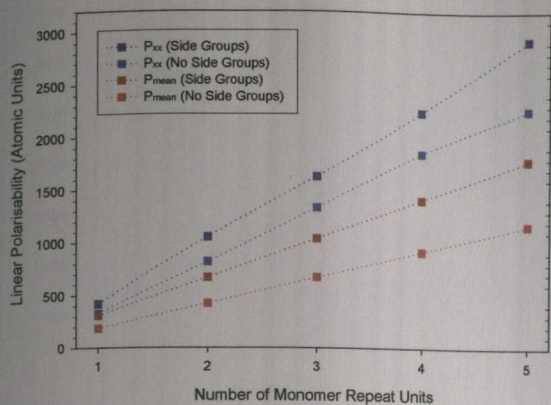


**Figure 4.24:** Evolution of PM3 calculated linear polarisability for Pyridinyl PAE oligomers

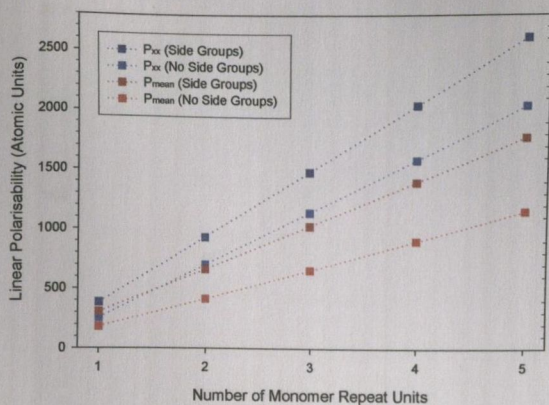


**Figure 4.25:** Evolution of PM3 calculated linear polarisability for Pyridinyl PAV oligomers

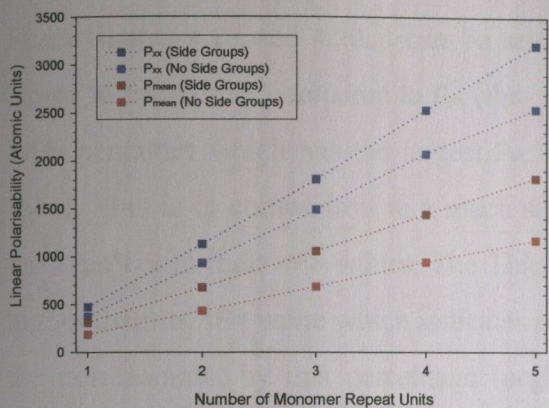


**Figure 4.26:** Evolution of PM3 calculated linear polarisability for Thienyl PAE oligomers

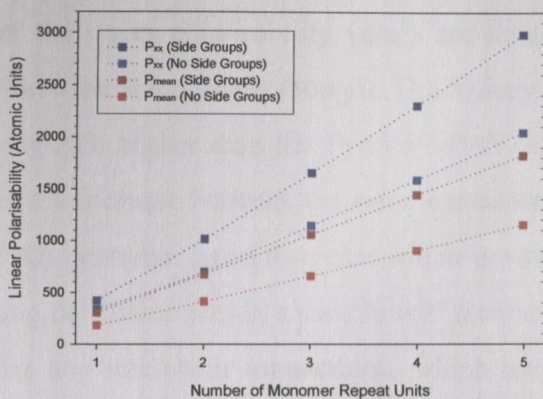


**Figure 4.27:** Evolution of PM3 calculated linear polarisability for Thienyl PAV oligomers

From the four figures above, it can be seen that the polarisability increases linearly on going from the monomeric to the pentameric state. It also shows that the oligomers with side groups have consistently higher values of polarisability compared to the oligomers without side groups. The polarisability ( $P$ ) measures the dipole moment of a molecule induced by an electric field. It is a tensor with components  $P_{ij}$ . These measure the dipole in the  $i$  direction induced by a field in the  $j$  direction. The polarisability component along the  $x$  direction is also consistently higher than the mean polarisability. This indicates that the  $P_{xx}$  polarisability is the dominant component and that if the trends for the second hyperpolarisability are similar then the nonresonant third order nonlinearity of a solid state sample may be maximised by aligning the polymer chains along one axis and using polarised light. In solution and solid state film, the polymer chain orientation is random and therefore the mean polarisability  $\langle P \rangle$ , is a better measurement for comparing trends. Figures 4.28 and 4.29 below, compare the calculated unbroadened absorption spectrum maximum (Abs.  $\lambda_{\max}$ ) for each of the four polymers pentamer oligomer.



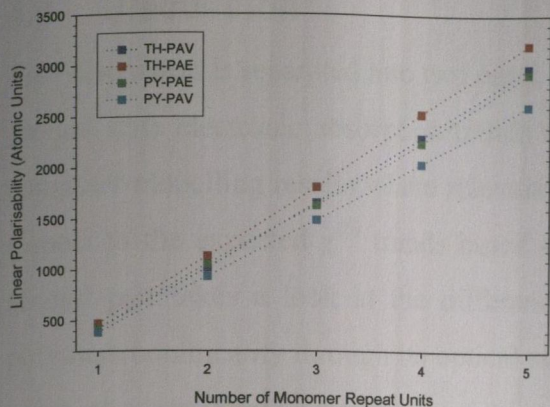


**Figure 4.28:** Comparison of  $P_{xx}$  linear polarisability for pentamers with and without side groups

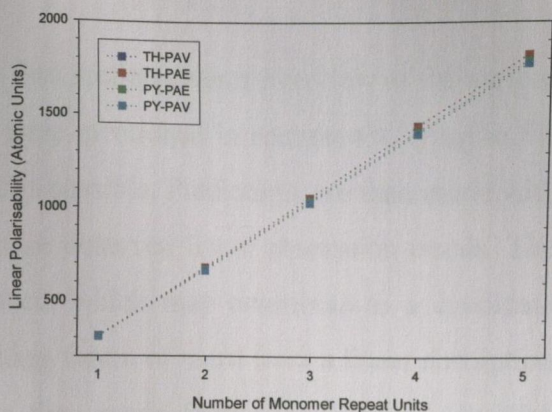


**Figure 4.29:** Comparison of  $P_m$  linear polarisability for pentamers with and without side groups

From figures 4.28 and 4.29 it can be seen that the mean polarisability values are much closer to each other compared to  $P_{xx}$  (they still have the same trends though). The Thienyl-PAE pentamer which has the largest  $P_{xx}$  value is 23% higher than the Pyridinyl-PAV  $P_{xx}$  value. This is in comparison to a much smaller 3% increase between the same pentamers with respect to their  $\langle P \rangle$  values. The Thienyl-PAE pentamer has a  $P_{xx}$  value which is 43% higher than its  $\langle P \rangle$  value which indicates aligning the chains within a sample will increase the non-resonant by this percentage (neglecting any interchain interactions, which may enhance or reduce this value in a solid state film).

Although the polarisability values in the two graphs above show no signs of saturating, the ratio between the values remains proportional up to the pentamers. This would indicate that longer oligomers will have larger polarisability values, which may translate into larger hyperpolarisability values. Even if this relationship is true, the polymer environment (in a solid state film for example) may disrupt the conjugation length (which is the length over which the backbone planarity is maintained without interruption) and thus nullify the possible hyperpolarisability increase. Experimental measurement would be the only way to validate this. However, the trends obtained from computer modelling of the polarisability indicate that (if the second hyperpolarisability is proportional to the linear polarisability) Thienyl-PAE should have the largest  $\chi^3$  value followed by Thienyl-PAV, Pyridinyl-PAE and Pyridinyl-PAV. This trend should be compared to the solution and solid state nonlinear measurements separately, due to the large blue-shift observed in the electronic absorption spectrum of Thienyl-PAV, on going from solution to solid state.

## 4.4 Discussion

This discussion is separated into two parts. The first section gives an overview of the various ground state electronic absorption trends that were mentioned in section 4.2, tying in the computer modelling results where relevant and/or possible. Predictions are then made with respect to the expected  $\chi^{(3)}$  trends based on these observed linear absorption trends. The second part takes a look at the different aspects which may contribute to a candidate polymer's nonlinearity through its optical switching figure of merit from a linear absorption point of view. Some tentative predictions are then made from a qualitative viewpoint relating to resonance enhancement effects and the optical switching figure of merit for the four polymers under investigation. These predictions will later be compared to the experimental results obtained in chapter six.

### 4.4.1 Linear Absorption Trends

In polymers the  $\pi$ - $\pi^*$  energy gap (HOMO-LUMO separation)  $E_g$  (and therefore the electronic properties) has an inverse dependence on the effective conjugation length (the length over which the backbone planarity is maintained without interruption)<sup>28</sup>. The  $\chi^{(3)}$  value increases as the extent of the  $\pi$  conjugation increases<sup>10</sup>, therefore the longer the wavelength of the ground state electronic absorption, the larger the nonresonant  $\chi^{(3)}$  value is likely to be<sup>10</sup>. The above dependencies are all primarily based on the assumption that the polymer backbone can be approximated to a one dimensional structure. From the earlier spectra and modelling, it can be deduced that for the four polymers in solution, this one dimensional structure approximation may be somewhat valid. The modelling showed that the oligomers *in vacuo* prefer to adopt a planar structure which maximises the  $\pi$ - $\pi$  overlap. For dilute solutions this may also be possible, where the polymer backbone on average, does not undergo any appreciable interaction with other polymer backbones. In very concentrated solutions and solid state, the polymer backbone may interact with other nearby backbones, due to aggregation effects. These interchain interactions can modify the electronic levels which will show up in the electronic spectra as long wavelength shoulders.

The  $\pi$ - $\pi^*$  energy gap can be expressed as the sum of different contributions:  $E_g = E_{\text{res}} + E_{\text{Peierls}} + E_{\text{sub}} + E_{\text{int}} + E_0$ <sup>29</sup>. The first two terms ( $E_{\text{res}} + E_{\text{Peierls}}$ ) give the contributions of the aromatic resonance and the degree of bond length alternation respectively and are characteristic of the polymer conjugated backbone.  $E_{\text{sub}}$  is related to the inductive or mesomeric electronic effects of substituents grafted on the conjugated main chain.  $E_{\text{int}}$  is

negative and its modulus increases with the interchain interactions. Aggregation effects, if present, will lead to an increase in interchain interactions, which will therefore increase the modulus of  $E_{int}$ , which in turn will reduce the  $\pi-\pi^*$  energy gap.  $E_0$  accounts for the mean deviation from planarity and arises from torsion of each monomer with respect to the adjacent ones. Figures 4.30 and 4.31 below compare the electronic absorption  $\lambda_{max}$  for each of the four polymers, first in solution and then in solid state.

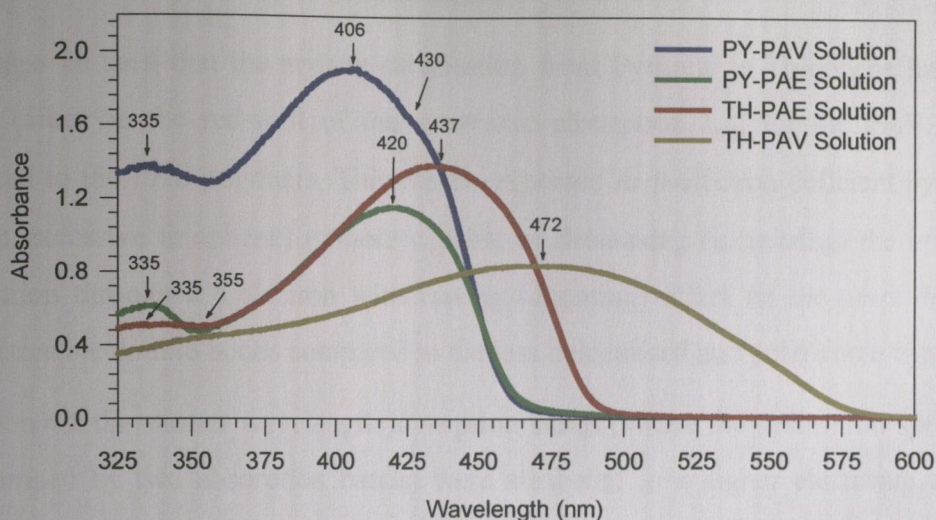


**Figure 4.30:** Absorption Spectra of all polymers in solution showing the relative differences in absorption maxima as well as absorption edges for each of the four polymers. The solvent is Toluene and the solution concentration is 0.250 g/l in each.

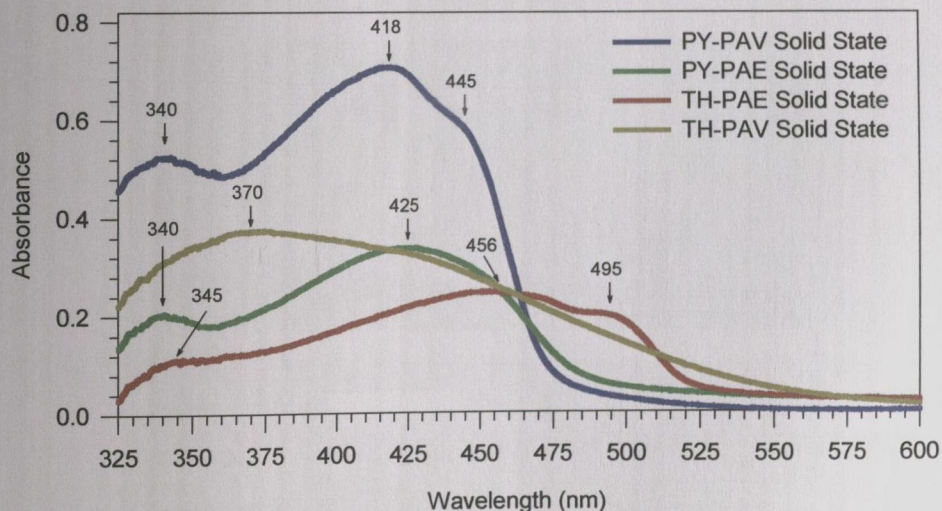


**Figure 4.31:** Absorption Spectra of all polymers in solid state showing the relative differences in absorption maxima as well as absorption edges for each of the four polymers. Thickness of the films are 52nm, 75nm, 230nm and 170nm for the Thienyl-PAE, Pyridinyl-PAE, Thienyl-PAV and Pyridinyl-PAV respectively.

As can be seen from the figures 4.30 and 4.31 both PAE and PAV polymers show similar trends (Thienyl-PAV solid state being the exception) in their absorption spectrum. The position of the absorption maximum depends on the nature of the arylene co-unit.

Replacement of the  $\pi$ -electron deficient pyridine unit with the  $\pi$ -electron excessive thiophene results in a red-shift of the electronic absorption  $\lambda_{\max}$ . Such a trend was also observed with other PAE<sup>30</sup> and PAV<sup>31</sup> polymers. The red-shift of the absorption maximum has been associated with a charge transfer from a thiophene ring to the ethynylenes (or vinylenes) unit which increases the length (stability) of the  $\pi$ -conjugation. It has been tentatively suggested that the position of the absorption maximum is related to the degree of destabilisation of the HOMO and stabilisation of the LUMO<sup>4</sup>.

It can also be seen that the arylene substitution from Pyridine to Thiophene has a much greater effect on the red-shift of the electronic absorption  $\lambda_{\max}$  for the PAV polymers compared to the PAE polymers. This can be expected as  $\pi$ -electron deficient pyridine ( $\pi$ -electron excessive thiophene) is more capable of decreasing (increasing) the effective  $\pi$ -conjugation through its electron withdrawing (donating) effect on the more delocalised and polarisable double bonds compared to the less delocalised and polarisable triple bonds.

In section 4.2 the shorter wavelength absorption bands (where the absorption spectra were characterised by two absorption bands) were attributed to a higher electronic transition. This is backed up by the computer modelling results (figure 4.32), which show a shorter wavelength electronic absorption (much weaker) for each of the four polymers.

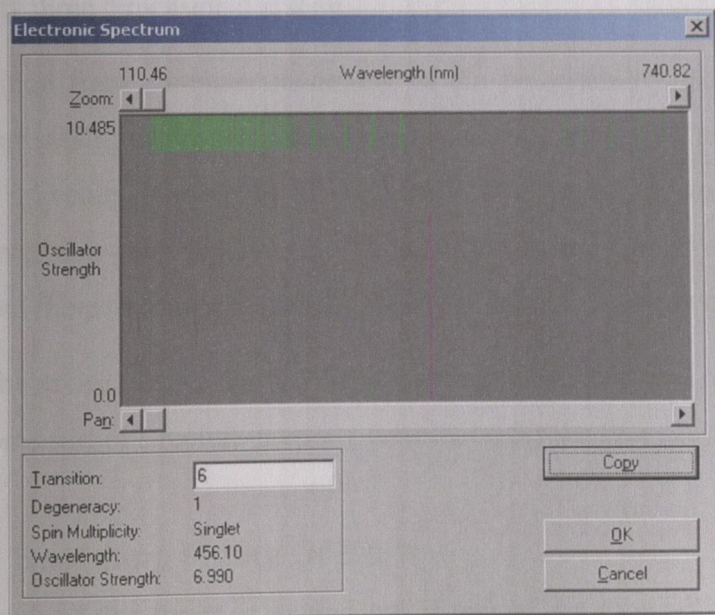


**Figure 4.32:** ZINDO/S calculated unbroadened electronic absorption for Thienyl PAV pentamer showing the shorter wavelength singlet absorption.

Predictions about the  $\chi^{(3)}$  value trend based on the solution and modelling HOMO-LUMO absorption maxima indicate that Thienyl-PAV should have the largest  $\chi^3$  value followed by Thienyl-PAE, Pyridinyl-PAV and Pyridinyl-PAE.

The solid state predictions are more complicated, due to the aggregation effects which can be clearly seen from the absorption spectra. These effects would indicate that the one dimensional backbone approximation on which most of the predictive models are based, are not valid. However, if valid, there are two separate predictions which can be made about the  $\chi^{(3)}$  value trend for each of the four polymers, based on their solid state electronic absorption spectra. Each prediction relates to which assumption is made regarding the effects of the long wavelength absorption shoulders (associated with partial conformation structuring/aggregation) which are present for the Pyridinyl-PAV and Thienyl-PAE solid state polymer spectra. The first solid state trend is based on the assumption that the longer wavelength shoulder, if present, has a significant or dominant effect on the  $\chi^3$  value. Under this assumption the Thienyl-PAE should have the largest  $\chi^3$  value followed by Pyridinyl-PAV, Pyridinyl-PAE and Thienyl-PAV. The second solid state trend is based on the assumption that the longer wavelength shoulder, if present, has not a significant or dominant effect on the  $\chi^3$  value. Under this assumption the Thienyl-PAE should have the largest  $\chi^3$  value followed by Pyridinyl-PAE, Pyridinyl-PAV and Thienyl-PAV. The author firmly believes that none of the solid state predictions will agree with the experimentally measured trends, due to the extreme simplicity of the models which are used to predict the effects of a clearly three dimensional system.

The trends obtained from computer modelling of the polarisability indicate that (if the second hyperpolarisability is proportional to the linear polarisability) Thienyl-PAE should have the largest  $\chi^3$  value followed by Thienyl-PAV, Pyridinyl-PAE and Pyridinyl-PAV. The author believes that these predictions will not agree with the solid state experimental measurements, but there may be some trend agreement with the solution measurements.

Comparison of the above predictions with the experimentally measured results in chapter 6 may elucidate some sort of structure-property correlation for the four polymers.

#### 4.4.2 Optical Switching Figure Of Merit

The main objective of this thesis is to find out if any of the four polymers studied, are suitable candidates for all optical switching applications over any part of the wavelength region spanning 465nm through 685nm. The material with the highest nonlinearity at a given wavelength is not necessarily the most suitable material for all optical switching at that wavelength. As mentioned in chapter 2, there are two figures of merit which indicate a

particular material's suitability for optical switching. The first figure of merit  $T$ , given in equation 4.1 is a measure of the materials suitability when nonlinear absorption (two-photon absorption) is present and the dominant imaginary process relative to linear absorption. This value should be below unity for favourable materials.

$$T = \frac{\lambda\beta}{2\eta_2} \quad 4.1$$

Conversely, the second figure of merit  $W$ , given in equation 4.2 is a measure of the material's suitability when linear absorption is the dominant imaginary process relative to nonlinear absorption. This value should be above unity for favourable materials.

$$W = \frac{\eta_2 I_0}{\alpha\lambda} \quad 4.2$$

Generally, it is the combination of equations 4.1 and 4.2, that govern a particular material's suitability as a worthy candidate for all-optical switching applications. This is because there is not always a wavelength range where linear absorption and nonlinear absorption are both negligible. This is particularly so for solid state polymer films where residual absorption (or scattering) can tail out significantly into the longer wavelength region of the spectrum<sup>32</sup>. Linear absorption (if present) plays a significant role in the determination of a given material's suitability through the  $W$  figure of merit. At the one photon resonance, the linear absorption coefficient is typically so large as to degrade the  $W$  figure of merit to well below any useful limit. Residual linear absorption may also have a detrimental effect if present at a particular wavelength.

The linear absorption has no contribution to the  $T$  figure of merit (equation 4.1). Instead it is the nonlinear absorption (if present) which plays the significant role. Nonlinear absorption is an intensity dependent effect and at high values, will impose a fundamental limit on the value of nonlinear refraction which will be needed to achieve a suitable figure of merit. It is possible for a material to have one favourable figure of merit, say  $W$ , while the other figure of merit  $T$  remains unfavourable, and *visa versa*.

At the one photon resonance wavelength ( $\lambda_{\max}$ ) the nonlinear absorption coefficient  $\beta$  has a negative value (saturable absorption is dominant). At the two photon resonance wavelength ( $\lambda_{\max}/2$ ) the nonlinear absorption coefficient  $\beta$  has a positive value (two-photon absorption is dominant). The nonlinear absorption coefficient  $\beta$  also has a positive value, in regions where reverse saturable absorption is present and is the dominant nonlinear process.

Consequently, if saturable absorption is present over a particular wavelength range (due to residual absorption) and either two-photon absorption or reverse saturable absorption is also present, then there may exist a wavelength region where the intensity dependent positive and negative absorptive nonlinearities, mathematically cancel each other out at a given intensity. In these cases the T figure of merit will be very favourable for nonlinear optical switching, since there is effectively no nonlinear absorption due to a dynamic equilibrium between the saturable absorption and the reverse saturable absorption. This leaves us in the state where the linear absorption as well as the nonlinear refractive index are the two contributing factors (through  $W$ ) which determine a particular polymers suitability for all optical switching for a given wavelength and intensity. Residual linear absorption (or scattering) which is usually present in these cases can often be the factor which rules out a particular material by degrading the  $W$  figure of merit<sup>32</sup>. Therefore, from a qualitative viewpoint, a material with an electronic absorption maximum as close to the chosen wavelength as possible (maximise the conjugation length), combined with a sharp absorption band cut-off and a low residual absorption is desirable. Figure 4.33 below shows the residual absorption spectra for each of the polymers in solid state.

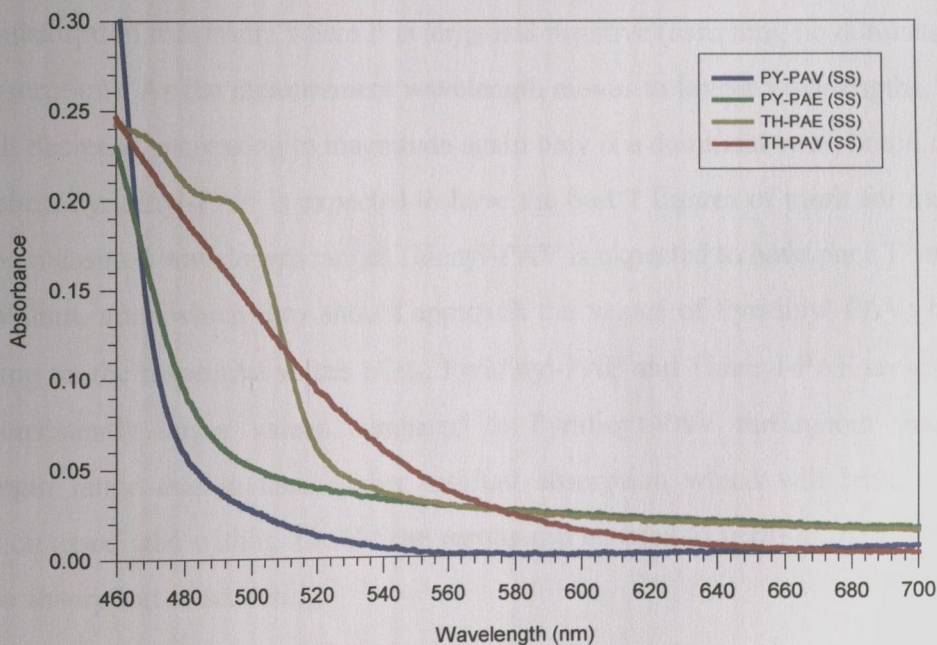


**Figure 4.33:** Absorption Spectra of all four polymers in solid state showing the differences in residual absorption. Thickness of the films are 52nm, 75nm, 230nm and 170nm for the Thienyl-PAE, Pyridinyl-PAE, Thienyl-PAV and Pyridinyl-PAV respectively.

From the spectra qualitative predictions can be made about which regions of the spectrum may be of significant interest with respect to the various phenomena mentioned above.

These qualitative predictions can be compared to the experimental dispersion measurements obtained later in chapter 6. The results of these comparisons may help to reduce the total number of wavelength measurements which are necessary to fully characterise, a future polymer's suitability for all optical switching application over a particular wavelength range.

Although there are some measurements carried out at 1064nm, most of the measurements (465nm through 685nm) are carried out at wavelengths spanning the one photon absorption  $\lambda_{\max}$  through to the start of the  $\lambda_{\max}/2$  where the two photon absorption resonance should be for each of the polymers.

From figure 4.33 it can be seen that Pyridinyl-PPV has the sharpest absorption band cut-off, which is also combined with the lowest residual absorption values from about 520nm through 685nm. The Thienyl-PAV spectrum does not have a sharp cut-off, but does have lower residual absorption than both of the PAE polymers for wavelengths longer than 580nm. Thienyl PAV and Pyridinyl PAV both have reasonably sharp absorption band cut-offs and similar residual absorption tails starting at 550nm and continuing beyond 700nm.

From a  $T$  figure of merit perspective, each polymer will have large values at their one photon absorption maximum where  $\beta$  is large and negative (assuming no dominant excited state absorption). As the measurement wavelength moves to longer wavelengths, the value of  $T$  will decrease, increasing in magnitude again only if a dominant two photon resonance approaches. Pyridinyl-PAV is expected to have the best  $T$  figures of merit for most, if not all of the measured wavelength range. Thienyl-PAV is expected to have poor  $T$  values until about 600nm, after which they should approach the values of Pyridinyl-PAV; how close depending on the respective values of  $\eta_2$ . Pyridinyl-PAE and Thienyl-PAE are expected to have consistently larger values compared to Pyridinyl-PAV throughout most of the wavelength range due to their higher residual absorption which will have a saturable absorption associated with it. The Z-Scan results can be used to verify if the absorption tail is due to absorption or scattering.

From a  $W$  figure of merit perspective any region where  $\beta$  is large and negative, will also have a corresponding linear absorption which is much more detrimental to the  $W$  figure of merit. Pyridinyl-PAV is expected to also have the best  $W$  figures of merit for most if not all of the wavelength range measured, depending on the  $\eta_2$  values of the other three polymers. The relatively large residual absorption for the other three polymers compared with



Pyridinyl-PAV is predicted to off-set any favourable  $\eta_2$  values, except maybe for Thienyl PAV at wavelengths longer than 640nm.

The predictions from the absorption spectra for the combined figures of merit trends, is that Pyridinyl-PAV will be most favourable over the greatest wavelength range, followed by Thienyl-PAV, which may or may not be more favourable for wavelengths longer than 640nm. The PAE polymers place will depend on their  $\eta_2$  values and the effects of the residual absorption/scattering.

## References

---

- 1 T. Miya, Y. Terunuma, T. Hosaka and T. Miyashita, *Electron. Lett.*, **15**, 106, (1979).
- 2 Khoe et al., "Status of GI-POF systems and related technologies" Proc. ECOC '99, Nice, France, 1999.
- 3 Shimada, Takahashi, Yamamoto, "Digital Home Network with POF", Proc. 8<sup>th</sup> Int'l POF Conference POF'99, Chiba (Jpn), 129, 1999.
- 4 Ziemann et al., "Comparison of source properties for polymer optical fiber links", Proc. 7<sup>th</sup> Int'l POF Conference POF'98, Berlin (Germany), 123, 1998.
- 5 A. Penzkofer, University of Regensburg, Germany, Technical report, ESPRIT Basic Research, 1996.
- 6 N. Ooba, S. Tomaru, T. Kurihara and T. Kaino, "Enhancement of Third-Order Optical Nonlinearity of Poly(aryleneethynylene)s by Introducing Heteroaromatic Rings into their  $\pi$ -Conjugation", 5<sup>th</sup> SPSJ International Polymer Conference, 1994.
- 7 J. Libert, J. Cornil, D. A. dos Santos, J.L. Brédas, "From Neutral Oligoanilines to Polyanilines: a Theoretical Investigation of the Chain-length dependence of the electronic and optical properties", *Phys. Rev. B*, **56**, 14, 8638, 1997.
- 8 S. R. Marder, C. B. Gorman, F. Meyers, J. W. Perry, G. Bourhill, J. L. Bredas and B. Pierce, "A Unified Description of Linear and Nonlinear Polarization in Organic Polymethine Dyes", *Science*, **265**, 632, 1994.
- 9 L. T. Cheng, W. Tam, S. R. Marder, A. E. Stiegman, G. Rikken, C. W. Spangler, "Experimental Investigations of Organic Molecular Nonlinear Optical Polarizabilities. 2. A Study of Conjugation Dependences", *J. Phys. Chem.*, **95**, 10643, 1991.
- 10 D. D. C. Bradley and Y. Mori, *Polym. Prepr. Jpn.*, **37**, 3151, 1988.
- 11 W. Holzer, A. Penzkofer, S. -H. Gong, D. D. C. Bradley, X. Long, W. J. Blau and A. P. Davey, "Excitation Intensity-Dependent Fluorescence Behaviour of Some Luminescent Polymers", *Polymer*, **39**, 16, 3651, 1998.
- 12 W. Holzer, A. Penzkofer, S. -H. Gong, D. D. C. Bradley, X. Long, and A. Bleyer, "Effective Stimulated Emission and Excited-State Absorption Cross-Section Spectra of poly(m-phenylenevinylene-co-2,5-dioctyl-p-phenylenevinylene) and t,t'-dicycloxy-II-distyrylbenzene", *Chemical Physics*, **224**, 315, 1997.
- 13 A. J. Heeger, S. Kivelson, J. R. Schrieffer, W. -P. Su, *Rev. Mod. Phys.* **60**, 781, 1988.
- 14 N. C. Greenham, R. H. Friend, "Solid State Physics", Vol. 49, Academic Press, San Diego, 2, 1995
- 15 R. Kersting, U. Lemmer, R. F. Mahrt, K. Leo, H. Kurz, H. Bässler, E. O. Göbel, *Phys. Rev. Lett.*, **70**, 3820, 1993.
- 16 B. Mollay, U. Lemmer, R. Kersting, R. F. Mahrt, H. Kurz, H. F. Kauffman, H. Bässler, *Phys. Rev. B.*, **50**, 10794, 1994.
- 17 Y. Qiu, L. Duan, X. Hu, D. Zhang, M. Zheng and F. Bai, "Electroluminescence Enhancement by Blending PVK with an Alternating Copolymer Containing Triphenylamine and Phenylene units", *Synthetic Metals*, **123**, 39, 2001.
- 18 M. Woodruff, "Enhanced Chain Order and Dependence of the Linear Absorption of poly(p-phenylenevinylene) on the Solution Environment of its Precursor Polymer", *Synthetic Metals*, **80**, 257, 1996.
- 19 A. Samoc, M. Samoc, M. Woodruff and B. Luther-Davies, "Tuning the Properties of poly(p-phenylenevinylene) for use in all optical switching", *Synthetic Metals*, **20**, 11, 1241, 1995.
- 20 W. Holzer, M. Pichlmaier, E. Drotleff, A. Penzkofer, D. D. C. Bradley, W. J. Blau, "Optical Constants Measurement of Luminescent Polymer Films, *Synthetic Metals*, **125**, 40, 2000.
- 21 S. Tokito, T. Tsutsui, and S. Saito, *Polym. Prepr. Jpn.*, **35**, 2614, 1986.

- 
- 22 J. L. Bredas, C. Adant, P. Tackx and A. Persoons, "Third-Order Nonlinear Optical Response in Organic Materials: Theoretical and Experimental Aspects", *Chem. Rev.*, 94, 243, 1994.
- 23 P. W. Atkins, "Quanta – A Handbook of Concepts", Second Edition, Oxford University Press, 1994
- 24 "Hyperchem Computational Chemistry – 366p" and "Hyperchem Reference Manual – 656p", Hypercube Inc., 1996.
- 25 J. Delhalle, M. Dory, J.G. Fripiat and J.M. Andre, "Theoretical Design of Organic Molecules and Polymers for Optoelectronics", *Nonlinear Optical Effects in Organic Polymers*, 13, 1989.
- 26 M. T. Zhao, B. P. Singh and P. N. Prasad, "A Systematic Study of Polarisability and Microscopic Third-Order Optical Nonlinearity in Thiophene Oligomers", *J. Chem. Phys.*, 89, 9, 1988.
- 27 O. O'Connor, "Soluble Conjugated Organic Polymers for Electroluminescent Applications", Ph.D. Thesis, Trinity College, 1997.
- 28 K.C. Rustagi, J. Ducuing, *Opt. Commun.*, 10, 258, 1994.
- 29 J. Roncali, *Chem. Rev.*, 97, 173, 1997.
- 30 N. Ooba, S. Tomaru, T. Kurihara, T. Kaino, W. Yamada, M. Takagi and T. Yamamoto, *Jpn. J. Appl. Phys.*, 34, 3139, 1995.
- 31 S. Tokito, T. Tsutsui, and S. Saito, *Polym. Prepr. Jpn.*, 35, 2614, 1986.
- 32 A. Driessen, H. J. Hoekstra, F. C. Blom, F. Horst, G. J. Krijnen, "Evaluation of Polymer Based Third Order Nonlinear Integrated Optics Devices", *Optical Materials*, 9, 329, 1998.

## 5 Experimental Details

This chapter begins with an introduction to the different measurements carried out on the polymer samples in this thesis. The subsequent sections deal with in detail, the different aspects relating to the subsequently mentioned measurements. Initially, the solution and solid state sample preparation details for each polymer are presented. This is followed with a description of the Z-Scan experimental set-up used. All the results obtained using the experimental set-ups are presented in chapter 6.

### 5.1 Introduction

As mentioned previously, solution measurements are usually the only measurements performed on new polymers which may be potential candidates for nonlinear optical devices. This is mainly due to the low quantity of polymer which is normally initially synthesised. However, most if not all potential device applications utilise the polymer in its solid state form. Film fabrication techniques are usually used to make the samples necessary for establishing a materials suitability for solid state nonlinear optical applications. These techniques need a relatively large amount of polymer compared to the solution measurements. The solid state nonlinear optical properties, if required, are then extrapolated (estimated) from the solution measurements. One consequence of this approach is that devices subsequently constructed based on these extrapolated solid state (solution) measurements often do not live up to the theoretical expectations. A detailed study of solution versus solid state nonlinear measurements will help to investigate if solution measurements alone give all the information necessary to establish a polymers suitability for all optical switching at any given wavelength.

To this end, Z-Scan experiments are performed on four different polymers (Thienyl-PAE, Pyridinyl-PAE, Thienyl-PAV & Pyridinyl-PAV) to ascertain their nonlinear optical properties at a variety of different wavelengths. The experiments are performed on two different laser systems. The first system, a Nd:YAG Laser produces pulses with a duration of 60ps and 35ps at wavelengths of 1064nm and 532nm respectively. Concentration dependent solution measurements as well as thin film solid state measurements are performed at both wavelengths. The second system is a nitrogen pumped dye laser. Solid state and solution dispersion measurements of the nonlinear refraction and absorption were carried out on the Dye laser over the wavelength range 465nm through 685nm in 10nm steps. The results of these measurements are then presented and discussed in chapter 6.

## 5.2 Sample Preparation

As mentioned in chapter 4, gram quantities of each polymers was synthesised. This single batch has provided (barely) sufficient material in order to provide both solution and solid state measurements. This section deals with the solution preparation. The solid state sample preparation is presented in section 5.3

### 5.2.1 Solution Samples

One of the first things which needs to be assessed when preparing polymer solutions for Z-Scan measurements is the polymer solubility limit (i.e. the amount of polymer which will completely dissolve in a given solution without precipitation). If the polymer has a low solubility limit this may hinder thin film formation as well as concentration dependent solution measurements where a large range of concentration is advantageous (1 $\mu$ m solid state film will need a solution of approximately 50g/l concentration) .

Toluene is the solvent for all the solution experiments. The purity of the toluene was superior to 99.5% and was purchased from Riedel-de-Haën. The reasons for choosing Toluene as solvent are outlined below.

- 1 Toluene is a common solvent for all four polymers. This simplified comparisons when it comes to absorption measurements and nonlinear optical measurements.
- 2 Toluene is used as the reference material with respect to the Z-Scan apparatus baseline calibration. Toluene has no measurable nonlinear absorption over the wavelength range measured in this thesis.
- 3 Toluene, when used as the solvent produced the best optical quality solid state films when using the spin coating technique for thin film generation.

The solubility limits for each of the four polymers was found by adding an appropriate amount of polymer to the solvent in order to make a solution of a particular concentration. The solution was then sonicated for half an hour to ensure complete dissolution of the polymer. The solution is then centrifuged for 15 minutes and checked for polymer precipitation. If precipitate is present then that solution concentration is above the solubility limit. Precipitation test was also preformed 24 hours later. This is an important step for concentrations approaching the solubility limit. The polymers were recovered for solutions over the solubility limit by solvent evaporation.

### Thienyl PAE Solutions

No more than 3g/l of the Thienyl PAE polymer could be dissolved in Toluene at room temp without precipitation. This relatively low solubility limit is attributed to the rigid, linear structure of the polymer imparted by the carbon-carbon triple bonds as discussed in chapter 4. Six different solutions of varying concentrations were made up in 5cm<sup>3</sup> batches.

Thienyl PAE Polymer Solutions						
Solution Number	1	2	3	4	5	6
Concentration (g/l)	0.100 ± 0.001	0.250 ± 0.003	0.500 ± 0.005	0.750 ± 0.008	1.000 ± 0.010	2.500 ± 0.025

**Table 5.1:** Different solution concentrations of Thienyl PAE polymer in Toluene solvent. The table also contains the error for each concentration.

### Pyridinyl PAE Solutions

Again, no more than 3g/l of the Pyridinyl PAE polymer could be dissolved in Toluene at room temp without precipitation. This is again attributed to the rigid, nearly linear structure of the polymer again imparted by the carbon-carbon triple bonds. Six different solutions of varying concentrations were also made up in 5cm<sup>3</sup> batches.

Pyridinyl PAE Polymer Solutions						
Solution Number	1	2	3	4	5	6
Concentration (g/l)	0.100 ± 0.001	0.250 ± 0.003	0.500 ± 0.005	0.750 ± 0.008	1.000 ± 0.010	2.500 ± 0.025

**Table 5.2:** Different solution concentrations of Thienyl PAE polymer in Toluene solvent. The table also contains the error for each concentration.

### Thienyl PAV Solutions

The solubility limit of Thienyl PAV was found to be approximately 9g/l in Toluene. The increase in solubility (as predicted in chapter 4) is attributed to the less rigid backbone double bonds which impart an alternating non-linear polymer backbone structure. This alternating backbone structure can be seen as an increase in disorder, which is a contributing factor in polymer solubility. Another way to increase the disorder of this system (and therefore increase the solubility) is to add longer side groups. Eight different solutions of varying concentrations were made up in 5cm<sup>3</sup> batches.

## Thienyl PAV Polymer Solutions

Solution Number	1	2	3	4
Concentration (g/l)	$0.100 \pm 0.001$	$0.250 \pm 0.003$	$0.500 \pm 0.005$	$0.750 \pm 0.008$
Solution Number	5	6	7	8
Concentration (g/l)	$1.000 \pm 0.010$	$2.500 \pm 0.025$	$0.500 \pm 0.050$	$7.500 \pm 0.075$

**Table 5.3:** Different solution concentrations of Thienyl PAV polymer in Toluene solvent. The table also contains the error for each concentration.

## Pyridinyl PAV Solutions

The solubility limit of Pyridinyl PAV was found to be approximately 23g/l in Toluene. The increase in solubility compared to the two PAE polymers is again attributed to the less rigid backbone double bonds which impart an alternating non-linear polymer backbone structure. For this polymer ten different solutions of varying concentrations were made up in 5cm<sup>3</sup> batches.

## Pyridinyl PAV Polymer Solutions

Solution Number	1	2	3	4	5
Concentration (g/l)	$0.100 \pm 0.001$	$0.250 \pm 0.003$	$0.500 \pm 0.005$	$0.750 \pm 0.008$	$1.000 \pm 0.010$
Solution Number	6	7	8	9	10
Concentration (g/l)	$2.500 \pm 0.025$	$5.000 \pm 0.050$	$7.500 \pm 0.075$	$10.000 \pm 0.100$	$20.000 \pm 0.200$

**Table 5.4:** Different solution concentrations of Pyridinyl PAV polymer in Toluene solvent. The table also contains the error for each concentration.

The Thienyl and Pyridinyl PAE polymers have solubility limits in Toluene which are considerably lower than the their PAV counterparts. In both cases this is attributed to the polymers rigid, linear backbone structure which is imparted by the carbon-carbon triple bonds. The octyl side groups which are there to enhance the polymers solubility do not appear to be of sufficient length for both of the PAE polymers. Increasing the length of these side groups should help to increase the solubility of both the PAE polymers. Solubility experiments were previously carried out on Thienyl PAE polymer which had octa-decyl side groups attached instead of octyl sidegroups. In those measurements solubility limits in excess of 6g/l were reported, when using Toluene as the solvent at room temperature. The low solubility of the PAE polymers has consequences when it comes to thin film formation as will be discussed in the next section.

## 5.2.2 Solid State Samples

The solid state films used for the measurements in this thesis were all fabricated on 50mm diameter borosilicate disks using the spin coating technique<sup>1</sup>. In order to ensure clean, particle free films all spin coating was performed in a laminar flow cabinet. The spin coater used was a Convac Model 1001. The substrate is held in place on the chuck by a rotary vacuum, while a uniform film of solution is pipetted onto the whole of the substrate surface. This is followed by the rapid centripetal acceleration of the substrate to angular velocities between 100 and 10,000rpm depending on the required film thickness (higher angular velocities producing thinner films). This results in the uniform distribution of the polymer solution over the substrate. The excess solution is ejected. The solvent boils off rapidly during the coating process leaving a uniform polymer layer on the substrate with a thickness which is dependent on the spinning speed. Films produced at high angular frequencies tend to be much smoother and homogenous. This is dependent on high concentration solutions being available to work with. A polymer solution concentration of ~100g/l typically results in film thickness of ~2 $\mu$ m using a spinning speed of 1000rpm.

The polymer film thickness were not chosen arbitrarily. It was decided to fabricate thin films of sufficient thickness (where possible) to give a response in the Z-Scan experiment comparable to the Toluene reference sample. This process facilitated the most accurate comparison between the solution and solid state nonlinear optical measurements as no changes, other than changing of samples had to be made to the optical components within the system. This was accomplished initially through trial and error process. Films of different thickness were produced for each polymer in turn and a Z-Scan measurement was taken (532nm and 1064nm). Results (if measurable) were compared to a Toluene reference sample in a 1mm cuvette, and these dictated whether the film thickness should be increased or decreased. This in turn lead to a spinning formula which could be adhered to, to produce a film which would give a measurable response at the same power levels as the Toluene reference sample in the 1mm cuvette.

### Thienyl PAE Solid State

A 2.5 g/l Thienyl PAE polymer solution was used to fabricate a series of films with spin speeds varying between 1000 and 200rpm. None of these single layer films gave any measurable response in the Z-Scan experiment. At this stage a drop cast technique was used to make a thick film (~50 $\mu$ m). The film had poor optical quality but still gave a very large response compared to the toluene reference sample. After some investigation it was



found a multiple layer technique would have to be used to achieve a film with a thickness large enough to allow direct comparative measurements. Films produced with spin speeds of 200rpm and lower were of unacceptably poor optical quality. The lowest spin speed with acceptable optical film quality was found to be 300rpm. A spinning speed of 400rpm was then chosen as this had significantly better optical quality over most of the diameter of the substrate, especially after multiple layer depositions. After each layer is spun the film was baked at 60°C for two hours to ensure complete solvent removal. This was an important step for multiple layers as otherwise the solution tended to dissolve the film already on the substrate, leading to poor quality optical films. After every few layers the sample was again tested in the Z-Scan apparatus. The Thienyl PAE solid state film which was used for all the solid state measurements in this thesis consisted of 6 layers of 2.5g/l polymer in Toluene solution spun at 400rpm.

The film thickness was found to be  $52 \pm 3\text{nm}$  which corresponds to an error of 5.8%. The film thickness was measured directly using a commercial Zygo optical profilometer. In this method a scratch was made on the film and two monochromatic light beams are reflected, one off the substrate at the scratch and one off the film surface. The interference of these beams was used to calculate the film thickness. Three different measurements were carried out on each polymer film. This could only be done after all the measurements were completed, as the method above destroys the sample.

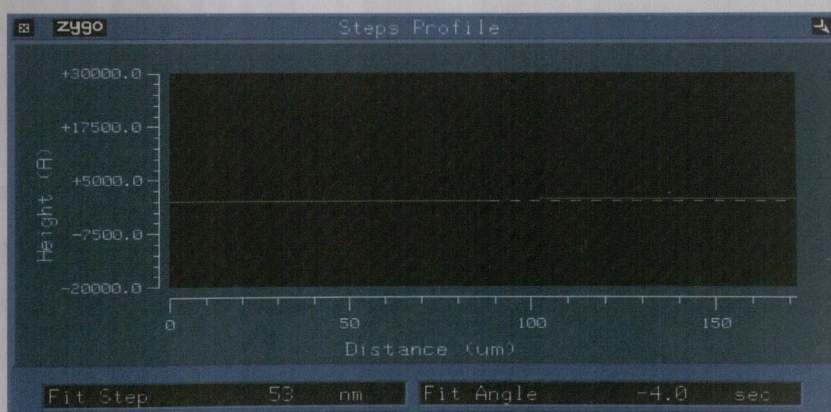


**Figure 5.1:** Thickness measurement of Thienyl PAE solid state film. The film thickness was measured at  $52 \pm 3\text{nm}$  using a Zygo optical profilometer. The above diagram corresponds to one of three separate thickness measurements.

### Pyridinyl PAE Solid State

A 2.5 g/l Pyridinyl PAE polymer solution was also used to fabricate a series of films with spin speeds varying between 500 and 200rpm. None of these single layer films gave any measurable response in the Z-Scan experiment. To produce films of good optical quality

and thick enough to give a measurable signal in direct comparative measurements a multiple layer technique had to be used. The fabrication process followed the same procedure mentioned above for Thienyl PAE polymer. The Pyridinyl PAE solid state film which was used for all the solid state measurements in this thesis consisted of 7 layers of 2.5g/l polymer in Toluene solution spun at 400rpm. The film thickness as measured using the Zygo optical profilometer was found to be  $75 \pm 4\text{nm}$  which corresponds to an error of 5.3%. Again the thickness measurements were performed after all the nonlinear optical experiments were finished.

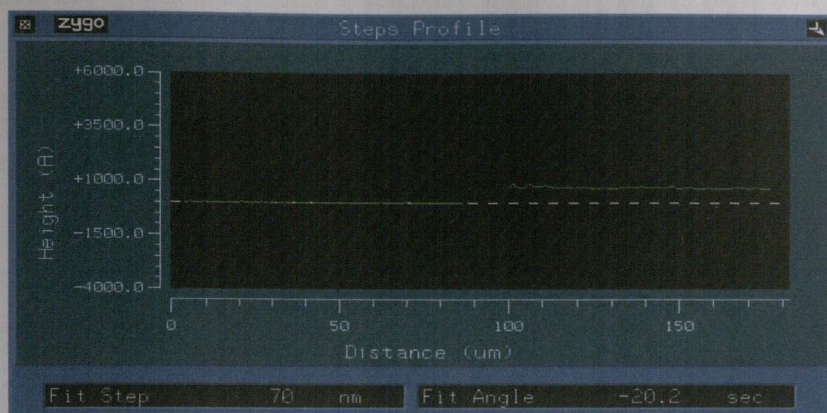


**Figure 5.2:** Thickness measurement of Pyridinyl PAE solid state film. The film thickness was measured at  $75 \pm 4\text{nm}$  using a Zygo optical profilometer. The diagram above corresponds to one of three separate thickness measurements.

### Thienyl PAV Solid State

A 7.5 g/l Thienyl PAV polymer solution was also used to fabricate a series of films with spin speeds varying between 800 and 200rpm. None of these single layer films gave any measurable response in the Z-Scan experiment. To produce films of good optical quality and thick enough to give a measurable signal in direct comparative measurements a multiple layer technique had to be used, as with the previous two polymers. The fabrication process followed the same procedure described above for Thienyl PAE polymer.

The Thienyl PAV solid state film which was used for all the solid state measurements in this thesis consisted of 6 layers of 7.5g/l polymer in Toluene solution spun at 500rpm. The increase in spin speed was used as it gave a better quality film than the films produced at 400rpm. The film thickness as measured using the Zygo optical profilometer was found to be  $230 \pm 10\text{nm}$  which corresponds to an error of 4.4%.

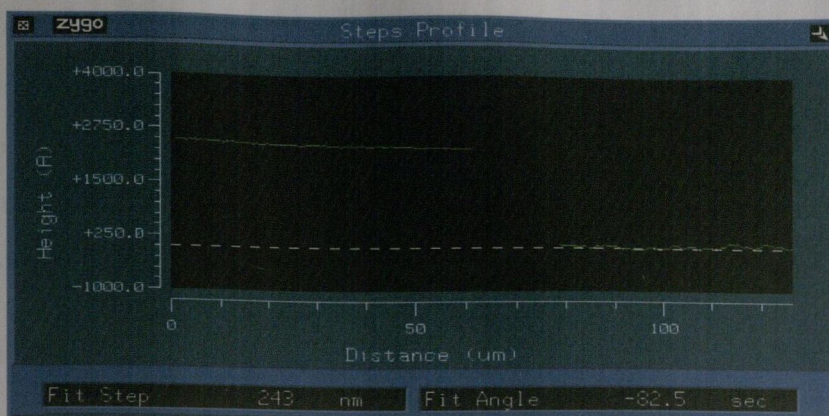


**Figure 5.3:** Thickness measurement of Thienyl PAV solid state film. The film thickness was measured at  $230 \pm 10\text{nm}$  using a Zygo optical profilometer. The diagram above corresponds to one of three separate thickness measurements.

### Pyridinyl PAV Solid State

A 20.0g/l Pyridinyl PAV polymer solution was also used to fabricate a series of films with spin speeds varying between 1000 and 200rpm. One of the single layer films gave a measurable response in the Z-Scan experiment. Unfortunately this happened to be the film spun at 200rpm which had poor optical quality. While the signal was measurable, direct comparison with the Toluene reference was not possible due the considerably higher beam intensity which had to be used on the film. Once again to produce films of good optical quality and thick enough to give a measurable signal in direct comparative measurements, a multiple layer technique had to be used. The fabrication process followed the same procedure outlined above for Thienyl PAE polymer. The Pyridinyl PAV solid state film which was used for all the solid state measurements in this thesis consisted of 3 layers of 20.0g/l polymer in Toluene solution spun at 500rpm. The film thickness as measured using the Zygo optical profilometer was found to be  $170 \pm 9\text{nm}$  corresponding to an error of 5.3%.

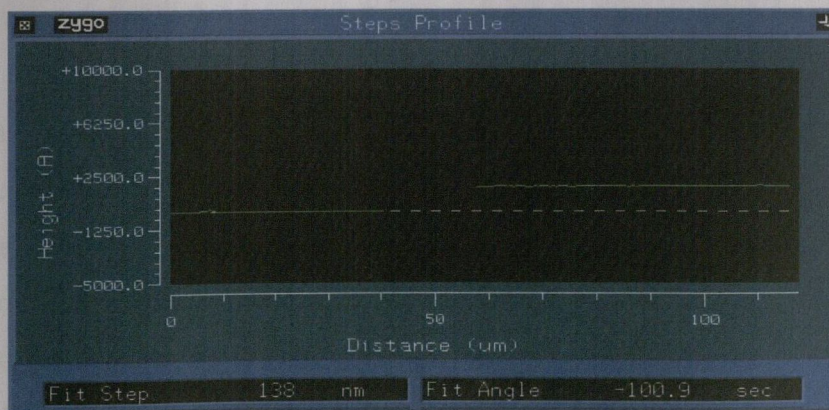


**Figure 5.4:** Thickness measurement of Pyridinyl PAV solid state film. The film thickness was measured at  $170 \pm 9\text{nm}$  using a Zygo optical profilometer. The above diagram corresponds to one of three separate thickness measurements.

## 5.3 Z-Scan Apparatus

Measurements were taken on two different laser systems. A Nd:YAG laser and a Nitrogen pumped dye laser. The YAG laser data analysis calculations were based on the Gaussian spatial beam profile Z-Scan technique and the Dye laser calculations done were based on the top-hat spatial beam profile Z-Scan technique, both of which are described in chapter 3.

### 5.3.1 Experimental Overview

A schematic representation of the generic Z-Scan Apparatus is shown in figure 5.5. The Nd:YAG laser was a active and passively mode-locked Continuum PY60 Series Nd:YAG. It delivers single pulses at 10Hz, with a full width half maximum (FWHM) pulse-width of 40ps at 1064nm, i.e. an  $e^{-1}$  pulse-width of 24ps<sup>2</sup>. Pulses of energy ~35mJ are producible at 1.06 $\mu$ m and up to ~15mJ at the second harmonic wavelength, 532nm. The typical beam profile at the output of the laser was not that of a perfect Gaussian<sup>3</sup>. For absolute values to be extracted from the Z-scan data, the beam profile must be well characterised by either a Gaussian profile or a Top-Hat profile, as discussed in chapter 3.

The Nd:YAG contained a conventional resonator, whose fundamental mode (TEM<sub>00</sub>) is that of a Gaussian wave. The laser profile departs from this theoretical function due to imperfections in the laser optics. Spatial filtering is one method which can be used to remove random fluctuations from the intensity profile of a laser beam<sup>4</sup>. An ideal coherent, collimated laser beam behaves as if generated by a distant point source. Spatial filtering involves focusing the beam, producing an image of the “source” with all the imperfections defocused in an annulus about the axis. A circular pinhole centered on the axis can block the unwanted noise annulus while passing most of the lasers energy. The diameter of the pinhole is approximately  $\lambda f/\omega_r$ , where  $f$  is the focal length of the lens,  $\lambda$  is the laser wavelength, and  $\omega_r$  is the laser beam radius. It was decided, instead, to smooth the laser beam with a 1.00mm aperture, which is the same technique used in reference 3 for Z-Scan solution measurements. The beam goes through aperture 1 (figure 5.5) where it is diffracted. In the far field, the beam profile of a normally incident plane-wave field on a circular aperture is given by a  $\text{somb}^2$  function<sup>5</sup>. A Gaussian profile has a very similar (<0.2% error) intensity profile compared with the central portion of the  $\text{somb}^2$  function<sup>3</sup>. The idea was to select the central part of the diffraction pattern to get a smooth profile approaching a Gaussian, by using a second (aperture 2) to “clip” the wings in the far-field.

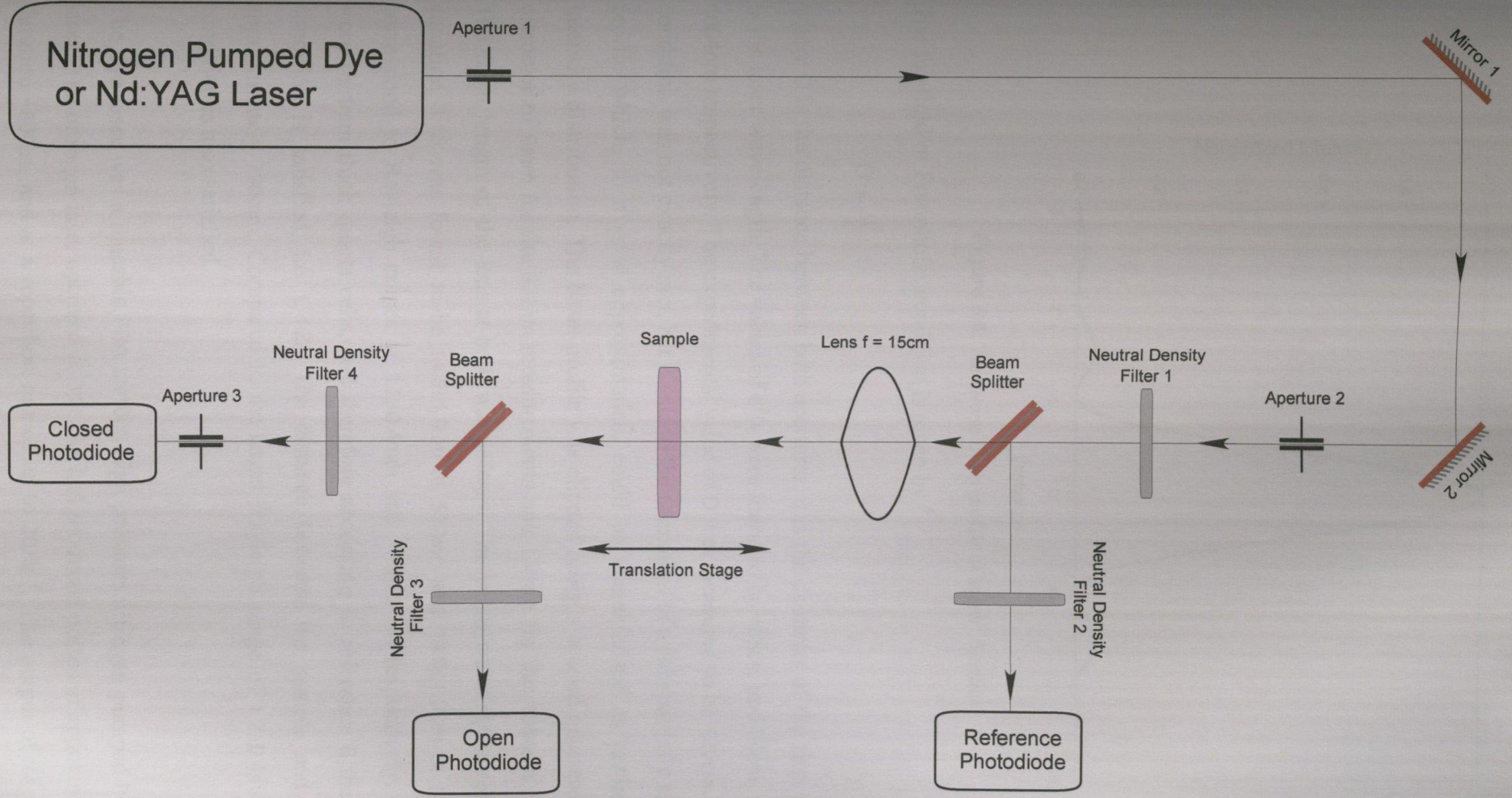


**Figure 5.5:** Schematic representation of the Z-Scan set-up used for all experiments. The Nd:YAG Laser set-up uses all three apertures. The Dye Laser set-up only uses apertures 2 and 3.

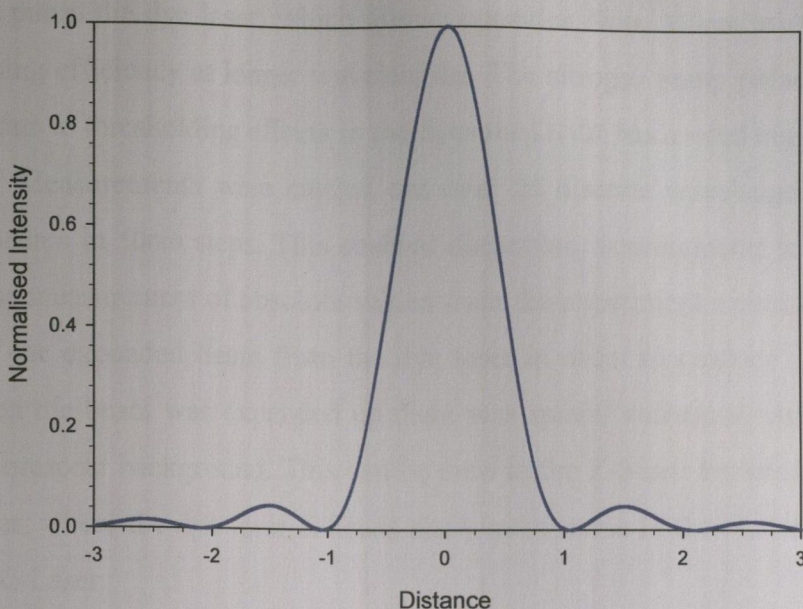


**Figure 5.6:** Transverse beam profile of  $\text{sinc}^2$  function.

The far-field or Fraunhofer condition is given by <sup>5</sup>

$$D \gg \frac{d^2}{\lambda} \quad 5.1$$

where  $D$  is the distance between both apertures,  $d$  is the diameter of the first aperture and  $\lambda$  is the laser wavelength. The values of  $d^2/\lambda$  were found to be 188cm and 94cm, for 532nm and 1064nm respectively. The experimental value of  $D$  was measured to be 420cm. The far-field condition was not exactly met, but it led to the formation of a substantially smoother beam profile which, to a good approximation, could be characterised as having a Gaussian intensity distribution. The beam profile was clipped using a second aperture, which had a diameter of 9mm for the 532nm measurements and 13mm for the 1064nm measurements. The focal length of the lens at both was 150mm. The beam waist measured according to equation 3.1b was found to be  $14.5 \pm 1.9 \mu\text{m}$  at 532nm and  $19.3 \pm 1.3 \mu\text{m}$  at 1064nm, which correspond to Rayleigh ranges of  $1.2 \pm 0.4 \text{mm}$  and  $1.1 \pm 0.2 \text{mm}$  respectively. The solutions were in 1mm thick quartz cells, and therefore according to reference 6 the thin medium condition is satisfied, i.e.  $L < Z_0$ . The distance between the sample and aperture 3 is approximately 790mm. Compared to the larger Rayleigh range of  $1.2 \pm 0.4 \text{mm}$  the far-field condition is also satisfied.

The dye laser was a tuneable PRA LN1000 high pressure nitrogen pumped PRA LN107 dye laser. The nitrogen laser operated at 337.1nm and produced pulses of approximately 1mJ, of duration  $\sim 800 \text{ps}$ , and at a repetition rate of up to 20Hz <sup>7</sup>. The output of the nitrogen laser

was used to pump the dye laser, which allows operation from 350nm to 950nm, although with decreasing efficiency at longer wavelengths. The nitrogen pump pulse has a width of ~800ps, but due to thresholding effects in the dyes the LN107 has a rated output pulse length of ~500ps<sup>8</sup>. Measurements were carried out over 23 discrete wavelengths, from 465nm through to 685nm in 10nm steps. This enabled dispersion measurements to be carried out. To enable the measurement of absolute values from the experiment a circular aperture was used to clip the expanded beam from the dye laser in order to produce a top-hat spatial profile. When the beam was expanded up there was spatial variations which were visible against a fluorescent background. This can be seen in the Z-Scans between the YAG laser and Dye laser, where the dye laser Z-Scans show more noise in the closed aperture traces than the YAG Laser.

### 5.3.2 Data Capture

A computer was used to take all measurements relating to the Z-Scan experiment. Data was recorded from three photodiodes, one recorded the reference energy, one the open aperture energy and the third recorded the closed aperture energy. The photodiode signals were digitised by a Strawberry Tree Flash 12, 1 MHz A/D card stored on a computer. Software, written in C, controlled this card and collected the experimental data, analysed it and then displayed it graphically. The translation stage was computer controlled and operated using the same software described below.

The complete source code listing for the control software used for the Z-Scan measurements is listed in Appendix 1. A parameter input file was used to control the various parameters which had to be taken into consideration when performing a Z-Scan experiment. The file takes the form:

```
ZSCANUSER\KIERAN\ 20 0.25 100 800 0.5 0
```

The first parameter is the directory where the data was saved to. The filename was a default one called Z-Scan.dat, which needed to be renamed after each Z-Scan to make sure that it did not get overwritten by the subsequent measurements. This helped to ensure that the particular results just measured were looked at straight away and a decision made whether to keep the results or to discard them.

The first number was the total distance the translation stage moved, in millimeters. Valid numbers were 1, 2, 3, 4, 5, 6, 7, 8, 9, 10, 11, 12, 13, 14, 15, 16, 17, 18, 19, 20, 21, 22, 23, 24, 25,

26, 27, 28, 29 and 30. This number was chosen depending on the focal length of the Z-Scan lens used within the experiment.

The second number was the step size. This is the distance between successive Z-Scan steps. Valid numbers were 0.1, 0.2, 0.25, 0.5, 1.0, 2.0 and 2.5. Smaller distances between successive steps increased the number of data points that were recorded for the Z-Scan measurement. However this came at the cost of longer measurement times.

The third number was the number of data points to which the pulses were digitised. Valid numbers were 50, 75, 100, 125, 150, 175 and 200. This number depended on the pulse width received from the photodiodes. Choosing a larger number increased the accuracy of the peak voltage detection. However on the Nd:YAG laser, which operates at a repetition rate of 10Hz, a larger number means that not every successive laser shot would be measured, due to the extra processing time. This led to increased measurement times.

The fourth number was the resolution of the stepper motor i.e. the number of steps it took to move the stepper motor 1mm. The Nd:YAG stepper motor had a resolution of 800 steps per millimeter, while the dye laser stepper motor had a resolution of 80 steps per millimeter. The same model stepper motor control box was used on both experiments, but there were different stepper motors for each system.

The fifth number was the trigger voltage. Valid numbers were any number between 0 and 10 volts. This needed to be chosen carefully before each experiment. This was due to the fact that the intensity of the laser pulses changed between different samples and the response of the silicon detectors was wavelength dependent. The trigger voltage was chosen before each Z-Scan run to ensure that it was high enough so that no stray or background light may accidentally trigger a measurement. It also needed to be set low enough so that it could successfully be triggered by whatever voltage was produced by the reference photodiode.

The sixth number was the number of points to be sampled before the trigger. This number had to be less than the number of data points that the pulses were digitised to. This was necessary to ensure that the baseline voltage was digitised for each pulse measured.

## 5.4 Z-Scan Measurements

This section presents the experimental measurement techniques which are used for each of the Z-Scan set-ups. Some of the experimental Z-Scan traces are presented which outline



the different types of nonlinear effects which are encountered for each of the polymers, in solution as well as solid state.

### 5.4.1 Nd:YAG Laser Measurements

Concentration dependent solution measurements as well as thin film solid state measurements were performed at 532nm and 1064nm. The toluene solvent was purchased from Riedel-de-Haën, and its purity was superior to 99.8%. The same cell was used for all the solution experiments and it was fixed, which means that there was no alteration of the background due to surface imperfections or wedge in the cell between different samples. A syringe was used to fill and empty the cell. A baseline measurement with Toluene was the first measurement taken and all subsequent concentration measurements were taken using the most dilute concentration first. This process minimised the effects of cross contamination of concentrations. After each series of measurements the cells were cleaned out as thoroughly as possible before the next set of measurements at higher concentrations.

The solid state samples were made thick enough so that no change to the experiment had to be made for solid state measurements except to change the relevant sample. This is valid for most wavelengths except when the Z-Scan wavelength was at or near the absorption band gap of the polymer. Here resonant enhancements took place and extra neutral density filters had to be put in place to reduce the intensity of the beam to facilitate measurements. The solid state samples were always inserted so that the film side of the substrate was facing the Z-Scan beam. During the run the sample moves from the focusing lens towards the detector, so  $-z$  is the pre focal region and  $+z$  is the pre focal region.

The typical z-step is 0.5mm for the YAG laser over a total scan length of 20mm. Data for each z-position were averaged over, typically 30 shots. From chapter 2, it is recommended that the sample be scanned by at least  $\pm Z_0$ . This condition is therefore satisfied at each wavelength. The closed aperture had a diameter of  $7.00 \pm 0.05$ mm, and the aperture linear transmittance (S) was measured to be 0.10 at 532nm and 0.05 at 1064nm. For each measurement Z-Scans were repeatedly taken until no change between the consecutive runs was noted apart from the slight change in normalization signal. This ensured that no damage was caused to the sample during the first run. The first run was then chosen for analysis. This procedure typically involved only 2 consecutive Z-Scans as the results were mostly repeatable. Figures 5.7 through 5.13 show typical Z-Scan traces obtained from the Nd:YAG laser apparatus.

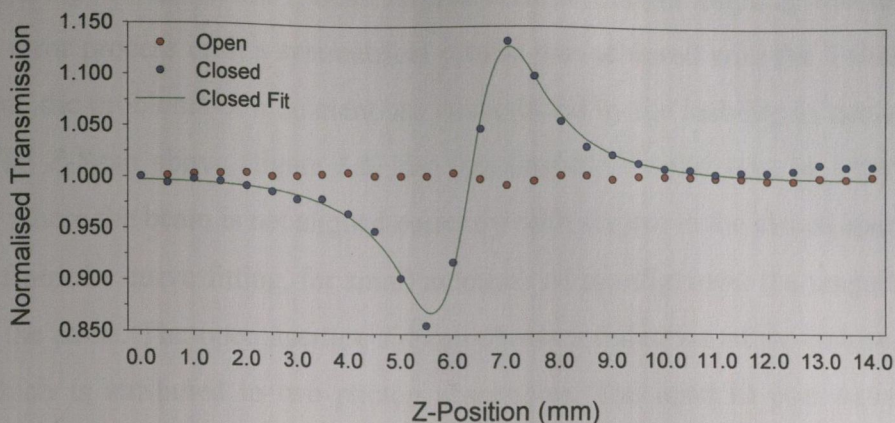


**Figure 5.7** : Z-Scan trace taken for Toluene solvent at 532nm.

The above figure shows the Z-Scan trace taken for Toluene at 532nm. The closed fit uses equation 3.25 to determine a value for the phase change  $\Delta\Phi_0$ . Once  $\Delta\Phi_0$  is known  $\eta_2$  may be calculated from equation 3.12.

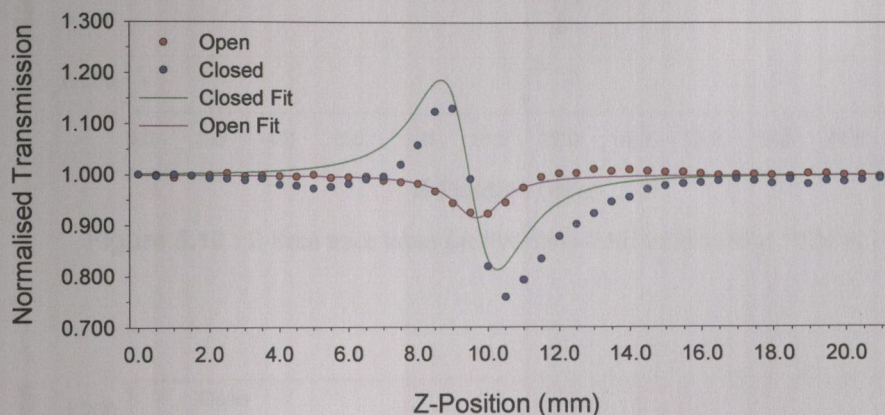


**Figure 5.8** : Z-Scan trace taken for Pyridinyl-PAV solid state at 532nm.

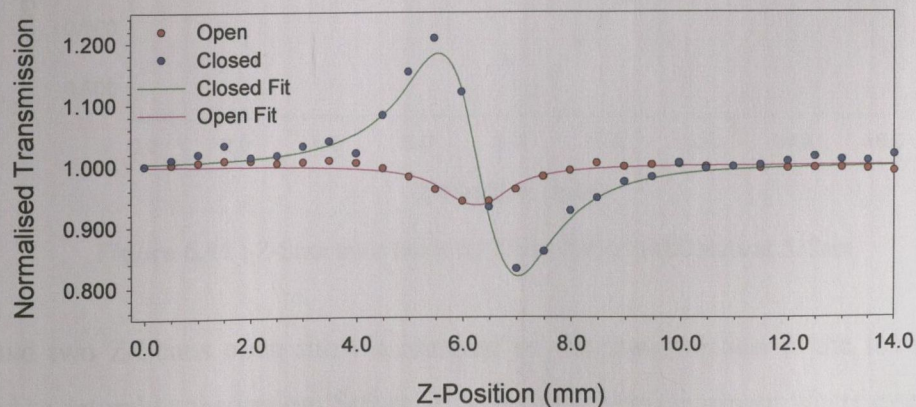


**Figure 5.9** : Z-Scan trace taken for Thieryl-PAE 2.5g/l solution at 532nm.

Beam centring for the closed Z-Scan is problematic. Correct aligning was attained via a trial and error process until a symmetrical profile was achieved with the Toluene solution. At 1064nm the problems of alignment are exacerbated by the inability to actually view the beam. The Z-Scan above (figure 5.8) for Pyridinyl-PAV solid state at 532nm shows an example where the beam is not aligned correctly with respect to the closed aperture. As can be seen from the curve fitting, for small amounts of misalignment the magnitude of  $\Delta T_{p-v}$  remains the same. The open aperture Z-Scan shows a reduction of the transmission at the focus which is attributed to two photon absorption. The open fit uses equation 3.32 to determine a value for the nonlinear absorption  $\beta$ .

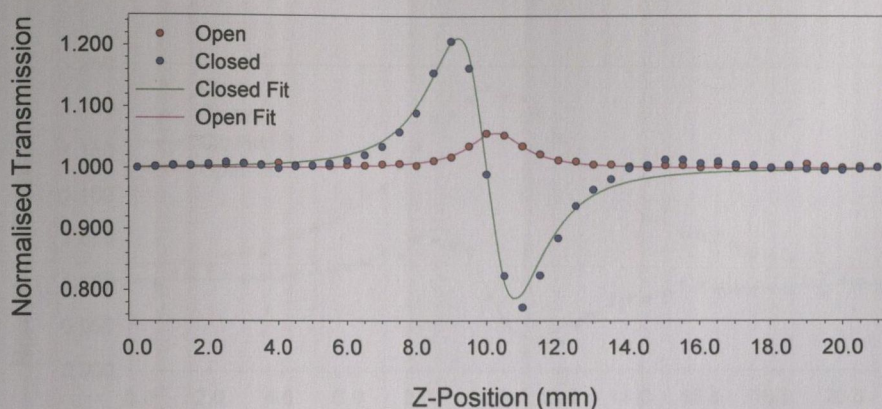


**Figure 5.10** : Z-Scan trace taken for Pyridinyl-PAE solid state at 532nm.

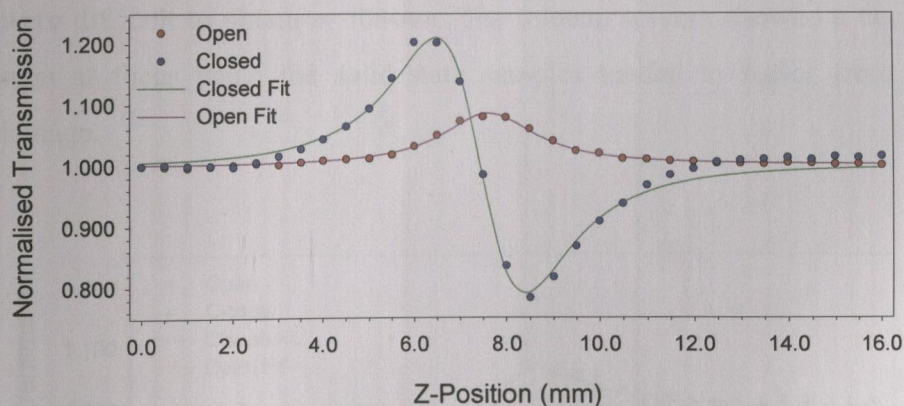


**Figure 5.11** : Z-Scan trace taken for Thienyl-PAE solid state at 532nm.

The above two Z-Scans open show an increase of the transmission at the focus which is attributed to saturable absorption. Saturable absorption was dominant wherever there was a high level of linear absorption. Note that  $\eta_2$  and  $\beta$  are regarded as the effective third order nonlinearities as they may contain some higher order components.

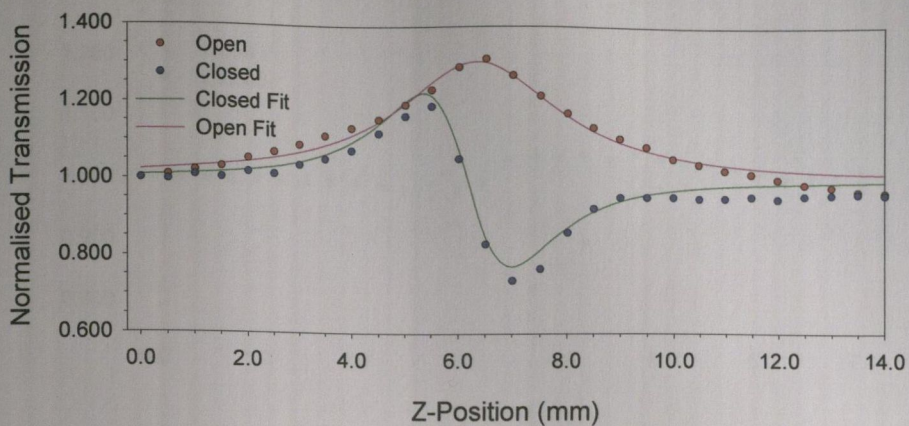


**Figure 5.12 :** Z-Scan trace taken for Thieryl-PAV 0.1g/l solution at 532nm.

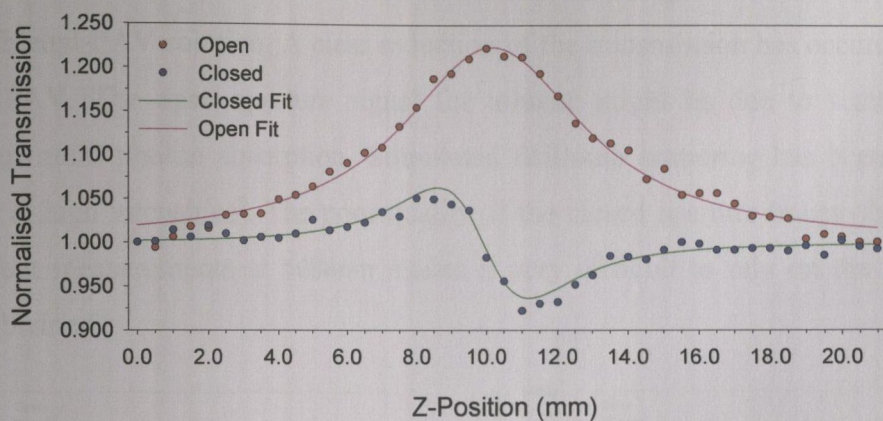


**Figure 5.13 :** Z-Scan trace taken for Thieryl-PAV solid state at 532nm.

Results were difficult to obtain at 1064nm. The toluene solvent showed a decrease in the transmission at focus while the solid state samples tended to suffer from irreversible sample damage.

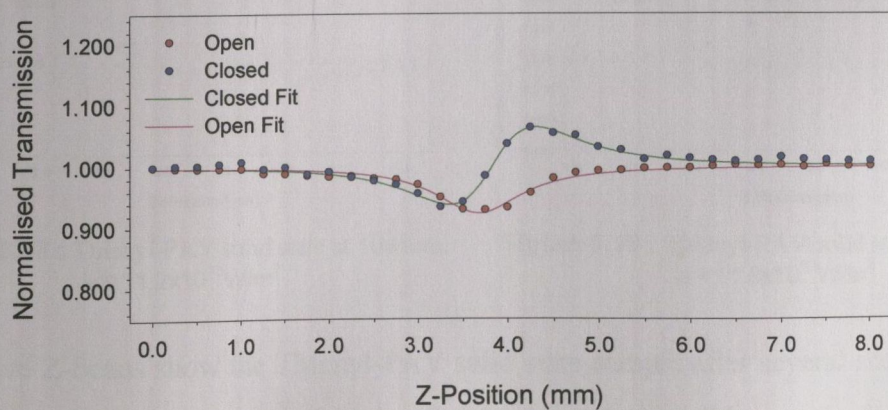


**Figure 5.14 :** Z-Scan trace taken for Toluene solvent at 1064nm.

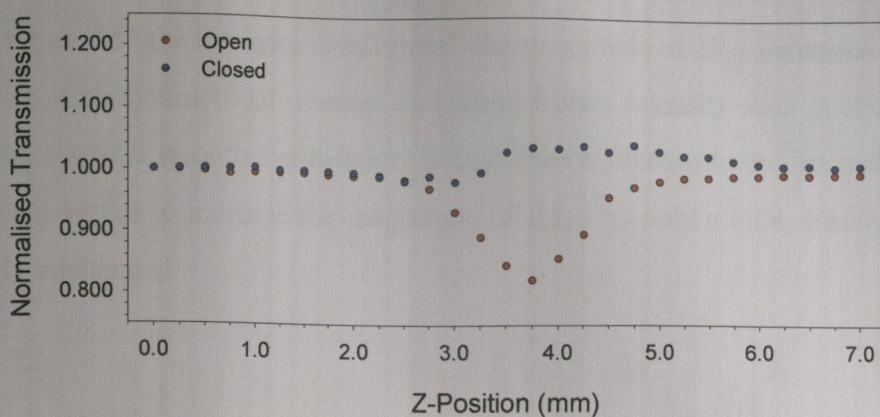


**Figure 5.15** : Z-Scan trace taken for Thienyl-PAV solid state at 1064nm.

Figure 5.14 shows the Z-Scan for toluene at 1064nm, while figure 5.15 shows the Z-scan for 7.50g/l Thienyl-PAV solution. A clear reduction of the transmission has occurred due to the Thienyl-PAV. The open aperture signal for toluene might be due to scattering by the sample or multi photon absorption. Stimulated Brillouin scattering has been observed in Toluene at high intensities<sup>9</sup>. The poor quality of the closed aperture traces obtained for all the solvent measurements at 1064nm makes it very difficult to rely on the experimental values obtained.

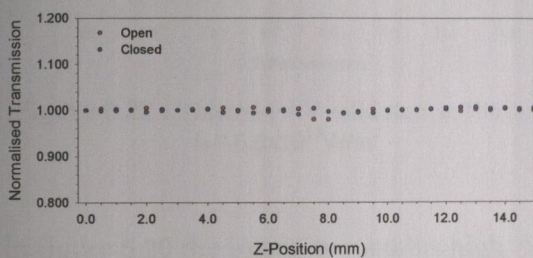


**Figure 5.16** : Thienyl-PAV solid state at 1064nm.  
 $I_0 = 7.1 \times 10^{13} \text{W/m}^2$

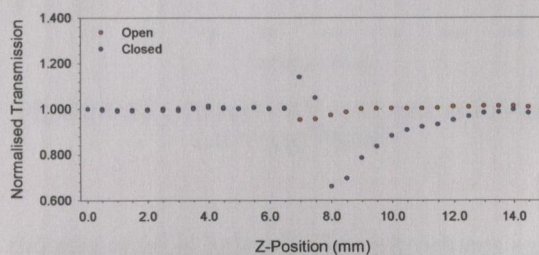


**Figure 5.17** : Thienyl-PAV solid state at 1064nm.  
 $I_0 = 10.8 \times 10^{13} \text{W/m}^2$

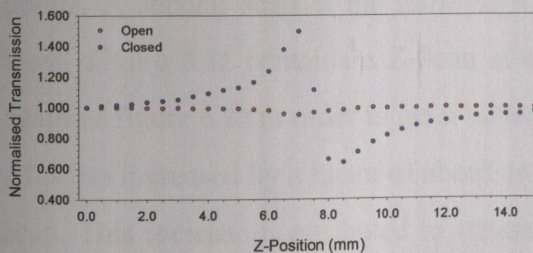


**Figure 5.18** : Thienyl-PAV solid state at 1064nm.  
 $I_0 = 11.2 \times 10^{13} \text{W/m}^2$

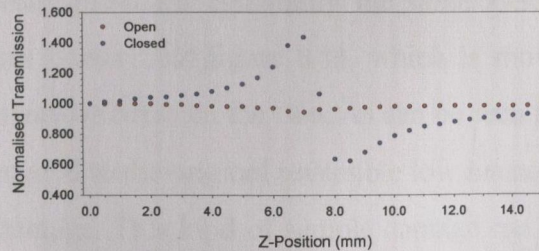


**Figure 5.19** : Thienyl-PAV solid state at 1064nm.  
 $I_0 = 11.8 \times 10^{13} \text{W/m}^2$

The above Z-Scans show the Thienyl-PAV solid state sample after several scans where the intensity is increased. The sample seemed to undergo irreversible sample damage. Figure 5.16 shows a Z-Scan for  $I_0 = 7.1 \times 10^{13} \text{W/m}^2$ . The result was reversible, in that reducing the

beam intensity served to reduce the closed aperture Z-Scan trace below the detectability limit. In figure 5.17 the intensity is increased; the magnitude of  $\Delta T_{p-v}$  increases dramatically, although in a un-symmetrical manner. A second higher intensity scan is shown in figure 5.18 which shows a smooth symmetrical Z-Scan curve. Increasing the intensity higher still (figure 5.19) serves to increase the magnitude of  $\Delta T_{p-v}$  by only a little, leaving the Z-Scan essentially unchanged.

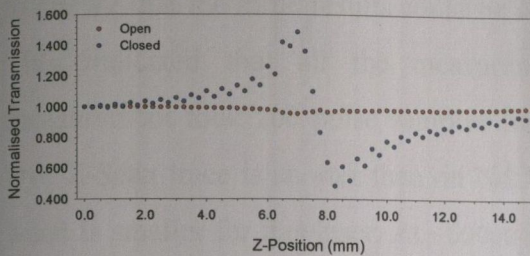


**Figure 5.20 :** Thienyl-PAV solid state at 1064nm.  
 $I_0 = 11.0 \times 10^{13} \text{W/m}^2$

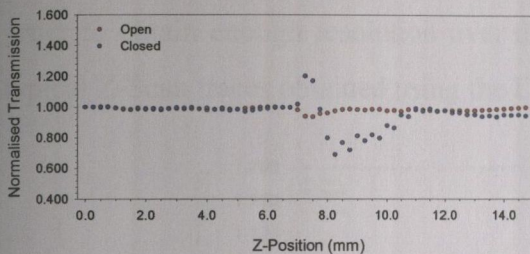


**Figure 5.22 :** Thienyl-PAV solid state at 1064nm.  
 $I_0 = 6.8 \times 10^{13} \text{W/m}^2$

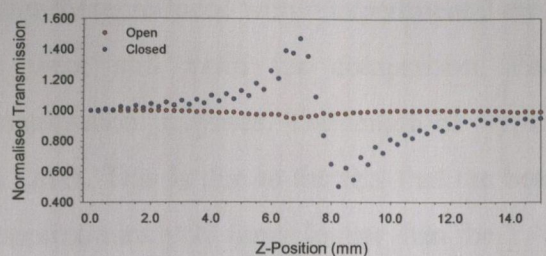


**Figure 5.21 :** Thienyl-PAV solid state at 1064nm.  
 $I_0 = 11.5 \times 10^{13} \text{W/m}^2$

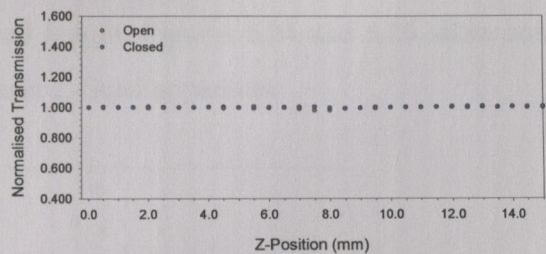


**Figure 5.23 :** Thienyl-PAV solid state at 1064nm.  
 $I_0 = 7.1 \times 10^{13} \text{W/m}^2$

In figure 5.20 the intensity remains high, while the step-size is halved. This introduces extra points into the Z-Scan, which are consistently lower in magnitude compared to the original points. A second scan at the same high intensity produced essentially the same Z-Scan trace. Figure 5.22 contains a Z-Scan at a lower power than figure 5.16, which is shown again as figure 5.23 in order to get a better comparison between the two. As can be seen the  $\Delta T_{p-v}$  has increased by a factor of about 50, compared to the original reversible low intensity scan. This increase is attributed to structural damage. This kind of sample damage can be detected, however, by changing the step size as shown in the above figures. All solid state film Z-Scans at 532nm were subsequently re-checked. The test was also included as part of the Dye laser measurements.

## 5.4.2 Dye Laser Measurements

The Dye laser Z-scan measurements were carried out in a similar manner to the YAG laser. Measurements were carried out over 23 discrete wavelengths, from 465nm through to 685nm in 10nm steps. All solution measurements were carried out on the 2.5g/l concentration solutions. To minimise aberrations, the Toluene sample was the first and last measurement at each wavelength. Measurements were taken on the pure Toluene solution to ensure that the same results could be consistently reproduced within experimental error. This indicated that all the measurements were still valid for comparison. Each measurement took 200 pulse samples for normalisation purposes. The length of typical Dye Z-Scan trace is shorter than on Nd:YAG Laser. This is due to the fact that the beam waist is smaller for this laser. At  $\sim 500\text{ps}$  it is approximately 20 times longer than the YAG laser pulse length. In order to increase the peak power per pulse a lens with a short focal length, or a wider diameter beam, is needed to attain the required peak power needed to detect any nonlinear optical response. The interval is reduced from 0.5mm to 0.25mm in order to obtain enough resolution over the scan length. Figures 5.24 and 5.25 show some typical Z-Scan traces obtained using the Dye laser Z-Scan apparatus.

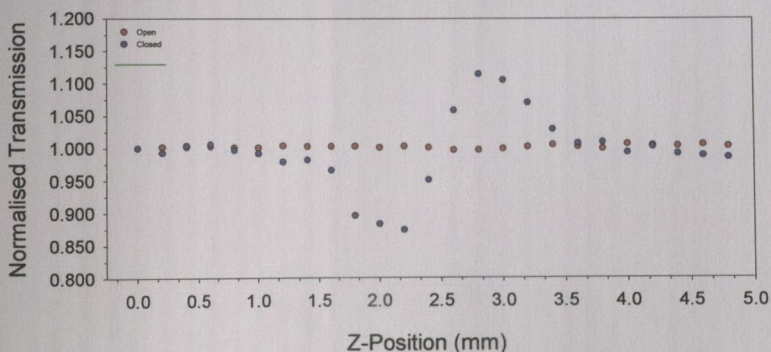


**Figure 5.24** : Z-Scan trace taken for Toluene solvent at 565nm

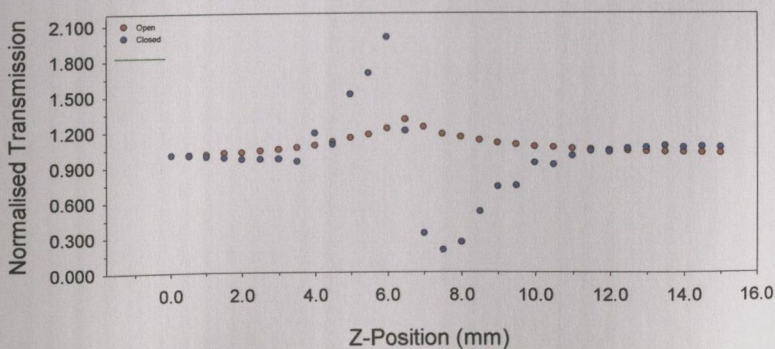


**Figure 5.25** : Z-Scan trace taken for Thienyl-PAV solid state at 475nm

The Z-Scan results were analysed using the technique of Zhao and Palffy-Muhoray (chapter 3), who derived the results of performing a Z-scan using a focused “top-hat” beam<sup>10</sup>. As a general trend, it was more difficult to get reliable results at longer wavelengths. This was due to two main reasons. Firstly, it was more difficult to get the required energy per pulse out of the dye laser at the longer wavelengths. The beam diameter necessary to achieve the required intensity to see any nonlinear effects had to be increased. This had the effect of increasing the spatial noise in the signal, which reduced the minimum detectable signal, and also adding noise onto a relatively large signal. As a secondary fact was that the nonlinearity of the polymers decreased as the measurements became more and more off resonance.



## References

---

- 1 Y. Umeda M.Sc. Thesis, T.C.D. 1993
- 2 Ph.D. thesis by Joe Callaghan, Trinity College Dublin. Dept. of Pure and Applied Physics, Cpt. 3
- 3 Ph.D. thesis by Emmanuel Bourdin, Trinity College Dublin, Dept. of Pure and Applied Physics, Chapter 4
- 4 R. Guenther, "Modern Optics", John Wiley & Sons, 409, 1990
- 5 R. G. Wilson, "Fourier Series and optical Transform Techniques in Contemporary Optics, Chapter 10, 1995
- 6 M. Sheik-Bahae, A. A. Said, T. H. Wei, D. J. Hagan, and E.W. Van Stryland, "Sensitive Measurement of Optical Nonlinearities Using a Single Beam", JQE, **QE26**, 760 (1990).
- 7 Ph.D. thesis by Paul G Horan, Trinity College Dublin, Dept. of Pure and Applied Physics, Cpt. 4
- 8 Ph.D. thesis by Hugh J Byrne, Trinity College Dublin, Dept. of Pure and Applied Physics, Cpt. 4
- 9 J. F. Ready, "Effects of High Power Laser Radiation", Academic Press, New York, Chapter 6, 1971
- 10 W.Zhao, P. Palffy-Muhoray, "Z-scan technique using top-hat beams" Appl. Phys. Lett. **63**, 1613 (1993).

## 6 Results and Discussion

In this chapter the results of the Z-Scan experimental procedures on all four polymers are presented. The results are grouped together by polymer type in order to present the results in as coherent a manner as possible. The chapter can be essentially described as being divided into five separate sections. Each of the first four sections is dedicated exclusively to one of the four polymers and contains a complete set of results pertaining to that polymer only. The fifth section contains a general discussion, where comparisons are made between the four different polymers, and related where possible to the predictions based on the electronic absorption measurements and computer modelling in chapter 4.

For each polymer dispersion measurements performed from 465nm through 685nm in 10nm steps using the Dye Laser set-up are presented first. The value of the third order nonlinear refraction coefficient  $\eta_2$ , and the third order nonlinear absorption coefficient  $\beta$  for the polymer in solution as well as the solid state are given first in a tabulated format. These values are then plotted graphically to better illustrate any trends which may exist. The measurements performed at 1064nm and 532nm using the Nd:YAG Laser set-up are the next results to be presented, initially in table form, and then again in graphical form. The polymers suitability for nonlinear optical switching is then investigated through the  $T$  and  $W$  figures of merit which were discussed in chapters 2 and 4.

### 6.1 Pyridinyl PAV Results

Section 6.1 contains all the nonlinear optical results obtained from Z-Scan measurements of the third order nonlinear refraction  $\eta_2$ , and the third order nonlinear absorption  $\beta$  for the Pyridinyl PAV polymer. Solid state and solution dispersion measurements from 465nm through 685nm in 10nm steps were carried out on using the Dye Laser Z-Scan configuration described in chapter 5. Solid state and concentration dependent solution measurements were also carried out at 532nm and 1064nm using the Nd:YAG Z-Scan configuration described in chapter 5.

#### 6.1.1 Solution and Solid State Measurements

Table 6.1.1 below contains the measured third order nonlinear refraction  $\eta_2$  and third order nonlinear absorption values component  $\beta$  for the Pyridinyl-PAV polymer as measured using the Dye Laser Z-Scan apparatus.

### Pyridinyl-PAV (DYE Laser 465-685nm)

Wavelength	$\eta_2$ Solid State ( $\times 10^{-14} \text{ m}^2/\text{W}$ )	$\eta_2$ Solution ( $\times 10^{-18} \text{ m}^2/\text{W}$ )	$\beta$ Solid State ( $\times 10^{-8} \text{ m/W}$ )	$\beta$ Solution ( $\times 10^{-12} \text{ m/W}$ )
465nm	-24.300 $\pm$ 3.159	-13.380 $\pm$ 1.069	-32.800 $\pm$ 4.592	-15.500 $\pm$ 1.240
475nm	-7.620 $\pm$ 1.753	-3.980 $\pm$ 0.318	-8.900 $\pm$ 2.136	14.700 $\pm$ 1.323
485nm	-6.570 $\pm$ 1.840	-2.390 $\pm$ 0.191	-5.080 $\pm$ 1.473	15.900 $\pm$ 1.250
495nm	-4.910 $\pm$ 1.620	-1.030 $\pm$ 0.093	-3.200 $\pm$ 1.088	21.500 $\pm$ 1.692
505nm	-3.830 $\pm$ 1.494	-1.140 $\pm$ 0.103	-0.053 $\pm$ 0.021	22.000 $\pm$ 2.200
515nm	-4.180 $\pm$ 2.048	-1.010 $\pm$ 0.101	14.690 $\pm$ 6.168	19.800 $\pm$ 2.178
525nm	-3.940 $\pm$ 1.970	-0.950 $\pm$ 0.010	32.735 $\pm$ 14.730	14.700 $\pm$ 1.764
535nm	-5.850 $\pm$ 2.925	-0.619 $\pm$ 0.074	2.035 $\pm$ 0.977	11.100 $\pm$ 1.332
545nm	-2.100 $\pm$ 1.050	-0.430 $\pm$ 0.006	2.110 $\pm$ 1.055	1.210 $\pm$ 0.169
555nm	-1.390 $\pm$ 0.695	-0.200 $\pm$ 0.003	1.690 $\pm$ 0.845	1.160 $\pm$ 0.174
565nm	-1.750 $\pm$ 0.875	-0.564 $\pm$ 0.083	0.460 $\pm$ 0.230	2.910 $\pm$ 0.466
575nm	-0.150 $\pm$ 0.080	-0.270 $\pm$ 0.004	0.500 $\pm$ 0.250	1.610 $\pm$ 0.274
585nm	-0.900 $\pm$ 0.500	-0.460 $\pm$ 0.008	0.440 $\pm$ 0.220	1.180 $\pm$ 0.212
595nm	-2.900 $\pm$ 1.450	-0.300 $\pm$ 0.005	1.070 $\pm$ 0.535	0.180 $\pm$ 0.030
605nm	-0.170 $\pm$ 0.080	-0.490 $\pm$ 0.009	0.850 $\pm$ 0.430	0.280 $\pm$ 0.060
615nm	-1.280 $\pm$ 0.640	-0.490 $\pm$ 0.010	0.750 $\pm$ 0.370	0.130 $\pm$ 0.030
625nm	-1.040 $\pm$ 0.520	-0.400 $\pm$ 0.008	1.020 $\pm$ 0.510	0.590 $\pm$ 0.130
635nm	-1.660 $\pm$ 0.830	-0.140 $\pm$ 0.003	1.040 $\pm$ 0.520	1.770 $\pm$ 0.407
645nm	No Scan	-0.170 $\pm$ 0.004	No Scan	2.390 $\pm$ 0.574
655nm	No Scan	No Scan	No Scan	No Scan
665nm	-0.460 $\pm$ 0.230	-0.170 $\pm$ 0.004	0.310 $\pm$ 0.150	0.620 $\pm$ 0.160
675nm	-0.090 $\pm$ 0.040	-0.290 $\pm$ 0.008	0.390 $\pm$ 0.190	0.930 $\pm$ 0.260
685nm	-0.160 $\pm$ 0.080	-0.317 $\pm$ 0.086	0.170 $\pm$ 0.080	0.963 $\pm$ 0.270

**Table 6.1.1:** The real component  $\eta_2$  and imaginary component  $\beta$  of  $\chi^{(3)}$  for the Pyridinyl-PAV polymer. The Solution measurements were all performed on a concentration of 2.5 g/l of the polymer in Toluene Solvent. All the above measurements were performed using the Nitrogen pumped DYE Laser set-up.

Figures 6.1.1 through 6.1.4 below show the above data in graphical format. Each graph also shows the linear absorption spectrum for Pyridinyl-PAV to help facilitate trend correlation.

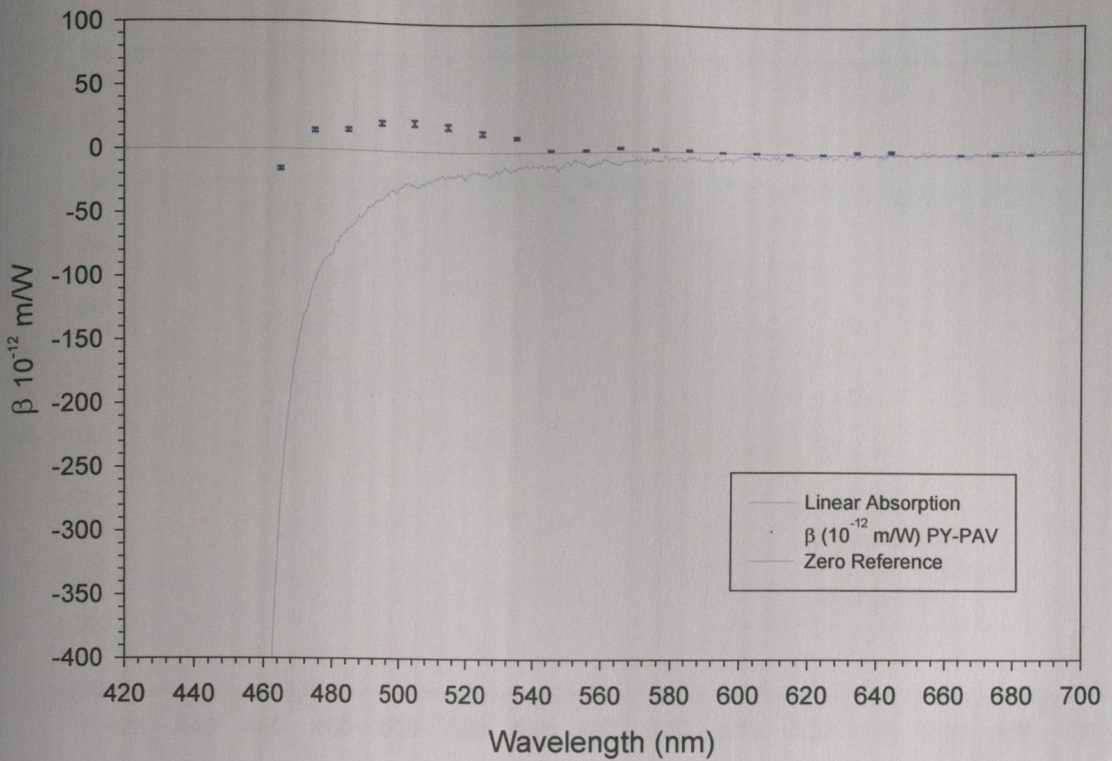


**Figure 6.1.1:** The dispersion of the imaginary component  $\beta$  of  $\chi^{(3)}$  for 2.5 g/l Pyridinyl-PAV polymer Solution. The wavelength range is from 465nm to 685nm in 10nm steps and uses the values in Table 6.1.1. The linear absorption trend for Pyridinyl-PAV in solution is also included for comparison.

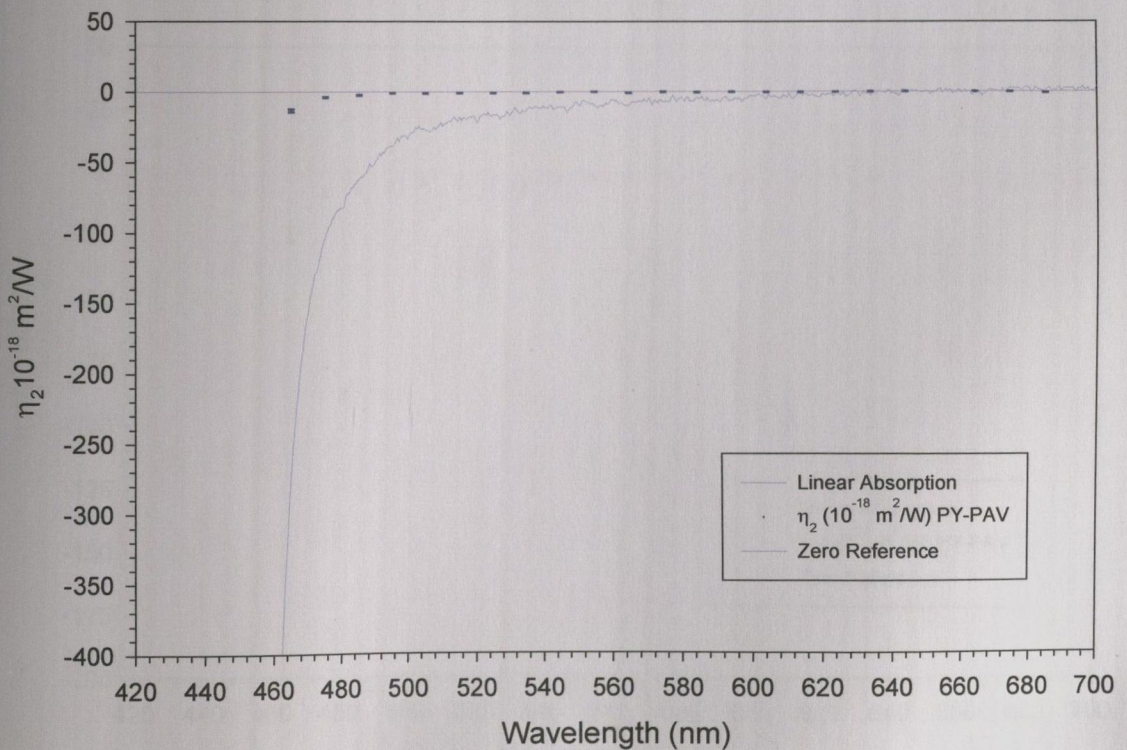


**Figure 6.1.2:** The dispersion of the real component  $\eta_2$  of  $\chi^{(3)}$  for 2.5 g/l Pyridinyl-PAV polymer Solution. The wavelength range is from 465nm to 685nm in 10nm steps and uses the values in Table 6.1.1. The linear absorption trend for Pyridinyl-PAV in solution is also included for comparison.

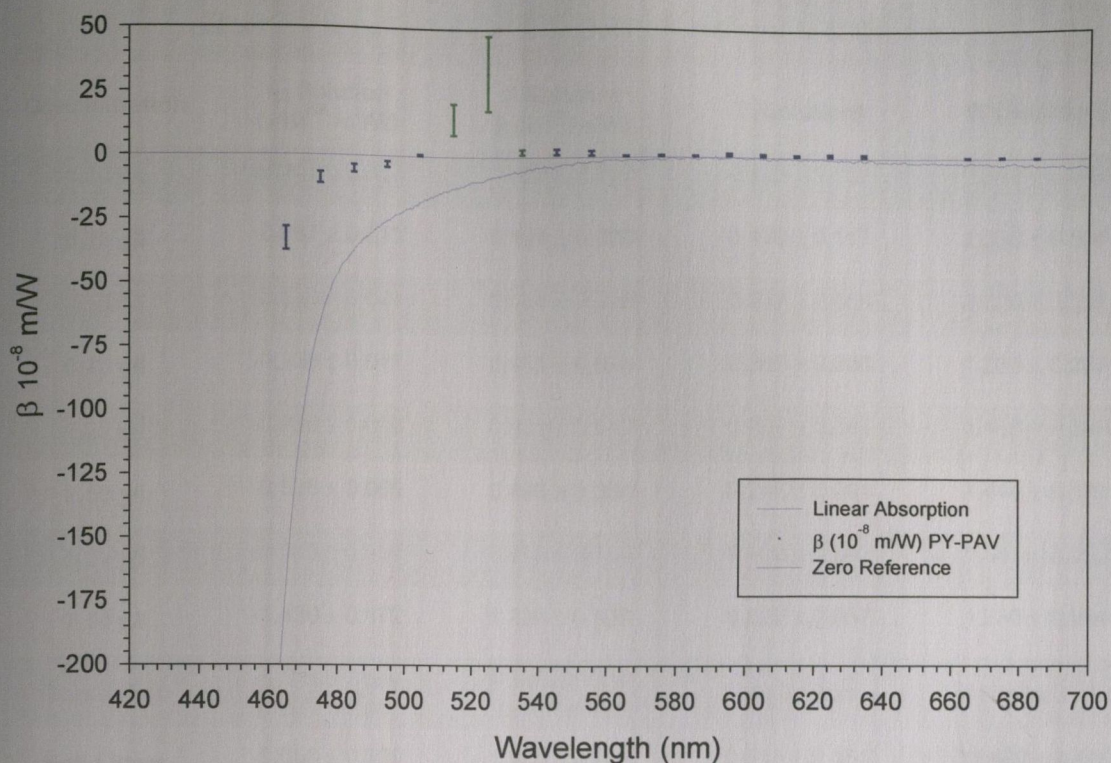


**Figure 6.1.3:** The dispersion of the imaginary component  $\beta$  of  $\chi^{(3)}$  for a 170nm thick **Pyridinyl-PAV Solid State** polymer **Film**. The wavelength range is from 465nm to 685nm in 10nm steps and uses the values in Table 6.1.1. The linear absorption trend for the same Solid State Film is also included for comparison.

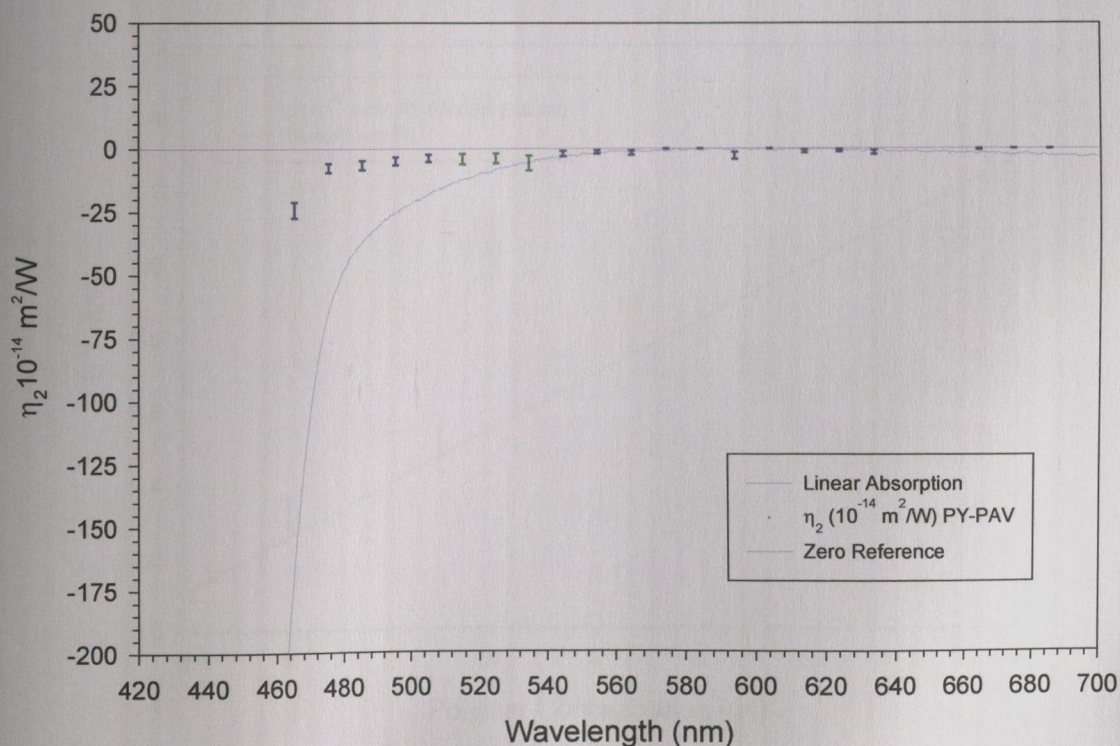


**Figure 6.1.4:** The dispersion of the real component  $\eta_2$  of  $\chi^{(3)}$  for a 170nm thick **Pyridinyl-PAV Solid State** polymer **Film**. The wavelength range is from 465nm to 685nm in 10nm steps and uses the values in Table 6.1.1. The linear absorption trend for the same Solid State Film is also included for comparison.

### Pyridinyl-PAV (YAG Laser 532nm)

Concentration	$\eta_2$ Solution ( $\times 10^{-18}$ m <sup>2</sup> /W)	$\beta$ Solution ( $\times 10^{-12}$ m/W)	T (Solution)	W (Solution)
0.10 g/l	$-0.057 \pm 0.007$	$0.092 \pm 0.012$	$0.428 \pm 0.107$	$3.840 \pm 0.883$
0.25 g/l	$-0.087 \pm 0.010$	$0.154 \pm 0.020$	$0.470 \pm 0.117$	$2.330 \pm 0.536$
0.50 g/l	$-0.173 \pm 0.021$	$0.154 \pm 0.020$	$0.237 \pm 0.059$	$2.320 \pm 0.534$
0.75 g/l	$-0.138 \pm 0.017$	$0.185 \pm 0.024$	$0.359 \pm 0.090$	$1.230 \pm 0.283$
1.00 g/l	$-0.220 \pm 0.026$	$0.321 \pm 0.042$	$0.387 \pm 0.097$	$1.480 \pm 0.340$
2.50 g/l	$-0.538 \pm 0.065$	$0.496 \pm 0.064$	$0.245 \pm 0.061$	$1.444 \pm 0.332$
5.00 g/l	$-1.140 \pm 0.137$	$0.813 \pm 0.106$	$0.190 \pm 0.047$	$1.531 \pm 0.352$
7.50 g/l	$-1.430 \pm 0.172$	$1.220 \pm 0.159$	$0.227 \pm 0.057$	$1.280 \pm 0.294$
Description	$\eta_2$ Solid State ( $\times 10^{-14}$ m <sup>2</sup> /W)	$\beta$ Solid State ( $\times 10^{-8}$ m/W)	T (Solid State)	W (Solid State)
Solid State	$-0.658 \pm 0.329$	$1.520 \pm 0.760$	$0.614 \pm 0.461$	$11.400 \pm 8.550$

**Table 6.1.2:** The real component  $\eta_2$  and imaginary component  $\beta$  of  $\chi^{(3)}$  for the Pyridinyl-PAV polymer at 532nm. The Solution measurements were all performed in Toluene Solvent. Also included are the nonlinear optical switching figures of merit **T** and **W**. All the above measurements were performed using the YAG Laser set-up.

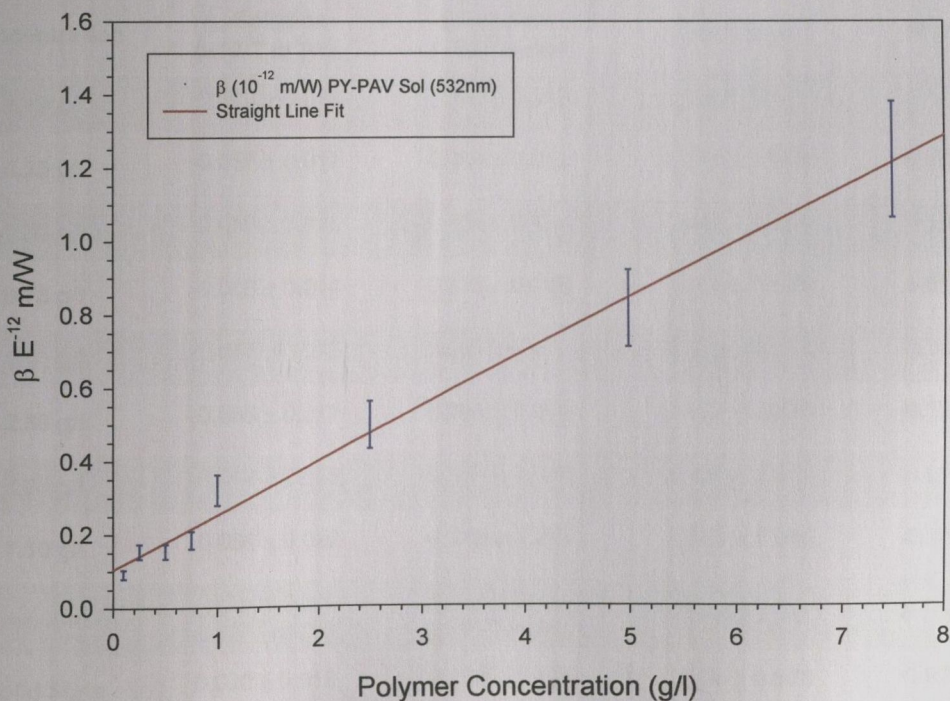


**Figure 6.1.5:** The imaginary component  $\beta$  of  $\chi^{(3)}$  for Pyridinyl-PAV polymer Solution as a function of solution concentration at 532nm. The solution concentration ranges from 0.10g/l up to 7.50g/l and uses the values in Table 6.1.2. Also included is a best straight line fit to all data points.

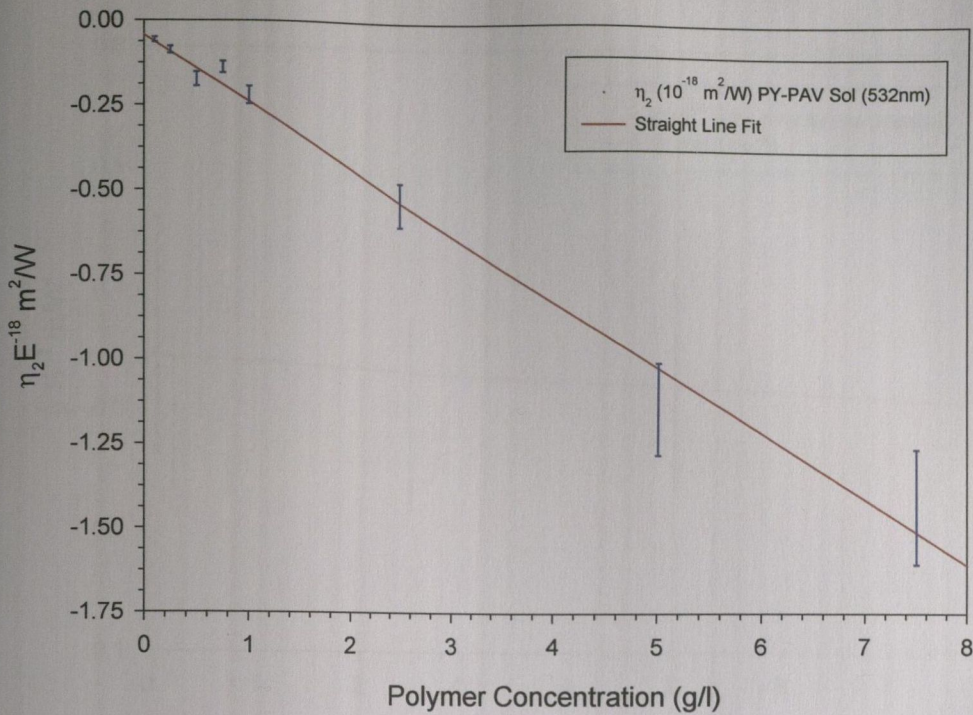


**Figure 6.1.6:** The real component  $\eta_2$  of  $\chi^{(3)}$  for Pyridinyl-PAV polymer Solution as a function of solution concentration at 532nm. The solution concentration ranges from 0.10g/l up to 7.50g/l and uses the values in Table 6.1.2. Also included is a best straight line fit to all data points.

### Pyridinyl-PAV (YAG Laser 1064nm)

Concentration	$\eta_2$ Solution ( $\times 10^{-18} \text{ m}^2/\text{W}$ )	$\beta$ Solution ( $\times 10^{-12} \text{ m/W}$ )	T (Solution)	W (Solution)
0.10 g/l	$-0.050 \pm 0.013$	$0.362 \pm 0.098$	$3.852 \pm 2.041$	$7.155 \pm 3.649$
0.25 g/l	$-0.067 \pm 0.017$	$0.299 \pm 0.082$	$2.374 \pm 1.258$	$3.830 \pm 1.953$
0.50 g/l	$-0.056 \pm 0.015$	$0.401 \pm 0.108$	$3.810 \pm 2.019$	$1.601 \pm 0.816$
0.75 g/l	$-0.053 \pm 0.014$	$0.315 \pm 0.085$	$3.162 \pm 1.676$	$1.014 \pm 0.517$
1.00 g/l	$-0.047 \pm 0.013$	$0.363 \pm 0.099$	$4.109 \pm 2.178$	$0.661 \pm 0.337$
2.50 g/l	$-0.066 \pm 0.017$	$0.298 \pm 0.080$	$2.402 \pm 1.273$	$0.372 \pm 0.190$
5.00 g/l	$-0.074 \pm 0.019$	$0.319 \pm 0.086$	$2.290 \pm 1.214$	$0.210 \pm 0.107$
7.50 g/l	$-0.086 \pm 0.022$	$0.319 \pm 0.086$	$2.010 \pm 1.065$	$0.183 \pm 0.093$
Description	$\eta_2$ Solid State ( $\times 10^{-14} \text{ m}^2/\text{W}$ )	$\beta$ Solid State ( $\times 10^{-8} \text{ m/W}$ )	T (Solid State)	W (Solid State)
Solid State	$0.020 \pm 0.010$	$0.050 \pm 0.025$	$1.304 \pm 0.978$	$0.212 \pm 0.159$

**Table 6.1.3:** The real component  $\eta_2$  and imaginary component  $\beta$  of  $\chi^{(3)}$  for the Pyridinyl-PAV polymer at 1064nm. The Solution measurements were all performed in Toluene Solvent. Also included are the nonlinear optical switching figures of merit **T** and **W**. All the above measurements were performed using the YAG Laser set-up.

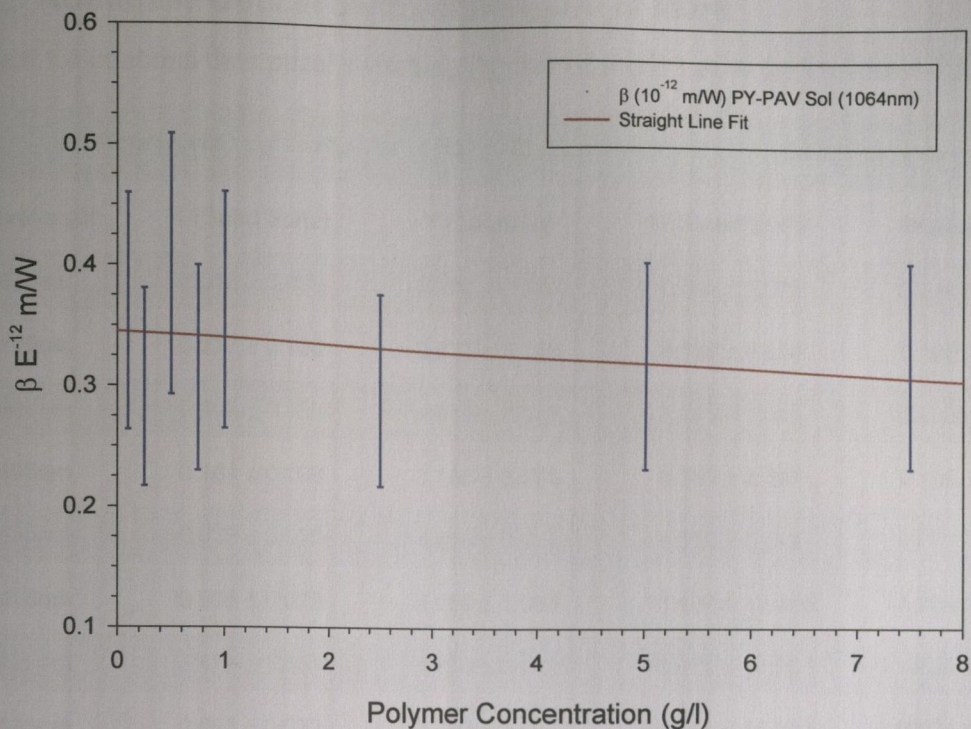


**Figure 6.1.7:** The imaginary component  $\beta$  of  $\chi^{(3)}$  for Pyridinyl-PAV polymer Solution as a function of solution concentration at 1064nm. The solution concentration ranges from 0.10g/l up to 7.50g/l and uses the values in Table 6.1.3. Also included is a best straight line fit to all data points.

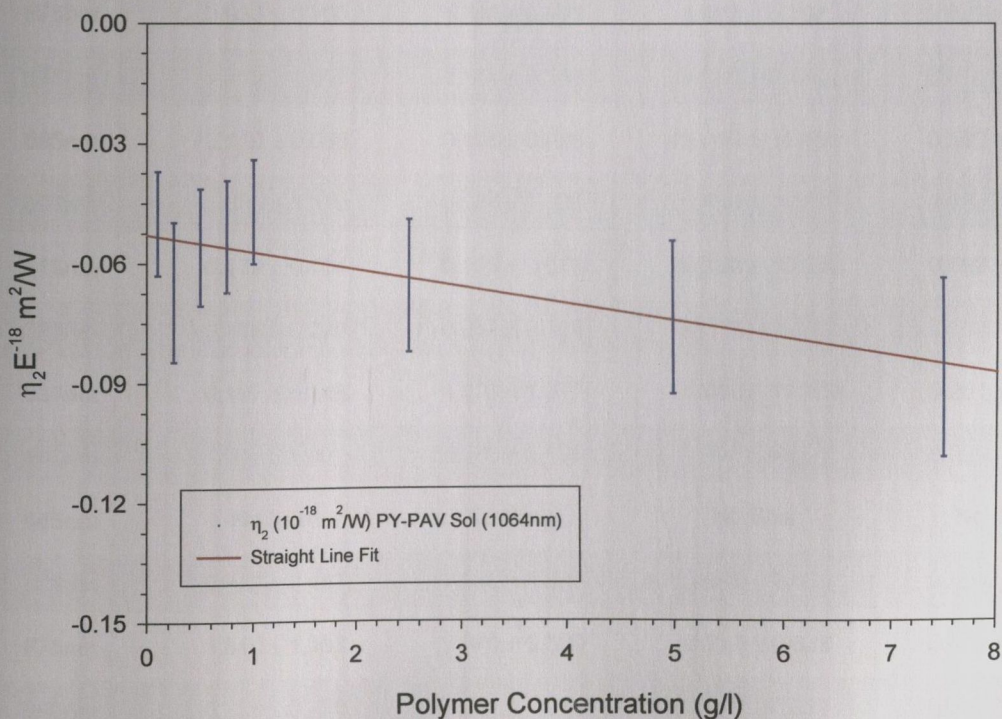


**Figure 6.1.8:** The real component  $\eta_2$  of  $\chi^{(3)}$  for Pyridinyl-PAV polymer Solution as a function of solution concentration at 1064nm. The solution concentration ranges from 0.10g/l up to 7.50g/l and uses the values in Table 6.1.3. Also included is a best straight line fit to all data points.



## 6.1.2 Nonlinear Optical Switching Figure of Merit

Table 6.1.4 contains the optical switching figures of merit T & W for Pyridinyl-PAV.

<b>Pyridinyl-PAV (DYE Laser 465-685nm)</b>				
<b>Wavelength</b>	<b>T (Solid State)</b>	<b>T (Solution)</b>	<b>W (Solid State)</b>	<b>W (Solution)</b>
465nm	0.313 ± 0.084	0.270 ± 0.041	1.640 ± 0.312	0.134 ± 0.017
475nm	0.277 ± 0.130	0.877 ± 0.149	2.130 ± 0.831	0.180 ± 0.027
485nm	0.190 ± 0.108	1.613 ± 0.242	3.280 ± 1.607	0.205 ± 0.031
495nm	0.161 ± 0.108	5.166 ± 0.775	4.740 ± 2.797	0.199 ± 0.034
505nm	0.035 ± 0.026	4.850 ± 0.921	8.650 ± 6.142	0.561 ± 0.095
515nm	0.906 ± 0.679	5.060 ± 1.063	16.490 ± 12.435	0.824 ± 0.157
525nm	2.178 ± 1.634	4.050 ± 0.932	18.670 ± 14.003	0.820 ± 0.172
535nm	0.093 ± 0.072	4.796 ± 1.103	59.080 ± 44.310	0.874 ± 0.219
545nm	0.273 ± 0.205	0.762 ± 0.206	15.500 ± 11.625	0.387 ± 0.097
555nm	0.335 ± 0.251	1.580 ± 0.458	13.400 ± 10.050	0.213 ± 0.058
565nm	0.075 ± 0.056	1.458 ± 0.423	26.800 ± 20.100	0.960 ± 0.298
575nm	0.933 ± 0.700	1.740 ± 0.574	1.022 ± 0.767	0.227 ± 0.070
585nm	1.410 ± 1.057	0.744 ± 0.260	1.030 ± 0.773	0.656 ± 0.216
595nm	0.110 ± 0.083	0.175 ± 0.065	42.200 ± 31.650	0.583 ± 0.204
605nm	1.570 ± 1.178	0.174 ± 0.068	1.430 ± 1.073	0.697 ± 0.258
615nm	0.179 ± 0.134	0.193 ± 0.079	13.800 ± 10.350	0.592 ± 0.231
625nm	0.305 ± 0.229	0.252 ± 0.108	10.770 ± 8.077	0.693 ± 0.284
635nm	0.197 ± 0.148	4.170 ± 1.877	14.910 ± 11.183	0.261 ± 0.112
645nm	No Scan	4.670 ± 2.195	No Scan	0.299 ± 0.135
655nm	No Scan	No Scan	No Scan	No Scan
665nm	0.222 ± 0.167	3.050 ± 1.555	2.180 ± 1.635	0.464 ± 0.227
675nm	1.510 ± 1.133	1.070 ± 0.589	0.717 ± 0.538	0.876 ± 0.464
685nm	0.353 ± 0.265	1.041 ± 0.551	0.782 ± 0.587	0.600 ± 0.330

**Table 6.1.4:** The nonlinear optical switching figures of merit **T** and **W** for the **Pyridinyl-PAV** polymer. The Solution measurements were all performed on a concentration of 2.5 g/l of the polymer in Toluene Solvent. All the above measurements were performed using the Nitrogen pumped **DYE Laser** set-up.

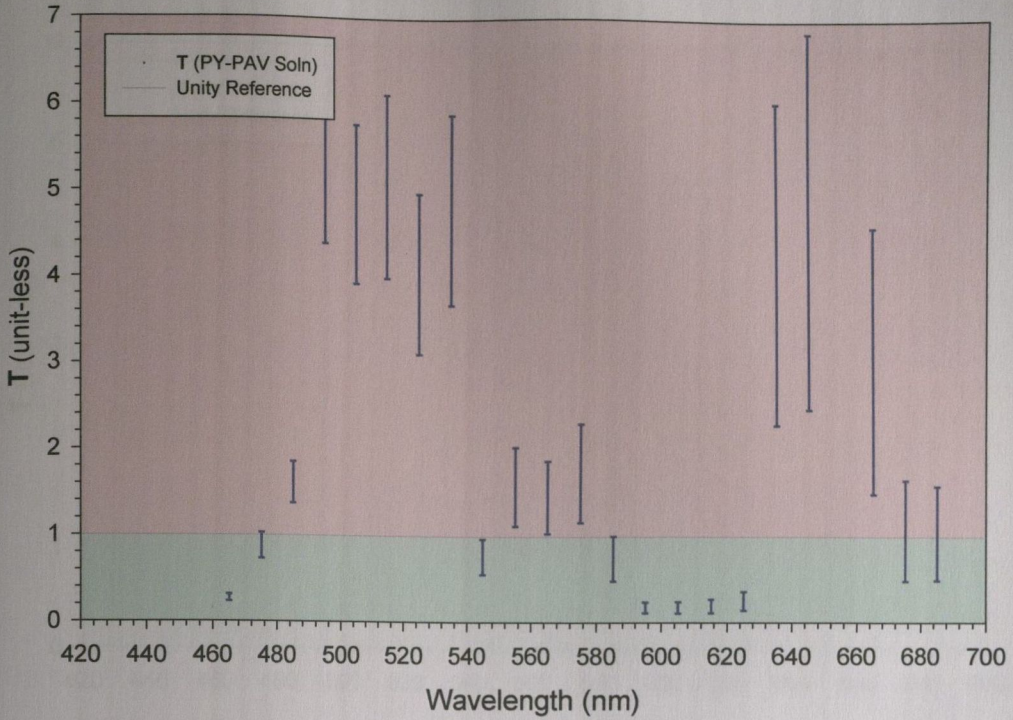


**Figure 6.1.9:** The dispersion of the  $T$  Figure of Merit for 2.5 g/l Pyridinyl-PAV polymer Solution. The wavelength range is from 465nm to 685nm in 10nm steps and uses the values in Table 6.1.4. The graph is colour coded - green where  $T$  is favourable and red where  $T$  is unfavourable for all optical switching.

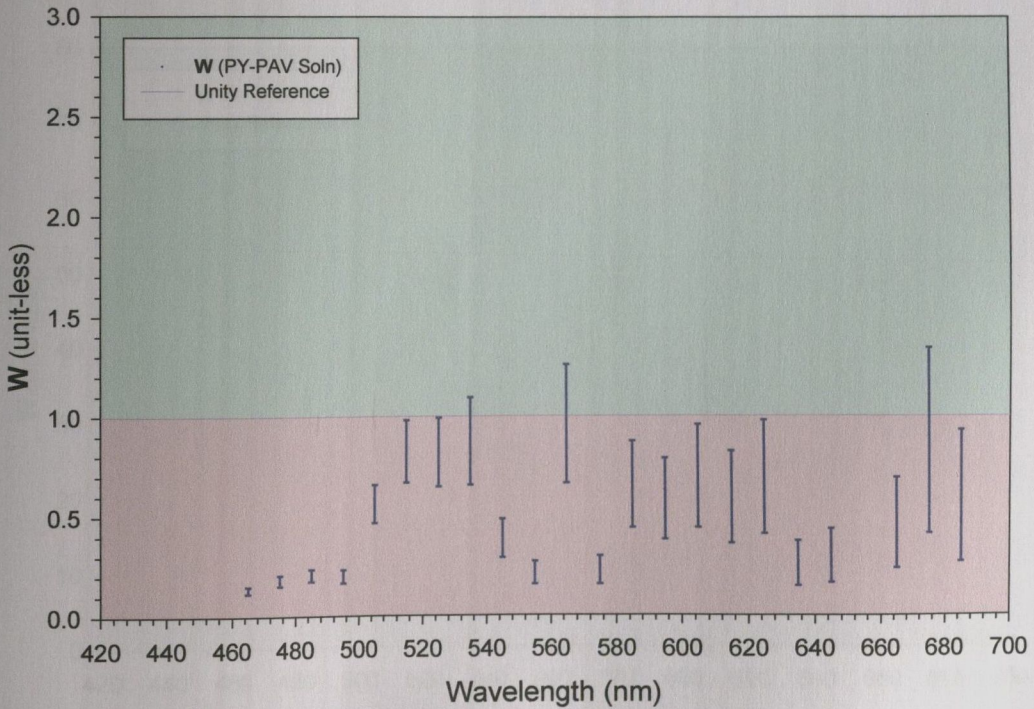


**Figure 6.1.10:** The dispersion of the  $W$  Figure of Merit for 2.5 g/l Pyridinyl-PAV polymer Solution. The wavelength range is from 465nm to 685nm in 10nm steps and uses the values in Table 6.1.4. The graph is colour coded - green where  $W$  is favourable and red where  $W$  is unfavourable for all optical switching.

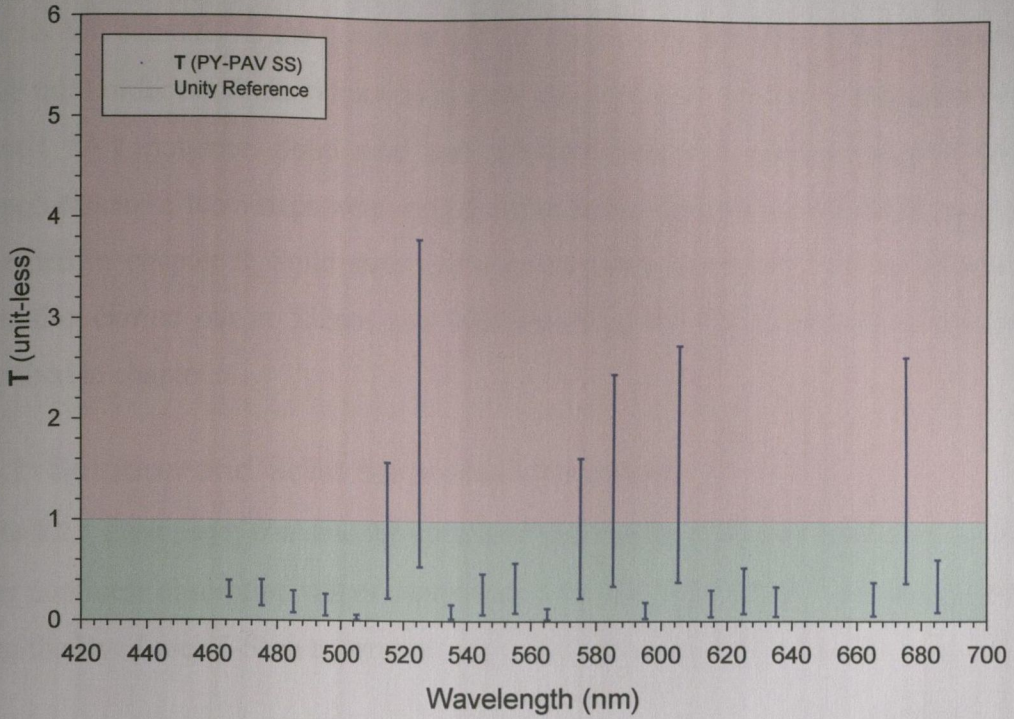


**Figure 6.1.11:** The dispersion of the  $T$  Figure of Merit for a 170nm thick Pyridinyl-PAV Solid State Film. The wavelength range is from 465nm to 685nm and uses the values in Table 6.1.4. The graph is colour coded - green where  $T$  is favourable and red where  $T$  is unfavourable for all optical switching.

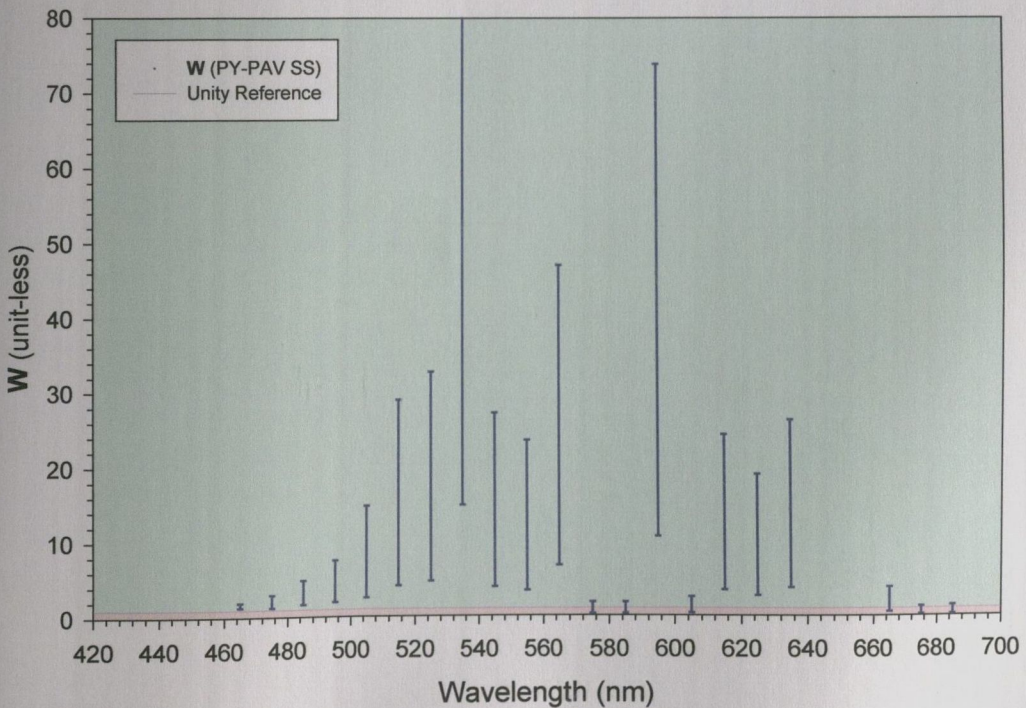


**Figure 6.1.12:** The dispersion of the  $W$  Figure of Merit for a 170nm thick Pyridinyl-PAV Solid State Film. The wavelength range is from 465nm to 685nm and uses the values in Table 6.1.4. The graph is colour coded - green where  $W$  is favourable and red where  $W$  is unfavourable for all optical switching.

## 6.2 Thienyl PAV Results

This section contains all the nonlinear optical results obtained from Z-Scan measurements of the third order nonlinear refraction  $\eta_2$ , and the third order nonlinear absorption  $\beta$  for the Thienyl PAV polymer. Solid state and solution dispersion measurements from 465nm through 685nm in 10nm steps were carried out on using the Dye Laser Z-Scan configuration described in chapter 5. Solid state and concentration dependent solution measurements were also carried out at 532nm and 1064nm using the Nd:YAG Z-Scan configuration described in chapter 5.

### 6.2.1 Solution and Solid State Measurements

Table 6.2.1 (next page) contains the measured third order nonlinear refraction  $\eta_2$  and third order nonlinear absorption values component  $\beta$  for the Thienyl-PAV polymer as measured using the Dye Laser Z-Scan apparatus.

Solution measurements from 465nm through to 565nm could not be obtained due to the magnitude of linear absorption which was present at these wavelengths.

### Thienyl-PAV (DYE Laser 465-685nm)

Wavelength	$\eta_2$ Solid State ( $\times 10^{-14}$ m <sup>2</sup> /W)	$\eta_2$ Solution ( $\times 10^{-18}$ m <sup>2</sup> /W)	$\beta$ Solid State ( $\times 10^{-8}$ m/W)	$\beta$ Solution ( $\times 10^{-12}$ m/W)
465nm	-15.200 ± 1.976	No Scan	-31.100 ± 4.043	No Scan
475nm	-8.100 ± 1.539	No Scan	-16.500 ± 3.300	No Scan
485nm	-7.040 ± 1.338	No Scan	-12.500 ± 2.500	No Scan
495nm	-5.250 ± 1.050	No Scan	-9.920 ± 2.083	No Scan
505nm	No Scan	No Scan	No Scan	No Scan
515nm	-9.150 ± 1.922	No Scan	-8.308 ± 1.826	No Scan
525nm	-2.620 ± 0.576	No Scan	-3.748 ± 0.862	No Scan
535nm	-2.767 ± 0.664	No Scan	-3.406 ± 0.852	No Scan
545nm	-2.210 ± 0.575	No Scan	-1.910 ± 0.516	No Scan
555nm	-1.960 ± 0.549	No Scan	-2.190 ± 0.635	No Scan
565nm	-3.470 ± 1.110	No Scan	-1.490 ± 0.492	No Scan
575nm	-5.430 ± 1.955	-27.200 ± 1.904	-1.640 ± 0.607	-51.200 ± 4.096
585nm	-2.870 ± 1.148	-6.710 ± 0.537	0.470 ± 0.190	3.040 ± 0.274
595nm	-2.220 ± 1.043	-2.570 ± 0.206	0.800 ± 0.390	7.100 ± 0.639
605nm	-1.500 ± 0.750	-1.460 ± 0.146	1.620 ± 0.810	3.930 ± 0.432
615nm	-0.670 ± 0.340	-0.860 ± 0.090	0.950 ± 0.480	2.690 ± 0.323
625nm	-2.000 ± 1.000	-0.880 ± 0.110	2.020 ± 1.010	2.620 ± 0.314
635nm	-0.970 ± 0.490	-0.610 ± 0.080	1.030 ± 0.515	3.030 ± 0.424
645nm	-1.140 ± 0.570	-0.710 ± 0.100	1.310 ± 0.655	3.360 ± 0.504
655nm	-0.970 ± 0.490	-0.650 ± 0.100	1.190 ± 0.595	3.070 ± 0.491
665nm	-0.400 ± 0.200	-0.610 ± 0.100	1.180 ± 0.590	1.810 ± 0.308
675nm	-0.060 ± 0.030	-0.520 ± 0.090	0.400 ± 0.200	1.900 ± 0.342
685nm	-0.040 ± 0.020	-0.420 ± 0.070	0.970 ± 0.490	1.490 ± 0.283

**Table 6.2.1:** The real component  $\eta_2$  and imaginary component  $\beta$  of  $\chi^{(3)}$  for the Thienyl-PAV polymer. The Solution measurements were all performed on a concentration of 2.5 g/l of the polymer in Toluene Solvent. All the above measurements were performed using the Nitrogen pumped DYE Laser set-up.

Figures 6.2.1 through 6.2.4 below show the above data in graphical format. Each graph also shows the linear absorption spectrum for Thienyl-PAV to help facilitate trend correlation.

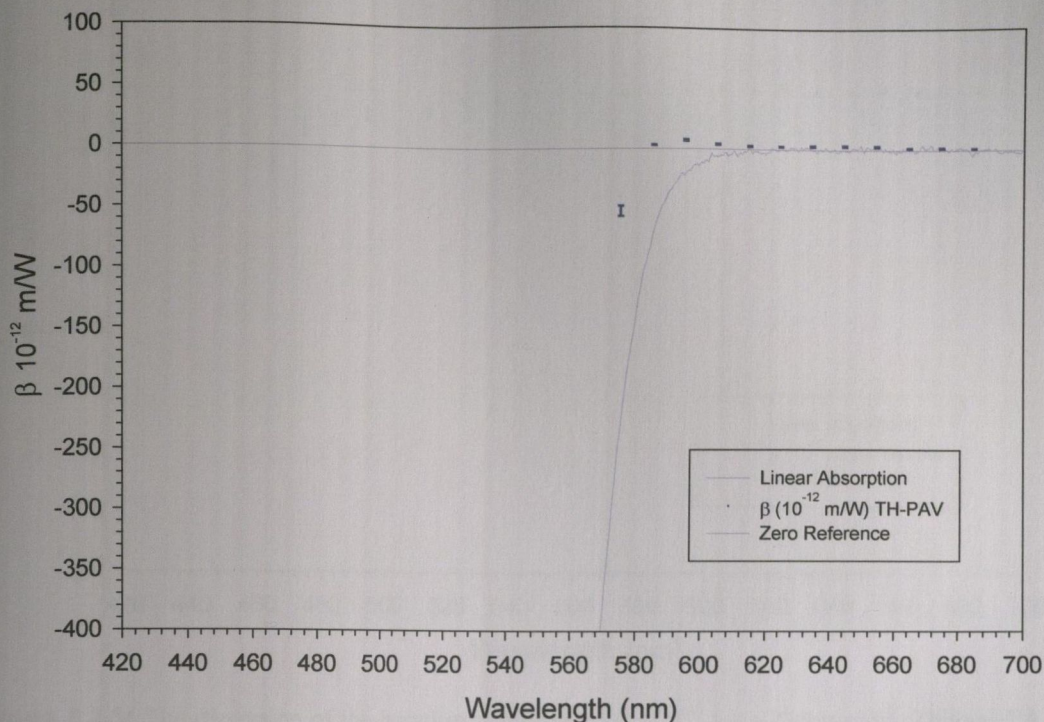


**Figure 6.2.1:** The dispersion of the imaginary component  $\beta$  of  $\chi^{(3)}$  for 2.5 g/l Thienyl-PAV polymer Solution. The wavelength range is from 465nm to 685nm in 10nm steps and uses the values in Table 6.2.1. The linear absorption trend for Thienyl-PAV in solution is also included for comparison.

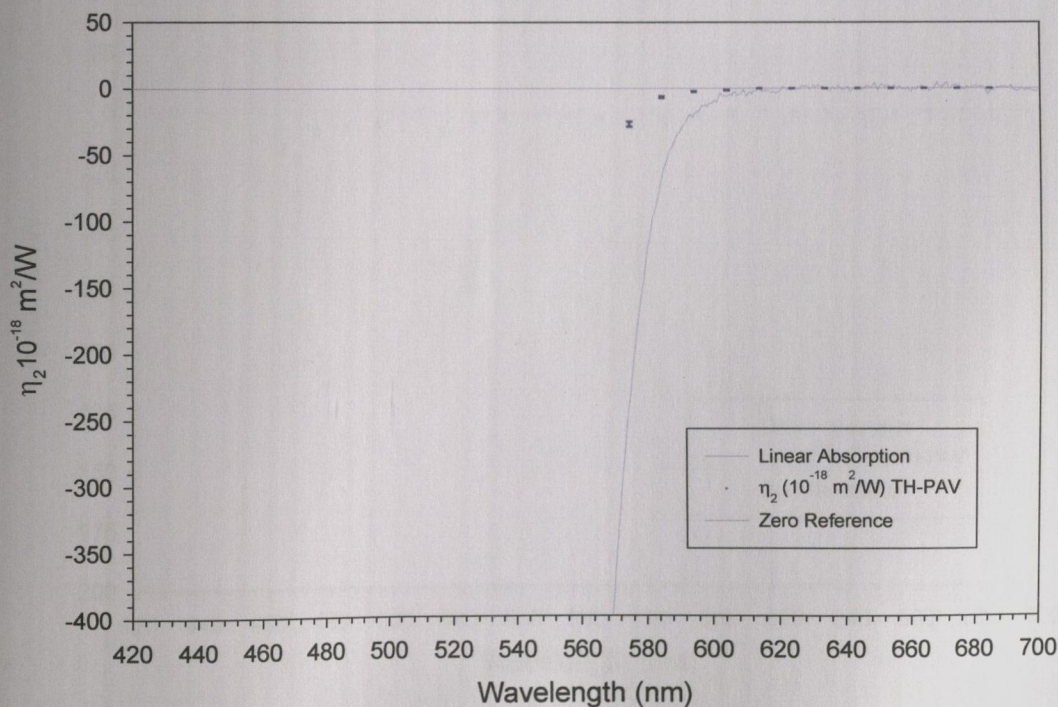


**Figure 6.2.2:** The dispersion of the real component  $\eta_2$  of  $\chi^{(3)}$  for 2.5 g/l Thienyl-PAV polymer Solution. The wavelength range is from 465nm to 685nm in 10nm steps and uses the values in Table 6.2.1. The linear absorption trend for Thienyl-PAV in solution is also included for comparison.

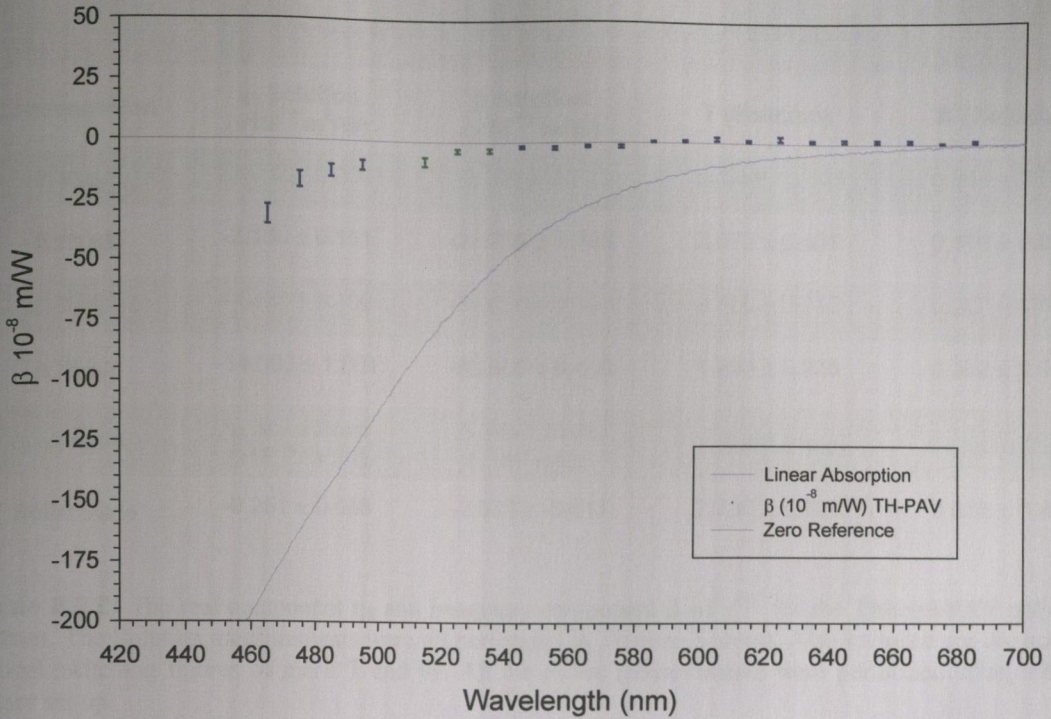


**Figure 6.2.3:** The dispersion of the imaginary component  $\beta$  of  $\chi^{(3)}$  for a 230nm thick **Thienyl-PAV Solid State polymer Film**. The wavelength range is from 465nm to 685nm in 10nm steps and uses the values in Table 6.2.1. The linear absorption trend for the same Solid State Film is also included for comparison.

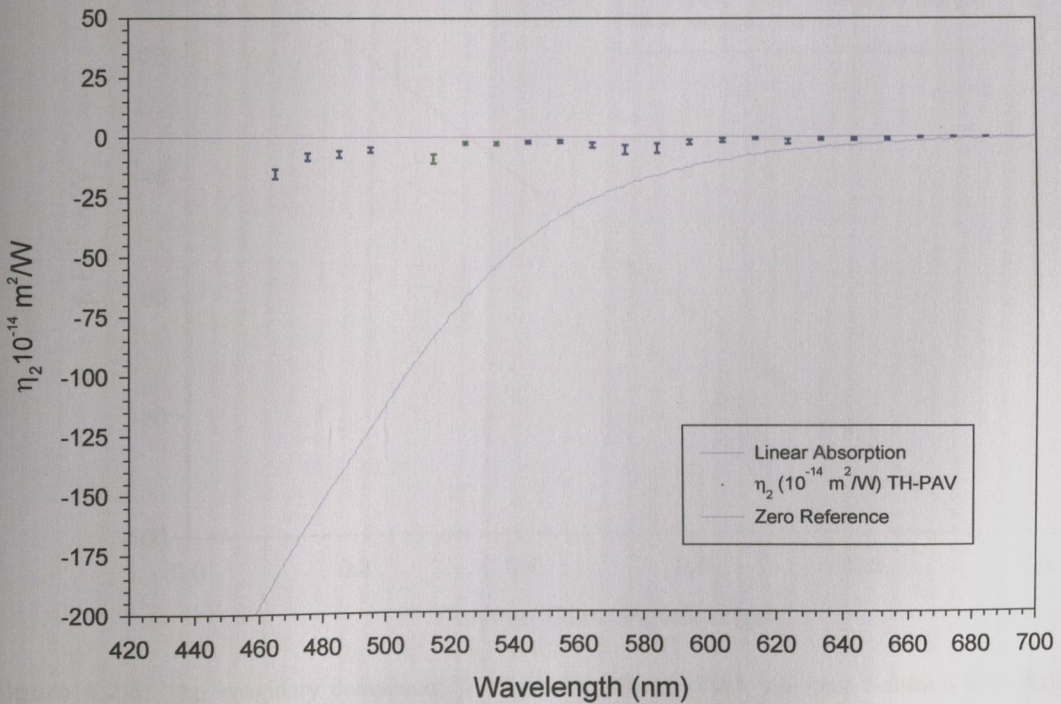


**Figure 6.2.4:** The dispersion of the real component  $\eta_2$  of  $\chi^{(3)}$  for a 230nm thick **Thienyl-PAV Solid State polymer Film**. The wavelength range is from 465nm to 685nm in 10nm steps and uses the values in Table 6.2.1. The linear absorption trend for the same Solid State Film is also included for comparison.

### Thienyl-PAV (YAG Laser 532nm)

Concentration	$\eta_2$ Solution ( $\times 10^{-18} \text{ m}^2/\text{W}$ )	$\beta$ Solution ( $\times 10^{-12} \text{ m/W}$ )	T (Solution)	W (Solution)
0.10 g/l	$-0.056 \pm 0.004$	$-9.130 \pm 0.730$	$43.368 \pm 6.505$	$0.012 \pm 0.002$
0.25 g/l	$-2.160 \pm 0.151$	$-21.700 \pm 1.736$	$2.672 \pm 0.401$	$0.178 \pm 0.023$
0.50 g/l	$-7.850 \pm 0.550$	$-51.300 \pm 4.104$	$2.100 \pm 0.315$	$0.267 \pm 0.035$
0.75 g/l	$-14.300 \pm 1.001$	$-80.500 \pm 6.440$	$1.497 \pm 0.225$	$0.392 \pm 0.051$
Description	$\eta_2$ Solid State ( $\times 10^{-14} \text{ m}^2/\text{W}$ )	$\beta$ Solid State ( $\times 10^{-8} \text{ m/W}$ )	T (Solid State)	W (Solid State)
Solid State	$-0.251 \pm 0.058$	$-2.570 \pm -0.617$	$2.730 \pm 1.283$	$0.633 \pm 0.247$

**Table 6.2.2:** The real component  $\eta_2$  and imaginary component  $\beta$  of  $\chi^{(3)}$  for the Thienyl-PAV polymer at 532nm. The Solution measurements were all performed in Toluene Solvent. Also included are the nonlinear optical switching figures of merit **T** and **W**. All the above measurements were performed using the YAG Laser set-up.

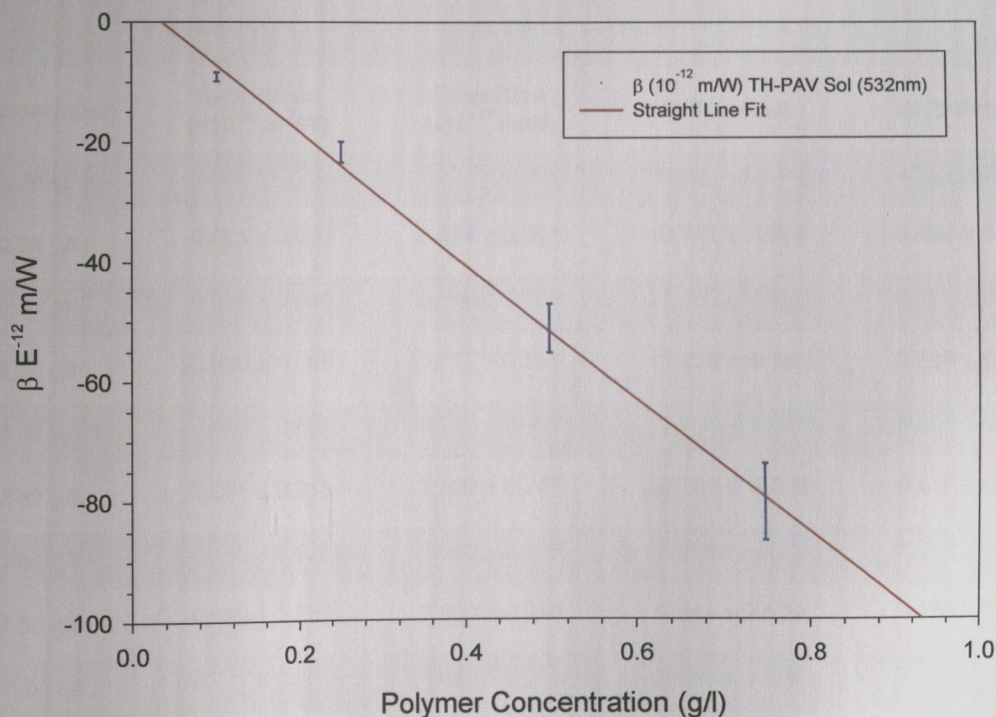


**Figure 6.2.5:** The imaginary component  $\beta$  of  $\chi^{(3)}$  for Thienyl-PAV polymer Solution as a function of solution concentration at 532nm. The solution concentration ranges from 0.10g/l up to 0.75g/l and uses the values in Table 6.2.2. Also included is a best straight line fit to all data points.



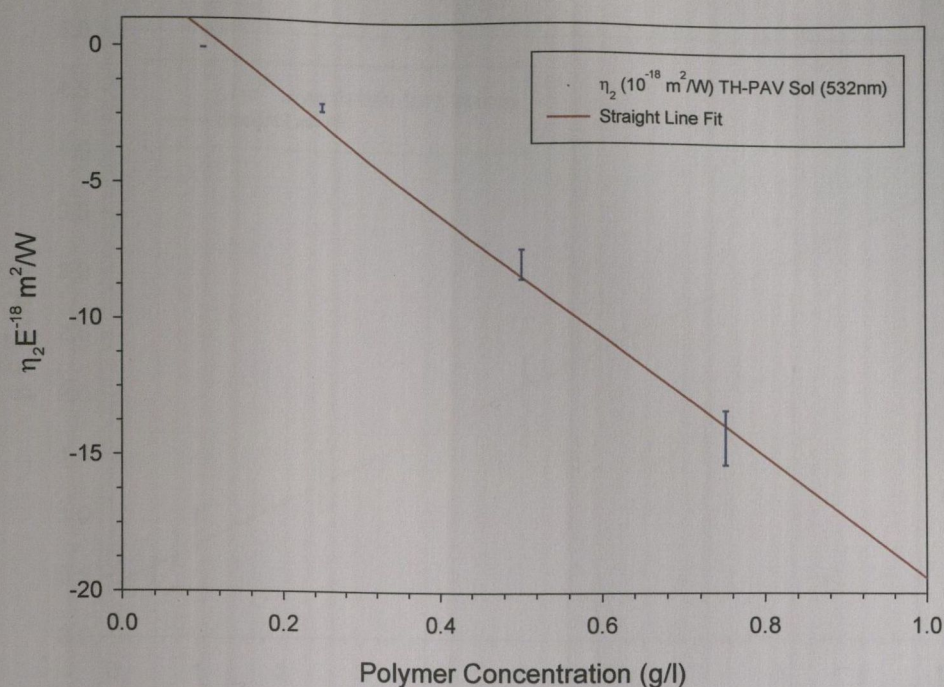


**Figure 6.2.6:** The real component  $\eta_2$  of  $\chi^{(3)}$  for Thienyl-PAV polymer Solution as a function of solution concentration at 532nm. The solution concentration ranges from 0.10g/l up to 0.75g/l and uses the values in Table 6.2.2. Also included is a best straight line fit to all data points.

### Thienyl-PAV (YAG Laser 1064nm)

Concentration	$\eta_2$ Solution ( $\times 10^{-18} \text{ m}^2/\text{W}$ )	$\beta$ Solution ( $\times 10^{-12} \text{ m/W}$ )	T (Solution)	W (Solution)
0.10 g/l	$-0.009 \pm 0.002$	$0.557 \pm 0.106$	$32.925 \pm 12.182$	$0.513 \pm 0.180$
0.25 g/l	$-0.021 \pm 0.003$	$0.424 \pm 0.081$	$10.741 \pm 3.974$	$0.402 \pm 0.141$
0.50 g/l	$-0.025 \pm 0.005$	$0.549 \pm 0.105$	$11.683 \pm 4.323$	$0.291 \pm 0.102$
0.75 g/l	$-0.039 \pm 0.006$	$0.717 \pm 0.136$	$11.219 \pm 4.151$	$0.256 \pm 0.090$
1.00 g/l	$-0.043 \pm 0.007$	$0.890 \pm 0.169$	$11.011 \pm 4.074$	$0.344 \pm 0.120$
2.50 g/l	$-0.071 \pm 0.013$	$1.300 \pm 0.247$	$13.600 \pm 5.032$	$0.116 \pm 0.041$
5.00 g/l	$-0.139 \pm 0.025$	$1.990 \pm 0.378$	$7.616 \pm 2.818$	$0.158 \pm 0.055$
7.50 g/l	$-0.199 \pm 0.036$	$2.560 \pm 0.486$	$6.844 \pm 2.532$	$0.150 \pm 0.053$
10.00 g/l	$-0.337 \pm 0.061$	$4.090 \pm 0.777$	$6.460 \pm 2.390$	$0.192 \pm 0.067$
Description	$\eta_2$ Solid State ( $\times 10^{-14} \text{ m}^2/\text{W}$ )	$\beta$ Solid State ( $\times 10^{-8} \text{ m/W}$ )	T (Solid State)	W (Solid State)
Solid State	$-0.064 \pm 0.032$	$0.190 \pm 0.095$	$1.570 \pm 1.178$	$1.420 \pm 1.065$

**Table 6.2.3:** The real component  $\eta_2$  and imaginary component  $\beta$  of  $\chi^{(3)}$  for the Thienyl-PAV polymer at 1064nm. The Solution measurements were all performed in Toluene Solvent. Also included are the nonlinear optical switching figures of merit **T** and **W**. All the above measurements were performed using the YAG Laser set-up.

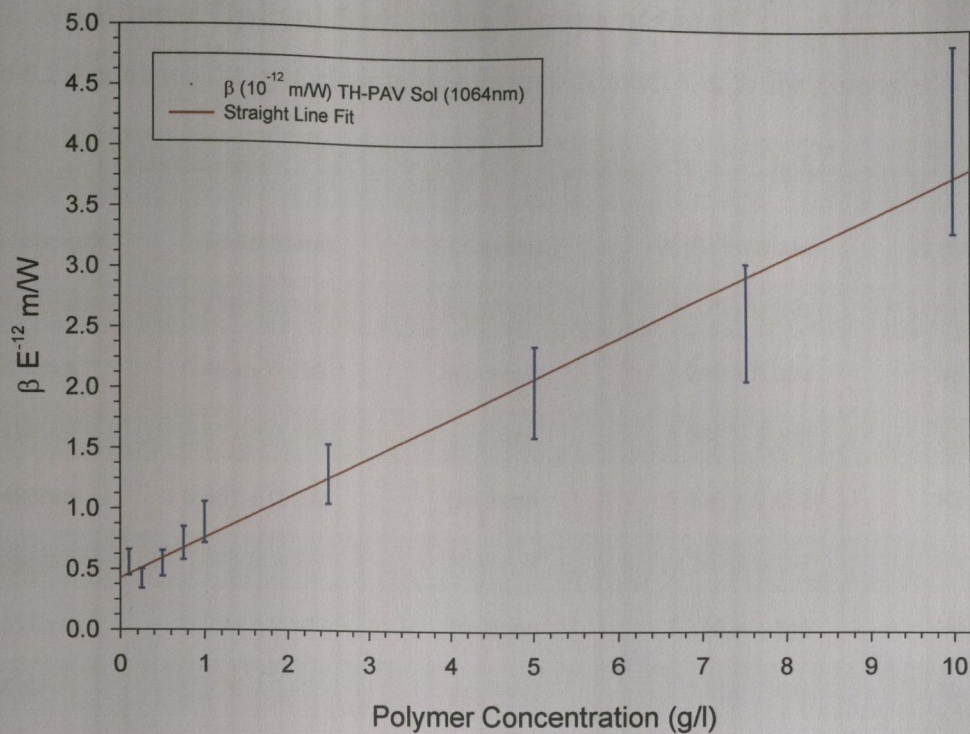


**Figure 6.2.7:** The imaginary component  $\beta$  of  $\chi^{(3)}$  for Thienyl-PAV polymer Solution as a function of solution concentration at 1064nm. The solution concentration ranges from 0.10g/l up to 10.00g/l and uses the values in Table 6.2.3. Also included is a best straight line fit to all data points.

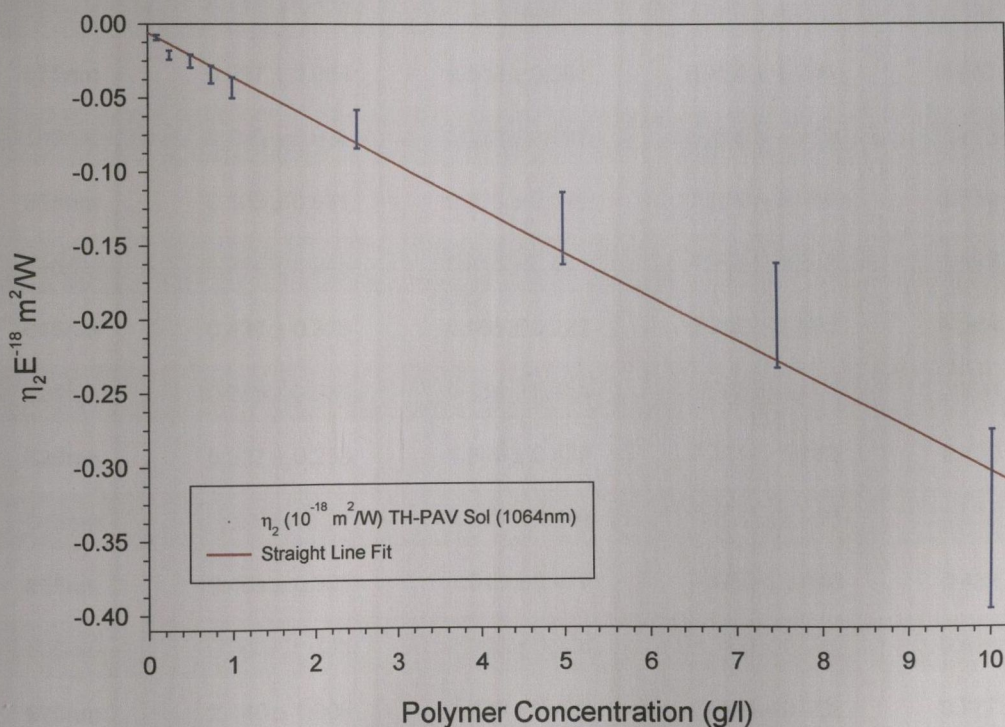


**Figure 6.2.8:** The real component  $\eta_2$  of  $\chi^{(3)}$  for Thienyl-PAV polymer Solution as a function of solution concentration at 1064nm. The solution concentration ranges from 0.10g/l up to 10.00g/l and uses the values in Table 6.2.3. Also included is a best straight line fit to all data points.

## 6.2.2 Nonlinear Optical Switching Figure of Merit

Table 6.2.4 contains the optical switching figures of merit **T** & **W** for Thienyl-PAV.

<b>Thienyl-PAV (DYE Laser 465-685nm)</b>				
<b>Wavelength</b>	<b>T (Solid State)</b>	<b>T (Solution)</b>	<b>W (Solid State)</b>	<b>W (Solution)</b>
465nm	0.475 ± 0.124	No Scan	1.280 ± 0.230	No Scan
475nm	0.484 ± 0.189	No Scan	1.240 ± 0.384	No Scan
485nm	0.431 ± 0.168	No Scan	1.250 ± 0.388	No Scan
495nm	0.467 ± 0.192	No Scan	1.430 ± 0.458	No Scan
505nm	No Scan	No Scan	No Scan	No Scan
515nm	0.234 ± 0.102	No Scan	7.270 ± 2.545	No Scan
525nm	0.375 ± 0.170	No Scan	2.110 ± 0.781	No Scan
535nm	0.329 ± 0.162	No Scan	3.927 ± 1.610	No Scan
545nm	0.236 ± 0.125	No Scan	1.980 ± 0.891	No Scan
555nm	0.309 ± 0.176	No Scan	2.300 ± 1.127	No Scan
565nm	0.121 ± 0.079	No Scan	7.440 ± 4.241	No Scan
575nm	0.087 ± 0.064	0.542 ± 0.081	6.450 ± 4.193	0.430 ± 0.056
585nm	0.048 ± 0.036	0.132 ± 0.022	6.305 ± 4.729	0.470 ± 0.070
595nm	0.108 ± 0.081	0.823 ± 0.140	7.810 ± 5.858	0.619 ± 0.093
605nm	0.326 ± 0.245	0.814 ± 0.171	4.290 ± 3.218	0.387 ± 0.074
615nm	0.437 ± 0.328	0.965 ± 0.222	2.740 ± 2.055	0.364 ± 0.076
625nm	0.315 ± 0.236	0.934 ± 0.224	12.100 ± 9.075	0.524 ± 0.115
635nm	0.337 ± 0.253	1.590 ± 0.429	7.270 ± 5.453	0.429 ± 0.107
645nm	0.369 ± 0.277	1.530 ± 0.444	8.330 ± 6.248	0.531 ± 0.143
655nm	0.401 ± 0.301	1.540 ± 0.477	7.520 ± 5.640	0.482 ± 0.140
665nm	0.980 ± 0.735	0.982 ± 0.324	2.700 ± 2.025	0.424 ± 0.131
675nm	2.140 ± 1.605	1.230 ± 0.431	0.945 ± 0.709	0.777 ± 0.256
685nm	8.410 ± 6.308	1.230 ± 0.455	0.402 ± 0.302	0.474 ± 0.166

**Table 6.2.4:** The non-linear optical switching figures of merit **T** and **W** for the Thienyl-PAV polymer. The Solution measurements were all performed on a concentration of 2.5 g/l of the polymer in Toluene Solvent. All the above measurements were performed using the Nitrogen pumped DYE Laser set-up.

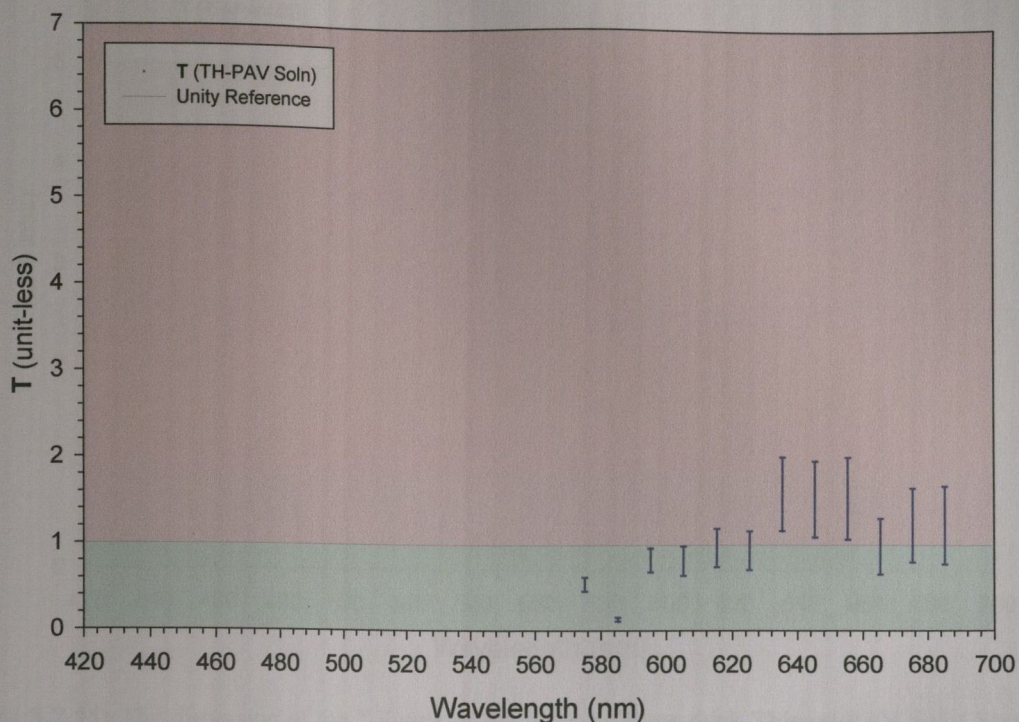


**Figure 6.2.9:** The dispersion of the **T** Figure of Merit for 2.5 g/l **Thienyl-PAV** polymer **Solution**. The wavelength range is from 465nm to 685nm in 10nm steps and uses the values in Table 6.2.4. The graph is colour coded - green where **T** is favourable and red where **T** is unfavourable for all optical switching.

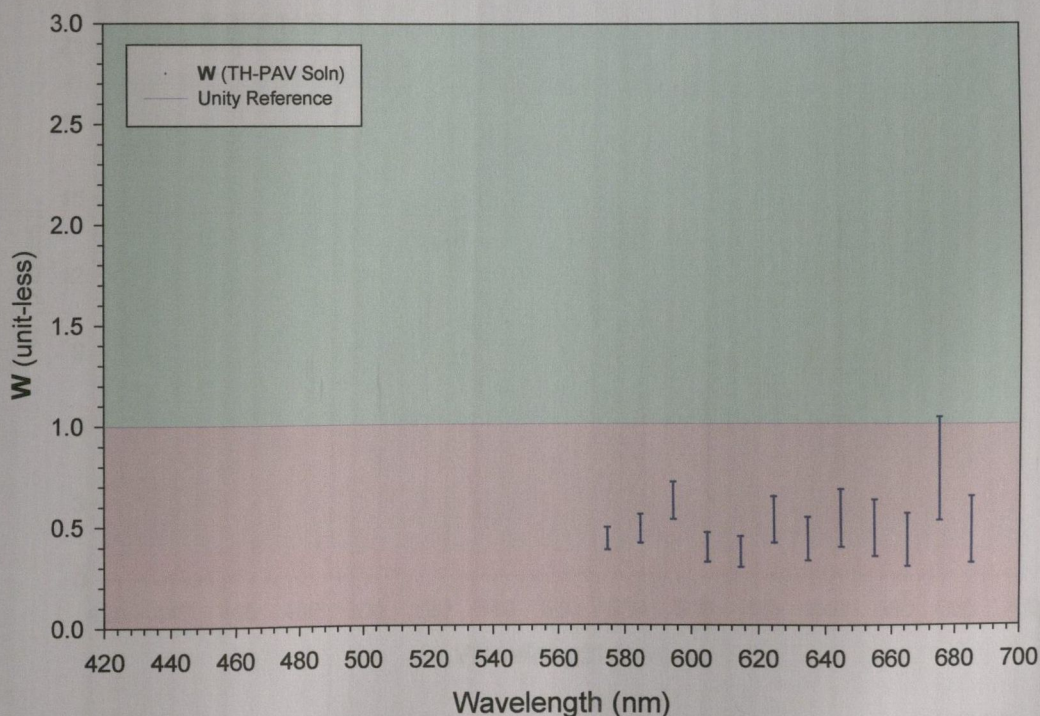


**Figure 6.2.10:** The dispersion of the **W** Figure of Merit for 2.5 g/l **Thienyl-PAV** polymer **Solution**. The wavelength range is from 465nm to 685nm in 10nm steps and uses the values in Table 6.2.4. The graph is colour coded - green where **W** is favourable and red where **W** is unfavourable for all optical switching.

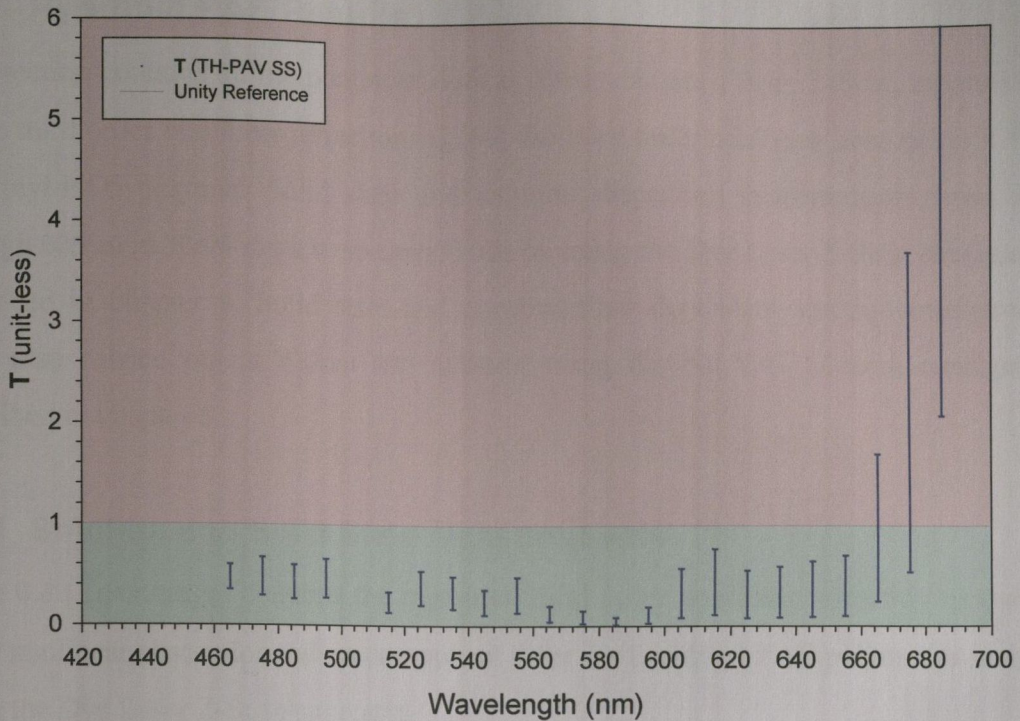


**Figure 6.2.11:** The dispersion of the **T** Figure of Merit for a 230nm thick **Thienyl-PAV Solid State Film**. The wavelength range is from 465nm to 685nm and uses the values in Table 6.2.4. The graph is colour coded - green where **T** is favourable and red where **T** is unfavourable for all optical switching.

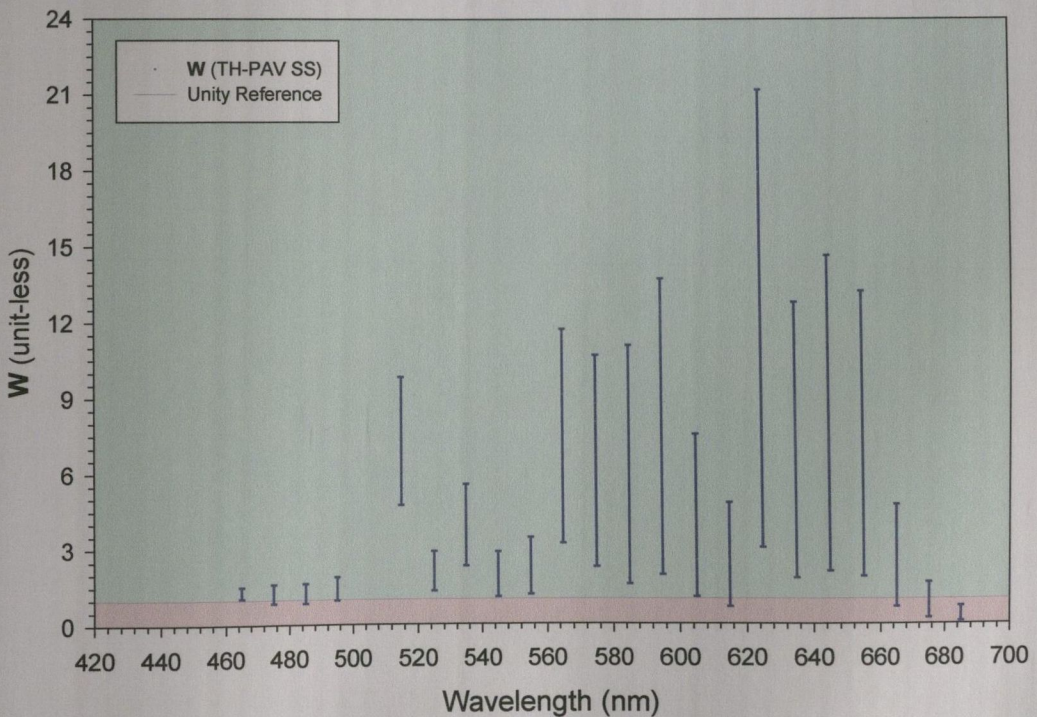


**Figure 6.2.12:** The dispersion of the **W** Figure of Merit for a 230nm thick **Thienyl-PAV Solid State Film**. The wavelength range is from 465nm to 685nm and uses the values in Table 6.2.4. The graph is colour coded - green where **W** is favourable and red where **W** is unfavourable for all optical switching.

### 6.3 Pyridinyl PAE Results

This section contains all the nonlinear optical results obtained from Z-Scan measurements of the third order nonlinear refraction  $\eta_2$ , and the third order nonlinear absorption  $\beta$  for the Pyridinyl-PAE polymer. Solid state and solution dispersion measurements from 465nm through 685nm in 10nm steps were carried out on using the Dye Laser Z-Scan configuration described in chapter 5. Solid state and concentration dependent solution measurements were also carried out at 532nm and 1064nm using the Nd:YAG Z-Scan configuration described in chapter 5.

#### 6.3.1 Solution and Solid State Measurements

Table 6.3.1 (next page) contains the measured third order nonlinear refraction  $\eta_2$  and third order nonlinear absorption values component  $\beta$  for the Pyridinyl-PAE polymer as measured using the Dye Laser Z-Scan apparatus.

### Pyridinyl-PAE (DYE Laser 465-685nm)

Wavelength	$\eta_2$ Solid State ( $\times 10^{-14} \text{ m}^2/\text{W}$ )	$\eta_2$ Solution ( $\times 10^{-18} \text{ m}^2/\text{W}$ )	$\beta$ Solid State ( $\times 10^{-8} \text{ m/W}$ )	$\beta$ Solution ( $\times 10^{-12} \text{ m/W}$ )
465nm	$-12.200 \pm 1.586$	$-59.100 \pm 4.137$	$-74.400 \pm 10.416$	$-64.000 \pm 5.120$
475nm	$-11.600 \pm 2.436$	$-32.800 \pm 2.296$	$-34.700 \pm 7.634$	$43.300 \pm 3.660$
485nm	$-11.600 \pm 2.784$	$-17.000 \pm 1.190$	$-23.200 \pm 5.800$	$57.560 \pm 4.870$
495nm	$-8.190 \pm 2.129$	$-6.530 \pm 0.457$	$-14.400 \pm 3.888$	$55.360 \pm 4.680$
505nm	$-7.980 \pm 2.234$	$-3.310 \pm 0.232$	$-8.390 \pm 2.433$	$54.430 \pm 4.600$
515nm	$-7.030 \pm 2.039$	$-3.120 \pm 0.218$	$-12.110 \pm 3.633$	$44.600 \pm 3.770$
525nm	$-3.280 \pm 1.017$	$-2.780 \pm 0.222$	$-4.326 \pm 1.384$	$28.500 \pm 2.410$
535nm	$-3.820 \pm 1.222$	$-2.080 \pm 0.166$	$-3.182 \pm 1.050$	$26.100 \pm 2.210$
545nm	$-3.670 \pm 1.211$	$-1.490 \pm 0.119$	$-4.090 \pm 1.391$	$9.860 \pm 0.887$
555nm	$-4.930 \pm 1.676$	$-1.100 \pm 0.088$	$-3.130 \pm 1.096$	$9.170 \pm 0.825$
565nm	$-2.980 \pm 1.043$	$-1.240 \pm 0.112$	$-4.240 \pm 1.526$	$17.300 \pm 1.730$
575nm	$-1.640 \pm 0.590$	$-1.180 \pm 0.106$	$-4.340 \pm 1.606$	$14.500 \pm 1.450$
585nm	$-1.200 \pm 0.444$	$-1.040 \pm 0.095$	$-1.880 \pm 0.714$	$8.220 \pm 0.822$
595nm	$-3.940 \pm 1.537$	$-1.000 \pm 0.100$	$-2.490 \pm 0.996$	$5.780 \pm 0.636$
605nm	$-1.830 \pm 0.714$	$-0.891 \pm 0.089$	$-2.990 \pm 1.196$	$3.100 \pm 0.341$
615nm	$-2.730 \pm 1.119$	$-0.673 \pm 0.065$	$-3.680 \pm 1.546$	$2.690 \pm 0.323$
625nm	$-3.050 \pm 1.281$	$-0.778 \pm 0.086$	$-3.950 \pm 1.699$	$3.020 \pm 0.362$
635nm	$-3.640 \pm 1.565$	$-0.954 \pm 0.114$	$-4.010 \pm 1.764$	$5.450 \pm 0.654$
645nm	$-2.780 \pm 1.223$	$-0.830 \pm 0.100$	$-4.460 \pm 2.007$	$6.040 \pm 0.785$
655nm	$-1.130 \pm 0.508$	$-0.780 \pm 0.090$	$-3.700 \pm 1.702$	$5.360 \pm 0.697$
665nm	$-2.540 \pm 1.168$	$-0.730 \pm 0.100$	$-3.890 \pm 1.789$	$6.430 \pm 0.900$
675nm	$-0.940 \pm 0.460$	$-0.780 \pm 0.100$	$-1.890 \pm 0.945$	$6.220 \pm 0.871$
685nm	$-0.740 \pm 0.370$	$-0.690 \pm 0.100$	$-0.390 \pm 0.190$	$8.380 \pm 1.257$

**Table 6.3.1:** The real component  $\eta_2$  and imaginary component  $\beta$  of  $\chi^{(3)}$  for the Pyridinyl-PAE polymer. The Solution measurements were all performed on a concentration of 2.5 g/l of the polymer in Toluene Solvent. All the above measurements were performed using the Nitrogen pumped DYE Laser set-up.

Figures 6.3.1 through 6.3.4 below show the above data in graphical format. Each Figure also shows the linear absorption spectrum for Pyridinyl-PAE to help facilitate trend correlation.

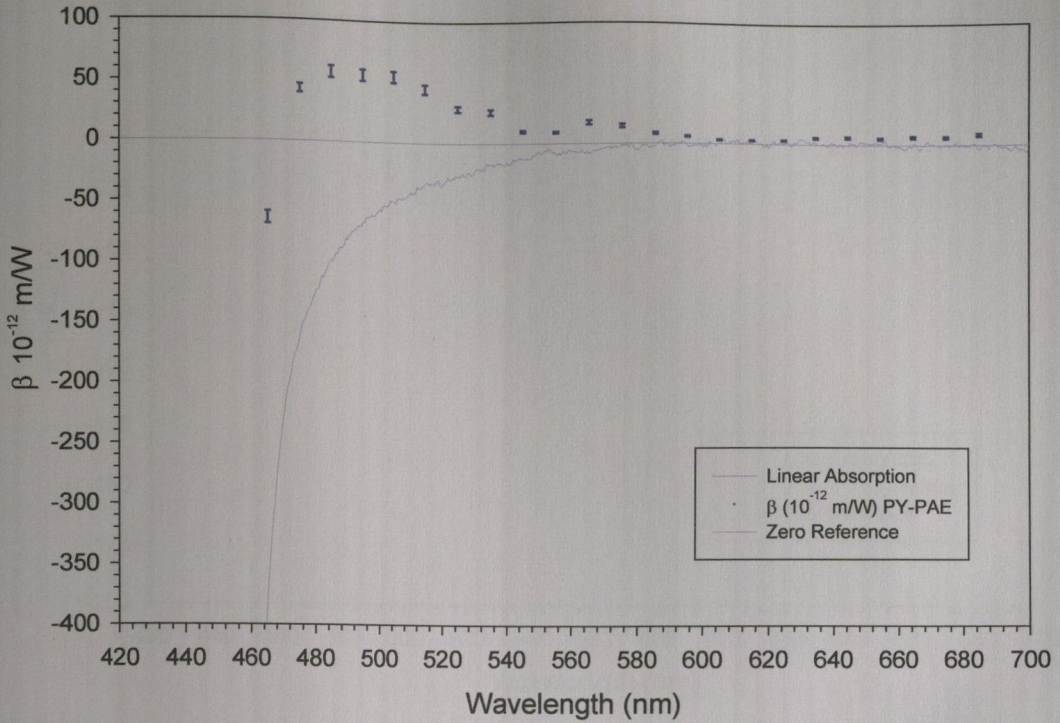


**Figure 6.3.1:** The dispersion of the imaginary component  $\beta$  of  $\chi^{(3)}$  for 2.5 g/l Pyridinyl-PAE polymer Solution. The wavelength range is from 465nm to 685nm in 10nm steps and uses the values in Table 6.3.1. The linear absorption trend for Pyridinyl-PAE in solution is also included for comparison.

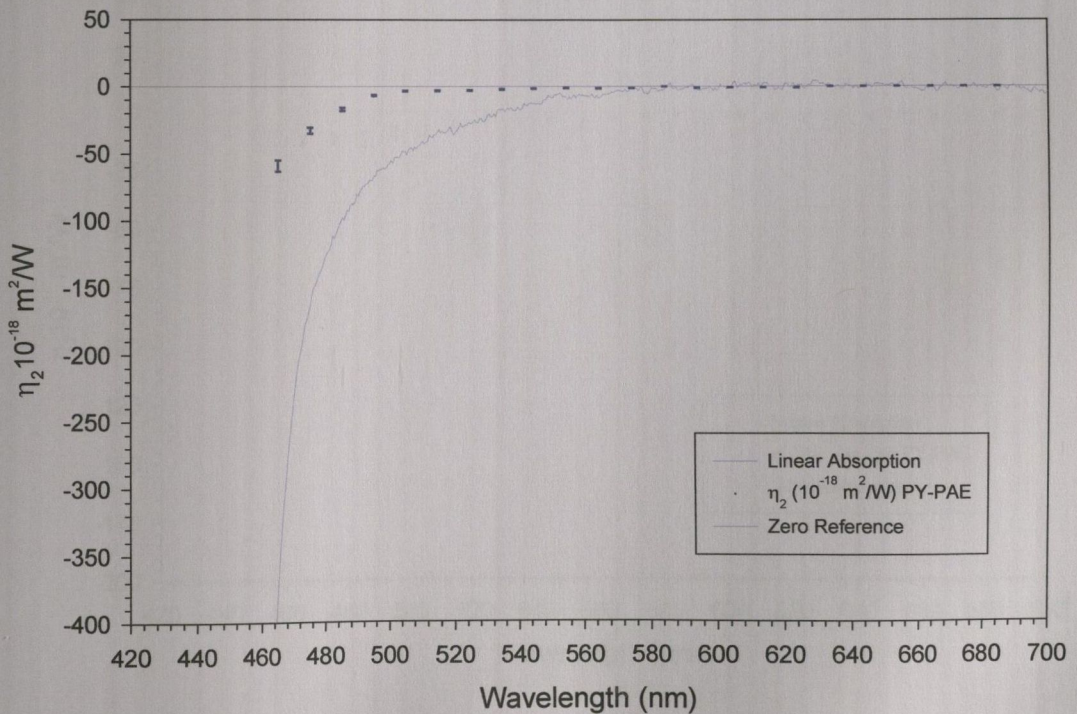


**Figure 6.3.2:** The dispersion of the real component  $\eta_2$  of  $\chi^{(3)}$  for 2.5 g/l Pyridinyl-PAE polymer Solution. The wavelength range is from 465nm to 685nm in 10nm steps and uses the values in Table 6.3.1. The linear absorption trend for Pyridinyl-PAE in solution is also included for comparison.



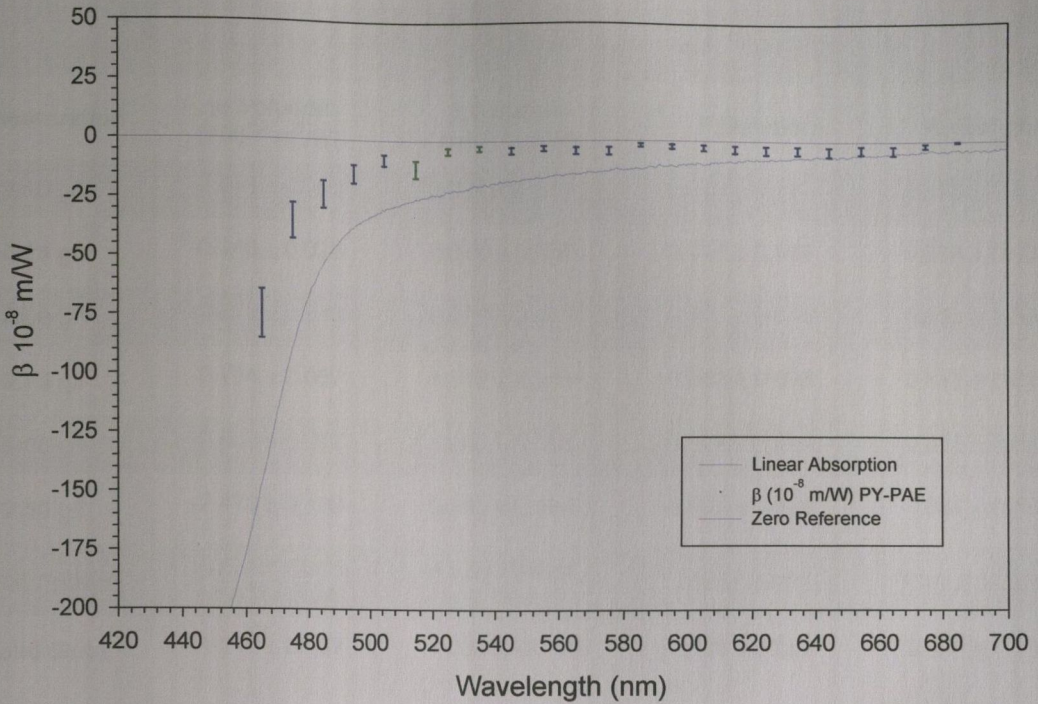


**Figure 6.3.3:** The dispersion of the imaginary component  $\beta$  of  $\chi^{(3)}$  for a 75nm thick Pyridinyl-PAE Solid State polymer Film. The wavelength range is from 465nm to 685nm in 10nm steps and uses the values in Table 6.3.1. The linear absorption trend for the same Solid State Film is also included for comparison.

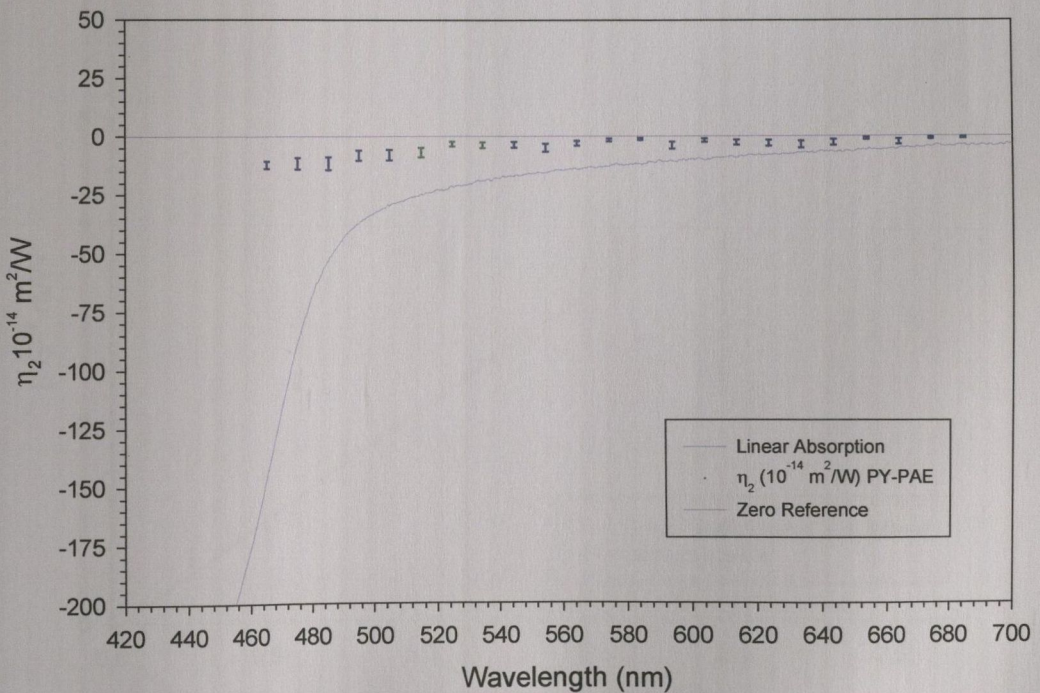


**Figure 6.3.4:** The dispersion of the real component  $\eta_2$  of  $\chi^{(3)}$  for a 75nm thick Pyridinyl-PAE Solid State polymer Film. The wavelength range is from 465nm to 685nm in 10nm steps and uses the values in Table 6.3.1. The linear absorption trend for the same Solid State Film is also included for comparison.

### Pyridinyl-PAE (YAG Laser 532nm)

Concentration	$\eta_2$ Solution ( $\times 10^{-18} \text{ m}^2/\text{W}$ )	$\beta$ Solution ( $\times 10^{-12} \text{ m/W}$ )	T (Solution)	W (Solution)
0.10 g/l	$-0.081 \pm 0.006$	$0.204 \pm 0.018$	$0.670 \pm 0.114$	$0.559 \pm 0.084$
0.25 g/l	$-0.246 \pm 0.020$	$0.648 \pm 0.058$	$0.701 \pm 0.119$	$0.678 \pm 0.102$
0.50 g/l	$-0.471 \pm 0.038$	$0.877 \pm 0.079$	$0.494 \pm 0.084$	$0.650 \pm 0.098$
0.75 g/l	$-0.714 \pm 0.057$	$1.510 \pm 0.136$	$0.563 \pm 0.096$	$0.657 \pm 0.099$
1.00 g/l	$-0.900 \pm 0.072$	$1.960 \pm 0.176$	$0.579 \pm 0.099$	$0.620 \pm 0.093$
2.50 g/l	$-2.470 \pm 0.198$	$5.380 \pm 0.484$	$0.581 \pm 0.099$	$0.681 \pm 0.102$
Description	$\eta_2$ Solid State ( $\times 10^{-14} \text{ m}^2/\text{W}$ )	$\beta$ Solid State ( $\times 10^{-8} \text{ m/W}$ )	T (Solid State)	W (Solid State)
Solid State	$-1.210 \pm 0.387$	$-1.780 \pm -0.570$	$0.393 \pm 0.252$	$2.070 \pm 1.180$

**Table 6.3.2:** The real component  $\eta_2$  and imaginary component  $\beta$  of  $\chi^{(3)}$  for the **Pyridinyl-PAE** polymer at **532nm**. The Solution measurements were all performed in Toluene Solvent. Also included are the nonlinear optical switching figures of merit **T** and **W**. All the above measurements were performed using the **YAG Laser** set-up.

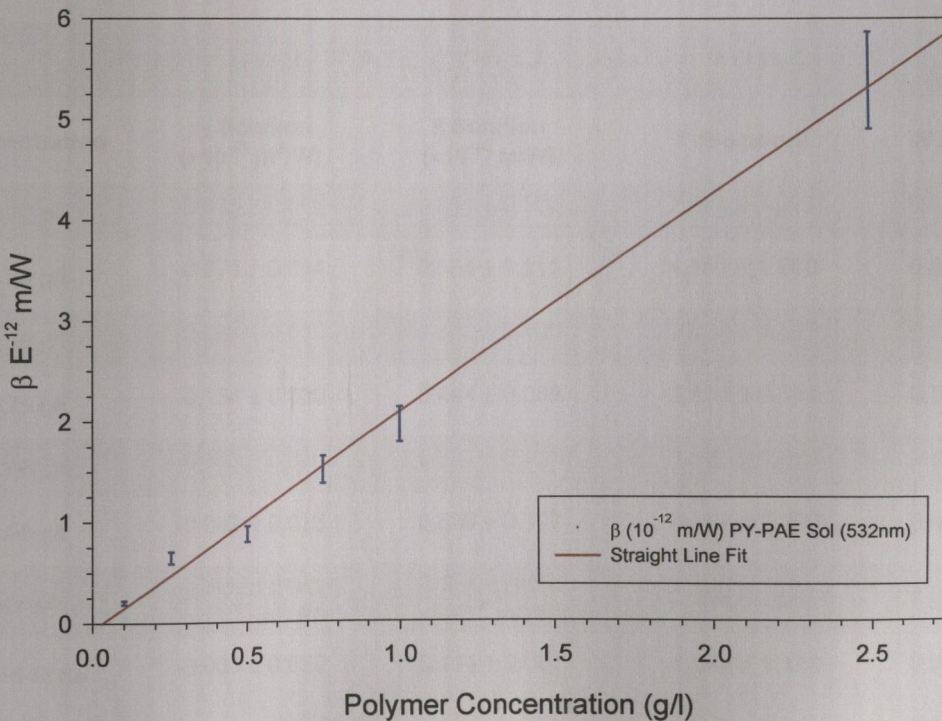


**Figure 6.3.5:** The imaginary component  $\beta$  of  $\chi^{(3)}$  for **Pyridinyl-PAE** polymer **Solution** as a function of solution concentration at **532nm**. The solution concentration ranges from **0.10g/l** up to **2.50g/l** and uses the values in Table 6.3.2. Also included is a best straight line fit to all data points.

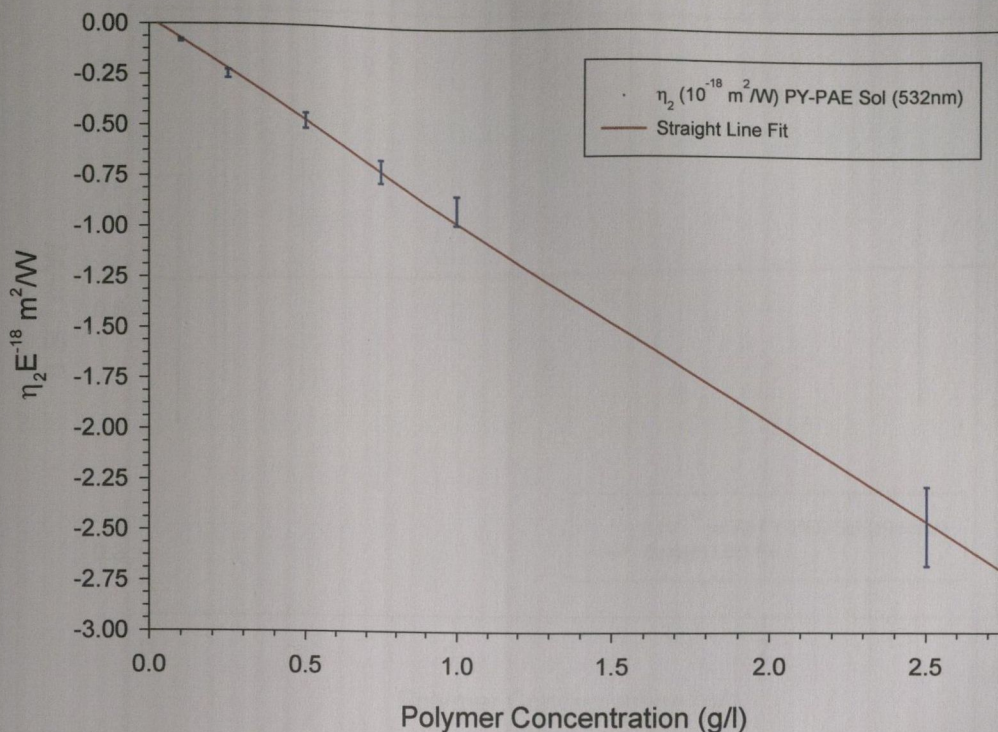


**Figure 6.3.6:** The real component  $\eta_2$  of  $\chi^{(3)}$  for Pyridinyl-PAE polymer Solution as a function of solution concentration at 532nm. The solution concentration ranges from 0.10g/l up to 2.50g/l and uses the values in Table 6.3.2. Also included is a best straight line fit to all data points.

### Pyridinyl-PAE (YAG Laser 1064nm)

Concentration	$\eta_2$ Solution ( $\times 10^{-18} \text{ m}^2/\text{W}$ )	$\beta$ Solution ( $\times 10^{-12} \text{ m/W}$ )	T (Solution)	W (Solution)
0.10 g/l	-0.036 ± 0.008	0.511 ± 0.102	7.554 ± 3.021	0.997 ± 0.379
0.25 g/l	-0.071 ± 0.014	0.554 ± 0.111	4.151 ± 1.660	0.806 ± 0.306
0.50 g/l	-0.094 ± 0.019	0.542 ± 0.106	3.068 ± 1.227	0.533 ± 0.203
0.75 g/l	-0.154 ± 0.030	0.444 ± 0.089	1.534 ± 0.614	0.583 ± 0.222
1.00 g/l	-0.143 ± 0.028	0.601 ± 0.120	2.236 ± 0.894	0.400 ± 0.152
2.50 g/l	-0.382 ± 0.076	0.536 ± 0.107	0.747 ± 0.299	0.433 ± 0.165
Description	$\eta_2$ Solid State ( $\times 10^{-14} \text{ m}^2/\text{W}$ )	$\beta$ Solid State ( $\times 10^{-8} \text{ m/W}$ )	T (Solid State)	W (Solid State)
Solid State	-0.039 ± 0.020	0.114 ± 0.057	1.544 ± 1.158	0.057 ± 0.043

**Table 6.3.3:** The real component  $\eta_2$  and imaginary component  $\beta$  of  $\chi^{(3)}$  for the Pyridinyl-PAE polymer at 1064nm. The Solution measurements were all performed in Toluene Solvent. Also included are the nonlinear optical switching figures of merit **T** and **W**. All the above measurements were performed using the YAG Laser set-up.

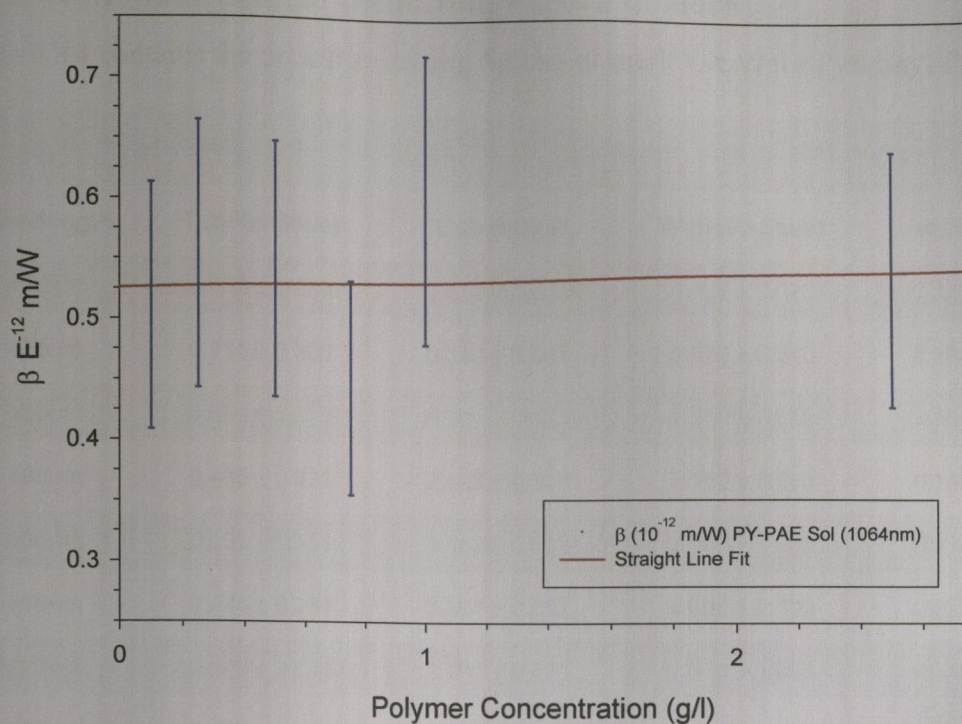


**Figure 6.3.7:** The imaginary component  $\beta$  of  $\chi^{(3)}$  for Pyridinyl-PAE polymer Solution as a function of solution concentration at 1064nm. The solution concentration ranges from 0.10g/l up to 2.50g/l and uses the values in Table 6.3.3. Also included is a best straight line fit to all data points.

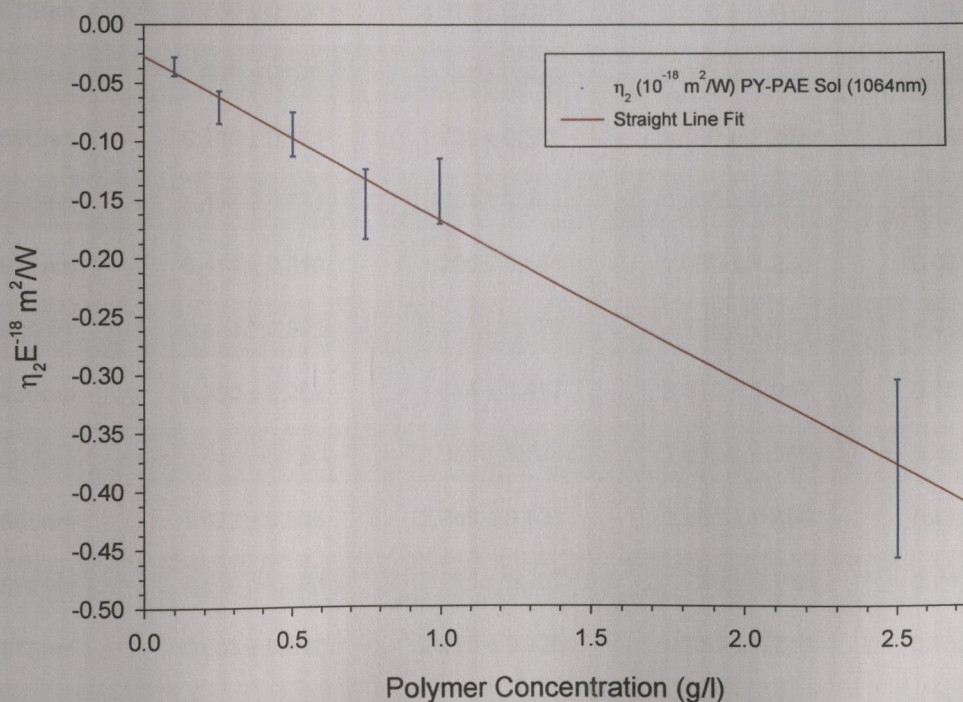


**Figure 6.3.8:** The real component  $\eta_2$  of  $\chi^{(3)}$  for Pyridinyl-PAE polymer Solution as a function of solution concentration at 1064nm. The solution concentration ranges from 0.10g/l up to 2.50g/l and uses the values in Table 6.3.3. Also included is a best straight line fit to all data points.

### 6.3.2 Nonlinear Optical Switching Figure of Merit

Table 6.3.4 contains the optical switching figures of merit **T** & **W** for Pyridinyl-PAE.

<b>Pyridinyl-PAE (DYE Laser 465-685nm)</b>				
<b>Wavelength</b>	<b>T (Solid State)</b>	<b>T (Solution)</b>	<b>W (Solid State)</b>	<b>W (Solution)</b>
465nm	1.420 ± 0.383	0.252 ± 0.038	0.399 ± 0.076	0.125 ± 0.016
475nm	0.711 ± 0.306	0.313 ± 0.047	0.972 ± 0.340	0.264 ± 0.034
485nm	0.684 ± 0.335	0.821 ± 0.123	1.550 ± 0.635	0.254 ± 0.033
495nm	0.435 ± 0.231	2.098 ± 0.314	1.950 ± 0.878	0.187 ± 0.024
505nm	0.265 ± 0.151	4.152 ± 0.622	3.800 ± 1.862	0.213 ± 0.028
515nm	0.444 ± 0.261	3.681 ± 0.552	4.690 ± 2.392	0.323 ± 0.042
525nm	0.346 ± 0.218	2.691 ± 0.404	1.970 ± 1.083	0.310 ± 0.047
535nm	0.170 ± 0.111	3.356 ± 0.503	2.120 ± 1.208	0.433 ± 0.065
545nm	0.303 ± 0.203	1.890 ± 0.321	1.820 ± 1.074	0.203 ± 0.030
555nm	0.176 ± 0.121	2.320 ± 0.394	2.640 ± 1.610	0.196 ± 0.029
565nm	0.402 ± 0.285	3.930 ± 0.707	2.420 ± 1.525	0.392 ± 0.067
575nm	0.760 ± 0.555	3.610 ± 0.686	0.616 ± 0.400	0.193 ± 0.033
585nm	0.495 ± 0.371	2.312 ± 0.439	0.663 ± 0.444	0.308 ± 0.053
595nm	0.188 ± 0.141	1.720 ± 0.361	3.190 ± 2.265	0.446 ± 0.085
605nm	0.495 ± 0.371	1.053 ± 0.221	0.908 ± 0.645	0.271 ± 0.049
615nm	0.414 ± 0.310	1.229 ± 0.184	1.630 ± 1.223	0.031 ± 0.004
625nm	0.404 ± 0.303	1.212 ± 0.279	2.150 ± 1.612	0.401 ± 0.084
635nm	0.350 ± 0.262	1.814 ± 0.417	2.610 ± 1.957	0.536 ± 0.114
645nm	0.518 ± 0.389	2.350 ± 0.564	1.810 ± 1.358	0.461 ± 0.101
655nm	1.072 ± 0.804	2.240 ± 0.538	0.661 ± 0.496	0.412 ± 0.091
665nm	0.510 ± 0.383	2.913 ± 0.787	1.290 ± 0.968	0.340 ± 0.085
675nm	0.683 ± 0.512	2.690 ± 0.726	0.951 ± 0.713	0.750 ± 0.188
685nm	0.179 ± 0.134	4.140 ± 1.201	0.494 ± 0.371	0.435 ± 0.117

**Table 6.3.4:** The nonlinear optical switching figures of merit **T** and **W** for the Pyridinyl-PAE polymer. The Solution measurements were all performed on a concentration of 2.5 g/l of the polymer in Toluene Solvent. All the above measurements were performed using the Nitrogen pumped DYE Laser set-up.

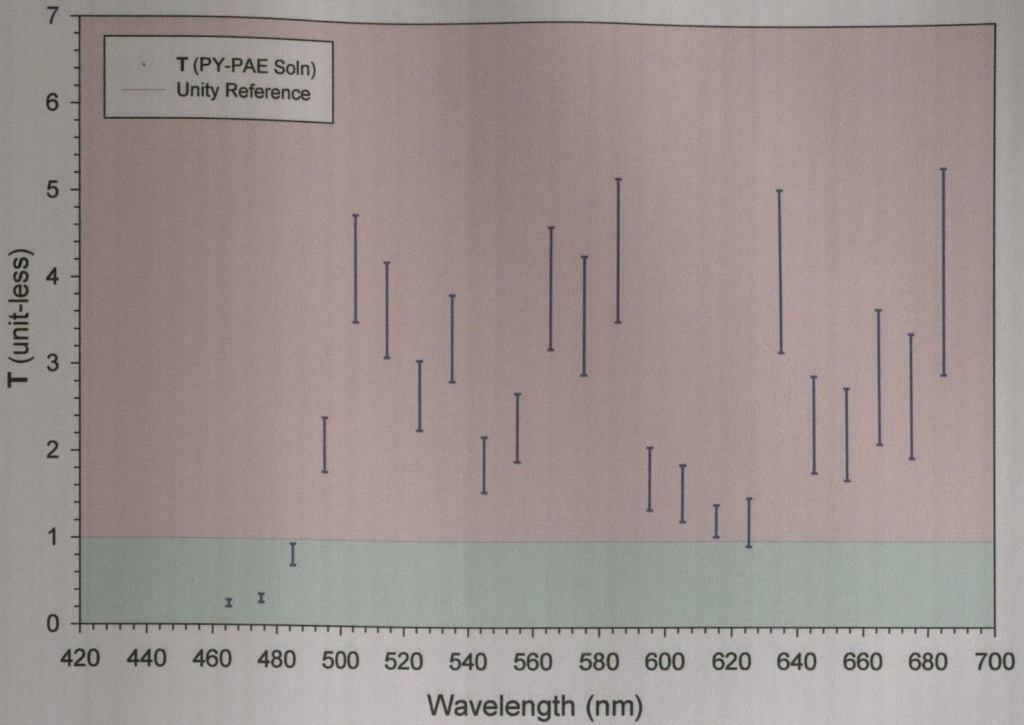


**Figure 6.3.9:** The dispersion of the **T** Figure of Merit for 2.5 g/l **Pyridinyl-PAE** polymer **Solution**. The wavelength range is from 465nm to 685nm in 10nm steps and uses the values in Table 6.3.4. The graph is colour coded - green where **T** is favourable and red where **T** is unfavourable for all optical switching.

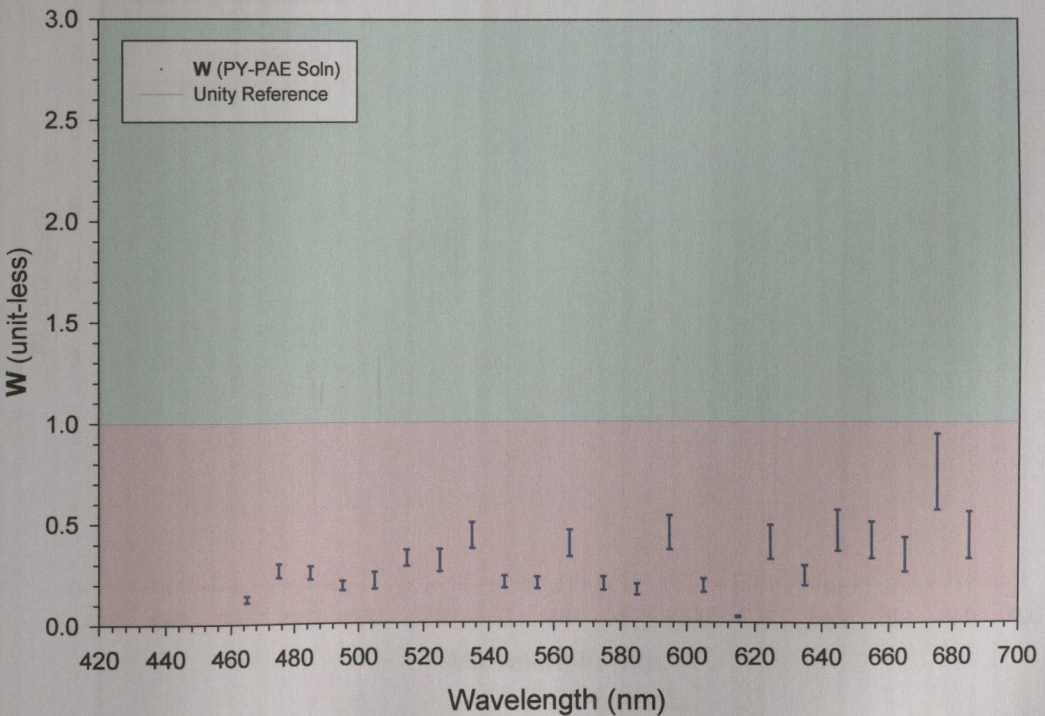


**Figure 6.3.10:** The dispersion of the **W** Figure of Merit for 2.5 g/l **Pyridinyl-PAE** polymer **Solution**. The wavelength range is from 465nm to 685nm in 10nm steps and uses the values in Table 6.3.4. The graph is colour coded - green where **W** is favourable and red where **W** is unfavourable for all optical switching.

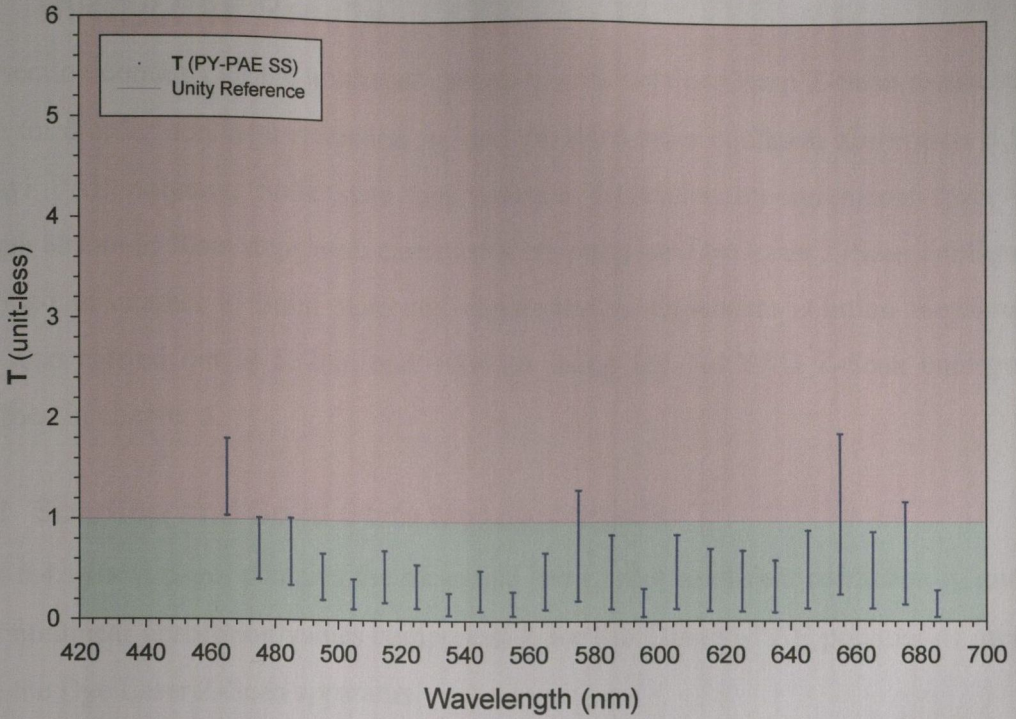


**Figure 6.3.11:** The dispersion of the **T** Figure of Merit for a 75nm thick **Pyridinyl-PAE Solid State Film**. The wavelength range is from 465nm to 685nm and uses the values in Table 6.3.4. The graph is colour coded - green where **T** is favourable and red where **T** is unfavourable for all optical switching.

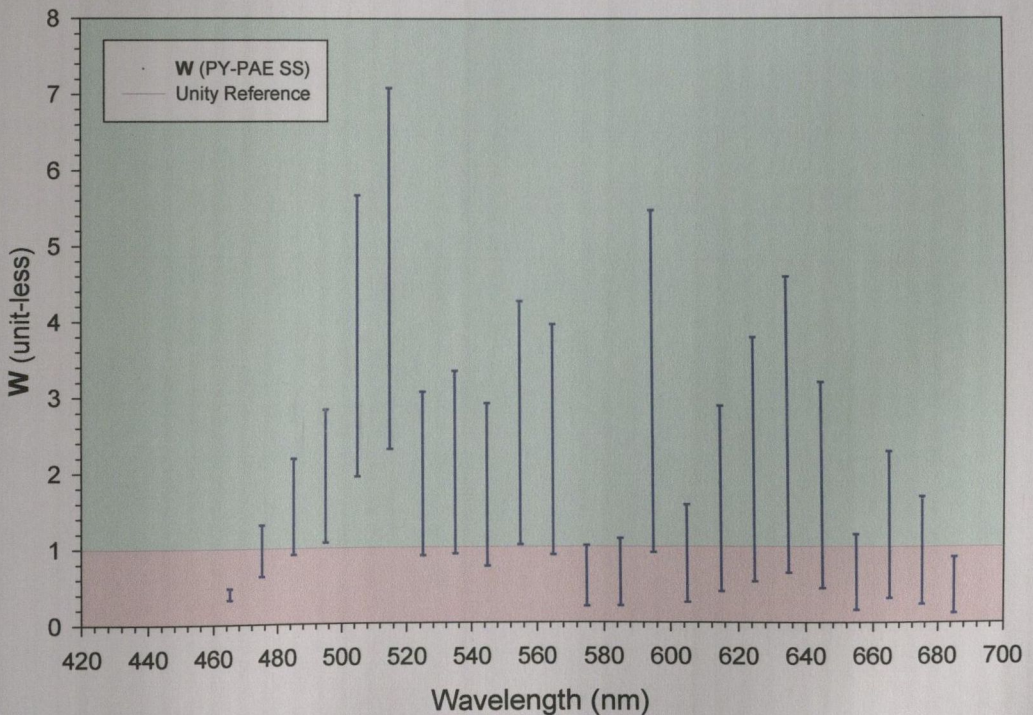


**Figure 6.3.12:** The dispersion of the **W** Figure of Merit for a 75nm thick **Pyridinyl-PAE Solid State Film**. The wavelength range is from 465nm to 685nm and uses the values in Table 6.3.4. The graph is colour coded - green where **W** is favourable and red where **W** is unfavourable for all optical switching.

## 6.4 Thienyl PAE Results

This section contains all the nonlinear optical results obtained from Z-Scan measurements of the third order nonlinear refraction  $\eta_2$ , and the third order nonlinear absorption  $\beta$  for the Thienyl PAE polymer. Solid state and solution dispersion measurements from 465nm through 685nm in 10nm steps were carried out on using the Dye Laser Z-Scan configuration described in chapter 5. Solid state and concentration dependent solution measurements were also carried out at 532nm and 1064nm using the Nd:YAG Z-Scan configuration described in chapter 5.

### 6.4.1 Solution and Solid State Measurements

Table 6.4.1 (next page) contains the measured third order nonlinear refraction  $\eta_2$  and third order nonlinear absorption values component  $\beta$  for the Thienyl-PAE polymer as measured using the Dye Laser Z-Scan apparatus.



### Thienyl-PAE (DYE Laser 465-685nm)

Wavelength	$\eta_2$ Solid State ( $\times 10^{-14}$ m <sup>2</sup> /W)	$\eta_2$ Solution ( $\times 10^{-18}$ m <sup>2</sup> /W)	$\beta$ Solid State ( $\times 10^{-8}$ m/W)	$\beta$ Solution ( $\times 10^{-12}$ m/W)
465nm	-14.540 ± 1.890	-283.900 ± 19.810	-143.000 ± 20.020	-432.500 ± 36.600
475nm	-8.950 ± 1.790	-111.740 ± 7.819	-82.000 ± 17.220	-185.500 ± 14.800
485nm	-7.670 ± 1.534	-54.740 ± 3.829	-76.200 ± 16.002	-71.200 ± 5.690
495nm	-7.170 ± 1.434	-17.780 ± 1.265	-56.800 ± 11.928	6.900 ± 0.552
505nm	-8.280 ± 1.739	-5.807 ± 0.406	-32.000 ± 7.040	38.000 ± 3.040
515nm	-12.900 ± 3.096	-3.590 ± 0.287	-30.550 ± 7.630	39.200 ± 3.528
525nm	-2.950 ± 0.826	-2.470 ± 0.198	-7.070 ± 2.050	36.500 ± 3.285
535nm	-4.990 ± 1.259	-2.190 ± 0.175	-7.293 ± 2.260	17.800 ± 1.602
545nm	-5.050 ± 1.616	-1.350 ± 0.122	-5.460 ± 1.802	7.800 ± 0.780
555nm	-3.770 ± 1.282	-0.814 ± 0.073	-6.120 ± 2.142	7.350 ± 0.735
565nm	-3.580 ± 1.289	-0.900 ± 0.090	-5.160 ± 1.909	16.300 ± 1.793
575nm	-10.300 ± 3.811	-0.760 ± 0.080	-10.500 ± 3.990	6.400 ± 0.768
585nm	-1.470 ± 0.573	-0.681 ± 0.082	-2.290 ± 0.916	4.210 ± 0.547
595nm	-3.040 ± 1.216	-0.560 ± 0.070	-6.190 ± 2.538	2.790 ± 0.391
605nm	-4.070 ± 1.709	-0.620 ± 0.090	-5.770 ± 2.481	2.240 ± 0.336
615nm	-1.890 ± 0.813	-0.136 ± 0.018	-3.770 ± 1.659	1.290 ± 0.194
625nm	-1.980 ± 0.891	-0.702 ± 0.078	-4.530 ± 2.084	1.160 ± 0.197
635nm	-1.210 ± 0.545	-0.605 ± 0.102	-2.270 ± 1.044	2.390 ± 0.430
645nm	-2.720 ± 1.251	-0.520 ± 0.100	-3.830 ± 1.800	3.030 ± 0.606
655nm	-1.440 ± 0.706	-0.490 ± 0.100	-4.670 ± 2.335	2.270 ± 0.477
665nm	-1.442 ± 0.675	-0.479 ± 0.101	-4.610 ± 2.305	1.800 ± 0.396
675nm	-1.190 ± 0.619	-0.390 ± 0.090	-2.210 ± 1.171	2.370 ± 0.569
685nm	-3.010 ± 1.625	-0.480 ± 0.110	-1.200 ± 0.660	3.770 ± 0.905

**Table 6.4.1:** The real component  $\eta_2$  and imaginary component  $\beta$  of  $\chi^{(3)}$  for the Thienyl-PAE polymer. The Solution measurements were all performed on a concentration of 2.5 g/l of the polymer in Toluene Solvent. All the above measurements were performed using the Nitrogen pumped DYE Laser set-up.

Figures 6.4.1 through 6.4.4 below show the above data in graphical format. Each Figure also shows the linear absorption spectrum for Thienyl-PAE to help facilitate trend correlation.

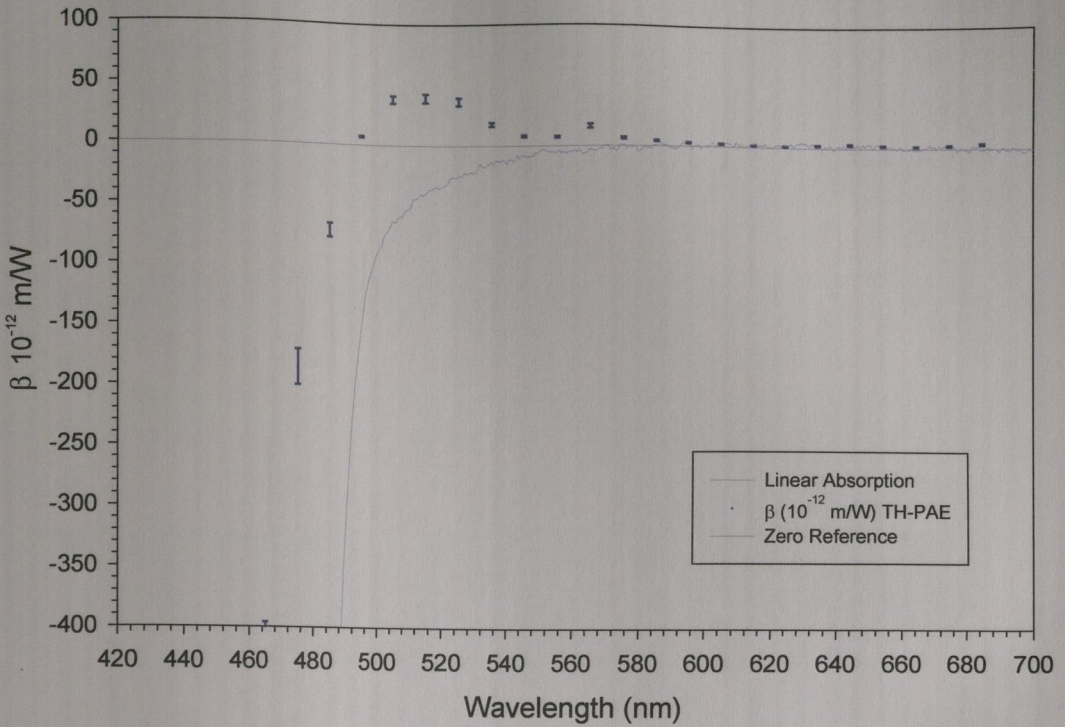


**Figure 6.4.1:** The dispersion of the imaginary component  $\beta$  of  $\chi^{(3)}$  for 2.5 g/l **Thienyl-PAE** polymer **Solution**. The wavelength range is from 465nm to 685nm in 10nm steps and uses the values in Table 6.4.1. The linear absorption trend for **Thienyl-PAE** in solution is also included for comparison.

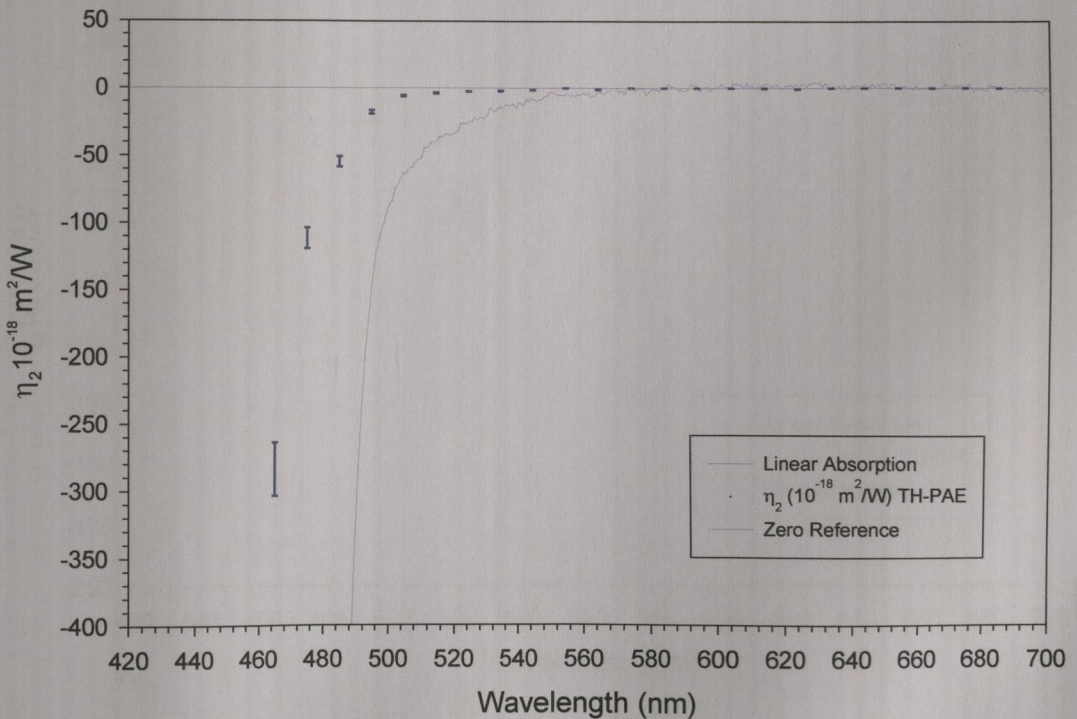


**Figure 6.4.2:** The dispersion of the real component  $\eta_2$  of  $\chi^{(3)}$  for 2.5 g/l **Thienyl-PAE** polymer **Solution**. The wavelength range is from 465nm to 685nm in 10nm steps and uses the values in Table 6.4.1. The linear absorption trend for **Thienyl-PAE** in solution is also included for comparison.

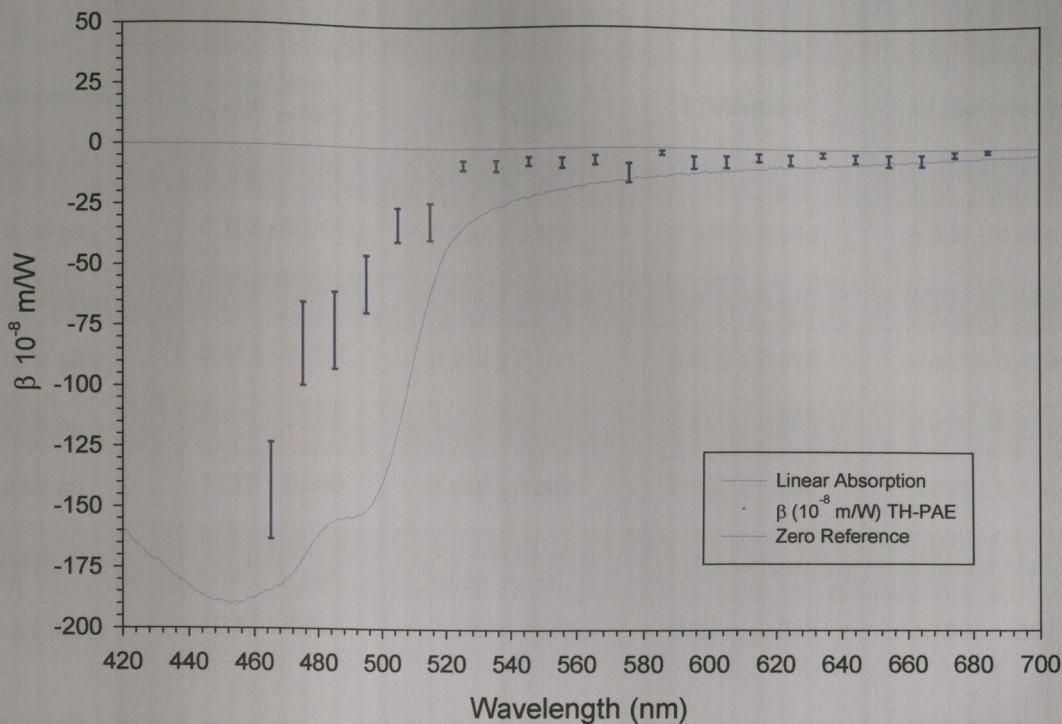


**Figure 6.4.4:** The dispersion of the imaginary component  $\beta$  of  $\chi^{(3)}$  for a 52nm thick **Thienyl-PAE Solid State polymer Film**. The wavelength range is from 465nm to 685nm in 10nm steps and uses the values in Table 6.4.1. The linear absorption trend for the same Solid State Film is also included for comparison.

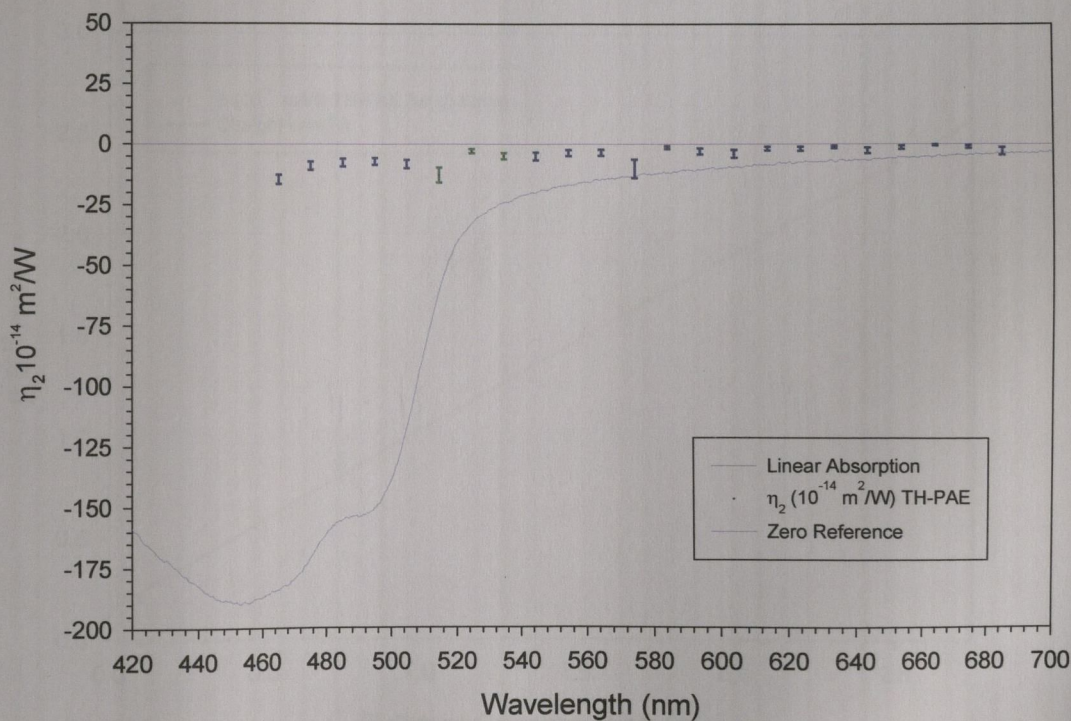


**Figure 6.4.5:** The dispersion of the real component  $\eta_2$  of  $\chi^{(3)}$  for a 52nm thick **Thienyl-PAE Solid State polymer Film**. The wavelength range is from 465nm to 685nm in 10nm steps and uses the values in Table 6.4.1. The linear absorption trend for the same Solid State Film is also included for comparison.

### Thienyl-PAE (YAG Laser 532nm)

Concentration	$\eta_2$ Solution ( $\times 10^{-18}$ m <sup>2</sup> /W)	$\beta$ Solution ( $\times 10^{-12}$ m/W)	T (Solution)	W (Solution)
0.10 g/l	$-0.065 \pm 0.005$	$0.212 \pm 0.019$	$0.868 \pm 0.148$	$0.928 \pm 0.139$
0.25 g/l	$-0.183 \pm 0.015$	$0.337 \pm 0.030$	$0.490 \pm 0.083$	$1.040 \pm 0.156$
0.50 g/l	$-0.331 \pm 0.027$	$0.547 \pm 0.049$	$0.440 \pm 0.075$	$0.253 \pm 0.038$
0.75 g/l	$-0.452 \pm 0.037$	$0.854 \pm 0.077$	$0.503 \pm 0.085$	$0.857 \pm 0.129$
1.00 g/l	$-0.587 \pm 0.048$	$1.138 \pm 0.102$	$0.516 \pm 0.088$	$0.839 \pm 0.126$
2.50 g/l	$-1.220 \pm 0.098$	$2.310 \pm 0.208$	$0.507 \pm 0.086$	$0.690 \pm 0.104$
Description	$\eta_2$ Solid State ( $\times 10^{-14}$ m <sup>2</sup> /W)	$\beta$ Solid State ( $\times 10^{-8}$ m/W)	T (Solid State)	W (Solid State)
Solid State	$-1.730 \pm 0.519$	$-2.600 \pm -0.806$	$0.399 \pm 0.243$	$1.700 \pm 0.901$

**Table 6.4.2:** The real component  $\eta_2$  and imaginary component  $\beta$  of  $\chi^{(3)}$  for the **Thienyl-PAE** polymer at **532nm**. The Solution measurements were all performed in Toluene Solvent. Also included are the nonlinear optical switching figures of merit **T** and **W**. All the above measurements were performed using the **YAG Laser** set-up.

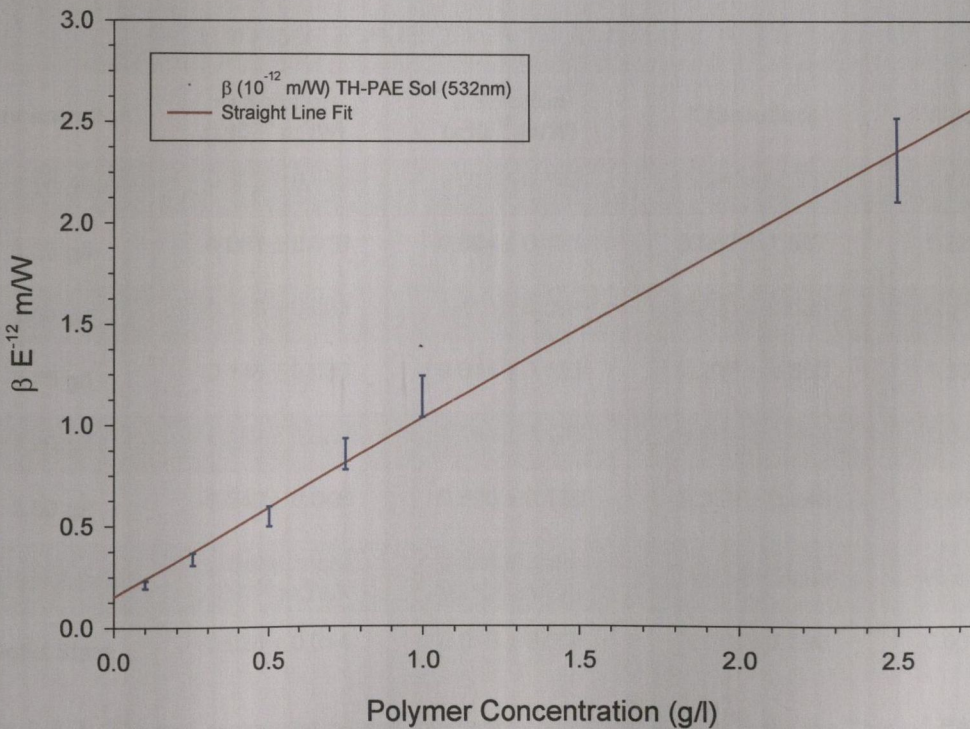


**Figure 6.4.6:** The imaginary component  $\beta$  of  $\chi^{(3)}$  for **Thienyl-PAE** polymer **Solution** as a function of solution concentration at 532nm. The solution concentration ranges from 0.10g/l up to 2.50g/l and uses the values in Table 6.4.2. Also included is a best straight line fit to all data points.

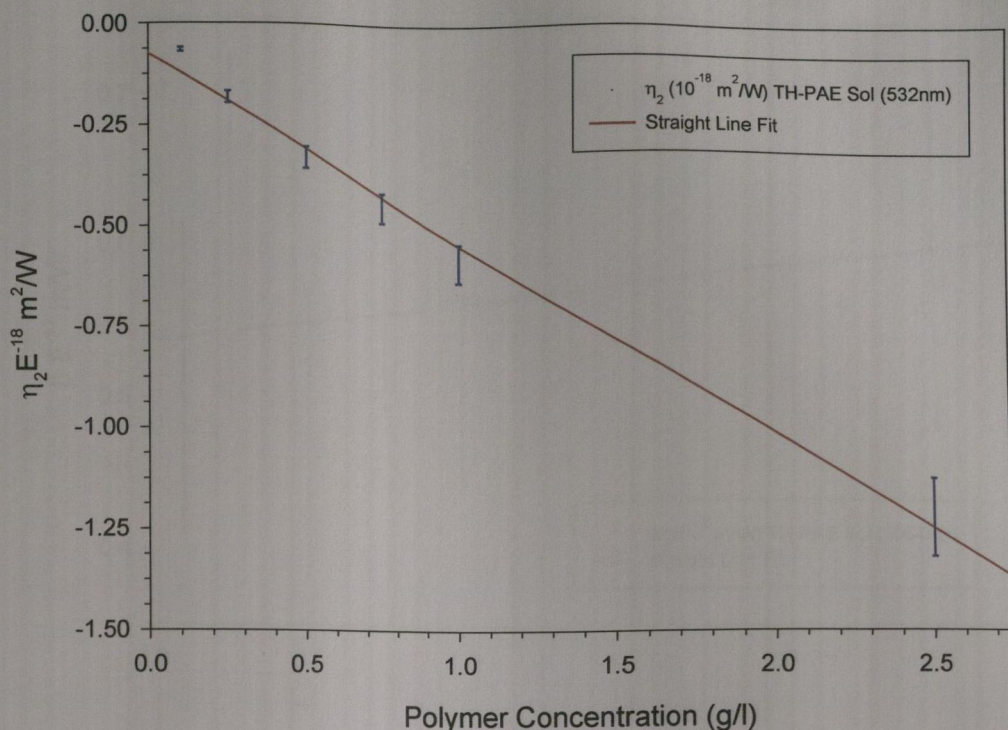


**Figure 6.4.7:** The real component  $\eta_2$  of  $\chi^{(3)}$  for **Thienyl-PAE** polymer **Solution** as a function of solution concentration at 532nm. The solution concentration ranges from 0.10g/l up to 2.50g/l and uses the values in Table 6.4.2. Also included is a best straight line fit to all data points.

### Thienyl-PAE (YAG Laser 1064nm)

Concentration	$\eta_2$ Solution ( $\times 10^{-18} \text{ m}^2/\text{W}$ )	$\beta$ Solution ( $\times 10^{-12} \text{ m/W}$ )	T (Solution)	W (Solution)
0.10 g/l	-0.023 ± 0.005	0.512 ± 0.102	11.843 ± 4.737	1.610 ± 0.612
0.25 g/l	-0.081 ± 0.016	0.604 ± 0.121	3.967 ± 1.587	1.221 ± 0.444
0.50 g/l	-0.113 ± 0.023	0.476 ± 0.095	2.241 ± 0.896	1.548 ± 0.588
0.75 g/l	-0.148 ± 0.030	0.614 ± 0.123	2.207 ± 0.883	1.351 ± 0.513
1.00 g/l	-0.152 ± 0.030	0.544 ± 0.108	1.904 ± 0.762	1.041 ± 0.396
2.50 g/l	-0.240 ± 0.048	0.599 ± 0.120	2.370 ± 0.948	0.659 ± 0.250
Description	$\eta_2$ Solid State ( $\times 10^{-14} \text{ m}^2/\text{W}$ )	$\beta$ Solid State ( $\times 10^{-8} \text{ m/W}$ )	T (Solid State)	W (Solid State)
Solid State	-0.028 ± 0.014	0.016 ± 0.008	3.113 ± 2.335	0.031 ± 0.023

**Table 6.4.3:** The real component  $\eta_2$  and imaginary component  $\beta$  of  $\chi^{(3)}$  for the **Thienyl-PAE** polymer at 1064nm. The Solution measurements were all performed in Toluene Solvent. Also included are the nonlinear optical switching figures of merit **T** and **W**. All the above measurements were performed using the **YAG Laser** set-up.

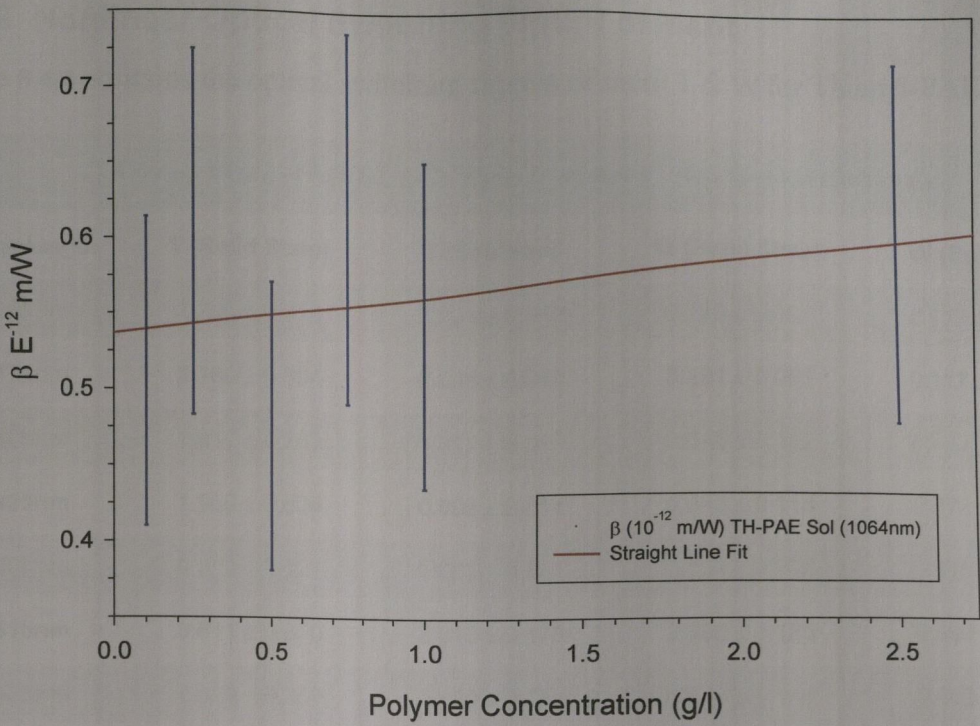


**Figure 6.4.8:** The imaginary component  $\beta$  of  $\chi^{(3)}$  for Thienyl-PAE polymer Solution as a function of solution concentration at 1064nm. The solution concentration ranges from 0.10g/l up to 2.50g/l and uses the values in Table 6.4.3. Also included is a best straight line fit to all data points.

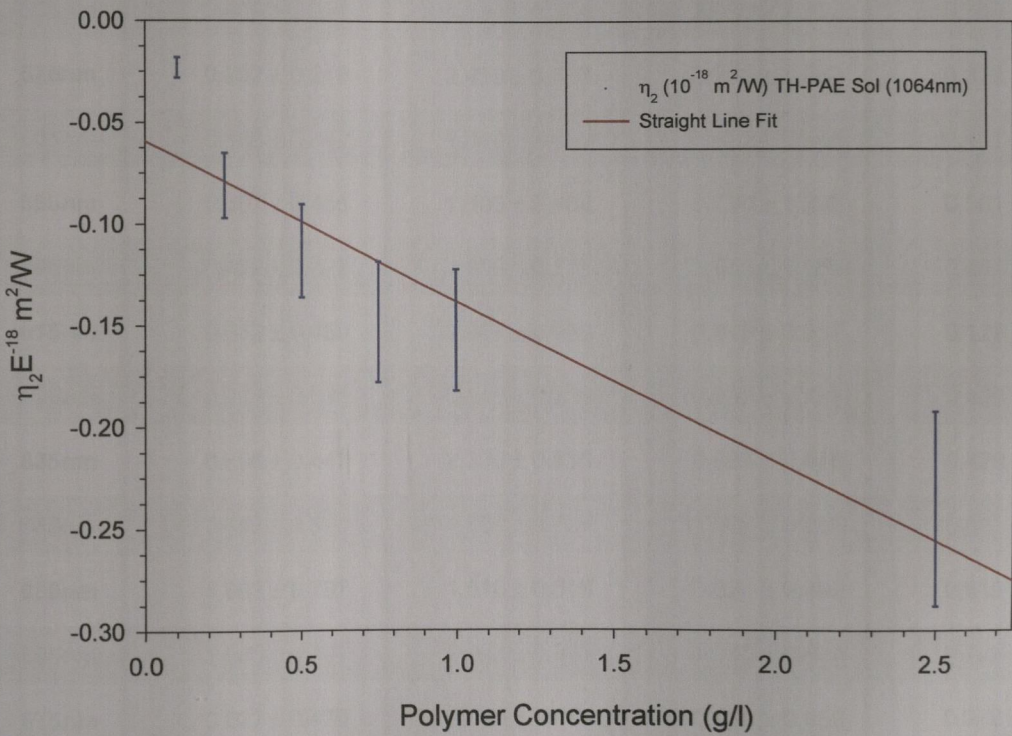


**Figure 6.4.9:** The real component  $\eta_2$  of  $\chi^{(3)}$  for Thienyl-PAE polymer Solution as a function of solution concentration at 1064nm. The solution concentration ranges from 0.10g/l up to 2.50g/l and uses the values in Table 6.4.3. Also included is a best straight line fit to all data points.

## 6.4.2 Nonlinear Optical Switching Figure of Merit

Table 6.4.4 contains the optical switching figures of merit **T** & **W** for Thienyl-PAE.

<b>Thienyl-PAE (DYE Laser 465-685nm)</b>				
<b>Wavelength</b>	<b>T (Solid State)</b>	<b>T (Solution)</b>	<b>W (Solid State)</b>	<b>W (Solution)</b>
465nm	2.290 ± 0.618	0.354 ± 0.053	0.270 ± 0.051	0.119 ± 0.016
475nm	2.180 ± 0.894	0.394 ± 0.059	0.281 ± 0.093	0.117 ± 0.015
485nm	1.910 ± 0.783	0.315 ± 0.047	0.340 ± 0.112	0.182 ± 0.023
495nm	1.960 ± 0.804	0.096 ± 0.014	0.343 ± 0.113	0.373 ± 0.048
505nm	0.978 ± 0.421	1.652 ± 0.247	0.834 ± 0.292	0.445 ± 0.057
515nm	0.611 ± 0.300	2.810 ± 0.478	2.890 ± 1.185	0.539 ± 0.081
525nm	0.629 ± 0.359	3.880 ± 0.660	0.904 ± 0.443	0.459 ± 0.069
535nm	0.359 ± 0.223	2.170 ± 0.369	4.592 ± 2.433	0.841 ± 0.126
545nm	0.295 ± 0.192	1.570 ± 0.298	1.590 ± 0.906	0.360 ± 0.061
555nm	0.450 ± 0.311	2.500 ± 0.475	1.390 ± 0.848	0.295 ± 0.050
565nm	0.407 ± 0.297	4.160 ± 0.874	2.050 ± 1.332	0.740 ± 0.141
575nm	0.292 ± 0.219	2.420 ± 0.557	2.750 ± 1.843	0.279 ± 0.059
585nm	0.456 ± 0.342	1.810 ± 0.453	0.631 ± 0.448	0.451 ± 0.104
595nm	0.607 ± 0.455	1.490 ± 0.402	1.770 ± 1.292	0.561 ± 0.140
605nm	0.429 ± 0.322	1.090 ± 0.316	1.540 ± 1.155	0.451 ± 0.122
615nm	0.612 ± 0.459	2.917 ± 0.963	0.849 ± 0.637	0.128 ± 0.042
625nm	0.715 ± 0.536	0.516 ± 0.170	1.050 ± 0.788	0.839 ± 0.260
635nm	0.596 ± 0.447	2.330 ± 0.816	0.635 ± 0.476	0.428 ± 0.141
645nm	0.453 ± 0.340	1.890 ± 0.737	1.300 ± 0.975	0.681 ± 0.252
655nm	1.063 ± 0.797	1.510 ± 0.619	0.651 ± 0.488	0.613 ± 0.239
665nm	1.063 ± 0.797	0.923 ± 0.397	0.545 ± 0.409	0.723 ± 0.296
675nm	0.627 ± 0.470	2.040 ± 0.959	0.913 ± 0.685	0.922 ± 0.415
685nm	0.137 ± 0.103	2.700 ± 1.269	1.520 ± 1.140	0.734 ± 0.330

**Table 6.4.4:** The nonlinear optical switching figures of merit **T** and **W** for the **Thienyl-PAE** polymer. The Solution measurements were all performed on a concentration of 2.5 g/l of the polymer in Toluene Solvent. All the above measurements were performed using the Nitrogen pumped **DYE Laser** set-up.

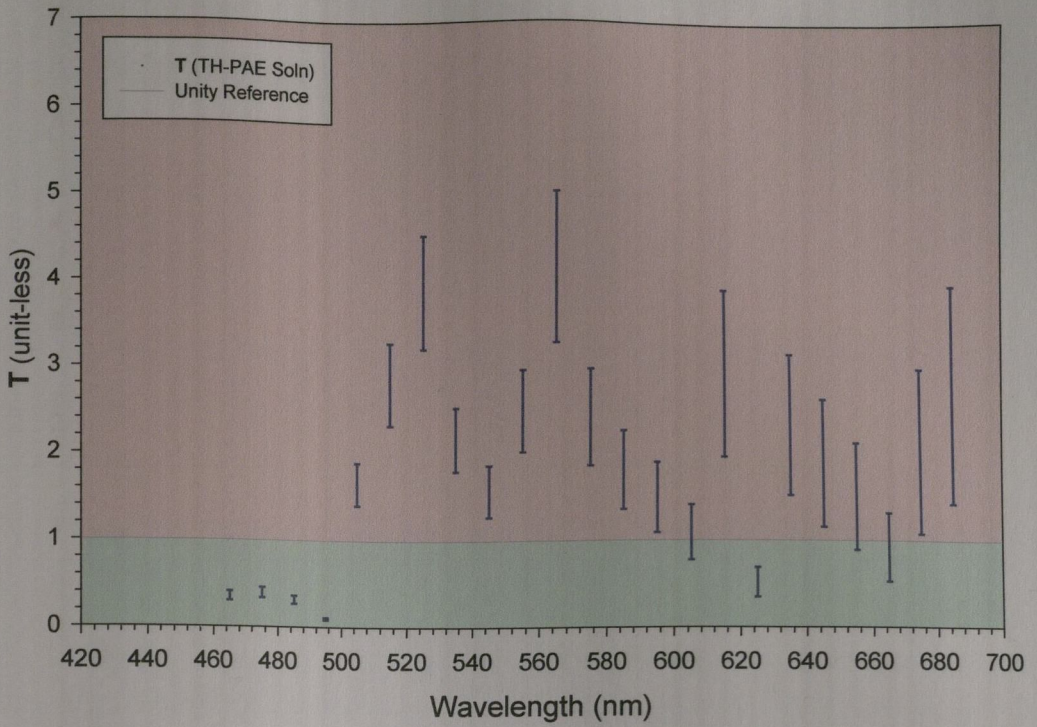


**Figure 6.4.10:** The dispersion of the **T** Figure of Merit for 2.5 g/l **Thienyl-PAE** polymer **Solution**. The wavelength range is from 465nm to 685nm in 10nm steps and uses the values in Table 6.4.4. The graph is colour coded - green where **T** is favourable and red where **T** is unfavourable for all optical switching.

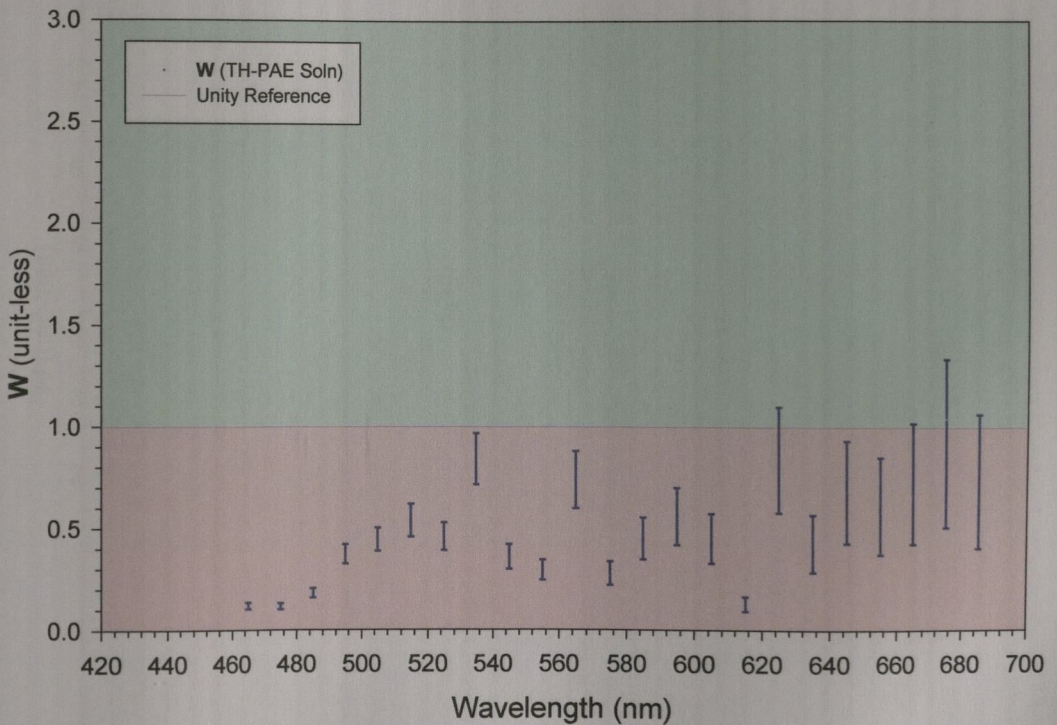


**Figure 6.4.11:** The dispersion of the **W** Figure of Merit for 2.5 g/l **Thienyl-PAE** polymer **Solution**. The wavelength range is from 465nm to 685nm in 10nm steps and uses the values in Table 6.4.4. The graph is colour coded - green where **W** is favourable and red where **W** is unfavourable for all optical switching.



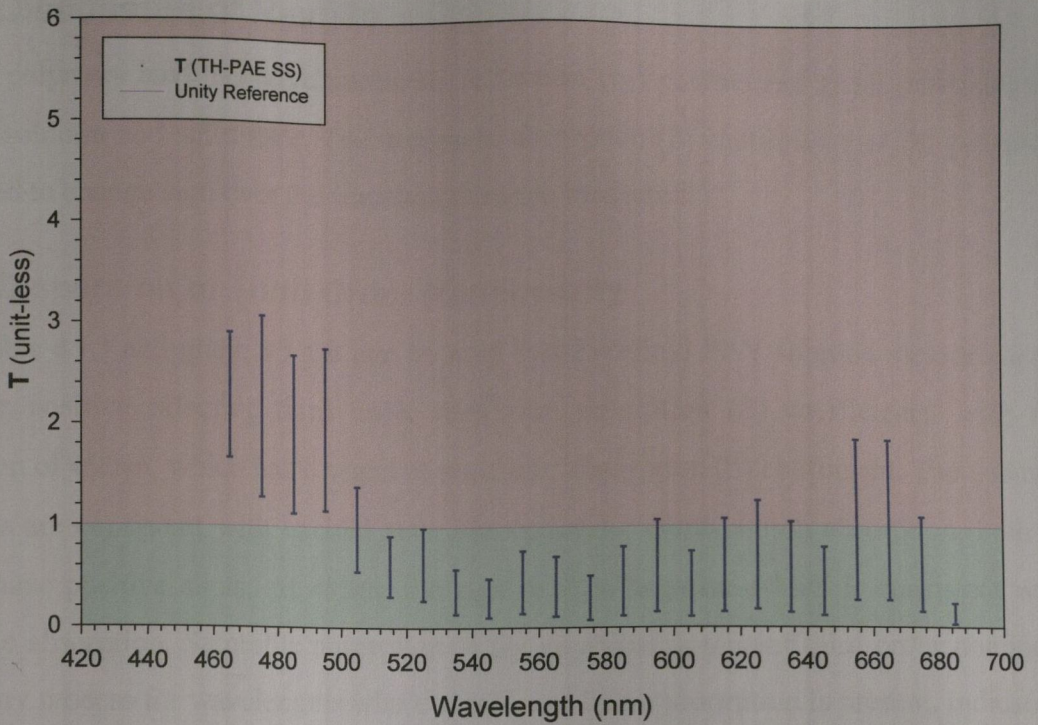


**Figure 6.4.12:** The dispersion of the **T** Figure of Merit for a 52nm thick **Thienyl-PAE Solid State Film**. The wavelength range is from 465nm to 685nm and uses the values in Table 6.4.4. The graph is colour coded - green where **T** is favourable and red where **T** is unfavourable for all optical switching.

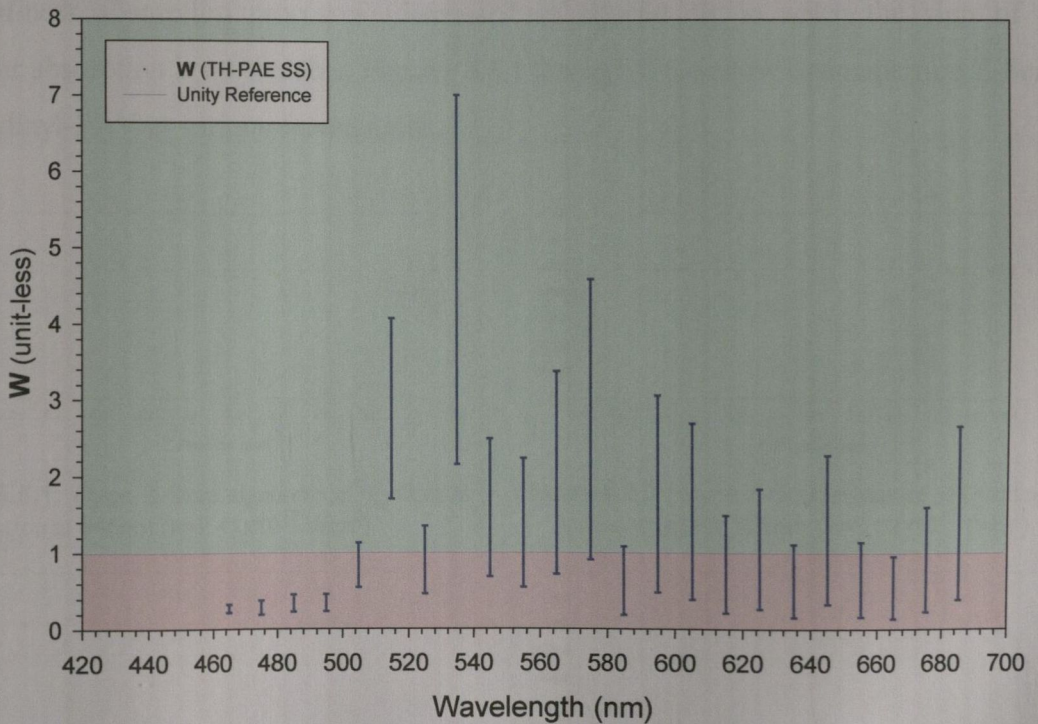


**Figure 6.4.13:** The dispersion of the **W** Figure of Merit for a 230nm thick **Thienyl-PAE Solid State Film**. The wavelength range is from 465nm to 685nm and uses the values in Table 6.4.4. The graph is colour coded - green where **W** is favourable and red where **W** is unfavourable for all optical switching.

## 6.5 Discussion of Results

All the polymers have negative nonlinear refraction ( $\eta_2$ ) coefficients at all wavelengths, both in solution and solid state. The nonlinear absorption ( $\beta$ ) coefficients of the polymers are found to change sign over the wavelength range measured.

### 6.5.1 Dispersion of Third Order Nonlinearity

From table 6.1.1 and graph 6.1.1 it can be seen that Pyridinyl PAV solution measurements all have positive effective third order nonlinear absorption ( $\beta$ ) coefficients, with the exception of 465nm, which has a negative nonlinear absorption ( $\beta$ ) coefficient. The positive  $\beta$  values are consistent with excited state absorption or multi-photon absorption, both of which have positive signs. At 465nm the sign of  $\beta$  is negative which is consistent with saturable absorption. Saturable absorption is the expected dominant third order nonlinear imaginary process for wavelengths where significant linear absorption is present, indicating that the ground state absorption cross section is larger than the excited state absorption cross section (c.f. chapter 2).

Analysis of the Z-scans experimental traces are useful when trying to elucidate which of the nonlinear absorption processes (discussed in chapter 2), to which the sign of the nonlinear absorption is attributable. Figures 6.5.1 through 6.5.4 show open aperture Z-Scans for Pyridinyl-PAV at various wavelengths.

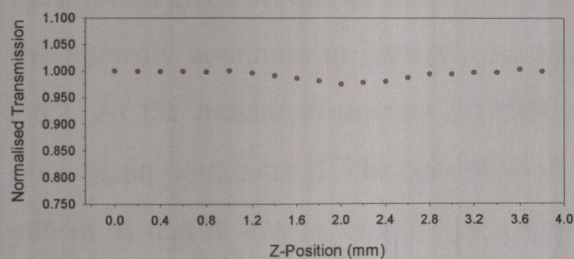


**Figure 6.5.1:** Open Z-Scan signature of Pyridinyl-PAV solution at 645nm ( $I_0=2.41 \times 10^{13} \text{ W/m}^2$ )

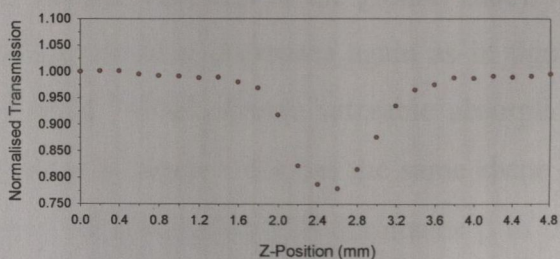


**Figure 6.5.2:** Open Z-Scan signature of Pyridinyl-PAV solution at 505nm ( $I_0=3.52 \times 10^{13} \text{ W/m}^2$ )

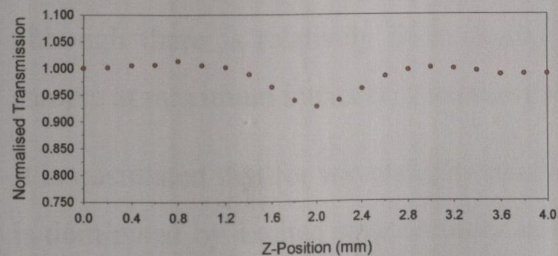


**Figure 6.5.3:** Open Z-Scan signature of Pyridinyl-PAV solution at 475nm ( $I_0=1.48 \times 10^{13} \text{ W/m}^2$ )

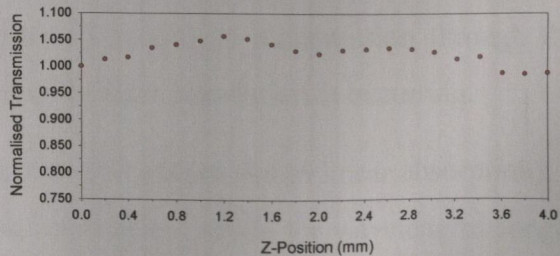


**Figure 6.5.4:** Open Z-Scan signature of Pyridinyl-PAV solution at 465nm ( $I_0=0.91 \times 10^{13} \text{ W/m}^2$ )

Figure 6.5.1 shows that for Pyridinyl-PAV solution at 645nm, as the on-axis intensity increases from a low value (linear regime) at a z-position of 0.0mm, to an on-axis maximum intensity ( $I_0=2.41 \times 10^{13} \text{ W/m}^2$ ) at a z-position of 2.0mm, the transmission through the sample decreases. Pyridinyl-PAV solution has a very low linear absorption at this wavelength, therefore the decrease in transmission with increasing intensity is attributed to multi-photon absorption, namely two photon absorption.

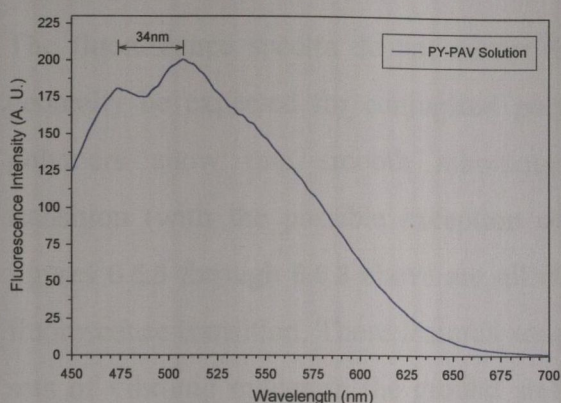
Figure 6.5.2 shows that at 505nm there is a considerable decrease (~25%) in the amount of light passing through the same Pyridinyl-PAV sample as the intensity passes through its maximum on-axis value of  $3.52 \times 10^{13} \text{ W/m}^2$ . This wavelength is located at the long wavelength side of the main absorption band for Pyridinyl-PAV, where an appreciable amount of ground state absorption exists. If the incident intensity is well above the saturation intensity, the excited state can become significantly populated. Electrons in the excited state may undergo absorption which promotes them to higher-lying states (whose energy separation is usually smaller than the ground state separation). When the absorption cross-section of the excited state is larger than that of the ground state, the transmission through the sample decreases with increasing intensity. This type of excited-state absorption is called reverse saturable absorption and is discussed in chapter 2.

Figure 6.5.3 shows that at 475nm, however, the initial increase in intensity leads to an increase in sample transmission, which is consistent with the onset of saturable absorption (absorption cross-section of the excited state is smaller than that of the ground state). As the intensity continues to increase, the sample transmission decreases again as in figure 6.5.2. At the maximum on-axis intensity of  $1.48 \times 10^{13} \text{ W/m}^2$  reverse saturable absorption once again dominates  $\beta$ . The open Z-Scan signature in figure 6.5.4 has the same shape at 465nm as that at 475nm, except that saturation of the absorption still dominates  $\beta$  as the intensity passes through its maximum on-axis value of  $0.91 \times 10^{13} \text{ W/m}^2$ . The change from saturable absorption to reverse saturable absorption as the intensity increases signifies that although there is relatively little change (overall decrease) in transmission through the sample at maximum intensity, a substantial change in level population is occurring.

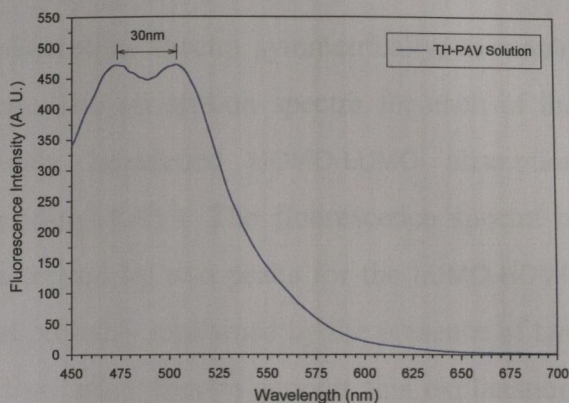
It is postulated that for wavelengths between 475nm and 605nm (large linear absorption),  $\beta$  is dominated by excited state (reverse saturable) absorption, while for wavelengths longer than 605nm (where there is relatively little residual absorption),  $\beta$  is dominated by two photon absorption.

The reverse saturable absorption behaviour seen for all polymer solutions appears in only one (Pyridinyl PAV) of the solid state dispersion measurements of  $\beta$ . This is consistent with the absorption spectra in chapter 4, which show that the Pyridinyl-PAV absorption spectrum undergoes the least amount of change on going from solution to solid state.

Figure 6.1.1 also shows what appears to be two peaks (505nm and 565nm) over the range of wavelengths where  $\beta$  is dominated by reverse saturable absorption. These peaks are also present (to a greater or lesser extent) for the other three polymers Figures 6.2.1, 6.3.1 and 6.4.1). Figures 6.5.5 through 6.5.8 help to explain the proposed origin of the two peaks and their relative magnitudes for each of the four polymers.



**Graph 6.5.5:** Fluorescence spectrum of Pyridinyl-PAV polymer solution (0.25 g/l in Toluene)



**Graph 6.5.6:** Fluorescence spectrum of Thienyl-PAV polymer solution (0.25 g/l in Toluene)

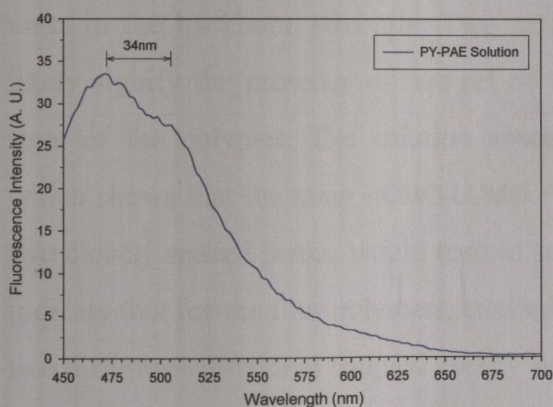


**Figure 6.5.7:** Fluorescence spectrum of Pyridinyl-PAE polymer solution (0.25 g/l in Toluene)

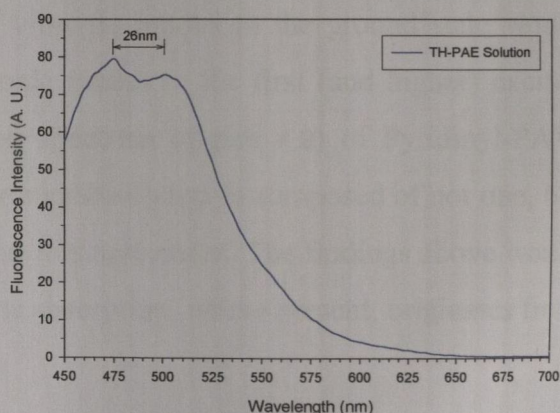


**Figure 6.5.8:** Fluorescence spectrum of Thienyl-PAE polymer solution (0.25 g/l in Toluene)

The four figures above show low intensity, steady state fluorescence spectra for each of the polymers in toluene solution. The spectrum obtained in each case has two peaks located close together at the emission maximum. In electronic absorption which occurs on a timescale of  $\sim 10^{-15}$  seconds, the vast majority of transitions from the ground state take place from the lowest vibrational level ( $S_{00}$  level). The molecule is excited from its lowest

ground state to any or all of the vibrational levels in the first excited state. The excited molecule then rapidly cascades down the vibrational manifold, losing its vibrational energy to establish thermal equilibrium with its surroundings. This process, which is one of simple thermal relaxation, occurs on a timescale of  $\sim 10^{-13}$  s and may be represented as  $S_{1V} \rightarrow S_{10}$ . A molecule that has been radiatively excited and subsequently undergone a vibrational relaxation to the lowest vibronic level of its excited state, may then relax radiatively into the ground state vibrational manifold over a timescale of 1-100ns. A fluorescence spectrum yields information concerning the vibrational energy level distribution in the ground state, whereas an absorption spectrum yields information on the vibrational energy distribution in the excited state.

The fluorescence spectra do not mirror the absorption spectra symmetrically, as would generally be expected for conjugated polymers. The absorption spectra for each of the polymers show one smooth inhomogeneously broadened HOMO-LUMO absorption transition (with the possible exception of Pyridinyl-PAV). The fluorescence spectra in figures 6.5.5 through 6.5.8 above are all characterised by two peaks for the LUMO-HOMO fluorescence transition. These features are most probably explained by the presence of two sets of vibronic modes in the ground state<sup>1</sup>. Excitation spectra support this explanation. Excitation spectra of both peaks are identical, indicating they originate from the same transition<sup>2</sup>. This duality probably originates from the alternance of the different polymer co-units in the backbone structure. Two sets of vibronic modes in the ground state would likely signify the presence of two set of vibronic modes in the first (and higher) excited state of the polymer. The solution absorption spectrum (figure 4.9) of Pyridinyl-PAV, which shows that the main HOMO-LUMO electronic absorption is composed of not one, but two closely spaced peaks, would tend to support this agreement. The findings above would indicate that for the four polymers, excited state absorption, where present, originates from two different vibrational coupled energy levels.

The absorption cross-section for each excited state (each polymer) will be different, and their respective ratio to the ground state absorption cross-sections will govern whether saturable absorption or reverse saturable dominate the nonlinear absorption spectra. Under this assumption, the ratio of separation in wavelength between the two fluorescence peaks for each of the four polymers, should correlate to the ratio of separation in wavelength between the two reverse saturation of absorption peaks. In figure 6.5.9 this correlation is

shown, indicating that the reverse saturable absorption double peaks do in fact originate from excited state absorption from two different vibrationally coupled states.

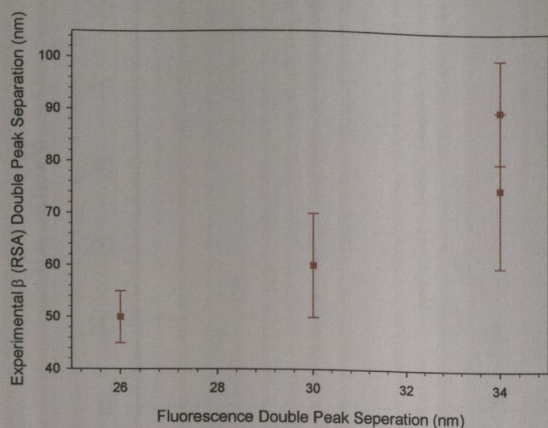


**Figure 6.5.9:** Plot of fluorescence double peak  $\lambda$  separation vs. measured double peak maximum RSA  $\beta \lambda$  separation for all four polymer solutions.

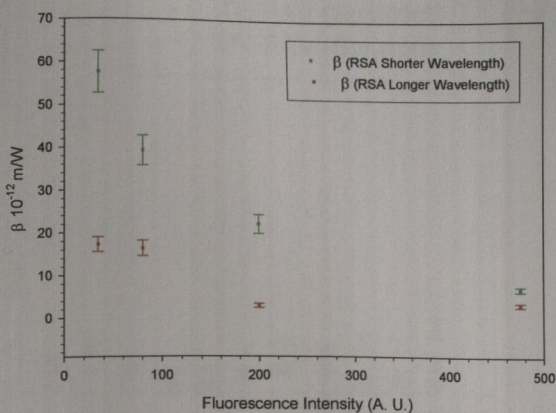


**Figure 6.5.10:** Plot of maximum measured RSA  $\beta$  values vs. maximum fluorescence intensity for all four polymer solutions.

Figure 6.5.10 indicates that there is also a correlation between the reverse saturable absorption maximum value and the maximum fluorescence intensity for each polymer. The trend is less clear for the long wavelength maxima and may be associated with resolution of the low values observed in the Z-Scan traces. Electronic contributions to nonlinear refractive index  $\eta_2$  arise from virtual transitions and response times are typically of the order  $10^{-15}$  seconds. Usually the  $\eta_2$  value of  $\pi$ -electron conjugated polymers depends on the conjugation length. The  $\eta_2$  value has been reported to be proportional to the minus 6<sup>th</sup> power of the optical bandgap energy<sup>3</sup>. Increasing the  $\pi$  conjugation length sequence reduces the optical bandgap energy. Resonant enhancement of  $\eta_2$  may occur whenever there is linear or nonlinear absorption. The excitation of electrons from the electronic ground state to an excited state (or valence band) results in a electronic population redistribution which is responsible for the modification of the materials refractive index (which may be quantified through the Kramers-Kronig relationships). Response times in the resonantly enhanced case are of the order  $10^{-9}$  seconds because the electrons may take a time interval of typically 0.1ns to 30ns to relax back to their ground state configuration<sup>4</sup>. Large values for  $\alpha$  and  $\beta$  are detrimental to the all optical switching figure of merits. From graph 6.1.2, it can be seen that  $\eta_2$  is noticeably resonantly enhanced for wavelengths of 485nm and shorter. This is expected and corresponds with the onset of the linear optical absorption. Figures 6.5.11 through 6.5.14 show how the solid state and solution  $\eta_2$  and  $\beta$  values vary for all polymers over the wavelength range of 465nm through 685nm.

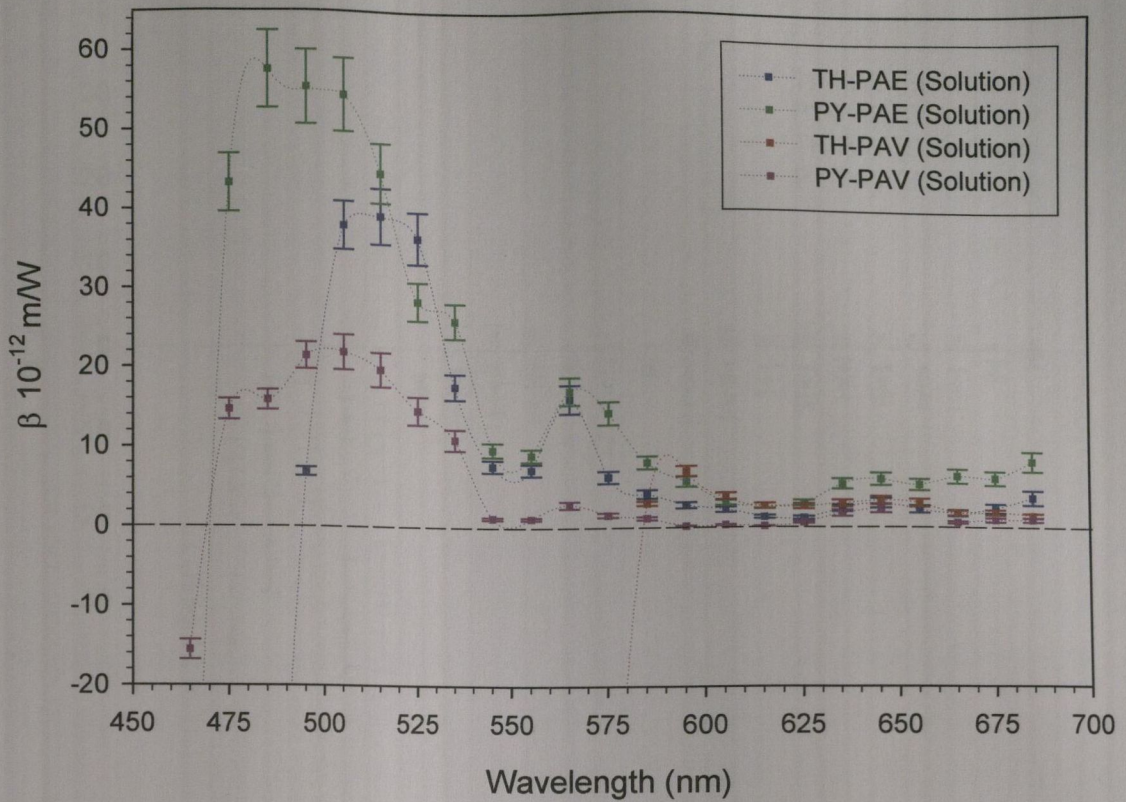


**Figure 6.5.11:** The dispersion of the imaginary component  $\beta$  of  $\chi^{(3)}$  for all four polymer **Solutions**. The wavelength range is from 465nm through 685nm in 10nm steps and uses the values in Tables 6.1.1, 6.2.1, 6.3.1 and 6.4.1. The dotted curves are present to serve as a guide to the eye only.

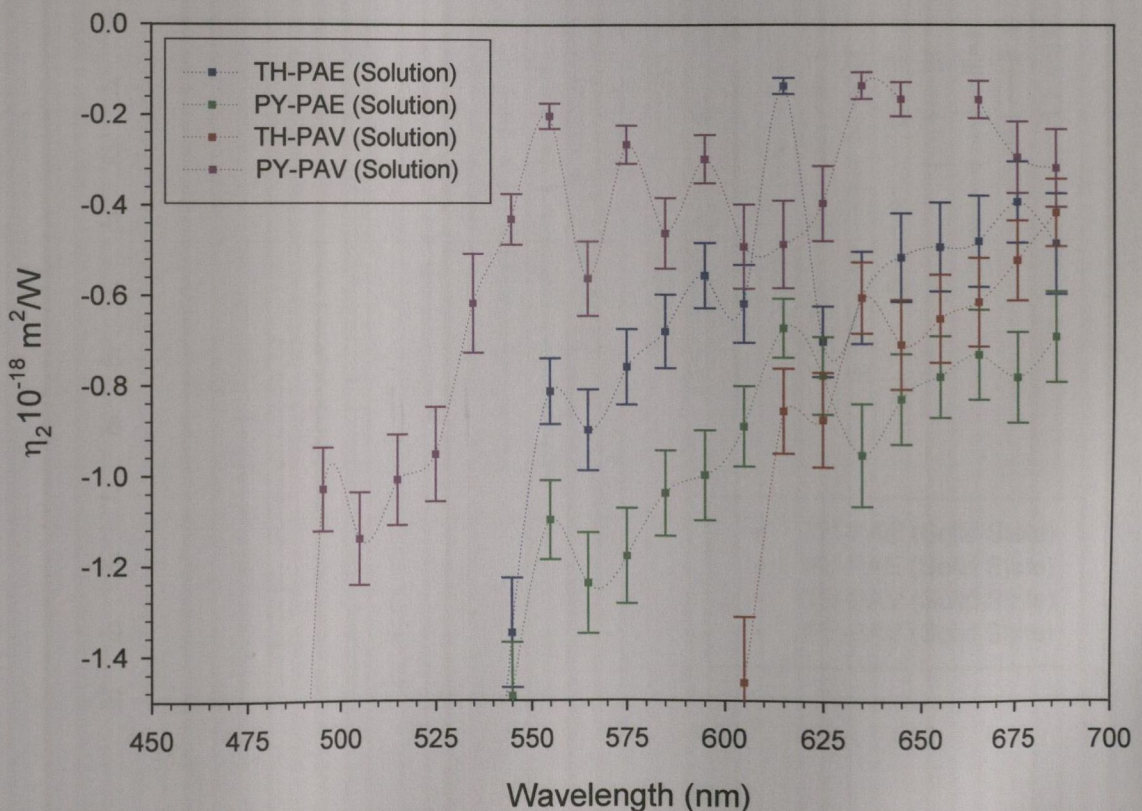
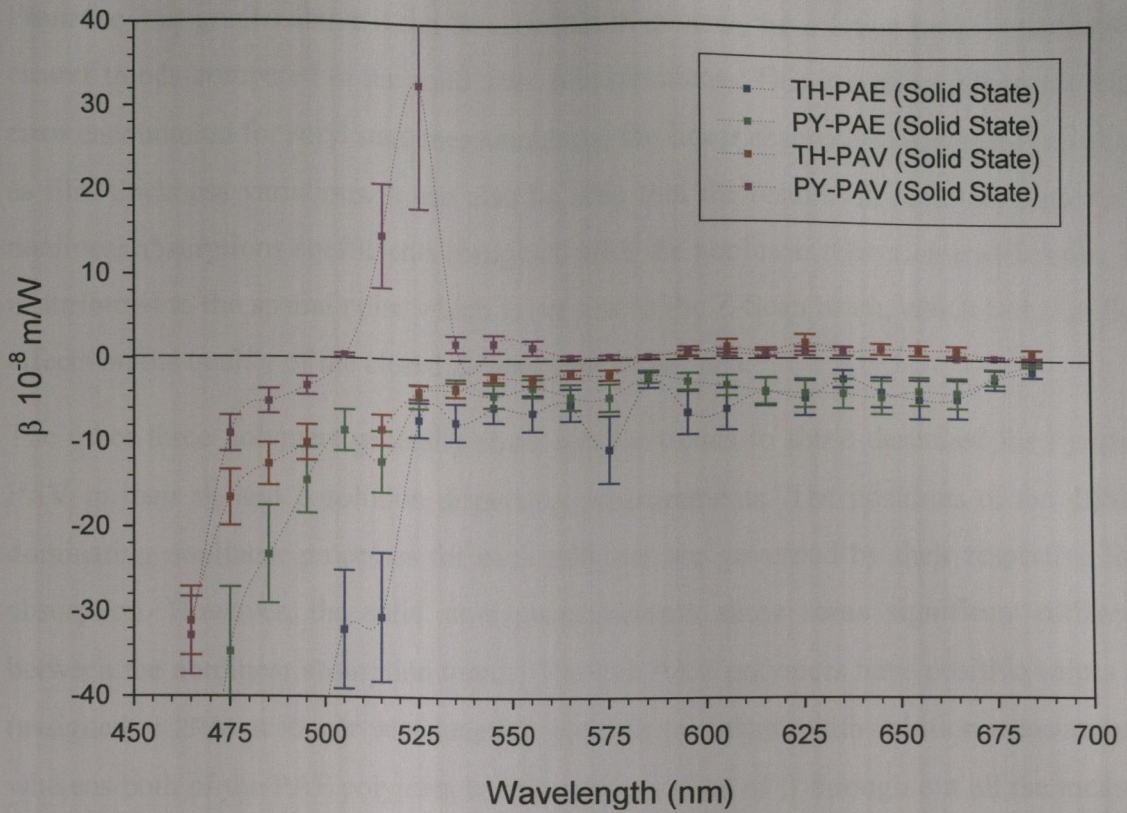
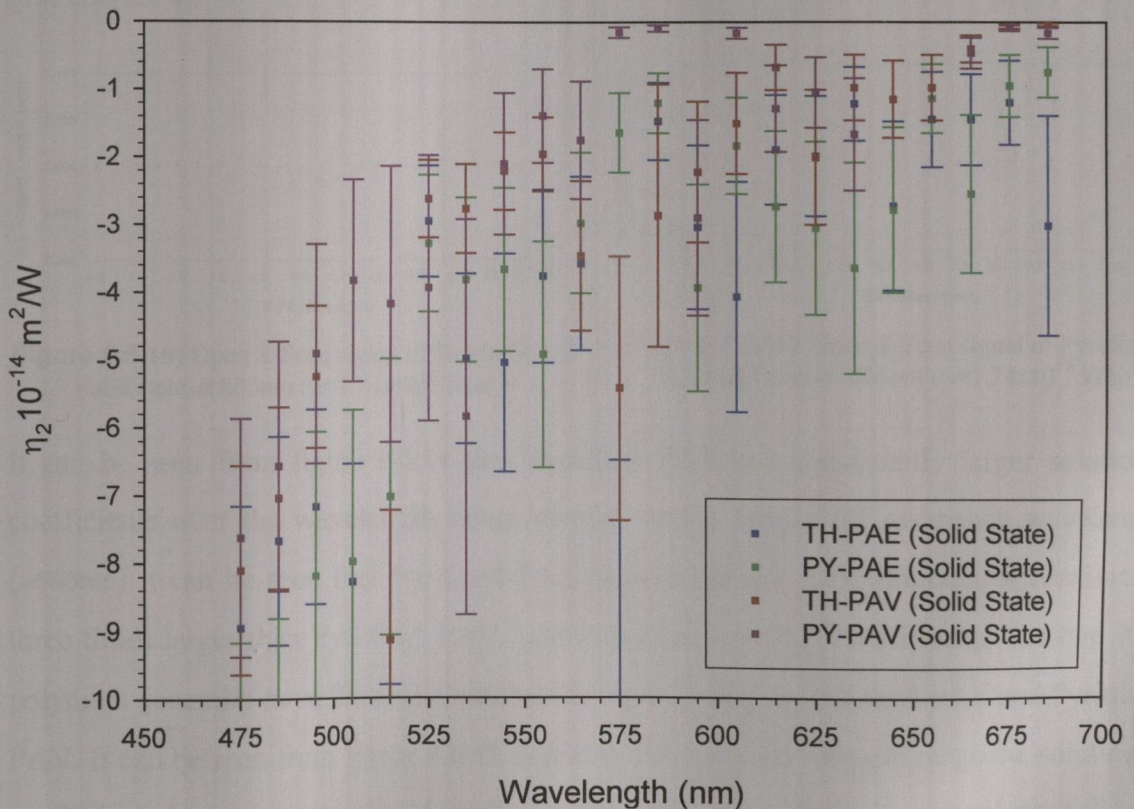


**Figure 6.5.12:** The dispersion of the real component  $\eta_2$  of  $\chi^{(3)}$  for all four polymer **Solutions**. The wavelength range is from 465nm through 685nm in 10nm steps and uses the values in Tables 6.1.1, 6.2.1, 6.3.1 and 6.4.1. The dotted curves are present to serve as a guide to the eye only.



**Graph 6.5.13:** The dispersion of the imaginary component  $\beta$  of  $\chi^{(3)}$  for all four polymer **Solid State Films**. The wavelength range is from 465nm through 685nm in 10nm steps and uses the values in Tables 6.1.1, 6.2.1, 6.3.1 and 6.4.1. The dotted curves are present to serve as a guide to the eye only.



**Graph 6.5.14:** The dispersion of the real component  $\eta_2$  of  $\chi^{(3)}$  for all four polymer **Solid State Films**. The wavelength range is from 465nm through 685nm in 10nm steps and uses the values in Tables 6.1.1, 6.2.1, 6.3.1 and 6.4.1. The dotted curves are not include as they further complicate the graph.



From the four graphs above it can be seen that in general, the solution measurements show clearer trends compared to the solid state measurements. This is attributable to the higher error encountered for solid state measurements; the linear absorption coefficient ( $\alpha$ ) as well as film thickness variations. It can also be seen that the results are more accurate for the nonlinear absorption coefficients compared with the nonlinear refraction coefficients. This is attributed to the spatial noise which is present in the Z-Scan beam, which had significant effects on the quality of the closed Z-Scan traces obtained.

The other three polymers generally show similar trends to those described for Pyridinyl-PAV in their  $\eta_2$  and  $\beta$  solution dispersion measurements. The positions of the different dominating nonlinear processes for each polymer are governed by their respective linear absorption. However, the solid state measurements show some significant differences between the nonlinear absorption trends. The two PAV polymers have positive values of  $\beta$  (assigned to 2PA) at longer wavelengths, which is consistent with solution measurements, whereas both of the PAE polymers have negative values of  $\beta$  through out all the measured wavelength range. This is illustrated in figures 6.5.15 and 6.5.16. The negative values of  $\beta$  are attributed to the residual absorption still present in the ground state electronic spectra (c.f. chapter 4).

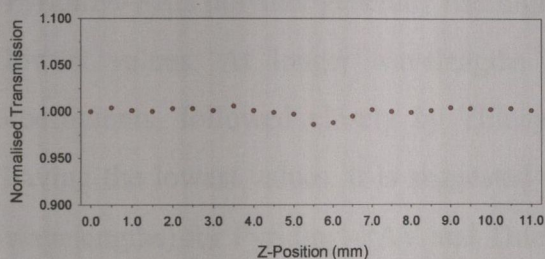


**Figure 6.5.15:** Open Z-Scan signal of Thienyl-PAV solid state at 665nm ( $I_0=1.74 \times 10^{13} \text{ W/m}^2$ )

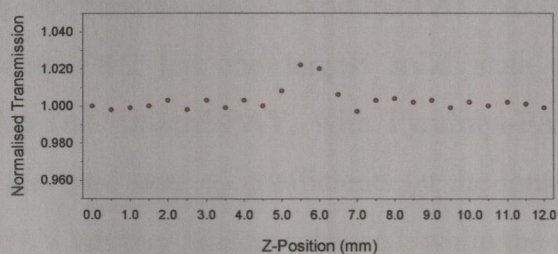


**Figure 6.5.16:** Open Z-Scan signal of Pyridinyl-PAE solid state at 665nm ( $I_0=1.74 \times 10^{13} \text{ W/m}^2$ )

It can be seen from figure 6.5.11 that Pyridinyl PAE has consistently larger solution  $\beta$  coefficients over the wavelength range shown. At the longer off resonance wavelengths ( $>595\text{nm}$ ) it can be seen that Pyridinyl-PAE has the highest  $\beta$  coefficients, approximately three times larger than Pyridinyl PAV, which has the lowest  $\beta$  coefficients. The two PAV polymers generally have  $\beta$  coefficients which are in-between Pyridinyl-PAE and Pyridinyl-PAV. It can be seen from figure 6.5.12 that over the same wavelength range the solution  $\eta_2$  coefficients have the same trend, with Pyridinyl-PAE having the largest values, followed by Thienyl PAV, Thienyl-PAE and Pyridinyl-PAV. It is therefore suggested that the solution  $\eta_2$  coefficients, are two photon enhanced. The start of the two photon absorption

band can be seen for Pyridinyl-PAE at 685nm. This corresponds with the shorter wavelength one photon ground state electronic absorption peak at 335nm for Pyridinyl PAE in solution.

The dispersion trends for the solid state film measurements are more difficult to identify. The difference in sign between the solid state  $\beta$  coefficients can clearly be seen in figure 6.5.11. Pyridinyl-PAV still has the lowest  $\beta$  coefficients at longer (off one-photon resonance) wavelengths, close to the values of Thienyl PAV. This is consistent with the solution measurements. Pyridinyl-PAE and Thienyl-PAE solid state  $\beta$  coefficients have opposite signs (attributed to saturable absorption) compared with solution measurements (two photon absorption). Both of the PAE polymers have  $\beta$  coefficients which are approximately four times larger (although different sign) than their PAV counterparts. This should have significant impact for the figure of merit calculations, since it can be seen from figure 6.5.12 that the two PAE polymers do not generally have  $\eta_2$  coefficients which are consistently four times larger than the two PAV polymers. This would indicate that the PAV polymers should have better T and W values compared with their PAE counterparts. Although the trends are not clear cut in figure 6.5.12, it can be seen that more often than not, the PAE polymers have higher  $\eta_2$  coefficients compared to the PAV polymers. The Pyridinyl-PAE polymer generally has higher  $\eta_2$  coefficients, while Pyridinyl PAV has the lowest values. At longer wavelengths Pyridinyl-PAE has the largest solid state  $\eta_2$  coefficients, followed closely by Thienyl-PAE and Thienyl-PAV, with Pyridinyl-PAV having the lowest values. It is suggested that the solid state  $\eta_2$  coefficients (at the longer wavelengths) for Pyridinyl-PAV and Thienyl-PAV are two photon enhanced, while the  $\eta_2$  coefficients for Pyridinyl-PAE and Thienyl-PAE are one photon enhanced.

The above dispersion trends for  $\beta$  and  $\eta_2$  coefficients do not agree with the prediction in chapter 4, which are based on the linear absorption spectra. Pyridinyl-PAE clearly has the largest solution  $\eta_2$  coefficient, which is at odds with the predicted trends. If the solution trends are compared with intra-(polymer) family trend predictions, then the linear absorption spectra predictions for the PAV polymers do agree with the observed trends. The same cannot be said about the PAE trends which are still at odds with the predictions. None of the solid state predictions (all together or intra-family) in chapter 4, agree with the observed experimental results. For the PAV polymers it is predicted that Pyridinyl-PAV should have larger  $\eta_2$  coefficients compared to Thienyl-PAV, which is again in contrast

with the experimental measurements. The experimental measurements show that the one dimensional backbone approximation which most of the predictive models in chapter 4 are based on, are too simplistic to adequately predict the nonlinear absorption or refraction trends for the four polymers in this thesis. The author would have great reservations if the predictions had indeed worked out as it is his firm belief that the solid state samples in particular must be modelled in three dimensions. Approximating a complex three-dimensional aggregated system as a pseudo one-dimensional system is a gross oversimplification. These findings would seem to limit the usefulness of experimental ground state electronic absorption as a predictive tool for the nonlinear optical absorption or refraction trends of newly synthesised polymers, particularly ones belonging to the PAE family of polymers.

One of the questions that this thesis also aims to address is to assess if solution measurements may be used to check for a polymers suitability for all optical switching at a given wavelength. This would be of great significance due to the nature of polymer synthesis, where it is much more economical, both financially and time wise to produce small milligram quantities of a new polymer, compared to the gram quantities necessary to fully facilitate proper solid state film formation and subsequent nonlinear measurements.

### 6.5.2 Nonlinear Optical Switching Figure Of Merit

One of the main requirements for all-optical switching materials is that they have suitable nonlinear optical figures of merit. The material should have a large nonlinear optical refractivity, which allows for switching of low light intensities as well as small device dimensions. As outlined in chapters 2 and 4, there are two figures of merit which indicate a particular material's suitability for optical switching. The first figure of merit  $T$ , is a measure of the materials suitability when nonlinear absorption the dominant imaginary process relative to linear absorption, and should be below unity for favourable materials. It is a measure of the materials ability to achieve the required nonlinear phase shift given an arbitrary interaction length. This will happen as long as the refractive nonlinearity is proportionately better than the absorptive nonlinearity at any given wavelength.

$$T = \frac{\lambda\beta}{2\eta_2} \quad 6.1$$

The second figure of merit  $W$ , is a measure of the materials suitability when linear absorption is the dominant imaginary process relative to nonlinear absorption. This value should be above unity for favourable materials. It's the combination of the above two

equations that govern a particular materials suitability as a worthy candidate for all-optical switching applications.

$$W = \frac{\eta_2 I_0}{\alpha \lambda} \quad 6.2$$

Ideally both equations should be favourable for a given wavelength. This is particularly so for the solid state PAE polymers, which have significant residual absorption at longer wavelengths. The solution and solid state  $\tau$  and  $W$  figure of merits were calculated for each polymer at all wavelength using the  $\beta$  and  $\eta_2$  coefficients obtained from Z-Scan experiments. Tables 6.x.1 ( $x=1,2,3,4$ ) contain the results of the calculations, which are subsequently plotted in figures 6.x.10 through 6.x.13 ( $x=1,2,3,4$ ). The resulting figures have shaded areas; green wherever the relevant figure of merit is favourable for all optical switching and red where unfavourable. Solution measurements were included in order to compare the solid state and solution trends.

As can be seen from the graphs, all four polymer have favourable solid state figures of merit over some part of the wavelength range. The Pyridinyl-PAV has the most favourable figures of merit ( $W_{\max}=59\pm44$ ), followed closely by Thienyl-PAV ( $W_{\max}=12\pm9$ ). Pyridinyl-PAE ( $W_{\max}=4.7\pm2.4$ ) and Thienyl-PAE ( $W_{\max}=4.5\pm2.4$ ) have figures of merit which are consistently less favourable than their PAV counterparts, despite the fact that Pyridinyl-PAE has  $\eta_2$  coefficients which are consistently larger than Pyridinyl-PAV. This is attributed to the significantly higher long wavelength solid state residual absorption (and subsequent nonlinear saturable absorption) which both of PAE polymers show in their linear absorption spectra. Pyridinyl-PAV and Thienyl-PAV both have solid state  $\beta$  coefficients which change sign (passing through zero) from negative (SA) to positive (2PA) as the measurements move from shorter to longer wavelengths. A zero value for  $\beta$  will give very a favourable (low)  $\tau$  figure of merit. The  $W$  figure of merit will then be the main determining factor in determining a materials suitability. Pyridinyl-PAV solid state  $\beta$  coefficients change sign between 505nm and 515nm, while Thienyl-PAV solid state  $\beta$  coefficients change sign between 575nm and 585nm. Both  $W$  figures of merit are still favourable at these wavelengths as can be seen in figures 6.1.11 and 6.2.11.

The solid state films generally have their best figure of merit values at different wavelength regions of the spectrum compared to solution measurements. The higher residual absorption in the solid state compared to the solutions, affects the figure of merits significantly. Consequently, if solution measurements are only carried out, wavelength

regions which would be favourable for optical switching where the switch has a predefined operational wavelength range, may no longer be favourable for the solid state counterpart. Solution measurements alone cannot therefore be used to characterise a polymers suitability for solid state all optical switching applications. Solution measurements can be used to determine if a particular polymer has a larger nonlinear refractive index compared to a known sample. This can be useful in cases where only very small samples of polymer are available. However, if the aim of the experiment is to see if a polymer is a suitable candidate for all optical switching at any particular wavelength, then all relevant measurements must be carried out on the polymer in solid state form.

### 6.5.3 Resonant versus Non-Resonant Nonlinearity

Another requirement for all-optical switching materials is that they have fast response and decay times, thus enabling high bandwidth operation. If the switch is operated under off resonance conditions, the response time of the switch is typically  $\sim 10^{-15}$  seconds. If the nonlinearity is resonantly enhanced then the response time may increase to  $\sim 10^{-9}$  seconds. Figures 6.x.5 through 6.x.8 (x=1,2,3,4) can be used to see the effects of resonant enhancement of  $\eta_2$ , through two photon absorption and saturable absorption, compared with three photon absorption enhancement of  $\eta_2$ . At 532nm Thienyl-PAV solutions have negative  $\beta$  coefficients due to saturation of absorption. The other three polymers have positive  $\beta$  coefficients due to two photon absorption or reverse saturable absorption. At 1064nm Thienyl-PAV solution has a third-order two-photon enhanced  $\eta_2$  coefficient, due to the linear absorption at 532nm, whereas Pyridinyl-PAE at the same wavelength has a three photon enhanced  $\eta_2$  coefficient (no absorption at 532nm).

#### Solid State – YAG Laser 532nm

Polymer	$\eta_2$ Solid State ( $\times 10^{-14}$ m <sup>2</sup> /W)	$\beta$ Solid State ( $\times 10^{-8}$ m/W)	T (Solid State)	W (Solid State)
Thienyl - PAE	$-1.730 \pm 0.519$	$-2.600 \pm -0.806$	$0.399 \pm 0.243$	$1.700 \pm 0.901$
Pyridinyl - PAE	$-1.210 \pm 0.387$	$-1.780 \pm -0.570$	$0.393 \pm 0.252$	$2.070 \pm 1.180$
Thienyl - PAV	$-0.251 \pm 0.058$	$-2.570 \pm -0.617$	$2.730 \pm 1.283$	$0.633 \pm 0.247$
Pyridinyl - PAV	$-0.658 \pm 0.329$	$1.520 \pm 0.760$	$0.614 \pm 0.461$	$11.400 \pm 8.550$

**Table 6.5.1:** The real component  $\eta_2$  and imaginary component  $\beta$  of  $\chi^{(3)}$  for all four polymers at 532nm. Also included are the nonlinear optical switching figures of merit **T** and **W**. All the above measurements were performed using the YAG Laser set-up.

### Solid State – YAG Laser 1064nm

Polymer	$\eta_2$ Solid State ( $\times 10^{-14}$ m <sup>2</sup> /W)	$\beta$ Solid State ( $\times 10^{-8}$ m/W)	T (Solid State)	W (State)
Thienyl - PAE	$-0.028 \pm 0.014$	$0.016 \pm 0.008$	$3.113 \pm 2.335$	$0.031 \pm 0.023$
Pyridinyl - PAE	$-0.039 \pm 0.020$	$0.114 \pm 0.057$	$1.544 \pm 1.158$	$0.057 \pm 0.043$
Thienyl - PAV	$-0.064 \pm 0.032$	$0.190 \pm 0.095$	$1.570 \pm 1.178$	$1.420 \pm 1.065$
Pyridinyl - PAV	$-0.020 \pm 0.010$	$0.050 \pm 0.025$	$1.304 \pm 0.978$	$0.212 \pm 0.159$

**Table 6.5.2:** The real component  $\eta_2$  and imaginary component  $\beta$  of  $\chi^{(3)}$  for all four polymers at 1064nm. Also included are the nonlinear optical switching figures of merit **T** and **W**. All the above measurements were performed using the YAG Laser set-up.

Tables 6.5.1 and 6.5.2 combine the solid state results for all four polymers. The resonance enhancement at 532nm due to SA and 2PA can be clearly seen. While Pyridinyl-PAE has a  $\eta_2$  coefficient nearly twice that of Pyridinyl-PAV, the *W* figure of merit is much more favourable for Pyridinyl-PAE due to its lower residual linear absorption.

#### 6.5.4 Possible Thermal Contributions

As mentioned in chapter 3, the Z-scan method is sensitive to all nonlinear optical mechanisms that give rise to a change of the refractive index and/or absorption coefficient, so that determining the underlying physical processes present from a Z-scan is not in general possible. A series of Z-scans at varying pulse-widths, frequencies, focal geometries etc., along with a variety of other experiments are often needed to unambiguously determine the relevant mechanisms. Thermal nonlinearity always leads to a negative  $\eta_2$  value. To avoid thermal contributions the optical pulse length  $\tau_{FWHM}$  should be less than 100ps<sup>5</sup> or even tens of nanoseconds<sup>6</sup>. The build-up time  $\tau_{bu}$  of a thermal nonlinearity is given by<sup>7</sup>

$$\tau_{bu} = \frac{\omega_0}{v_s} \quad 6.3$$

where  $\omega_0$  is the beam waist at focus and  $v_s$  is the velocity of sound. For the 532nm laser measurements, the beam waist at focus was  $14.5 \pm 1.9 \mu\text{m}$  and the velocity of sound was taken as 1170m/s. This corresponds to a thermal nonlinearity build-up time of  $12.4 \pm 1.6 \text{ns}$ , which is 24 times longer than the Dye laser pulse lengths of 500ps. The thermal relaxation time  $\tau_r$  corresponding to the diffusion of whatever heating is generated per pulse is given by<sup>8</sup>

$$\tau_r = \frac{\omega_0^2}{4D} \quad 6.4$$

where  $\omega_0$  is the beam waist at focus and  $D$  is the diffusive coefficient. Taking the beam waist as  $14.5 \pm 1.9 \mu\text{m}$  once again and a diffusive coefficient of  $1 \times 10^{-3} \text{ cm}^2 \text{ s}^{-1}$ , gives a relaxation time of  $0.5 \pm 0.1 \text{ ms}$ , compared with the  $100 \text{ ms}$  separating each laser shot. It would appear that not only does the thermal nonlinearity not have time to build up, but it is also gone when the next laser shot arrives on the sample. If the thermal nonlinearity was of any consequence, the value of  $\eta_2$  would be building up as the experiment is continued. This effect would be characterised by an asymmetric Z-Scan signature, with the peak or valley enhanced, depending on which one is scanned last and the sign of the intrinsic nonlinearity to which the thermal component is added. The experimental Z-Scan signatures did not display such a feature. This arguments above would indicate that the origin of the third order  $\eta_2$  nonlinearity is not thermal.

### 6.5.5 Related Publications

It has become apparent to the author while reviewing the literature, that there are no publications which are directly relevant to the work presented in this thesis. In fact, this is the only study known to the author where four structurally related conjugated polymers have been studied over the  $465 \text{ nm}$  to  $685 \text{ nm}$  wavelength range, which encompasses the “fibre to the home” wavelengths, discussed in chapter 4. However, the most relevant and closely related publications, though sparse in number, are now reviewed.

The effective third order nonlinear refraction coefficients ( $\eta_2$ ) obtained for solid state films measured in this thesis range from a low of  $-2.00 \times 10^{-16} \text{ m}^2/\text{W}$  for Pyridinyl-PAV at  $1064 \text{ nm}$ , up to a maximum of  $-2.43 \times 10^{-13} \text{ m}^2/\text{W}$  for Pyridinyl-PAV at  $465 \text{ nm}$ . The increase of over three orders of magnitude at  $465 \text{ nm}$  is attributed to resonance enhancement, through saturation of the linear absorption at this wavelength. Similar trends are present for the other three polymers. The effective third order nonlinear absorption ( $\beta$ ) coefficients obtained for the solid state films ranged from  $+3.27 \times 10^{-7} \text{ m/W}$  (attributed to reverse saturable absorption) for Pyridinyl-PAV at  $525 \text{ nm}$  to  $-1.4 \times 10^{-6} \text{ m/W}$  (attributed to saturable absorption) for Thienyl-PAE at  $465 \text{ nm}$ .

Yang et al.<sup>9</sup> reports about the self-defocusing and nonlinear absorption in polythiophene thin films using the Z-Scan technique. Measurements are carried out at  $532 \text{ nm}$  using  $30 \text{ ps}$  pulses. The third order nonlinear refraction coefficient ( $\eta_2$ ) reported is  $-9.0 \times 10^{-15} \text{ m}^2/\text{W}$ , and is attributed to resonance enhancement, through saturation of the strong linear absorption ( $\alpha = 4 \times 10^4 \text{ cm}^{-1}$ ) at the wavelength measured. This is consistent with the results seen for all

four of the polymers in this thesis, in that saturable absorption is seen for all Z-Scan measurements which were carried out at one photon resonance wavelengths. The magnitude and sign of  $\eta_2$  for polythiophene is between the range reported for the polymers in this thesis. The negative sign of the nonlinearity is deemed consistent with other reported measurements relating to conjugated polymers.

Thakur et al.<sup>10</sup> reports about the measurement of the sign and magnitude of the off-resonant nonlinearities of polydiacetylene paratoluene-sulfonate (PTS) using Z-Scan. PTS has been looked at as a candidate material for all optical switching applications at infrared wavelengths. Measurements are carried out at 1064nm using 10ps pulse trains where the repetition rate and average power are controlled with a Pockels cell. They report a negative value of the intensity-dependent refractive index  $\eta_2 = (-1.5 \pm 0.5) \times 10^{-15} \text{ m}^2/\text{W}$  and a positive value of the intensity-dependent absorption coefficient  $\beta = (6.5 \pm 1.2) \times 10^{-6} \text{ m/W}$  which is attributed to two-photon absorption. This result is somewhat consistent with the results seen for the polymers in this thesis. Thienyl-PAV and Pyridinyl-PAV both have positive  $\beta$  values at the longer off resonance wavelengths, which is also attributed to two-photon absorption. Thienyl-PAE and Pyridinyl-PAE in contrast, have negative  $\beta$  values at the same longer wavelengths. These negative values are attributed to saturation of the residual linear absorption, which is present in both of the PAE polymers at these longer wavelengths. The author believes that two-photon absorption is also occurring at these longer wavelengths, but is not the dominant nonlinear absorptive process. The negative  $\beta$  values at the longer wavelengths can also be attributed to scattering by the solid state films, which may have a polycrystalline nature, owing to the rigid rod-like structure of the PAE polymers. The magnitude and sign of  $\eta_2$  for PTS is again between the range reported for the polymers in this thesis.

A study by Lawrence et al.<sup>11</sup> also reports about the measurement of the sign and magnitude of the off-resonant nonlinearities of single crystal polydiacetylene paratoluene-sulfonate (PTS). Measurements are carried out this time at 1600nm. They report a large purely refractive nonlinear index,  $\eta_2 = -2.2 \times 10^{-16} \text{ m}^2/\text{W}$ . There is no measurable two-photon absorption and the linear absorption  $\alpha$  is approximately  $1\text{cm}^{-1}$  making this material useful for all-optical switching applications at this wavelength. A plot of the effective  $\eta_2$  versus intensity shows a straight line with a negative slope indicating that there is a fifth order nonlinearity reducing the total index change at higher intensity levels. The lower value for



$\eta_2$  in this report compared with Thakur et al. is attributed to the fact that the  $\eta_2$  value for PTS at 1064nm is two photon enhanced, where as the value at 1600nm is the true off-resonance (electronic contribution only) value.

Another study by Underhill et al.<sup>12</sup> uses degenerate four wave mixing and Z-Scan to study nonlinear absorption and nonlinear refraction in PMMA films doped with Ni-dithiolene oligomers at 1064nm to determine their suitability for all-optical switching applications. They report favourable figures of merit for some of the compounds, but no linear coefficients are given.

In reviewing the above, the author feels that there is a need for more research to be carried out on new and existing materials within the wavelength range covered within this thesis.

## References

---

- 1 S. Hughes, J. M. Burzler, G. Spruce and B. S. Wherrett, *J. Opt. Soc. Am. B*, 12, 1888, 1995
- 2 Ph.D. thesis by Emmanuel Bourdin, Trinity College Dublin, Dept. of Pure and Applied Physics, Chapter 2
- 3 G.P. Agrawal, C. Cojan and C. Flytzanis, *Phys. Rev. B*, 17, 776, 1978
- 4 N. C. Greenham, R. H. Friend, *Solid State Physics*, Vol. 49, Academic Press, San Diego, 2, 1995
- 5 P. N. Prasad and D. J. Williams, "Introduction to Nonlinear Optical Effects in Molecules and Polymers, Wiley, New York, 1991
- 6 J. Staromlynska, R. M. Fortenberry, C. T. Seaton and G. I. Stegeman, "Electronic versus Thermal Response for Nonlinear Prism Coupling", *Appl. Opt.*, 31, 1170, 1992
- 7 J. Tian, C. Zhang, G. Zhang and J. Li, *Appl. Opt.*, 32, 6628, 1993
- 8 J. Sakai, "Phase Conjugate Optics", McGraw-Hill Inc., 135, 1992
- 9 Yang, L., Dorsinville, R., Wang, Q., Ye, P. and Alfano, R., Excited-state nonlinearity in polythiophene thin films investigated by the Z-Scan technique, *Opt. Lett.*, 17, 323-325, 1992
- 10 Thakur, M. and Quintero-Torres, R., The sign and magnitude of the off-resonant nonlinearities of polydiacetylene crystal measured by Z-Scan, *SPIE*, 2025, 446-449, 1993
- 11 Lawrence, B., Cha, M., Kang, J., Torruellas, W., Stegeman, G., Baker, G., Meth, J. and Etemad, S., Large purely refractive nonlinear index of a single crystal P-toluene sulphonate (PTS) at 1600nm, *Electron. Lett.*, 30, 447-448, 1994
- 12 Gall, G., King, T., Oliver, S., Capozzi, C., Seldon, A., Hill, C. and Underhill, A., Third-order optical properties of metal dithiolene and phthalocyanine doped sol-gel materials, *SPIE*, 2288, Sol-Gel Optics, 372-381, 1994

## 7 Conclusions

This chapter presents the conclusions that were determined, based on the results presented in chapters 4, 5 and 6. Additional experimental measurements that may be required are discussed, as well as some proposed improvements to the current Z-Scan experimental set-up.

### 7.1 Nonlinear Refraction and Absorption

Solid state and solution measurements of effective third order nonlinear absorption and refraction, have been carried out on Pyridinyl PAV, Thienyl-PAV, Pyridinyl-PAE and Thienyl-PAE using the Z-Scan experimental technique. The  $\eta_2$  coefficients obtained for solid state films ranged from  $-2.00 \times 10^{-16} \text{ m}^2/\text{W}$  for Pyridinyl-PAV at 1064nm, up to  $-2.43 \times 10^{-13} \text{ m}^2/\text{W}$  for Pyridinyl-PAV at 465nm, while the  $\beta$  coefficients obtained for the solid state films ranged from  $+3.27 \times 10^{-7} \text{ m/W}$  for Pyridinyl-PAV to  $-1.4 \times 10^{-6} \text{ m/W}$  for Thienyl-PAE.

There are differences between the semi-empirical calculated values for the HOMO-LUMO absorption maxima and the experimentally measured solution and solid state values. However, the calculated absorption trends agree with the experimentally measured solution HOMO-LUMO absorption trends. This agreement does not extend to the experimentally measured solid state HOMO-LUMO absorption trends, although the trends within each polymer family (for solution and solid state) are correct. The semi-empirical calculations which are performed *in vacuo*, do not take into account the aggregation effects which are seen to play a significant role in the four polymers solid state absorption spectra. The results indicate that semi-empirical calculations may, in closely related polymers families, be used to investigate the solution HOMO-LUMO absorption trends. Any trends obtained from semi empirical computer modelling of absorption must therefore be treated with caution when comparing polymers from different structural families in their solid state.

The results demonstrate that it is difficult to relate the nonlinear optical trends observed for the four measured polymers, to the variation in maximum ground state electronic absorption for each of the polymers, with any degree of certainty. This is true for solid state as well as for solution measurements. The experimental measurements show that the one dimensional backbone approximation on which most of the predictive models are based are too simplistic; approximating a complex three-dimensional aggregated system as a pseudo

one-dimensional system is a gross over-simplification. The findings would seem to limit the usefulness of using experimental ground state electronic absorption as a predictive tool for the nonlinear optical absorption or refraction trends of newly synthesised polymers, particularly those belonging to the PAE family of polymers.

The varying trends observed in nonlinear absorption measurements between solution and solid state (on-set of one photon resonance and dominant nonlinear absorption loss mechanism) indicate that solid state measurements must be performed if materials are being evaluated for solid state applications. Estimating the solid state nonlinear optical coefficients based on extrapolation of solution dispersion measurements (which are easier to apply) will lead to incorrect wavelength dependence.

## 7.2 Nonlinear Optical Switching Figures of Merit

All four polymers are suitable for all optical switching at various wavelengths. The PAV polymers have more favourable figures of merit for all optical switching over a greater wavelength range compared to the PAE polymers, even though the Thienyl-PAE polymer has  $\eta_2$  coefficients which are consistently larger than the Pyridinyl-PAV. This is attributed to the larger solid state residual ground state electronic absorption of the PAE polymers at longer wavelengths compared with their PAV counterparts. This lower first order linear absorption gives the PAV polymers better figures of merit for all optical switching at a given wavelength, outweighing the fact that the PAE polymers have consistently higher third order  $\eta_2$  coefficients compared with their PAV counterparts. The linear absorption spectra can therefore be used as a predictive tool in determining the possible trends for all-optical switching figures of merit.

## 7.3 Proposed Future Work

### Polymer Engineering

All four polymers have suitable nonlinear optical switching figures of merit over some of the wavelength range (465nm - 685nm). The next logical step would be to measure the nonlinear optical parameters in a channel waveguide structure, which would be much more complicated and time consuming. The polymer with the best figures of merit (Pyridinyl-PAE) has the sharpest band edge with the lowest longer wavelength residual absorption. This is however not the most nonlinear of the polymers in solid state. The computer

modelling of the ground state electronic spectra show that the pentamer oligomers have acquired long chain polymer absorption characteristics. It is suggested that Pyridinyl-PAE pentamers or hexamers with large side groups, may reduce the residual absorption seen in the Pyridinyl-PAE solid state spectra, thus improving the figures of merit. The subsequent solid state films should have a sharp absorption band (relative to the long chain polymer) due to the smaller amount of conjugation fluctuations expected for the rigid pentamers or hexamers. The large side groups should help to isolate the polymer chains, thus minimising polymer chain interaction effects. This should bring solution and solid measurement trends closer. The large side groups should also increase the solubility along with helping to make good quality films which is a requirement for all-optical switching materials. This is essential, if the material is going to be used in a waveguide structure, on which most current all-optical switch designs are based.

## Experiment Enhancements

The author believes that the measurement technique may be significantly improved by replacing the reference and open aperture photodiodes with two CCD arrays. A cross sectional snap shot of the beam is thus taken for each pulse. Geometrical calculations may then be performed on the resulting images which simulate different closed aperture as well as open aperture Z-Scans. The main benefits of this method can be summarised as follows.

### 1 Less Optics

There are less optics present in the system. This will reduce the spatial noise acquired by the beam when being reflected off, or transmitted through the (less than perfect) optical components.

### 2 Spatial Noise

Spatial noise can be measured and the particular pulse ignored, if above a user defined threshold. Spatial beam noise is considered to be the main source of noise in the experimental set-ups used for all measurements within the thesis. This spatial beam noise increases the detectability limit of the experiment. Reducing or eliminating the effects of the spatial noise, will increase the accuracy of the measurements.

However, substantial time and money would have to be invested in both acquiring the CCD arrays, controllers and digitisation equipment as well as the appropriate software.

### **Concluding Remarks**

It is not possible to unambiguously state whether or not the four polymers satisfy all the requirements for all optical switching. In order to remove the ambiguity and definitively establish the potential of these materials, it will be necessary to fully investigate their linear and nonlinear optical properties in a channel waveguide geometry. However, it is possible to unambiguously state that each of the four polymers which were assessed in this thesis, can not be ruled out as possible candidates for all optical switching at various wavelengths over the range 465nm to 685nm, based on the presented results.

## Appendix 1

This appendix contains the source code listing for the control software used for the Z-Scan measurements. The source language is a mixture of Ansi C and C++. The first listing is ZSCAN.C which is the code used to take the measurements as well as move the computer controlled translation stage. This is then followed by ZSCAN.BAT code listing which is the batch file containing parameters which define how the measurements are to be performed. This batch file is used to initialise the Z-Scan experiment.

### Z-Scan.C

```
#include <stdio.h>
#include <graphics.h>
#include <conio.h>
#include <stdlib.h>
#include <alloc.h>
#include <math.h>
#include <dos.h>
#include <string.h>
#include <dir.h>

#define INT_NO2 0X0b /* Used in SETPORT */
#define INT_EN2 0x2f9 /* Used in SETPORT */
#define MOD_CON2 0x2fc /* Used in SETPORT */

#define BUFFERLIMIT 600L /* Maximum SIZE (3*200) for Data Array (L standsfor Long Int) */
#define MaxTraces 100L /* Max Number of Traces (L standsfor Long Int) */

unsigned int SAMPLES_REQUESTED; /* Number of Samples to be taken */
unsigned int DISTANCE; /* Total distance the Z-Stage moves */
unsigned int NUMBER_OF_MOVES; /* Number of Moves Z-Stage makes during one Z-Scan */
unsigned int NUMBER_OF_STEPS_PER_MOVE; /* Stepsize * RESOLUTION of Stepper Motor */
unsigned int STABILITY_AVERAGING; /* Number of Averaging for Laser Stability */
unsigned int ZSCAN_AVERAGING; /* Number of Averaging for ZSCAN */

unsigned int RESOLUTION; /* RESOLUTION of Stepper Motor (80 Steps per mm) */
unsigned int DELAY_MOTOR=2; /* DELAY between Each step the stepper motor makes (mS) */
unsigned int COM;
unsigned int OUT_BYTE;
unsigned int DIRECTION;
unsigned int X;
unsigned int RETURN=0;
unsigned int OMASK; /* Used in SETPORT */
unsigned int NMASK; /* Used in SETPORT */
unsigned int MOTOR=4; /* Used in SETPORT */
unsigned int INTR_NO=0; /* Used in SETPORT */

unsigned int ADC_VAR_A[BUFFERLIMIT]; /* Used to send Parameters (CCALL) to ADC Card */
unsigned int ADC_VAR_B[BUFFERLIMIT]; /* Used to send Parameters (CCALL) to ADC Card */
unsigned int NUMCHANNELS=3; /* Number of Channels to be used */
unsigned int DELAY=1.0; /* Delay (in mS) to be used for all Channels */
unsigned int TRIGGERED=1; /* Trigger Enabled */
unsigned int TRIGGERMODE=1; /* Normal Trigger, Analog Trigger, Positive Slope */
unsigned int TRIGGERLEVEL; /* Trigger level 0-10V in 128 values */
```

```

unsigned int PRETRIGGER; /* Number of Points Before Trigger */
unsigned int USE_EXTENDED_BUFFER=1; /* Uses 64K On-Board Memory for Fast Readings */
unsigned int RESET; /* Used to put the ADC Board in & out of Extended Buffer Mode */
unsigned int RETRIGGER; /* Used in Conjunction with the Extended Buffer */
unsigned int ZSCAN; /* This is used to determine which plot to use in the graph function */
unsigned int COUNTER1; /* General Workhorse Integer used for Loops & Things */
unsigned int COUNTER2; /* General Workhorse Integer used for Loops & Things */
unsigned int COUNTER3; /* General Workhorse Integer used for Loops & Things */
unsigned int XVALUE; /* Used in Graph Function for Co-ordinates and Introduction */
unsigned int YVALUE; /* Used in Graph Function for Co-ordinates and Introduction */
unsigned int TEMP; /* Used as a general variable */
unsigned int NORMALISED; /* Switches between NORMALISED or UN-NORMALISED MAXY */

float REFERENCE[200]; /* Initialised array for Sampled data from ADC Card Channel 1 */
float OPEN_SCAN[200]; /* Initialised array for Sampled data from ADC Card Channel 2 */
float CLOSED_SCAN[200]; /* Initialised array for Sampled data from ADC Card Channel 3 */
float RESULTS_REFERENCE[1000]; /* Array to store MEAN of REFERENCE for Z position */
float RESULTS_OPEN_SCAN[1000]; /* Array to store MEAN of OPEN_SCAN for Z position */
float RESULTS_CLOSED_SCAN[1000]; /* Array to store MEAN of CLOSED_SCAN for Z position*/
float VOLTAGE; /* Used to Read in Trigger Voltage as a Float */
float ANALOGBUF[BUFFERLIMIT]; /* This Array Holds the Analog Values Sampled by Card */
float MAXY_REFERENCE; /* This is used to store the maximum value of Y for SAMPLE1 Array */
float MAXY_OPEN_SCAN; /* This is used to store the maximum value of Y for SAMPLE2 Array */
float MAXY_CLOSED_SCAN; /* This is used to store maximum value of Y for SAMPLE3 Array */
float MEAN_MAXY_REFERENCE_ARRAY[1000]; /* Mean max values of Y for SAMPLE1 Array */
float MEAN_MAXY_REFERENCE; /* Mean max values of Y for SAMPLE1 Array */
float MEAN_MAXY_OPEN_SCAN_ARRAY[1000]; /* Mean max values of Y for SAMPLE2 Array */
float MEAN_MAXY_OPEN_SCAN; /* Mean max value of Y for SAMPLE2 Array */
float MEAN_MAXY_CLOSED_SCAN_ARRAY[1000]; /* Mean max values of Y for SAMPLE3 Array*/
float MEAN_MAXY_CLOSED_SCAN; /* Mean max value of Y for SAMPLE3 Array */
float LASER_STABILITY; /* Used to Store the Value of the Reference for the Laser Stability */
float LASER_STABILITY_ARRAY[1000]; /* Values of the Reference for the Laser Stability */
float PERCENTAGE_VARIATION; /* Amount of Variation permitted during the Z-Scan */
float LOWER_LIMIT; /* Used for Percentage variation */
float UPPER_LIMIT; /* Used for Percentage variation */
float STEPSIZE; /* DISTANCE between steps */
float CURRENT_POSITION=0; /* Current position of Z-Stage (equals zero starting off) */
float REFERENCE_NORMAL; /* Holds normalisation constant to normalise to 1 */
float OPEN_NORMAL; /* Holds normalisation constant to normalise to 1 */
float CLOSED_NORMAL; /* Holds normalisation constant to normalise to 1 */

char INPUT; /* Used for General Input */
char INPUT2[2]; /* Used for General Input */
char TEXT[64]; /* Used for Getting Variables to the Screen in Text Mode & in the Introduction */
char *PATH; /* Used for storing the path name where the data files are to be saved */

FILE *fp2; /* fp2 is the file pointer for saving the data file at the end */

void CONVERT_STEP(void);
void MOVE_STAGE(void);
void SET_ZERO_POSITION(void);
void interrupt SIO_HANDLER(void);

int SET_UP_STEPPER_MOTOR(void); /* Declaration */

void GET_MAX_VALUE_OF_Y(void); /* Declaration of GET_MAX_VALUE_OF_Y */
void SET_UP_ADC_CARD(void); /* Used to initialise the Card with The Proper Settings */
void SET_UP_GRAPHICS(void); /* Declaration of Start up of the Graphics mode */
void ACQUIRE_SAMPLES(void); /* Used to get ONE set of Readings */
void TEXT1(void); /* Function to print some text to the Graphics screen */
void TEXT2(void); /* Function to print some text to the Graphics screen */
void TEXT3(void); /* Function to print some text to the Graphics screen */

```



```

void TEXT4(void); /* Function to print some text to the Graphics screen */
void GRAPH (void); /* Declaration of function graph */
void CCALL(const char *, float *, unsigned int *); /* Declaration for CCALL Function */
void INTRODUCTION_SCREEN(void); /* Introduction Screen */

main (int argc, char *argv[]) {
PATH=argv[1];
DISTANCE=atoi(argv[2]);
STEPSSIZE=atof(argv[3]);
SAMPLES_REQUESTED=atoi(argv[4]);
RESOLUTION=atoi(argv[5]);
VOLTAGE=atof(argv[6]);
PRETRIGGER=atoi(argv[7]);
NUMBER_OF_MOVES=(DISTANCE/STEPSSIZE); /* DISTANCE between steps */
NUMBER_OF_STEPS_PER_MOVE=(RESOLUTION*STEPSSIZE);
SET_UP_GRAPHICS();
if (argc!=8)
    {outtextxy(120,220,"DOOOooooohhhhHHHHH Wrong number of arguments - should be 6!");
/*This prints text to the graphics screen */
    delay(3000); /* Delays the computer by 1000 milliseconds */
    cleardevice(); /* Clears the entire screen */
    closegraph(); /* Ends Graphics Mode & resets to standard DOS Screen */
    exit(0);}
ZSCAN=0; /* The SAMPLES will be plotted by GRAPH() if ZSCAN=1 */
NORMALISED=0; /* MAXY_OPEN_SCAN Normalised or not */
INTRODUCTION_SCREEN();
SET_UP_ADC_CARD();
SET_UP_GRAPHICS();

LOOP1:
while(!kbhit()) { ACQUIRE_SAMPLES();
    GET_MAX_VALUE_OF_Y();
    GRAPH();
    TEXT2();
    TEXT4(); }

INPUT=getch();
if(INPUT=='x') goto CONTINUE_HERE;
goto LOOP1;

CONTINUE_HERE:
LASER_STABILITY_QUESTION:
cleardevice(); /* Clears the entire screen */
setcolor(13); /* Set Color to light Magenta */
settextstyle(7,0,0); /* Text Style Font,Direction(horiz or vert),Size(0) */
setusercharsize(1,1,1,1); /* This is used to size the simplex fonts */
outtextxy(10,110,"Now the Laser Stability will be Tested"); /* Prints text to the graphics screen */
settextstyle(2,0,0); /* Text Style Font,Direction(horiz or vert),Size(0) */
setusercharsize(1,1,2,1); /* This is used to size the simplex fonts */
outtextxy(165,225,"Enter the Number of shots (<999) to Average :"); /* Prints text to the screen */
setcolor(2); /* Set Color to Green */
COUNTER1=0;
COUNTER2=0;
do {INPUT=getch();
    TEXT[COUNTER1]=INPUT;
    if(INPUT == 'q') {closegraph();exit(0);}
    if(INPUT!=13) {outtextxy((431+COUNTER2),225,&INPUT);} /* This prints text to the screen */
    COUNTER2=COUNTER2+7;
    COUNTER1++;} while (INPUT!=13);
STABILITY_AVERAGING = atoi(TEXT);
if(STABILITY_AVERAGING>999) {goto LASER_STABILITY_QUESTION;}

```

```

LASER_STABILITY=0;
SET_UP_GRAPHICS();
ACQUIRE_SAMPLES();
GET_MAX_VALUE_OF_Y();
LASER_STABILITY_ARRAY[0]=MAXY_REFERENCE;
LASER_STABILITY=LASER_STABILITY_ARRAY[0]; /* Working out Mean Laser Stability */
GRAPH();
TEXT3();

COUNTER2=0;
settextstyle(2,0,0); /* Text Style Font,Direction(horiz or vert),Size(0) */
setusercharsize(1,1,2,1); /* This is used to size the simplex fonts */
setcolor(1); /* Blue */
outtextxy(475,45,"Sample Number ="); /* This prints text to the graphics screen */
sprintf(TEXT,"%3i",COUNTER2+1);
outtextxy(567,45,TEXT);

for (COUNTER2=1;COUNTER2<STABILITY_AVERAGING;COUNTER2++)
{ACQUIRE_SAMPLES();
GET_MAX_VALUE_OF_Y();
LASER_STABILITY_ARRAY[COUNTER2]=MAXY_REFERENCE;
LASER_STABILITY=0; /* Have to do this to get loop to work! */
for(COUNTER1=0;COUNTER1<=COUNTER2;COUNTER1++)
{LASER_STABILITY=LASER_STABILITY+LASER_STABILITY_ARRAY[COUNTER1];}
LASER_STABILITY=LASER_STABILITY/((float)(COUNTER2+1)); /* Work Mean Laser Stability */
GRAPH();
TEXT3(); /* Laser Stability */

settextstyle(2,0,0); /* Text Style Font,Direction(horiz or vert),Size(0) */
setusercharsize(1,1,2,1); /* This is used to size the simplex fonts */
setcolor(1); /* Blue */
outtextxy(475,45,"Sample Number ="); /* This prints text to the graphics screen */
sprintf(TEXT,"%3i",COUNTER2+1);
outtextxy(569,45,TEXT);}

setcolor(13); /* Set Color to light Magenta */
settextstyle(2,0,0); /* Text Style Font,Direction(horiz or vert),Size(0) */
setusercharsize(1,1,2,1); /* This is used to size the simplex fonts */
outtextxy(270,320,"Press a Key"); /* This prints text to the graphics screen */
getch();

cleardevice(); /* Clears the entire screen */
setcolor(13); /* Set Color to light Magenta */
settextstyle(7,0,0); /* Text Style Font,Direction(horiz or vert),Size(0) */
setusercharsize(1,1,1,1); /* This is used to size the simplex fonts */
outtextxy(55,70,"Now the Z-Scan will be Taken");
settextstyle(2,0,0); /* Text Style Font,Direction(horiz or vert),Size(0) */
setusercharsize(1,1,2,1); /* This is used to size the simplex fonts */
setcolor(2); /* Set Color to light Magenta */
outtextxy(70,150,"Channel 1 Reference, Channel 2 Open Aperture , Channel 3 Closed Aperture");
outtextxy(240,190,"All channels are 0-10V");
outtextxy(180,230,"Total Number of Samples per Channel is");
sprintf(TEXT,"%i",SAMPLES_REQUESTED);
outtextxy(408,230,TEXT);
outtextxy(200,270,"Total Distance Z-Stage moves is   mm");
sprintf(TEXT,"%i",DISTANCE);
outtextxy(387,270,TEXT);
outtextxy(210,310,"The Stepsize for this scan is   mm");
sprintf(TEXT,"%1.2f",STEPSIZE);
outtextxy(387,310,TEXT);
outtextxy(150,350,"Both the Open & Closed Aperture Z-Scan ARE Normalised to 1");
setcolor(13); /* Set Color to light Magenta */

```

```

settextstyle(2,0,0); /* Text Style Font,Direction(horiz or vert),Size(0) */
setusercharsize(1,1,2,1); /* This is used to size the simplex fonts */
outtextxy(270,430,"Press a Key"); /* This prints text to the graphics screen */
getch();

```

#### ZSCAN\_AVERAGING\_QUESTION:

```

cleardevice(); /* Clears the entire screen */
setcolor(13); /* Set Color to light Magenta */
settextstyle(7,0,0); /* Text Style Font,Direction(horiz or vert),Size(0) */
setusercharsize(1,1,1,1); /* This is used to size the simplex fonts */
outtextxy(80,110,"At Each Z-Scan Position . . ."); /* This prints text to the graphics screen */
settextstyle(2,0,0); /* Text Style Font,Direction(horiz or vert),Size(0) */
setusercharsize(1,1,2,1); /* This is used to size the simplex fonts */
outtextxy(165,225,"Enter the Number of shots (<999) to Average :"); /* Prints text to the screen */
setcolor(2); /* Set Color to Green */
COUNTER1=0;
COUNTER2=0;
do {INPUT=getch();
    TEXT[COUNTER1]=INPUT;
    sprintf(INPUT2,"%1c",INPUT);
    if(INPUT == 'q') {closegraph();exit(0);}
    if(INPUT!=13) {outtextxy((429+COUNTER2),225,INPUT2);} /* Prints text to the screen */
    COUNTER2=COUNTER2+7;
    COUNTER1++;} while (INPUT!=13);
ZSCAN_AVERAGING = atoi(TEXT);
if(ZSCAN_AVERAGING>999) {goto ZSCAN_AVERAGING_QUESTION;}

```

#### PERCENTAGE\_VARIATION\_QUESTION:

```

cleardevice(); /* Clears the entire screen */
setcolor(13); /* Set Color to light Magenta */
settextstyle(2,0,0); /* Text Style Font,Direction(horiz or vert),Size(0) */
setusercharsize(1,1,2,1); /* This is used to size the simplex fonts */
outtextxy(165,145,"The Mean Reference for Laser Stability was =");
sprintf(TEXT,"%5.3f",LASER_STABILITY);
outtextxy(427,145,TEXT);
outtextxy(168,210,"Enter Percentage Variation Permitted :"); /* Prints text to the graphics screen */
setcolor(2); /* Set Color to light Green */
COUNTER1=0;
COUNTER2=0;
do {INPUT=getch();
    TEXT[COUNTER1]=INPUT;
    sprintf(INPUT2,"%1c",INPUT);
    if(INPUT == 'q') {closegraph();exit(0);}
    if(INPUT!=13) {outtextxy((392+COUNTER2),210,INPUT2);} /* Prints text to graphics screen */
    COUNTER2=COUNTER2+7;
    COUNTER1++;} while (INPUT!=13);
PERCENTAGE_VARIATION = atof(TEXT);
if(PERCENTAGE_VARIATION>100.0) {goto PERCENTAGE_VARIATION_QUESTION;}
PERCENTAGE_VARIATION=PERCENTAGE_VARIATION/100.0;
LOWER_LIMIT=LASER_STABILITY*(1.00000-PERCENTAGE_VARIATION);
UPPER_LIMIT=LASER_STABILITY*(1.00000+PERCENTAGE_VARIATION);

```

```

SET_UP_STEPPER_MOTOR(); /* Set up the COM port Stuff */
DIRECTION=8; /* Should be moving towards MOTOR */
OUT_BYTE=MOTOR+DIRECTION;
NORMALISED=1; /* MAXY_OPEN_SCAN Normalised if NORMALISED=1 */
for (COUNTER2=0;COUNTER2<=NUMBER_OF_MOVES;COUNTER2++) /* Every 10mm */
    {for( ; ; ) {ACQUIRE_SAMPLES(); /* Infinite loop until within limits */
        GET_MAX_VALUE_OF_Y();
        cleardevice();
        setcolor(4); /* Set Color to light RED */
        settextstyle(7,0,0); /* Text Style Font,Direction(horiz or vert),Size(0) */

```

```

setusercharsize(1,1,1,1); /* This is used to size the simplex fonts */
if(MAXY_REFERENCE<LOWER_LIMIT) {outtextxy(92,200,"Reference is Low ");
continue;}
if(MAXY_REFERENCE>UPPER_LIMIT) {outtextxy(90,200,"Reference is High");
continue;}
break;}
MEAN_MAXY_REFERENCE_ARRAY[0]=MAXY_REFERENCE; /* 1st time around loop */
MEAN_MAXY_OPEN_SCAN_ARRAY[0]=MAXY_OPEN_SCAN;
MEAN_MAXY_CLOSED_SCAN_ARRAY[0]=MAXY_CLOSED_SCAN;
MEAN_MAXY_REFERENCE=MAXY_REFERENCE; /* 1st Graph turns out OK */
MEAN_MAXY_OPEN_SCAN=MAXY_OPEN_SCAN;
MEAN_MAXY_CLOSED_SCAN=MAXY_CLOSED_SCAN;
GRAPH();
COUNTER3=0; /* For Getting Sample no. to 1 in TEXT1() */
TEXT1();
for (COUNTER3=1;COUNTER3<ZSCAN_AVERAGING;COUNTER3++)
    {for( ; ) {ACQUIRE_SAMPLES(); /* Infinite loop until within limits */
        GET_MAX_VALUE_OF_Y();
        cleardevice();
        setcolor(4); /* Set Color to light RED */
        setttextstyle(7,0,0); /* Text Style Font,Direction(horiz or vert),Size(0) */
        setusercharsize(1,1,1,1); /* This is used to size the simplex fonts */
        if(MAXY_REFERENCE<LOWER_LIMIT) {outtextxy(92,200,"Reference is Low ");
        continue;}
        if(MAXY_REFERENCE>UPPER_LIMIT) {outtextxy(90,200,"Reference is High");
        continue;}
        break;}
MEAN_MAXY_REFERENCE_ARRAY[COUNTER3]=MAXY_REFERENCE;
MEAN_MAXY_OPEN_SCAN_ARRAY[COUNTER3]=MAXY_OPEN_SCAN;
MEAN_MAXY_CLOSED_SCAN_ARRAY[COUNTER3]=MAXY_CLOSED_SCAN;
MEAN_MAXY_REFERENCE=0; /* To get loop to work */
MEAN_MAXY_OPEN_SCAN=0;
MEAN_MAXY_CLOSED_SCAN=0;
for(COUNTER1=0;COUNTER1<ZSCAN_AVERAGING;COUNTER1++)
{MEAN_MAXY_REFERENCE=MEAN_MAXY_REFERENCE+MEAN_MAXY_REFERENCE_ARRAY[COUNTER1];
MEAN_MAXY_OPEN_SCAN=MEAN_MAXY_OPEN_SCAN+MEAN_MAXY_OPEN_SCAN_ARRAY[COUNTER1];
MEAN_MAXY_CLOSED_SCAN=MEAN_MAXY_CLOSED_SCAN+MEAN_MAXY_CLOSED_SCAN_ARRAY[COUNTER1];} /* Adding them all up! */
MEAN_MAXY_REFERENCE=MEAN_MAXY_REFERENCE/((float)(COUNTER1)); /* MAXY Ref */
MEAN_MAXY_OPEN_SCAN=MEAN_MAXY_OPEN_SCAN/((float)(COUNTER1)); /* MAXY Opn */
MEAN_MAXY_CLOSED_SCAN=MEAN_MAXY_CLOSED_SCAN/((float)(COUNTER1)); /* Clod */
GRAPH();
TEXT1();}
CURRENT_POSITION=CURRENT_POSITION+STEP_SIZE;
RESULTS_REFERENCE[COUNTER2]=MEAN_MAXY_REFERENCE; /* Array used to store the
MEAN value of REFERENCE for each Z-Stage position */
RESULTS_OPEN_SCAN[COUNTER2]=MEAN_MAXY_OPEN_SCAN; /* Array used to store the
MEAN value of OPEN_SCAN for each Z-Stage position */
RESULTS_CLOSED_SCAN[COUNTER2]=MEAN_MAXY_CLOSED_SCAN; /* Array used to store
the MEAN value of CLOSED_SCAN for each Z-Stage position */
MOVE_STAGE(); }

REFERENCE_NORMAL=(1.0/RESULTS_REFERENCE[0]); /* Normalisation for Reference */
OPEN_NORMAL=(1.0/RESULTS_OPEN_SCAN[0]); /* Normalisation constant for Open */
CLOSED_NORMAL=(1.0/RESULTS_CLOSED_SCAN[0]); /* Normalisation constant for Closed */

for (COUNTER2=0;COUNTER2<=NUMBER_OF_MOVES;COUNTER2++) {
RESULTS_REFERENCE[COUNTER2]=(RESULTS_REFERENCE[COUNTER2]*REFERENCE_N
ORMAL); /* To normalise to 1 */

```



```
for (COUNTER1=0;COUNTER1<NUMBER_OF_STEPS_PER_MOVE;COUNTER1++) {
outportb(COM,OUT_BYTE); /* C function to send info to hardware port */
delay(DELAY_MOTOR);}}
```

```
/****** Subroutine used in MOVE_STAGE *****/
```

```
void SET_ZERO_POSITION() {
DIRECTION=0; /* Moving away from MOTOR */
OUT_BYTE=MOTOR+DIRECTION;
for
(COUNTER1=0;COUNTER1<(NUMBER_OF_STEPS_PER_MOVE*(NUMBER_OF_MOVES+1));C
OUNTER1++) {
outportb(COM,OUT_BYTE); /* C function to send info to hardware port */
delay(DELAY_MOTOR);}}
```

```
/******/
```

```
void interrupt SIO_HANDLER(void) {
RETURN=inportb(COM);
X++;
outportb(0x20,0x20); }
```

```
/******/
```

```
int SET_UP_STEPPER_MOTOR(void) { /* Port 2 is Used */
COM=0x2f8;
INTR_NO=11;
outportb(0x2fb,0x83);
outportb(0x2f8,0x06);
outportb(0x2f9,0);
outportb(0x2fb,0x03);
X=0;
OMASK=inportb(0x21);
NMASK=OMASK & 0x0;
outportb(0x21,NMASK);
outportb(INT_EN2,1);
outportb(MOD_CON2,0x0b);
disable();
setvect(INT_NO2, SIO_HANDLER);
enable();
inportb(COM);
return 1;}
```

```
/****** Function for Getting Maximum Value of Y *****/
```

```
void GET_MAX_VALUE_OF_Y() {
MAXY_REFERENCE=fabs(REFERENCE[0]); /* First Point in the Array */
MAXY_OPEN_SCAN=fabs(OPEN_SCAN[0]); /* First Point in the Array */
MAXY_CLOSED_SCAN=fabs(CLOSED_SCAN[0]); /* First Point in the Array */
for (COUNTER1=0;COUNTER1<(SAMPLES_REQUESTED-1);COUNTER1++)
{if(MAXY_REFERENCE<(fabs(REFERENCE[COUNTER1+1])))
MAXY_REFERENCE=REFERENCE[COUNTER1+1];
if(MAXY_OPEN_SCAN<(fabs(OPEN_SCAN[COUNTER1+1])))
MAXY_OPEN_SCAN=OPEN_SCAN[COUNTER1+1];
if(MAXY_CLOSED_SCAN<(fabs(CLOSED_SCAN[COUNTER1+1])))
MAXY_CLOSED_SCAN=CLOSED_SCAN[COUNTER1+1];}
if(NORMALISED==1)
{MAXY_OPEN_SCAN=((MAXY_OPEN_SCAN/MAXY_REFERENCE)*LASER_STABILITY);
/* Normalise each pulse to the ref channel (LASER_STABILITY give values close to originals) */
MAXY_CLOSED_SCAN=((MAXY_CLOSED_SCAN/MAXY_REFERENCE)*LASER_STABILITY);}
/* Normalise each pulse to the ref channel (LASER_STABILITY give values close to originals) */
} /* End of Function */
```

```
/****** Function for Acquiring ONE Set of Samples *****/
```

```
void ACQUIRE_SAMPLES() {
ADC_VAR_A[0] = SAMPLES_REQUESTED; /* Between 0 - 65535 (Fast Mem on board = 64K) */
```

```

ADC_VAR_A[1] = 0; /* This means ZERO multiples of 65535 Samples */
CCALL("H", ANALOGBUF, ADC_VAR_A); /* Synchronized Analog Read 'H' For Fast Mode (The
Sampled Array is Stored in the Array ANALOGBUF) */
for (COUNTER1=0;COUNTER1<SAMPLES_REQUESTED;COUNTER1++) /* This for Loop
Assigns the ANALOGBUF values to their respective REFERENCE,2,3 Arrays */
{REFERENCE[COUNTER1]=ANALOGBUF[((3*COUNTER1)+0)];
OPEN_SCAN[COUNTER1]=ANALOGBUF[((3*COUNTER1)+1)];
CLOSED_SCAN[COUNTER1]=ANALOGBUF[((3*COUNTER1)+2)];}

/***** Set UP the ADC Card with all the Necessary Shit! *****/
void SET_UP_ADC_CARD() {
ADC_VAR_A[0]=NUMCHANNELS; /* ADC_VAR_A is used to program the ADC Card */
CCALL("N", ANALOGBUF, ADC_VAR_A); /* Tells ADC Card to sample 3 Analog Input channels */
ADC_VAR_A[0]=1; /* Sets the channel sequence 1 to reading channel 1 , want 1,3,5 */
ADC_VAR_A[1]=3; /* Sets the channel sequence 2 to reading channel 3, want 1,3,5 */
ADC_VAR_A[2]=5; /* Sets the channel sequence 3 to reading channel 5, want 1,3,5 */
CCALL("p", ANALOGBUF, ADC_VAR_A); /* ADC Card reads Input channels in sequence 1, 3, 5 */
ADC_VAR_A[0]=12; /* Set Resolution of ALL Input channels to 12 Bit Resolution */
CCALL("a", ANALOGBUF, ADC_VAR_A); /* Sets 12 Bit Resolution on ALL Input Channels */
CCALL("c", ANALOGBUF, ADC_VAR_A); /* Calibrate ALL Input Channels */
ANALOGBUF[0]=DELAY; /* Delay for all Channel 1 is 1 millisecond */
ANALOGBUF[1]=DELAY; /* Delay for all Channel 2 is 1 millisecond */
ANALOGBUF[2]=DELAY; /* Delay for all Channel 3 is 1 millisecond */
CCALL("j", ANALOGBUF, ADC_VAR_A); /* Set Delay for all Channels to 1 millisecond */
ADC_VAR_A[0]=0; /* Gain Range 0->+10V */
ADC_VAR_A[1]=0; /* Gain Range 0->+10V */
ADC_VAR_A[2]=0; /* Gain Range 0->+10V */
CCALL("r", ANALOGBUF, ADC_VAR_A); /* Set Gain Ranges for all channels to 0->+10V */
VOLTAGE=VOLTAGE/0.078125; /* Convert to a value from 0-128 */
VOLTAGE=VOLTAGE+0.5; /* Add 0.5 So Can Easily Round up to the Nearest Integer */
TRIGGERLEVEL=VOLTAGE; /* Convert from float to Integer */
TRIGGERLEVEL=128+TRIGGERLEVEL; /* Add 128 to make TrigLvl 0-10V */
ADC_VAR_A[0] = 0; /* Used to Shift the Board in & out of Extended Buffering Mode */
ADC_VAR_B[0] = USE_EXTENDED_BUFFER; /* Setting up the Parameter set */
ADC_VAR_B[1] = RESET; /* Setting up the Parameter set */
ADC_VAR_B[2] = RETRIGGER; /* Setting up the Parameter set */
ADC_VAR_B[3] = TRIGGERED; /* Setting up the Parameter set */
CCALL("P", ADC_VAR_B, ADC_VAR_A); /* Put the Parameter Set Settings in Place */
ADC_VAR_A[0] = 1; /* Used to set the Extended Buffering Parameters */
ADC_VAR_B[0] = SAMPLES_REQUESTED; /* Set High Speed Extended Buffering Parameters
(This number has to be between 0 and 65535 (Max Fast Memory on board = 64K)) */
ADC_VAR_B[1] = 0; /* High Speed Extended Buffering Parameters (Multiples of 65535 Points)*/
CCALL("P", ADC_VAR_B, ADC_VAR_A); /* High Speed Extended Buffering Parameters */
ADC_VAR_A[0] = 2; /* Used to set the High Speed Trigger Parameters */
ADC_VAR_B[0] = TRIGGERMODE;
ADC_VAR_B[1] = TRIGGERLEVEL;
ADC_VAR_B[2] = 65535; /* Timeout for Auto Mode (Auto Mode is not Enabled Here!) */
ADC_VAR_B[3] = 100; /* This is if it has a huge (>65535) Timeout */
ADC_VAR_B[4] = PRETRIGGER; /* Low Word (This number has to be between 0 and 65535 (Max
Fast Memory on board = 64K)) */
ADC_VAR_B[5] = 0; /* High Word (This is for Multiples of 65535 pretrigger points) */
CCALL("P", ADC_VAR_B, ADC_VAR_A); } /* Set the High Speed Trigger Parameters */

/***** Function for Initialising Graphics Mode *****/
void SET_UP_GRAPHICS() { /* Start up the Graphics mode & shit */
int gdriver = VGA, gmode=VGAHI, errorcode; /* VGA Graphics Driver with 640*480*16 Mode */
initgraph(&gdriver, &gmode, ""); /* Initialize Graphics Mode (EGAVGA.BGI in Current directory) */
setrgbpalette(60,20,20,20); /* Changed palette color 12 to very dark Grey - Used to change the
Colors of any of the 16 components of the palette to R,G,B values - Palette colors are 1-16
corrospnd to 1,2,3,4,5,6,7,56,57,58,59,60,61,62,63 */
setrgbpalette(62,24,24,24); /* Changed palette color 14 to lighter Very Dark Grey */
setrgbpalette(1,36,36,63); /* Changed palette color 1 (Blue) to Light Blue */

```

```

setrgbpalette(4,63,28,28); /* Changed palette color 4 (Red) to Light Red */
setrgbpalette(2,0,63,0);} /* Changed palette color 2 (Green) to Light Green */

/***** Function for Graphing Samples & Z-scan Results *****/
void GRAPH() {
cleardevice(); /* Clears the entire screen */
setlinestyle(0,0,3); /* Linestyle Solid Line,Solid Fill,3 Pixels thick */
setcolor(15); /* Hopefully White */
line(0,40,0,440);line(0,440,639,440); /* Drawing a Rectangular Border */
line(639,440,639,40);line(639,40,0,40); /* Drawing a Rectangular Border */
line(20,440,20,445);line(120,440,120,445);
line(220,440,220,445);line(320,440,320,445);
line(420,440,420,445);line(520,440,520,445);
line(620,440,620,445);

if(ZSCAN==0){ /* If it's NOT the Z-Scan plot then it draws in reference lines */
setlinestyle(1,0,1); /* Linestyle Dotted Line,Solid Fill,1 Pixels thick */
setcolor(12); /* Set pixel color to Very Dark Grey */
line(0,65,637,65);line(0,90,637,90);line(0,115,637,115); /* Draw some Gridlines */
line(0,165,637,165);line(0,190,637,190);line(0,215,637,215); /* Draw some Gridlines */
line(0,265,637,265);line(0,290,637,290);line(0,315,637,315); /* Draw some Gridlines */
line(0,365,637,365);line(0,390,637,390);line(0,415,637,415); /* Draw some Gridlines */
setcolor(14); /* Set pixel color to lighter Very Dark Grey */
line(0,140,637,140);line(0,240,637,240);line(0,340,637,340); /* Draw some Gridlines */
setcolor(13); /* Set Color to light Magenta */
settextstyle(7,0,0); /* Text Style Font,Direction(horiz or vert),Size(0) */
setusercharsize(2,1,19,20); /* This is used to size the simplex fonts */
outtextxy(75,0,"Sampled Pulse"); /* This prints text to the graphics screen */
settextstyle(2,0,0); /* Text Style Font,Direction(horiz or vert),Size(0) */
setusercharsize(1,1,1,1); /* This is used to size the simplex fonts */
outtextxy(265,460,"Time (Microseconds)"); /*This prints text to the graphics screen */
setcolor(15); /* Set Color to White */
outtextxy(18,446,"0"); /* This prints text to the graphics screen */
outtextxy(112,446,"100"); /* This prints text to the graphics screen */
outtextxy(212,446,"200"); /* This prints text to the graphics screen */
outtextxy(312,446,"300"); /* This prints text to the graphics screen */
outtextxy(412,446,"400"); /* This prints text to the graphics screen */
outtextxy(512,446,"500"); /* This prints text to the graphics screen */
outtextxy(612,446,"600"); /* This prints text to the graphics screen */

for (COUNTER1=0;COUNTER1<SAMPLES_REQUESTED;COUNTER1++)
{XVALUE=((3*COUNTER1+0)+20);
YVALUE=440-((fabs(REFERENCE[COUNTER1]*200))+0.5); /* Add 0.5 to help round off */
setcolor(1); /* Blue */
circle(XVALUE,YVALUE,1);
XVALUE=((3*COUNTER1+1)+20);
YVALUE=440-(fabs(OPEN_SCAN[COUNTER1]*200));
setcolor(4); /* Red */
circle(XVALUE,YVALUE,1);
XVALUE=((3*COUNTER1+2)+20);
YVALUE=440-(fabs(CLOSED_SCAN[COUNTER1]*200));
setcolor(2); /* Green */
circle(XVALUE,YVALUE,1);}

} /* End of If loop for Z-Scan */

else {
setcolor(13); /* Set Color to light Magenta */
settextstyle(7,0,0); /* Text Style Font,Direction(horiz or vert),Size(0) */
setusercharsize(2,1,19,20); /* This is used to size the simplex fonts */
outtextxy(95,0,"Z-Scan Data"); /* This prints text to the graphics screen */
settextstyle(2,0,0); /* Text Style Font,Direction(horiz or vert),Size(0) */

```



```

setusercharsize(1,1,1,1); /* This is used to size the simplex fonts */
outtextxy(260,460,"Distance (Millimeters)"); /*This prints text to the graphics screen */
setcolor(15); /* Set Color to White */
outtextxy(18,446,"0"); /* This prints text to the graphics screen */
outtextxy(118,446,"5"); /* This prints text to the graphics screen */
outtextxy(215,446,"10"); /* This prints text to the graphics screen */
outtextxy(315,446,"15"); /* This prints text to the graphics screen */
outtextxy(415,446,"20"); /* This prints text to the graphics screen */
outtextxy(515,446,"25"); /* This prints text to the graphics screen */
outtextxy(615,446,"30"); /* This prints text to the graphics screen */

for (COUNTER1=0;COUNTER1<=(NUMBER_OF_MOVES);COUNTER1++) /* Two Channels
(Open & Closed) */
{XVALUE=((20*COUNTER1+0)+20);
YVALUE=440-((fabs(RESULTS_REFERENCE[COUNTER1]*200))+0.5); /* Add 0.5 to round off */
  setcolor(1); /* Blue */
  circle(XVALUE,YVALUE,2);
  XVALUE=((20*COUNTER1+1)+20);
  YVALUE=440-(fabs(RESULTS_OPEN_SCAN[COUNTER1]*200));
  setcolor(4); /* Red */
  circle(XVALUE,YVALUE,2);
  XVALUE=((20*COUNTER1+2)+20);
  YVALUE=440-(fabs(RESULTS_CLOSED_SCAN[COUNTER1]*200));
  setcolor(2); /* Green */
  circle(XVALUE,YVALUE,2);}
} /* End of else loop */
} /* End of Graph */

void TEXT1() {
settextstyle(2,0,0); /* Text Style Font,Direction(horiz or vert),Size(0) */
setusercharsize(1,1,2,1); /* This is used to size the simplex fonts */
setcolor(1); /* Blue */
outtextxy(30,45,"Max Reference ="); /* This prints text to the graphics screen */
sprintf(TEXT,"%5.3f",MAXY_REFERENCE);
outtextxy(125,45,TEXT);
outtextxy(30,65,"MEAN Reference ="); /* This prints text to the graphics screen */
sprintf(TEXT,"%5.3f",MEAN_MAXY_REFERENCE);
outtextxy(130,65,TEXT);
setcolor(4); /* Red */
outtextxy(245,45,"Max Open Scan ="); /* This prints text to the graphics screen */
sprintf(TEXT,"%5.3f",MAXY_OPEN_SCAN);
outtextxy(340,45,TEXT);
outtextxy(245,65,"MEAN Open Scan ="); /* This prints text to the graphics screen */
sprintf(TEXT,"%5.3f",MEAN_MAXY_OPEN_SCAN);
outtextxy(345,65,TEXT);
setcolor(15); /* White */
outtextxy(135,85,"Current Position ="); /* This prints text to the graphics screen */
sprintf(TEXT,"%4.2f",CURRENT_POSITION);
outtextxy(245,85,TEXT);
outtextxy(375,85,"Sample Number ="); /* This prints text to the graphics screen */
sprintf(TEXT,"%3i",COUNTER3+1);
outtextxy(473,85,TEXT);
setcolor(2); /* Green */
outtextxy(475,45,"Max Closed Scan ="); /* This prints text to the graphics screen */
sprintf(TEXT,"%5.3f",MAXY_CLOSED_SCAN);
outtextxy(580,45,TEXT);
outtextxy(475,65,"MEAN Closed Scan ="); /* This prints text to the graphics screen */
sprintf(TEXT,"%5.3f",MEAN_MAXY_CLOSED_SCAN);
outtextxy(585,65,TEXT);}

void TEXT2() {
settextstyle(2,0,0); /* Text Style Font,Direction(horiz or vert),Size(0) */

```

```

setusercharsize(1,1,2,1); /* This is used to size the simplex fonts */
setcolor(1); /* Blue */
outtextxy(30,45,"Max Reference ="); /* This prints text to the graphics screen */
sprintf(TEXT,"%5.3f",MAXY_REFERENCE);
outtextxy(125,45,TEXT);
setcolor(4); /* Red */
outtextxy(245,45,"Max Open Scan ="); /* This prints text to the graphics screen */
sprintf(TEXT,"%5.3f",MAXY_OPEN_SCAN);
outtextxy(340,45,TEXT);
setcolor(2); /* Green */
outtextxy(475,45,"Max Closed Scan ="); /* This prints text to the graphics screen */
sprintf(TEXT,"%5.3f",MAXY_CLOSED_SCAN);
outtextxy(580,45,TEXT);}

void TEXT3() { /* Laser Stability */
settextstyle(2,0,0); /* Text Style Font,Direction(horiz or vert),Size(0) */
setusercharsize(1,1,2,1); /* This is used to size the simplex fonts */
setcolor(1); /* Blue */
outtextxy(30,45,"Max Reference ="); /* This prints text to the graphics screen */
sprintf(TEXT,"%5.3f",MAXY_REFERENCE);
outtextxy(125,45,TEXT);
outtextxy(245,45,"Mean Reference ="); /* This prints text to the graphics screen */
sprintf(TEXT,"%5.3f",LASER_STABILITY);
outtextxy(347,45,TEXT);}

void TEXT4() { /* Press a Key - X to Exit */
settextstyle(2,0,0); /* Text Style Font,Direction(horiz or vert),Size(0) */
setusercharsize(1,1,2,1); /* This is used to size the simplex fonts */
setcolor(13); /* LIGHT RED */
outtextxy(308,70,"X to Exit"); /* This prints text to the graphics screen */

void INTRODUCTION_SCREEN() { /* Introduction Screen */
setcolor(13); /* Set Color to light Magenta */
settextstyle(7,0,0); /* Text Style Font,Direction(horiz or vert),Size(0) */
setusercharsize(1,1,1,1); /* This is used to size the simplex fonts */
outtextxy(50,110,"Welcome to the World of Z-SCAN"); /* This prints text to the graphics screen */
settextstyle(2,0,0); /* Text Style Font,Direction(horiz or vert),Size(0) */
setusercharsize(1,1,2,1); /* This is used to size the simplex fonts */
outtextxy(200,225,"Program by Kieran Ryder : Copyright 1998"); /* Text to the graphics screen */
delay(1000);
cleardevice(); } /* Clears the entire screen */

```

---

## Z-Scan.BAT

```

@ECHO OFF
CD\
CD\APPLICS\ZSCAN
ZSCAN \USER\KIERAN\ 1 0.25 100 800 0.5 0
CD\
CD \USER\KIERAN\

```

The path is the directory that you want the data files saves in .

The first number is the total distance the z-stage moves in mm's (1 2 3 4 5 6 7 8 9 10 11 12 13 14 15 16 17 18 19 20 21 22 23 24 25 26 27 28 29 30)

The second number is the step size - the distance between successive steps (0.1 0.2 0.25 0.5 1.0 2.0 2.5)

The third number is the number of data points that pulse's are digitised to 50 75 100 125 150 175 200

The fourth number is the resolution of the stepper motor i.e. the number of steps in takes to move the stepper motor 1mm : 800 for Yag Lab stepper : 80 for N2 Dye Laser stepper

REM The fifth number is the trigger voltage (0->10 volts)

REM The sixth number is the number of points to be samples before the trigger (has to be less than the number of samples requested)